Identifying the molecular determinants of autophagic and mitophagic cell death

Dissertation

zur Erlangung des Doktorgrades

der Naturwissenschaften

vorgelegt am Fachbereich 14

der Johann Wolfgang Goethe-Universität

in Frankfurt am Main

von

Lisa Reisbeck

aus Frankfurt am Main

Frankfurt (2023)

(D 30)

Vom Fachbereich 14 der

Johann Wolfgang Goethe – Universität als Dissertation angenommen.

Dekan: Prof. Dr. Clemens Glaubitz

Gutachter: Prof. Dr. Rolf Marschalek

Prof. Dr. Donat Kögel

Datum der Disputation: 16.04.2024

Die Ergebnisse dieser Arbeit wurden bereits teilweise in folgenden Publikationen veröffentlicht:

Meyer N, Henkel L, Linder B, Zielke S, Tascher G, Trautmann S, Geisslinger G, Münch C, Fulda S, Tegeder I, et al. (2021). Autophagy activation, lipotoxicity and lysosomal membrane permeabilization synergize to promote pimozide- and loperamide-induced glioma cell death. *Autophagy* **11,** 3424–3443.

Reisbeck L, Linder B, Tascher G, Bozkurt S, Weber KJ, Herold-Mende C, van Wijk S, Marschalek R, Schaefer L, Münch C, et al. (2023). The iron chelator and OXPHOS inhibitor VLX600 induces mitophagy and an autophagy-dependent type of cell death in glioblastoma cells. *Am J Physiol Cell Physiol* **6,** C1451-C1469.

Table of contents

1. Introduction

1.1. Glioblastoma

The primary brain tumor glioblastoma (GBM) is the most invasive and deadliest glioma (Wilson, Karajannis and Harter 2014), representing about 50 % of all brain gliomas (Sanati et al. 2022). GBM, WHO (world health organization) grade 4, belongs to the group of adult-type diffuse gliomas and according to the 2021 WHO classification of tumors of the central nervous system represents now only *IDH1* (isocitrate dehydrogenase 1) wildtype (wt) GBM. *IDH*-mutant "GBM", which was considered to account for about 10 % of GBMs in the past (Parsons et al. 2008), is now classified as a different subtype of diffuse gliomas: either *IDH*-mutant astrocytoma or *IDH*-mutant and 1p/19q-codeleted oligodendroglioma (Louis et al. 2021). Three IDH isozymes exist: IDH1, IDH2 and IDH3 (Dalziel 1980). IDH1 is mainly cytoplasmic, while IDH2 and IDH3 are mostly present in the mitochondrial matrix (Plaut, Cook and Aogaichi 1983). IDH1 is the central enzyme in the tricarboxylic acid (TCA) cycle, catalysing the conversion of isocitrate into α-ketoglutarate, restoring NADPH (nicotinamide adenine dinucleotide phosphate hydrogen) (Geisbrecht and Gould 1999) and therefore plays a vital role in oxidative stress resistance (Shi et al. 2022). *IDH1* mutation (most common R132H (Gravendeel et al. 2010)) results in a neo-enzymatic activity of the IDH1 enzyme, converting isocitrate into 2-hydroxyglutarate, leading to decreased NADPH levels, which causes increased oxidative stress in the cells (Dang et al. 2009; Shi et al. 2022). Further, 2-hydroxyglutarate acts as a competitive inhibitor of α-ketoglutarate-dependent enzymes involved in collagen folding and maturation, HIF (hypoxia inducible factor) signaling and epigenetic regulation like deoxyribonucleic acid (DNA) and histone methylation (Cairns and Mak 2013). Interestingly, patients with *IDH1*-mutant glioma have a more favourable outcome compared to *IDH1*-wt GBM (Parsons et al. 2008), which may be explained by the fact that the loss of function of wt *IDH1* as an important component in the antioxidative defence machinery as well as in anti-apoptotic mechanisms may sensitize the tumor cells to oxidative stress and cell death (Mohrenz et al. 2013). Furthermore, typical molecular changes of GBM cells comprise *TERT* (telomerase reverse transcriptase)-promoter mutations, *EGFR* (epidermal growth factor receptor) amplification as well as gain of chromosome 7 paired with the loss of chromosome 10 (Louis et al. 2021).

Based on gene expression profiles, Phillips et al. (2006) described three GBM subtypes namely proneural, proliferative and mesenchymal. While the proneural subtype shows a better prognosis, the proliferative subtype that is characterized by an increased expression of genes indicative for cell proliferation, and the mesenchymal subtype, which activates gene expression programs representative of angiogenesis, have a poorer prognosis (Table 1). In 2010, Verhaak et al. expanded this classification and described four distinct subtypes: proneural, neural, classical and mesenchymal. As shown in Table 1 and Table 2 the proliferative subtype was subdivided into the classical and neural subtypes. The classical subtype is characterized by chromosome 7 amplification paired with chromosome 10 loss, *EGFR* amplification and the expression of neural precursor and stem cell markers like *NES* (nestin), *NOTCH3* (notch receptor 3) and *GLI2* (GLI family zinc finger 2), whereby the neural subtype is distinguished by the expression of neuron markers like *NEFL* (neurofilament light chain), *GABRA1* (gamma-aminobutyric acid type A receptor subunit alpha1), *SYT1* (synaptotagmin 1) and *SLC12A5* (solute carrier family 12 member 5). The mesenchymal subtype is defined by the expression of genes of the NF-κB pathway like *TRADD* (TNFRSF1A associated via death domain) and *RELB* (RELB proto-oncogene, NF-kB subunit), the expression of mesenchymal markers like *CHI3L1* (chitinase 3 like 1), *MET* (MET proto-oncogene, receptor tyrosine kinase) and *CD44* (CD44 molecule) and is the most aggressive subtype with the worst prognosis (Verhaak et al. 2010). Of note, research is still ongoing and the methods for genetic analysis are constantly improving, resulting in the regularly adjustment and update of the molecular classifications for GBM. Therefore, currently brain tumors are classified as GBM by histological and molecular features when exhibiting one or more of the following characteristics: microvascular proliferation, necrosis, *TERT* (telomerase reverse transcriptase)-promoter mutation, *EGFR* gene amplification, gain of chromosome 7 and/or loss of chromosome 10. Further, GBM can be divided into histological- and molecular-GBM, depending on the histological and molecular characteristics (Guo et al. 2023).

Table 1. Transcriptional classification of GBM tumors and typical genetic alterations. Based on Phillips et al. (2006) and adapted from Zhang et al. (2020).

	Proneural	**Proliferative**	**Mesenchymal**
Chromosome gain/loss	None	Gain on chr. 7, loss on chr. 10	Gain on chr. 7, loss on chr. 10
Biological process	Neurogenesis	Proliferation	Angiogenesis

Table 2. Transcriptional classification of GBM tumors and typical genetic alterations. Based on Verhaak et al. (2010) and adapted from Zhang et al. (2020)**.** *TP53* (tumor protein p53), *PIK3CA* (phosphatidylinositol-4,5-bisphosphate 3-kinase catalytic subunit alpha), *PDGFRA* (platelet derived growth factor receptor alpha), *NKX2-2* (NK2 homeobox 2), *OLIG2* (oligodendrocyte transcription factor 2), *SOX* (SRY-box transcription factor), *DCX* (doublecortin), *DLL3* (delta like canonical Notch ligand 3), *ASCL1* (achaete-scute family bHLH transcription factor 1), *TCF4* (transcription factor 4), *PTEN* (phosphatase and tensin homolog), *CDKN2A* (cyclin dependent kinase inhibitor 2A), *NF1* (neurofibromin 1).

	Proneural	**Neural**	**Classical**	**Mesenchymal**
Genetic alterations	*TP53*, *PIK3CA*, *IDH1*, *PDGFRA*		*PTEN*, *CDKN2A*, *EGFR*	*NF1*, *PTEN*
Marker expression	Oligodendrocytic development genes (*PDGFRA*, *NKX2-2*, *OLIG2*); Proneural development genes (*SOX*, *DCX*, *DLL3*, *ASCL1*, *TCF4*)	Neuron markers (*NEFL*, *GABRA1*, *SYT1*, *SLC12A5*)	Neural precursor and stem cell markers (*NES*, *NOTCH3*, *GLI2*)	NF-κB pathway (*TRADD*, *RELB*) and mesenchymal markers (*CHI3L1*, *MET*, *CD44*)

Recently, Garofano et al. (2021) further described four tumor states reliant on single cell ribonucleic acid (RNA)-sequencing, depending on either neurodevelopmental (neuronal, proliferative/progenitor) or metabolic (mitochondrial, glycolytic/plurimetabolic) features. The neuronal subgroup was defined to be characterized by the expression of neuronal markers at various stages of maturation as well as the enrichment of genes related, for example, to synapsis transmission and axonogenesis. The proliferative/progenitor subgroup was enriched in cells exhibiting neural progenitor features together with the enrichment of pathways associated with cell cycle progression, DNA replication, mitosis and DNA damage repair. The mitochondrial phenotype was described to rely exclusively on oxidative phosphorylation (OXPHOS) for energy production and thereto exhibited marked vulnerability to inhibitors of OXPHOS, whereby the glycolytic/plurimetabolic state was sustained by a large array of metabolic activities, including aerobic glycolysis as well as the metabolism of lipids, amino acids, steroids, iron and sulfur but excluded OXPHOS activities (Garofano et al. 2021).

Moreover, clinical studies showed that GBM cells are able to switch between different subtypes and especially important seems to be the switch to the mesenchymal subtype over the course of disease progression or recurrence (Matsumoto et al. 2022). The existence of

those different GBM subtypes as well as the fact that tumor cells can shift between them may explain the intra- and inter-tumoral heterogeneity that is one of the crucial factors hindering the therapeutic progress of GBM (Ichikawa et al. 2016).

1.1.1. New treatment perspectives

The standard therapy for GBM consists of a maximal safe surgical resection followed by long-course chemoradiotherapy with temozolomide (TMZ) over 6 weeks and subsequent monthly cycles of TMZ over 6 months (Stupp et al. 2005). The adjuvant treatment with tumor treating fields (TTF) to the 6 months of TMZ may be considered since clinical trials showed an improvement of the median overall survival of 4.9 months (Stupp et al. 2017). Nevertheless, the median overall survival is only 20.9 months after initial diagnosis (Stupp et al. 2017) and only about 6 months after recurrence for both TTF or chemotherapy alone (Stupp et al. 2012). As already mentioned, the tumor heterogeneity of GBM is one of the crucial factors hindering therapeutic success, but also the resistance to standard therapies including radiation and chemotherapy. Further, the high invading capacity of GBM cells, infiltrating the surrounding brain parenchyma, makes recurrence nearly unavoidable (Cuddapah et al. 2014; Yalamarty et al. 2023). Therefore, it is of great importance to investigate alternative treatment strategies. TTF was the first improvement since TMZ, increasing patient survival for a few months. TTF is an antimitotic treatment that selectively affects rapidly dividing tumor cells, leading to mitotic arrest and apoptosis. The low-intensity, intermediate-frequency (200 kHz) alternating electric fields are delivered via transducer arrays attached to the scalp and should be applied for at least 18 hours a day (Kirson et al. 2007; Giladi et al. 2015). In a clinical study by Stupp et al. (2017), the frequency of systemic adverse events was only slightly increased from 44 % in the TMZ-alone group to 48 % in the TTF-TMZ group, but 52 % of patients who received TTF-TMZ observed mild to moderate skin toxicity underneath the transducer arrays. However, the median overall survival was still only 20.9 months as compared to 16.0 months in the TMZ-alone group, underlining the importance for further research in this field.

Therapy research for GBM may include, but is not limited to, precision medicine, immunotherapy and repurposed medication (Figure 1). Precision medicine has the goal to develop individualized therapies for each patient, depending on the key genomic alterations of the respective tumor. Recently, a clinical trial used next-generation sequencing to identify targetable molecular alterations in newly diagnosed and recurrent GBM patients, for example,

CDKN2A, EGFR amplification and mutation, *PTEN* loss, *RB1* (RB transcriptional corepressor 1), *PIK3CA* and many other (Padovan et al. 2022). In addition, studies are currently ongoing analysing individualized treatments for specific mutation-positive gliomas, for example, using the BRAF (B-Raf proto-oncogene, serine/threonine kinase) inhibitor dabrafenib plus the MEK (MAP2K, mitogen-activated protein kinase) inhibitor trametinib for $BRAF^{V600E}$ mutation-positive high-grade and low-grade gliomas (NCT02034110) (Wen et al. 2022) or the NTRK (neurotrophic receptor tyrosine kinase) inhibitor larotrectinib for NTRK fusion-positive primary central nervous system tumors demonstrating stable responses (NCT02637687) (Doz et al. 2022). Possible difficulties may include tumor heterogeneity due to clonal evolution and molecular changes after recurrence, as well as potential poor target engagement.

Immunotherapy may include immune checkpoint blockade, cancer vaccines, virus-based therapy and cellular immunotherapy (Sim, Lorrey and Khasraw 2023). It should be noted that the immune microenvironment in the brain is highly distinct compared to other organs, which has to be taken into account (Sampson et al. 2020). Cancer vaccines can be used to induce immune responses against specific tumor-associated antigens. For example, rindopepimut is a peptide vaccine that targets the *EGFRvIII* mutation that is frequently expressed in GBM. Several clinical trials evaluated rindopepimut (CDX-110) in newly diagnosed or recurrent *EGFRvIII*-expressing GBM, showing an increased median overall survival of the vaccinated patients compared to the control group (NCT00458601, NCT00643097) (Sampson et al. 2010; Schuster et al. 2015). However, the follow up randomised, double-blind phase 3 trial was not able to validate those results, concluding no significant difference in the overall survival for vaccinated patients vs. the control cohort (NCT01480479) (Weller et al. 2017).

Further, virus-based therapies use oncolytic viruses to directly lyse tumor cells or use viral vectors that harbour novel genes to deliver them into cancer cells (Sim, Lorrey and Khasraw 2023). For example, the triple-mutated third-generation oncolytic herpes simplex virus type 1 G47Δ was used in a phase 2 single-arm trial in patients with residual or recurrent GBM after radiation therapy and TMZ, resulting in a survival benefit and a good safety profile, which led to the approval of G47Δ as the first oncolytic virus product in Japan (UMIN-CTR Clinical Trial Registry UMIN000015995) (Todo et al. 2022).

Repurposed medications aim to use already existing and well-tolerated medications that may show favourable effects against GBM. A phase 1b/2a trial investigated nine repurposed drugs

combined with TMZ for recurrent GBM, which were well-tolerated, but there was no evidence of any benefit from this regimen maybe also because of small patient number (NCT02770378) (Halatsch et al. 2021). In summary, the last decades show that efficient treatment of GBM remains exceedingly difficult. Nevertheless, there is no lack of innovative ideas and therefore several new treatment regimens are under clinical testing that hopefully may prolong patient survival in the future.

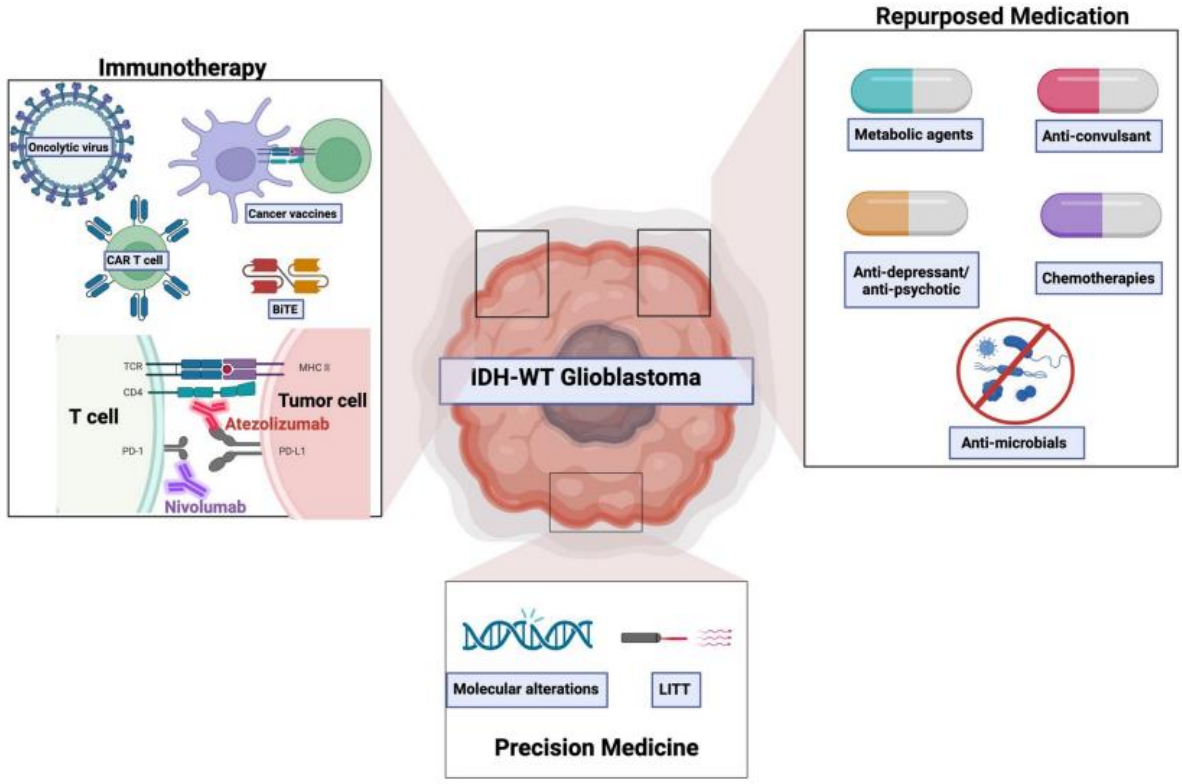

Figure 1. Novel treatment strategies currently investigated for GBM therapy. Three different fields of GBM therapy developed: immunotherapy, precision medicine and repurposed medication. Immunotherapy includes oncolytic viruses, cancer vaccines, and CAR (chimeric antigen receptor) T cells used to prime the immune cells for specific targets on the cancer cells. Precision medicine aims to tailor individualised medicine for each patient depending on the molecular alterations of the respective tumor and repurposed medication uses already developed and licensed drugs. Adapted from Sim, Lorrey and Khasraw (2023).

1.1.2. Glioma stem-like cells

Inter-tumoral as well as intra-tumoral heterogeneity are key characteristics of GBM as already suggested by the different transcriptomic subtypes (see also 1.1 Glioblastoma). The heterogeneity is thought to rely at least partly on a distinct GBM subpopulation the so-called glioma stem-like cells (GSC). GSCs, similar to conventional stem cells, have the ability to give rise to the downstream progenitor cells and differentiated cancer cells via asymmetric division, which form the main tumor mass while they renew themselves (Clarke et al. 2006; Bradshaw et al. 2016). The existence of brain cancer stem cells (CSCs) was initially discovered

in 2003, representing a new subpopulation that is thought to be largely responsible for tumor initiation, evolution, as well as the resistance to existing therapies (Singh et al. 2003). Initially, it was thought that tumor formation results from “normal” healthy cells that gather several mutations over time, resulting in the development of a highly proliferative cancer cell, which builds the whole tumor mass with all of the tumor cells harbouring the same genetic mutations (clonal evolution model). Later, after identifying the CSCs, a new model was developed where highly tumorigenic, self-renewing pluripotent CSCs are at the apex of a hierarchical organization, giving rise to the non-tumorigenic progenitor and differentiated cancer cells, forming the bulk tumor and creating an intra-tumoral phenotypic heterogeneity (Figure 2) (Kreso and Dick 2014; Bradshaw et al. 2016). Nevertheless, newer studies suggest that the CSC phenotype is not representing a rigid cellular population, but rather a plastic phenotypic state that undergoes transition in response to environmental inputs like chemotherapeutic treatments (Dirkse et al. 2019; Gupta et al. 2019; Suvà and Tirosh 2020). For example, Dirkse et al. (2019) analysed CSC markers on different GBM cultures, defined different subpopulations and revealed that most of the cultures contained a substantial amount of all identified subpopulations. Further, the authors showed that subpopulations change in response to different environmental triggers like hypoxia, differentiation inducers or TMZ treatment, which was reversible if cultures got back to the previous culture conditions. This suggests that cells expressing stem cell markers are not a rigid cell population, but somewhat a non-hierarchical, reversible state that is influenced by environmental conditions.

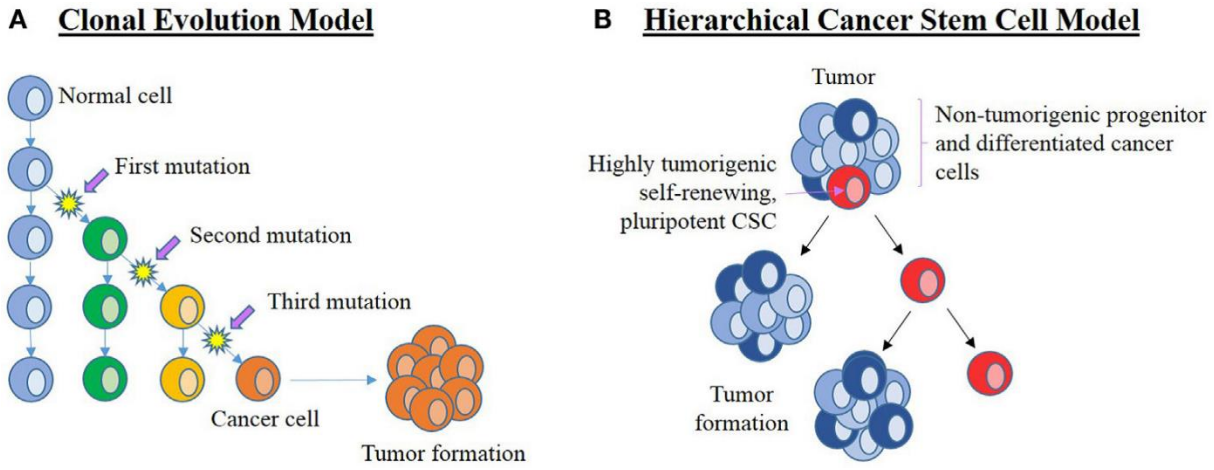

Figure 2. Tumor formation models. The initial model called clonal evolution model **(A)** describes the tumor formation as an accumulation of mutations that result in the development of a cancer cell, which give rise to all of the later tumor cells. In contrast, the hierarchical cancer stem cell model **(B)** includes cancer stem cells, which generate the non-tumorigenic progenitor and differentiated cancer cells that build the majority of the bulk tumor mass while they renew themselves at a comparatively lower rate via asymmetric division. Adapted from Bradshaw et al. (2016).

Furthermore, the existence of different metabolic phenotypes in GBM is now emerging and most likely contributes to therapy failure. Hoang-Minh et al. (2018) reported that the slow-cycling cancer stem-like cells showed heightened mitochondrial and OXPHOS activities paired with a higher sensitivity to OXPHOS inhibition, whereby the fast cycling cells that generate the main tumor mass relied more on glucose metabolism. In addition, it is increasingly recognized that GBM cells especially the GSCs can fulfil their energy demands also through alternative pathways like glutaminolysis (Yang et al. 2009; Venneti et al. 2015) or lipid metabolism (Lin et al. 2017). These observations further underscore the high variability of GBM tumors and stands in contrast to the initial hypothesis by Otto Warburg that cancer cells mainly maintain their energy demands through increased glycolysis and not via OXPHOS even when oxygen is sufficiently present (Warburg, Wind and Negelein 1927; Warburg 1956). Therefore, it will be of great importance to enhance the understanding of the intrinsic heterogeneity of GBM tumors to better tailor individualized therapies.

1.2. Autophagy

Autophagy is a pro-survival mechanism that is activated under nutrient deprivation to supply the cells with essential metabolic building blocks and energy when they cannot be obtained from the extracellular environment. Autophagy can be classified into macroautophagy, microautophagy and chaperone-mediated autophagy. Microautophagy describes the direct engulfment of selective (including the help of chaperones) or non-selective cellular material into vesicles, originated directly from lysosomal invagination. Chaperone-mediated autophagy includes the participation of the cytosolic HSC70 (heat shock cognate 70) chaperone that recognizes the substrate protein and transfers it to the lysosome. Macroautophagy (hereafter referred to as autophagy, Figure 3) includes the formation of double-membraned vesicles called autophagosomes that deliver the cargo to the lysosomes. Autophagy is genetically regulated by the autophagy-related genes (ATG) originally identified in yeast (Takeshige et al. 1992; Klionsky 2007). First, the initiation membrane is formed using pre-existing membrane reservoirs from, for example, the plasma membrane (Ravikumar et al. 2010), endoplasmic reticulum (ER) (Hayashi-Nishino et al. 2009), Golgi complex (Takahashi et al. 2011) or also mitochondria (Hailey et al. 2010), however the source of origin is still under debate (Hamasaki et al. 2013; Zhen and Stenmark 2023). The expansion of the initiation membrane is regulated by the ULK1/2 (unc-51 like autophagy activating kinase 1/2) complex, consisting of ULK1/2, ATG13, ATG101, ATG9 and RB1CC1 (RB1 inducible coiled-coil 1), resulting in the formation of

the phagophore (Suzuki et al. 2007; Hara et al. 2008; He and Klionsky 2009; Mercer, Kaliappan and Dennis 2009). The ULK1/2 complex is regulated by mTORC1 (mammalian target of rapamycin complex 1), which binds to and phosphorylates ULK1/2 and ATG13 under nutrient rich conditions and thereby inactivates the complex. If nutrients are scarce, mTORC1 dissociates from the complex, resulting in the dephosphorylation of ULK1/2 and ATG13 and the induction of autophagy (Hosokawa et al. 2009). Further, the nucleation of the phagophore is mediated by PIK3C3/VPS34 (phosphatidylinositol 3-kinase catalytic subunit type 3), BECN1 (beclin 1), AMBRA1 (autophagy and beclin 1 regulator 1), UVRAG (UV radiation resistance associated) and Bif-1/SH3GLB1 (SH3 domain containing GRB2 like, endophilin B1) (Kihara et al. 2001; Furuya et al. 2005; Fimia et al. 2007; Takahashi et al. 2007) followed by membrane elongation regulated by two different conjugation systems: The MAP1LC3 (LC3, microtubule associated protein 1 light chain 3) and the ATG5-ATG12-ATG16L1 conjugation system. MAP1LC3 belongs to the ATG8 family, which includes the GABARAPs (GABA type A receptor-associated protein), which were initially discovered in intracellular trafficking (Sagiv et al. 2000; Mansuy et al. 2004; Chen and Olsen 2007), but were also found to be involved in autophagy and to be associated with autophagosomes (Kabeya et al. 2004; Chakrama et al. 2010). The MAP1LC3 subfamily consists of LC3A with two alternatively spliced isoforms (LC3Aα and LC3Aβ), LC3B, LC3B2 and LC3C and the GABARAP subfamily composed of 3 members, GABARAP, GABARAPL1 (GABA type A receptor associated protein like 1) and GABARAPL2 (GABA type A receptor associated protein like 2) (Wang et al. 1999; Sagiv et al. 2000; He et al. 2003; Mansuy et al. 2004; Jacquet et al. 2021). Both protein families get processed by ATG4 into the cytosolic MAP1LC3-I or GABARAP-I form, which are subsequently conjugated to the lipid phosphatidylethanolamine (PE), resulting in the membrane bound MAP1LC3-II or GABARAP-II mediated by the second ATG5-ATG12-ATG16L1 conjugation system (Ichimura et al. 2000; Kirisako et al. 2000; Kuma et al. 2002; Hanada et al. 2007). ATG12 and ATG5 are covalently conjugated mediated by the E1 activating enzyme of ATG7 and the E2 conjugating enzyme ATG10 followed by noncovalent binding of ATG16L1 (Ohsumi 2001; Mizushima et al. 2003). The mature autophagosome, including the cargo, fuses with a lysosome facilitated by RAB7A (RAB7A, member RAS oncogene family), SNARE (soluble NSF (N-ethylmaleimide sensitive fusion protein) attachment protein receptor) proteins and LAMP2 (lysosomal associated membrane protein 2), resulting in the formation of the autophagolysosome. Due to the acidic environment as well as the lysosomal hydrolases, the cargo is degraded together

with the MAP1LC3-II/GABARAP-II proteins, decorating the inside of the autophagosome (Berg et al. 1998; Wang and Klionsky 2003; Gutierrez et al. 2004; Hubert et al. 2016).

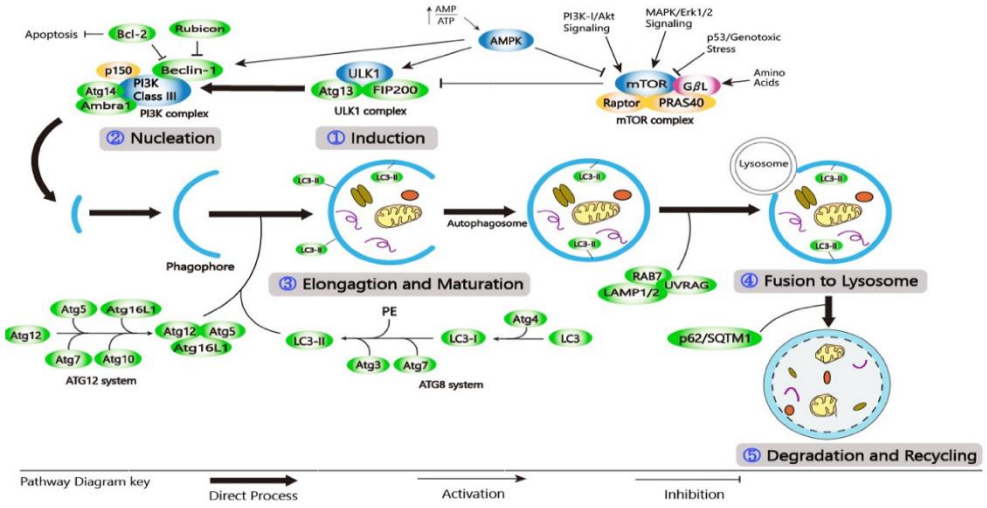

Figure 3. Molecular mechanisms of macroautophagy. The induction of autophagy starts with the ULK1 complex that is regulated by AMPK/PRKAA2 (protein kinase AMP-activated catalytic subunit alpha 2) and the mTOR (mammalian target of rapamycin) complex, sensing the nutritional status of the cell. The PIK3C3/PI3K complex regulates the nucleation of the phagophore followed by the elongation and maturation that is mediated by two conjugation systems: the ATG5-ATG12-ATG16L1 and the MAP1LC3/ATG8 conjugation system. The processing of MAP1LC3 into MAP1LC3-I and then MAP1LC3-II is mediated by ATG4, ATG3 and ATG7 and with the help of the ATG5-ATG12-ATG16L1 conjugation system MAP1LC3-II is embedded into the autophagosomal membrane, resulting in the formation of a major autophagosome that engulfs the cargo. Subsequently, the autophagosome fuses with a lysosome regulated by RAB7A (RAB7A, member RAS oncogene family), UVRAG (UV radiation resistance associated), SNARE (soluble NSF (N-ethylmaleimide sensitive fusion protein) attachment protein receptor) proteins and LAMP1/2 (lysosomal associated membrane protein 1/2), finally facilitating the degradation and recycling of the cargo. Figure adapted from Batara et al. (2021).

1.2.1. Selective forms of autophagy

The autophagic cargo can consist of unspecific “bulk”, i.e. non-selective cellular material, but also of specific substrates like organelles or bacteria (xenophagy). These selective forms of autophagy are not solely activated under nutrient starvation but also under nutrient rich conditions, serving as a quality control mechanism, recycling superfluous or damaged organelles or also as a defence mechanism against intracellular bacterial pathogens. According to the selective targets several pathways were classified, for example, mitophagy (mitochondria), lysophagy (lysosomes), aggrephagy (protein and RNA aggregates), xenophagy (intracellular pathogens), ER-phagy (ER), pexophagy (peroxisomes), ribophagy (ribosomes), ferritinophagy (ferritin) and lipophagy (lipid droplets) (Vargas et al. 2023). Selective autophagy involves distinct autophagic receptors that selectively target the cargo that is marked mostly by phosphorylation, ubiquitylation, acetylation or oligomerisation (Gubas and Dikic 2022). Those receptors, including p62/SQSTM1 (sequestosome 1), TAX1BP1 (Tax1 binding protein 1), NDP52/CALCOCO2 (calcium binding and coiled-coil domain 2), NBR1 (NBR1 autophagy cargo

receptor) and OPTN (optineurin), among others, are characterized by the presence of MAP1LC3-interacting region (LIR) domains and ubiquitin-binding domains allowing them to transfer the cargo to the MAP1LC3-II decorated autophagosomes, followed by the fusion with a lysosome and the degradation of the autophagosomal content (Kirkin and Rogov 2019).

1.2.1.1. Lysophagy

The selective removal of damaged lysosomes via the autophagic machinery is called lysophagy. Lysosomes are single membrane-bound vesicular structures that contain lysosomal hydrolases like cathepsins and harbour a low internal pH of around five, which is maintained by the v-ATPase (Mindell 2012; Gyparaki and Papavassiliou 2014; Song et al. 2020). Smaller lysosomal damage may trigger the recruitment of the ESCRT (endosomal sorting complexes required for transport) machinery, resulting from the leakage of Ca^{2+} after permeabilization of the lysosomal membrane that subsequently repairs the lysosomal damage (Radulovic et al. 2018; Skowyra et al. 2018). If the damage is too severe and cannot be fully repaired, damaged lysosomes are recognized by galectins (Radulovic et al. 2018). Galectins bind β-galactoside glycoconjugates that are located in the lysosomal lumen, which get exposed to the cytosol upon lysosomal membrane damage (Maejima et al. 2013). LGALS3 (galectin 3) may then be recognized by the E3 ubiquitin ligase TRIM16 (tripartite motif containing 16) that was reported to be necessary for the ubiquitylation of damaged lysosomes and the subsequent recruitment of the core autophagy regulators ULK1, BECN1 and ATG16L1, contributing to the autophagic sequestration of damaged lysosomes (Chauhan et al. 2016). In addition, the autophagy receptors TAX1BP1 (Tax1 binding protein 1) (Eapen et al. 2021) and SQSTM1 (Papadopoulos et al. 2017) were shown to translocate to damaged lysosomes and to be required for lysophagy as shown by CRISPR/Cas9-mediated knockout (KO) and siRNA (small interfering RNA) experiments, respectively. Moreover, the involvement of an ELDR complex (Endo-Lysosomal damage Response) was reported (Papadopoulos et al. 2017) including the AAA-ATPase p97/VCP (valosin containing protein), which translocates to damaged lysosomes facilitating their clearance by autophagy.

1.2.1.2. Mitophagy

Mitochondria are the “power houses” of the cells, producing energy in form of adenosine triphosphate (ATP) via OXPHOS that accounts for more than 90 % of the ATP produced in cells under aerobic conditions (Rodrigues and Ferraz 2020). Besides this, based on the current knowledge, mitochondria fulfil several other important cellular functions including the

participation in reactive oxygen species (ROS) (Brand 2016) and Ca^{2+} signaling (Hansford 1994; Carafoli 2003) as well as cell death (Yang et al. 1997; Kuwana et al. 2002). Therefore, a healthy mitochondrial network is of great importance for cell survival and is regulated by mitochondrial fission and fusion, the mitochondrial unfolded protein response (UPRmt) and mitophagy (Ni, Williams and Ding 2015). The dynamic fusion and fission of mitochondria is regulated, among other, by the dynamin-related GTPases mitofusin 1 and 2 as well as OPA1 (OPA1 mitochondrial dynamin like GTPase) and the dynamin-related protein 1 (DRP1/DNM1L), respectively (Friedman and Nunnari 2014; Ni, Williams and Ding 2015). The UPRmt is able to alleviate the burden of misfolded or damaged proteins mediated by chaperones such as HSP22/HSPB8 (heat shock protein family B (small) member 8), HSP60/HSPD1 (heat shock protein family D (Hsp60) member 1) and HSP70/HSPA (heat shock protein family A), acting as a first line of defence to combat insults to mitochondrial proteostasis (Moehle, Shen and Dillin 2019; Killackey, Philpott and Girardin 2020).

Mitophagy is the full selective removal of superfluous or damaged mitochondria that cannot be repaired by the previously mentioned mechanisms and therefore serves as a quality control mechanism to maintain mitochondrial homeostasis (Moehle, Shen and Dillin 2019). Similar to lysophagy, specific mitophagy receptors exist that most but not all contain a LIR domain that enables the recruitment of MAP1LC3 (and therefore autophagosomes) and are usually embedded in the outer mitochondrial membrane (OMM) (Noda, Ohsumi and Inagaki 2010; Birgisdottir, Lamark and Johansen 2013; Hamacher-Brady and Brady 2016; Wang, Liu and Lu 2019). So far, three canonical mitophagy pathways were described (Figure 4) of which the PINK1/Parkin pathway is the most studied one. Mitochondrial membrane depolarization in response to mitochondrial stress results in the accumulation of the PTEN-induced kinase 1 (PINK1) at the OMM. PINK1 recruits and activates the E3 ubiquitin ligase Parkin/PRKN (parkin RBR E3 ubiquitin protein ligase), followed by the ubiquitylation of mitochondrial proteins like the mitofusins or VDAC (voltage dependent anion channel) family members, which serves as a signal for different mitophagy receptors like OPTN (optineurin) (Wong and Holzbaur 2014) and NDP52/CALCOCO2 (calcium binding and coiled-coil domain 2) (Heo et al. 2015), facilitating the interaction with MAP1LC3 and forming a complex that is degraded by the autophagic machinery (Vara-Perez, Felipe-Abrio and Agostinis 2019). Furthermore, the mitophagy receptors BNIP3 (BCL2 interacting protein 3) and BNIP3L/NIX (BCL2 interacting protein 3 like), which belong to the BH3-only group of the BCL-2 family of proteins, can induce mitophagy

independent of PINK1 and Parkin. These proteins are located at the OMM and are able to directly bind MAP1LC3 via their LIR domains. Both are transcriptionally regulated by the hypoxia-inducible factor 1 α (HIF1A) and therefore thought to mediate hypoxia-triggered mitophagy (Bellot et al. 2009; Vara-Perez, Felipe-Abrio and Agostinis 2019). Though, in certain conditions they were reported to be also under the transcriptional regulation of FOXO3 (forkhead box O3) (Real et al. 2005; Chaanine et al. 2016) or NF-κB (Dhingra et al. 2013), suggesting their contribution in signalling pathways beyond hypoxia (Vara-Perez, Felipe-Abrio and Agostinis 2019). A third canonical mitophagy pathway involves the OMM protein FUNDC1 (FUN14-domain containing 1) that is also capable to directly bind MAP1LC3 and was shown to be regulated by phosphorylation within the LIR motif under hypoxia mediated by ULK1 (Wu et al. 2014; Vara-Perez, Felipe-Abrio and Agostinis 2019).

Apart from this, several new but less characterized receptors were described (Figure 5). For example, the OMM protein BCL2L13 (BCL2 like 13) that regulates mitophagy via binding of MAP1LC3 in addition to mediating mitochondrial fission (Murakawa et al. 2015) or PHB2 (prohibitin 2) that is an inner mitochondrial membrane (IMM) protein that regulates PINK1 stability on mitochondria and binds MAP1LC3 upon OMM rupture and is required for mitophagy following depolarization (Wei et al. 2017; Killackey, Philpott and Girardin 2020; Yan et al. 2020).

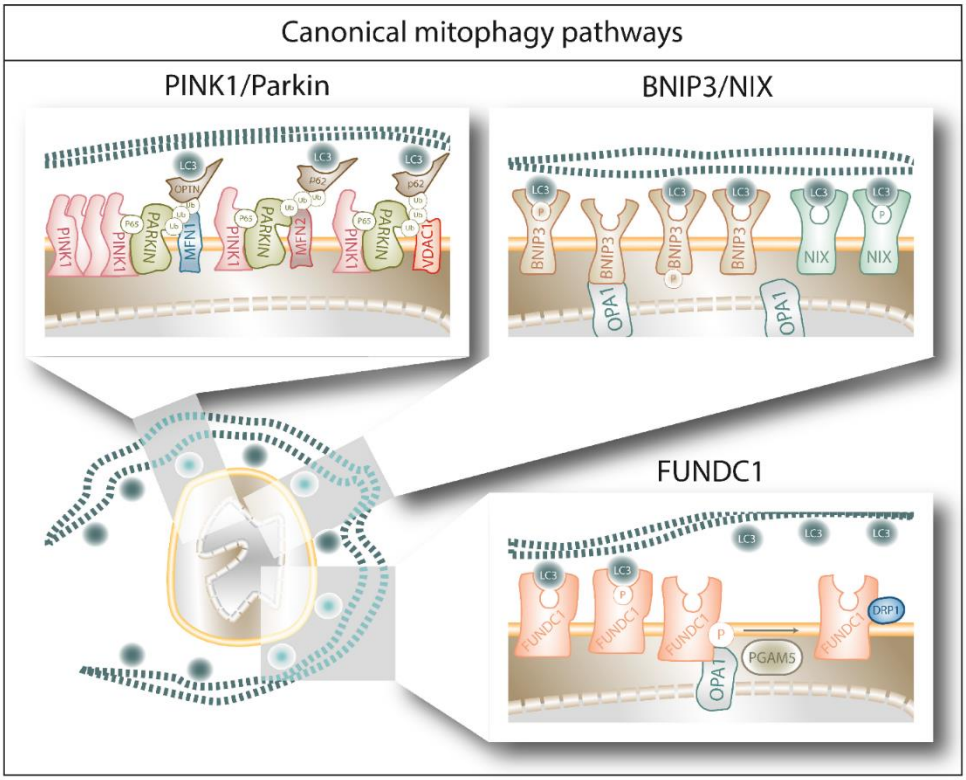

Figure 4. Canonical mitophagy pathways. Three canonical mitophagy pathways exist. The first pathway involves the kinase PINK1 that accumulates at the OMM upon mitochondrial depolarization and recruits the ubiquitin ligase Parkin that polyubiquitylates OMM proteins that further serve as a signal for different mitophagy receptors, which facilitate the sequestration by autophagosomes. The mitophagy receptors BNIP3 and BNIP3L/NIX mediate the second mitophagy pathway mainly under hypoxia. Both contain a LIR motif and thus are able to directly bind MAP1LC3 moderating the delivery to the autophagosomes. The third and last pathway is executed by the OMM protein FUNDC1 that is also capable to directly bind MAP1LC3 at the autophagosomal membrane. Adapted from Vara-Perez, Felipe-Abrio and Agostinis (2019).

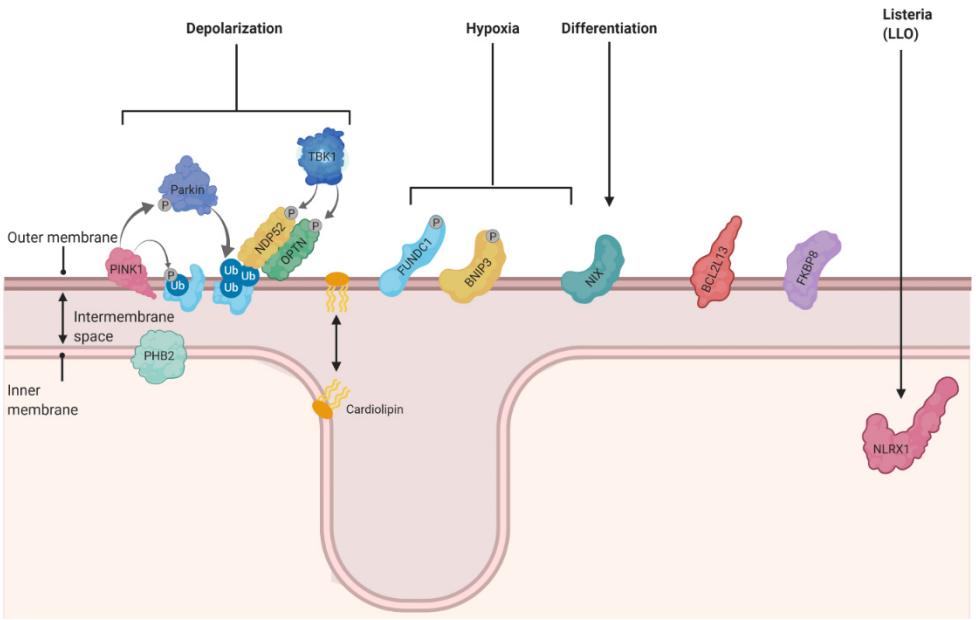

Figure 5. Other mitochondrial receptors described so far. Apart from the canonical mitophagy pathways, several other mitophagy receptors that either are embedded into the mitochondrial outer membrane like BCL2L13 (BCL2 like 13) and FKBP8 (FKBP prolyl isomerase 8) or sit in the inner mitochondrial membrane like PHB2 and the lipid cardiolipin were discovered. Adapted from Killackey, Philpott and Girardin (2020).

1.3. Regulated cell death

Cell death can be divided into regulated cell death (RCD) and accidental cell death. RCD relies on a distinct molecular machinery that can be modulated by pharmacological or genetic interventions, whereby accidental cell death is characterized by spontaneous catastrophic demise of cells that were exposed to severe stress like high temperature, extreme pH variations or shear forces (Galluzzi et al. 2015). RCD can either be activated as a physiological program for development or tissue turnover in the absence of any exogenous environmental insults, -named programmed cell death- (Conradt 2009), or as a result of interference with the intracellular or extracellular microenvironment to restore cellular homeostasis (Galluzzi et al. 2016). Initially, cell death was only classified depending on morphological characteristics (Schweichel and Merker 1973), but grounded on evidence from the last decades an increasing number of different cell death modalities have been characterized based on molecular parameters, too. Prominent cell death examples include apoptosis that can be activated by intrinsic or extrinsic stimuli, autophagy-dependent cell death (ADCD) that mechanistically depends on the autophagic machinery (or components thereof) and lysosome-dependent cell death (LDCD) that includes primary lysosomal membrane permeabilization (LMP) and the release of cathepsins (Galluzzi et al. 2018).

1.3.1. Apoptosis

Apoptosis is characterized by the activation of caspases that can either be activated via intrinsic or extrinsic stimuli (Figure 6). Intrinsic apoptosis is distinguished by intracellular stimuli that can both act in a positive or negative fashion. The intracellular release of pro-apoptotic factors from mitochondria after intracellular perturbations like DNA damage, ER stress or ROS overload act as positive stimuli, while the absence of certain growth factors, hormones or cytokines results in the loss of apoptotic suppression and subsequent activation of apoptosis. Intracellular stress signals result in the activation of BH3-only proteins as well as the executioner proteins BAX (BCL2 associated X, apoptosis regulator) or BAK1 (BCL2 antagonist/killer 1), leading to the permeabilization of the mitochondrial outer membrane (MOMP) and subsequent release of intermembrane space (IMS) components like cytochrome c (Kuwana et al. 2002). Cytochrome c binds to APAF1 (apoptotic protease-activating factor 1) resulting in the formation of the apoptosome (Chinnaiyan 1999). Further, the initiator caspase-9 is activated, which catalyses the proteolytic activation of caspase-3 and -7 terminating in apoptosis activation (Elmore 2007; Zaman, Wang and Gandhi 2014; Singh and

Lim 2022). Extrinsic apoptosis is regulated via extracellular ligands that can bind to two types of plasma membrane receptors: death or dependence receptors. Death receptors are activated by the binding of a distinct ligand like the FAS (Fas cell surface death receptor) ligand that binds the FAS receptors (Ashkenazi and Dixit 1998). In contrast, dependence receptors are activated when a specific ligand falls below a threshold (Goldschneider and Mehlen 2010). Receptor activation results in the formation of the death-inducing signal complex (DISC) that is associated with the adapter Fas associated via death domain (FADD) and the initiator caspase-8 and -10 followed by cleavage and activation of caspase-3 and -7 and the induction of apoptosis (Kischkel et al. 1995; Wajant 2002; Zaman, Wang and Gandhi 2014; Singh and Lim 2022). Caspase-3 and -7 regulate DNA fragmentation (Nagata 2005), phosphatidylserine (PS) exposure (Martin et al. 1996) and the formation of apoptotic bodies (Coleman et al. 2001). Intrinsic and extrinsic apoptosis crosstalk via BID (BH3 interacting domain death agonist) that can be cleaved by caspase-8 into a truncated version (tBID) during the extrinsic pathway and subsequently activates MOMP with cytochrome c release in the intrinsic pathway (Li et al. 1998).

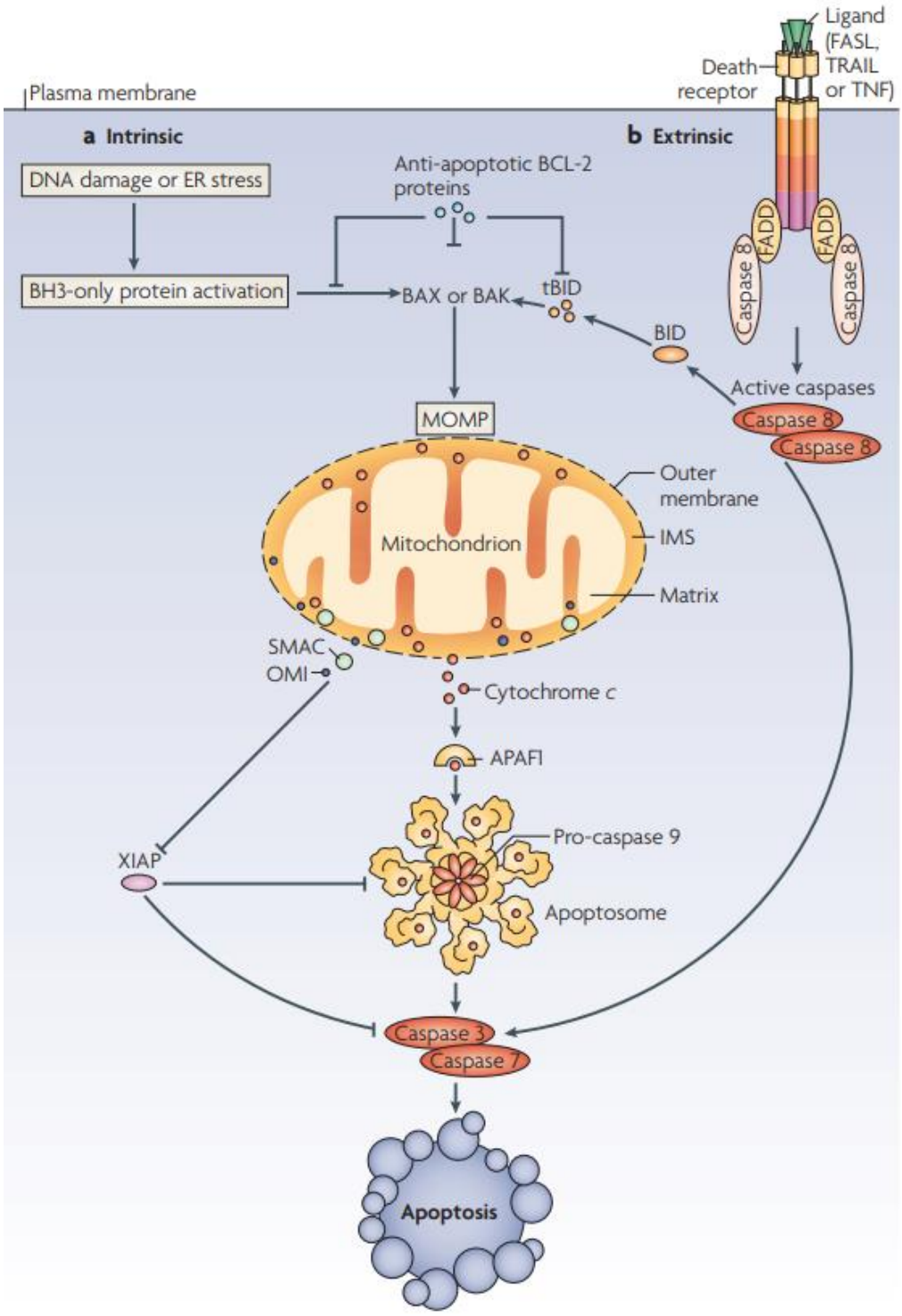

Figure 6. Intrinsic and extrinsic apoptosis. Apoptosis can be activated either by intracellular signals like oxidative stress or DNA damage (intrinsic pathway) or by extracellular signals via death receptors (e.g. TRAIL (TNFSF10, TNF superfamily member 10) and FAS (Fas cell surface death receptor)) (extrinsic pathway). The intrinsic pathway involves MOMP orchestrated by the BH3-only proteins BAX or BAK1, resulting in the release of cytochrome c that promotes the formation of the apoptosome. Further, caspase-9 is activated, which regulates caspase-3 activation. Ligand binding to the death receptor results in the activation of FADD (Fas associated via death domain) and caspase-8, mediating the activation of caspase-3 and resulting in the induction of apoptosis. Both pathways are connected by BID that is cleaved by caspase-8 into tBID activating MOMP. Adapted from Tait and Green (2010).

1.3.2. Autophagy-dependent cell death

Autophagy normally serves as a pro-survival mechanism that is activated under nutrient starvation or the presence of damaged organelles to ensure cellular homeostasis and cell survival. However, prolonged over activation of the autophagosomal pathway may lead to self-digestion beyond the point of survival and a type of cell demise called ADCD. ADCD was first described by Clarke (1990) by morphological features such as the formation of several autophagic vacuoles (autophagosomes) in dying cells. However, it must be taken into account that an accumulation of autophagosomes may not only result from an increase in autophagic flux, but also from a blockage of autophagosome removal. Consequently, criteria for the definition of ADCD were further defined on molecular/functional parameters. According to this, the term ADCD should only be used if the cell death relies exclusively on the autophagic pathway components shown by pharmacological inhibitors and/or genetic knockdown/knockout of ATGs, occurs independent of other programmed cell death forms and when autophagic flux is increased in the dying cells (Shen and Codogno 2011).

1.3.3. Lysosome-dependent cell death

Lysosome-dependent cell death (LDCD) involves the permeabilization of the lysosomal membrane (LMP) followed by the release of lysosomal contents including proteolytic enzymes of the cathepsin family. The molecular mechanisms upstream of LMP are not completely elucidated, but may involve the recruitment of the executioner protein BAX to the lysosomal membrane, followed by the activation of its pore-forming activity (Werneburg et al. 2007), the generation of ROS that destabilizes the lysosomal membrane upon lipid peroxidation (Kurz et al. 2008) or also lysosomotropic agents (Aits and Jäättelä 2013; Gómez-Sintes, Ledesma and Boya 2016). The release of the lysosomal hydrolases after LMP may further activate pro-apoptotic proteins like BID and BAX or inactivate anti-apoptotic proteins such as BCL2 (BCL2 apoptosis regulator), resulting in MOMP and the activation of caspases, facilitating the induction of the apoptotic pathway (Droga-Mazovec et al. 2008; Aits and Jäättelä 2013). However, LDCD does not necessarily involve MOMP and caspases nor an apoptotic phenotype (Brojatsch et al. 2015). Finally, the nomenclature committee on cell death recommend to define LDCD as a form of RCD that is characterized by LMP and the precipitation of cathepsins with optional involvement of MOMP and executioner caspases (Galluzzi et al. 2018).

1.4. Autophagy and mitophagy in cancer

Initially activation of autophagy was thought to protect the tumor cells from cell death in nutrient deprived and hypoxic regions where blood supply is no longer sufficient especially as tumors grow and become bigger. Nonetheless, further research on autophagy in cancer cells revealed that this process may also supress tumor growth by limiting cell proliferation and genomic instability during tumor formation or that drug-induced overactivation of autophagy results in ADCD (Figure 7) (Linder and Kögel 2019). Similarly, mitophagy could also play a dual role in cancer since several studies reporting a dysregulation of mitophagy-associated proteins, resulting in either tumor suppression or promotion, which seems to depend on the tumor type, too (Vara-Perez, Felipe-Abrio and Agostinis 2019).

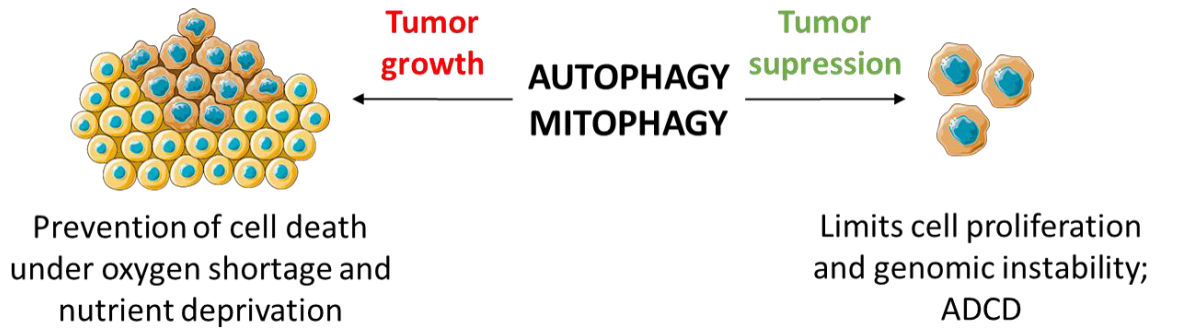

Figure 7. Dual role of autophagy and mitophagy in cancer. On the one hand autophagy and mitophagy can supress the formation of a tumor by limiting cell proliferation and genomic instability, but on the other hand promote the growth of a tumor in a nutrient and oxygen deprived environment. Further, overactivation of autophagy and mitophagy may also culminate in cell death. The Figure was partly generated using Servier Medical Art, provided by Servier, licensed under a Creative Commons Attribution 3.0 unported license.

1.4.1. Autophagy-dependent cell death in cancer

Several studies dealing with the role of autophagy in cancer reporting a dual role regarding tumorigenesis and tumor progression. Therefore, it has not been conclusively clarified whether autophagy should be turned on or off in cancer patients. The intermediate activation of autophagy as a stress response may protect the cancer cells from dying, while too low autophagy, making tumor cells vulnerable to metabolic stress, as well as too high levels, resulting in excessive self-digestion, may be detrimental for cancer cells (Figure 8) (Levine 2007).

On the one hand autophagy seems to be upregulated in a subset of solid tumors especially under metabolic stress when nutrients and oxygen are scarce, facilitating tumor cell survival (Liu and Ryan 2012). For example, Degenhardt et al. (2006) reported a pro-survival role for

autophagy in tumors generated from immortalized baby mouse kidney epithelial cells with apoptosis deficiency (BAX/BAK-deficient) and stable expression of EGFP (enhanced green fluorescent protein)-LC3. Following implantation *in vivo* autophagy was especially upregulated in the centre of the tumor mass where blood supply was not sufficient until tumor cells had established a blood supply and were no longer hypoxic. In addition, autophagy was also implicated in tumor cell migration (Qiang et al. 2014; Kenific et al. 2016) and metastasis (Macintosh et al. 2012) or the maintenance of CSCs (Zhu et al. 2013; Ojha et al. 2014a). Similarly in GBM, inhibition of autophagy using RNAi against *ATG7*, *ATG13* or *ULK1* in a *KRAS* (KRAS proto-oncogene, GTPase)-driven GBM mouse model significantly reduced GBM development (Gammoh et al. 2016) and drug-induced autophagy was shown to contribute to chemoresistance (Katayama et al. 2007).

Furthermore, autophagy was also reported to play an important role in therapy resistance. When autophagy is activated at a physiological level it may serve as a cytoprotective response against chemotherapeutics, enabling the tumor cells to survive and therefore the inhibition of autophagy in cancer treatment is also investigated (Ravi et al.; Ojha et al. 2014b; Shao et al. 2014). In GBM the most prominent example is the upregulation of cytoprotective autophagy following TMZ treatment of GBM patients, limiting its therapeutic efficacy and the induction of apoptosis (Yan et al. 2016). To overcome this challenges the combination treatment of conventional therapies like TMZ with autophagy inhibitors like chloroquine or in the future improved autophagy inhibitors is of great interest (Sotelo, Briceño and López-González 2006). A different strategy that is now investigated *in vitro* as well as *in vivo* involves the genetic regulation of autophagy using the CRISPR-Cas9 system or non-coding RNAs that knock out or inhibit genes of the autophagic machinery, respectively (Manea and Ray 2023). For example, *ATG5* KO impaired the viability of ovarian CSCs and in combination with carboplatin exhibited a synergistic effect *in vitro* as well as *in vivo* (Pagotto et al. 2017). Further, the overexpression of microRNA-30a inhibits autophagy by targeting *BECN1* and increased TMZ sensitivity in GBM cells (Xu et al. 2018).

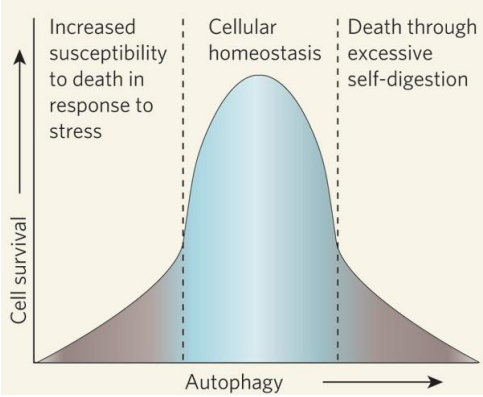

Figure 8. The homeostasis model of autophagy. The relationship between autophagy and cell survival depends strongly on the level of autophagy. Too low levels of autophagy limit the cellular stress response, increasing the susceptibility to death and too high levels of autophagy lead to death through excessive self-digestion. Only the intermediate activation of autophagy ensures cellular survival. Adapted from Levine (2007).

On the other hand it was repeatedly documented that various key autophagic proteins are dysregulated in cancer, suggesting a connection between reduced autophagy and tumor initiation. For example, *BECN1* is monoallelically deleted in several types of cancer such as breast, ovarian and prostate cancer (Aita et al. 1999) and re-expression of *BECN1* in MCF7 breast cancer cells reduced the malignant phenotype *in vitro* as well as their tumorigenic capacity *in vivo* (Liang et al. 1999). Similarly, *AMBRA1* was suggested as a haploinsufficient tumor suppressor gene since *AMBRA1*-deficiency correlates with increased tumorigenesis mainly dependent on c-Myc (MYC, MYC proto-oncogene, bHLH transcription factor) stabilization (Cianfanelli et al. 2015). Moreover, the stringent and prolonged overactivation of autophagy was also demonstrated to culminate in cancer cell death (ADCD) (Zielke et al. 2018; Meyer*, Henkel* et al. 2021; Reisbeck et al. 2023), which may open up an alternative cell death pathway as a therapeutic target (Kögel, Fulda and Mittelbronn 2010) especially for apoptosis resistant tumors like GBM. The combinatorial treatment of the repurposed tricyclic antidepressant imipramine (IM) and the anticoagulant ticlopidine (TIC) that inhibits the purinergic receptor $P2Y_{12}$ were shown to induce ADCD and to increase the survival of glioma-bearing mice, suggesting a potential clinical importance (Shchors, Massaras and Hanahan 2015). Indeed, just recently the effect of IM in patients with recurrent GBM was investigated in a clinical study (NCT04863950). Further, our group was involved in the identification of three drugs that induce ADCD in GBM cells namely STF-62247, the diphenylbutylpiperidine pimozide (PIMO) that targets D2 dopaminergic receptors and the piperidine derivative loperamide (LOP) that inhibits voltage-gated L-type calcium channels, emphasizing a potential clinical relevance of overactivated autophagy (ADCD) in GBM (Zielke et al. 2018).

In summary, it is assumed that the role of autophagy depends strongly on the tumor stage as well as the tumor type. In early tumorigenesis autophagy is thought to limit cell proliferation, genomic instability and therefore tumor progression. However, when the tumor is already formed, gets bigger and blood supply is no longer sufficient, autophagy may also promote the survival of tumor cells through recycling processes in the nutrient-deficient and hypoxic tumor regions (Liu and Ryan 2012). Therefore, the treatment with autophagy-inhibiting as well as -inducing agents needs to be carefully evaluated for specific cancer types and stages, but then it might be a promising strategy to overcome therapy or apoptosis resistance (Fulda and Kögel 2015; Linder and Kögel 2019).

1.4.2. Mitochondria in cancer therapy

1.4.2.1. The role of mitochondria and mitophagy in tumor development

An ever-increasing number of studies underlines the importance of mitophagy for tumor development as a tumor survival as well as a tumor suppressive mechanism. On the one hand increased mitophagy may reduce mitochondrial apoptosis, the main cell death pathway in cancer cells, but on the other hand ablation of mitophagy correlates with enhanced cancer development (Bernardini, Lazarou and Dewson 2017; Vara-Perez, Felipe-Abrio and Agostinis 2019). Therefore, similarly to autophagy, mitophagy could also have a dual role in cancer. It has been shown that several proteins involved in mitophagy are dysregulated in cancer patients, having tumor-promoting as well as tumor-suppressive functions depending on the tumor type (Bernardini, Lazarou and Dewson 2017; Kulikov et al. 2017). For example, the mitophagy receptor BNIP3 was reported to have a tumor promoter role in melanoma (Jiang, Yu and Li 2018), lung cancer (Karpathiou et al. 2013) and particularly in GBM (Hu et al. 2012) (Vara-Perez, Felipe-Abrio and Agostinis 2019), but has tumor suppressive functions in breast cancer (Niu et al. 2019). Further, *Parkin* is often lost in several cancers and also in GBM, suggesting a tumor suppressive role (Bernardini, Lazarou and Dewson 2017). Additionally, mitophagy is supposed to play an important role in therapy resistance. This is because several anti-cancer drugs induce mitochondrial dysfunction, leading to an increase in ROS production and cytochrome c release, finally activating the apoptotic pathway. In this context activation of mitophagy could reduce the activation of apoptosis (Vara-Perez, Felipe-Abrio and Agostinis 2019). This assumption is underpinned by several examples where the genetic inhibition of mitophagy pathways sensitizes cancer cells towards cell death induced by anticancer treatments (Abdrakhmanov et al. 2019; Wang et al. 2022). Nevertheless, mitophagy inhibition

may also promote tumor survival as it was shown for the antisense long non-coding RNA USP30-AS1. USP30-AS1 negatively regulates mitochondrial homeostasis and mitophagy in GBM cells and intriguingly expression of USP30-AS1 was shown to correlate with decreased GBM patient survival (Wang et al. 2021). Interestingly, the induction of lethal mitophagy in GBM cells after treatment with cannabidiol synergized with TMZ for GBM treatment *in vitro* as well as *in vivo* (Huang et al. 2021) and the treatment with AT 101 ([-]-gossypol), a natural compound from cotton seeds, induced mitochondrial dysfunction in GBM cells followed by mitophagic cell death (MCD) (Meyer et al. 2018), further supporting a dual role for mitophagy in cancer. Therefore, more research is necessary to fully understand the role of mitophagy in tumor progression, as well as cancer cell death, for the development of potential novel therapies.

1.4.2.2. The mitochondrial respiratory chain

Mitochondria are the main source of ATP, the universal energy currency of cells, which is produced through OXPHOS mainly in the electron transport chain (ETC) (Figure 9) (Mitchell 1961). The ETC consists of four multiprotein complexes sitting in the IMM, which are using the transfer of electrons to pump protons through the IMM into the mitochondrial IMS, resulting in the formation of a protonmotive force that is subsequently used by the ATP synthase/complex V to phosphorylate adenosine diphosphate (ADP) into ATP (Nolfi-Donegan, Braganza and Shiva 2020; Vercellino and Sazanov 2022). Energy from nutrients (glucose, fatty acids) that were pre-processed in glycolysis and the TCA cycle is introduced into the ETC in form of the reducing equivalents NADH (nicotinamide adenine dinucleotide) and $FADH_2$ (flavin adenine dinucleotide) (Krebs and Johnson 1980). First, complex I or NADH:ubiquinone oxidoreductase couples the reduction of quinone through oxidation of NADH to NAD^+ to the pumping of four protons into the IMS (Leif et al. 1995). Complex II or succinate dehydrogenase couples the oxidation of succinate to fumarate from the TCA cycle to the reduction of ubiquinone to ubiquinol, which is further transferred to complex III or coenzyme Q:cytochrome c oxidoreductase, entering the Q-cycle. During the Q-cycle electrons are transferred from ubiquinol across iron-sulfur (Fe-S) clusters, cytochrome b and finally cytochrome c while pumping a total of four protons into the IMS. Cytochrome c transfers the electrons to complex IV or cytochrome c oxidase to reduce oxygen to water and thereby transfers one proton to the IMS for each cytochrome c molecule, resulting in the pumping of four protons per each functional cycle. However, two protons are consumed in this process

leading to a total of two protons pumped into the IMS at complex IV. Finally, complex V exploits the proton gradient generated by complexes I, III and IV to phosphorylate ADP to ATP (Nolfi-Donegan, Braganza and Shiva 2020; Vercellino and Sazanov 2022).

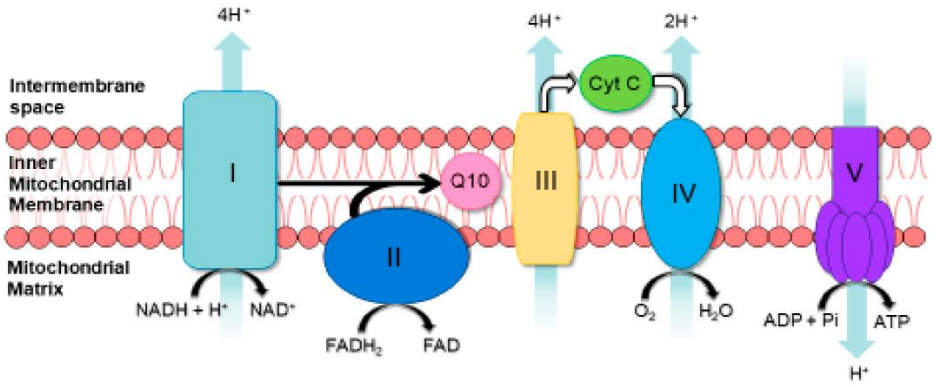

Figure 9. Model of the mitochondrial respiratory chain and complex V. The ETC consists of four complexes (complex I-IV), which couple the transport of electrons, donated by the reducing equivalents NADH and $FADH_2$ (flavin adenine dinucleotide) mainly coming from the TCA cycle, to the transport of protons from the mitochondrial matrix into the IMS. Finally, electrons are accepted by molecular oxygen, producing water and the protonmotive force generated by a total of 10 protons is used by complex V to phosphorylate ADP to ATP. Adapted from Turton et al. (2022).

1.4.2.3. Mitocans

Opposite to Warburg's hypothesis that cancer cells exclusively rely on aerobic glycolysis for energy production (Warburg 1956) it is now emerging that certain tumors can also upregulate OXPHOS in order to fulfil the increased energy needs of the cells (Ashton et al. 2018). For example, therapy resistant tumor cells showed an upregulation of mitochondrial OXPHOS activity and were specifically sensitive to OXPHOS inhibition (Hirpara et al. 2019). Further, especially CSCs were reported to increasingly rely on OXPHOS and lipid metabolism (Lin et al. 2017; Hoang-Minh et al. 2018). This opens up new avenues for cancer therapy, leading to the investigation of agents that modulate mitochondrial functions. Those drugs can be divided into two groups: mitochondria targeted and non-mitochondria targeted agents (D'Souza et al. 2011). Non-mitochondria targeted agents do not directly act on mitochondria, but on other subcellular components that subsequently lead to changes in mitochondria. The mitochondria targeting agents or mitocans (Table 3) are mostly low molecular-weight compounds that have a high affinity towards mitochondria because of their low molecular weight and/or their chemical properties. Mitocans were classified into nine different groups (Table 3) depending on their targeting site including Bcl-2 family proteins, ETC and mitochondrial DNA (Rohlena et al. 2011; Neuzil et al. 2013; Fialova et al. 2021). For example, the BH3 mimetic natural polyphenolic compound AT 101 targets the Bcl-2 family proteins by interacting with their BH3

binding domains, resulting in the activation of mitochondrial apoptosis (Oliver et al. 2005) and was further shown to induce MCD in GBM cells (see also above) (Meyer et al. 2018). The ETC is the major site of mitochondrial energy production through OXPHOS and plays a role in apoptosis (Lemarie and Grimm 2011). The fact that cancer cells show increased oxidative stress and a higher saturation of antioxidant defence makes them more susceptible for cell death induction by compounds that disrupt the cellular redox balance (Trachootham, Alexandre and Huang 2009). Targeting the ETC most often results in depolarized mitochondria, increased ROS formation, activation of AMPK signaling and ATP depletion (Fialova et al. 2021). All of the ETC complexes are possible targets, for example, complex I is inhibited by IACS-010759 resulting in reduced ATP formation together with decreased tumor growth and longer survival of patients with acute myeloid leukemia or neuroblastoma (Molina et al. 2018) and clinical trials are already under way (NCT02882321, NCT03291938). The natural polyphenolic compound resveratrol inhibits several ETC complexes but especially complex III resulting in mitochondria-mediated apoptosis (Zini et al. 1999; Tinhofer et al. 2001) and is already used in several clinical trials (NCT00256334 (Nguyen et al. 2009), NCT00920803 (Howells et al. 2011), NCT00433576). Another possibility to target the ETC is the use of iron chelators since the electron transfer between the ETC complexes depends strongly on Fe-S clusters and a breakdown would result in dysfunctional OXPHOS, diminished ATP levels and increased ROS levels. Additionally, iron overload is implicated with an elevated risk for tumor formation as well as tumor growth and increased intracellular iron levels are essential to facilitate the enhanced rate of cellular proliferation and DNA replication of tumor cells (Torti et al. 2018). Preclinical studies already revealed a potential therapeutic benefit using iron chelators like tachpyridine (Zhao et al. 2004), DpC (Guo et al. 2016) or VLX600 (Zhang et al. 2014; Fryknäs et al. 2016) for anti-cancer treatment and DpC (NCT02688101) as well as VLX600 (NCT02222363) (Mody et al. 2019) were already tested in clinical phase I studies. In summary, mitochondria targeting agents are a fascinating and promising new therapeutic class that may specifically address cancer cells that show an increased need for OXPHOS and/or iron.

Table 3. Classification of mitocans with examples. Adapted from Rohlena et al. (2011) and Fialova et al. (2021).

Class number	Type	Examples
1	Hexokinase inhibitors	2-deoxyglucose
2	Bcl-2 family proteins	AT 101
3	Thiol redox inhibitors	Arsenic trioxide
4	VDAC/ANT targeting drugs	Lonidamine
5	Electron transport chain	Metformin
6	Mitochondrial inner membrane	Rhodamine-123
7	Tricarboxylic acid cycle	Dichloroacetate
8	Mitochondrial DNA	Vitamin K3
9	Other (unknown) targets	Betulinic acid

2. Objective

The role of autophagy in cancer development and treatment is highly controversial since increased autophagy can lead to tumor survival as well as to cancer cell death, depending strongly on the tumor type as well as the tumor stage (Linder and Kögel 2019). Thereby, the activation of drug-induced autophagy-dependent cell death (ADCD) gained increasingly interest as an alternative treatment strategy for future cancer therapies especially for apoptosis-resistant tumor entities like glioblastoma (GBM) (Shchors, Massaras and Hanahan 2015; Zielke et al. 2018; Linder and Kögel 2019). GBM is one of the most deadly tumor diseases and although many research efforts are focused on new treatment strategies life expectancy for GBM patients is still very bad with only 20.9 months after initial diagnosis (Stupp et al. 2017) and only about 6 months after recurrence (Stupp et al. 2012).

The mechanisms of ADCD are diverse and not yet fully understood and there is increasing evidence that in addition to non-selective (bulk) autophagy, organelle-specific types of autophagy, e.g. lysophagy or mitophagy, are involved. Thereto, the aim of this thesis was to further elucidate the molecular determinants of drug-induced ADCD as well as the therapeutic relevance of organelle-specific autophagy pathways in ADCD. Previous work in our lab revealed the ADCD-inducing ability of STF-62247, pimozide (PIMO) and loperamide (LOP) as shown by cell death studies using autophagy-deficient GBM cell lines (Zielke et al. 2018). Interestingly, PIMO and LOP have been reported as lysosomotropic detergents that act as functional inhibitors of the acid sphingomyelinase (SMPD1) (FIASMAs) (Kornhuber et al. 2008; Kornhuber et al. 2011) and the loss of SMPD1 function is associated with lysosomal lipid storage diseases like the Niemann-Pick disease type A and B (Kuzu et al. 2017), resulting in lysosomal lipid accumulation and potentially in lysosomal membrane permeabilization (LMP) (Serrano-Puebla and Boya 2016). Reduced amounts of cytosolic cholesterol resulting from impaired lipid trafficking are well known to influence autophagy induction (Xu et al. 2010) and LMP may culminate in lysosome-dependent cell death (LDCD). The aim of this thesis was to further elucidate the underlying mechanisms of the PIMO- and LOP-induced ADCD by analysing cholesterol transport and LMP induction in order to investigate these hypotheses as well as to evaluate the benefits of those ADCD inducers for the potential usage in GBM therapy.

Furthermore, the usage of mitocans and the subsequent induction of cell-lethal mitophagy attracted increased interest for cancer therapy during the last years. Similarly to non-selective autophagy, mitophagy can be pro-survival as well as pro-death depending on the tumor type and stage (Vara-Perez, Felipe-Abrio and Agostinis 2019). Previous work in our lab revealed the induction of cell-lethal mitophagy after the induction of mitochondrial dysfunction by AT 101 in GBM cells (Meyer et al. 2018), highlighting the possible therapeutic function of mitophagy. In order to further investigate the molecular determinants of cell-lethal mitophagy in GBM, I made use of the mitocan VLX600 that was described as an iron chelator and oxidative phosphorylation (OXPHOS) inhibitor and to induce lethal mitochondrial dysfunction in colon carcinoma cells (Zhang et al. 2014; Fryknäs et al. 2016). Thereto, the second part of this thesis aimed to perform analysis of cell death, mitochondrial function/mitophagy and the global proteome using autophagy- and mitophagy-deficient GBM cells to elucidate the role of cell-lethal mitophagy in GBM as well as to investigate the role of iron chelation in this context. Interestingly, VLX600 was already used in a phase I study for refractory advanced solid tumors (Mody et al. 2019) and thereto the potential usage in GBM therapy was examined using an *ex vivo* tumor model.

3. Material

3.1. Cell culture

Table 4. Cell lines.

Cell line	Description and origin	Cell culture medium
GS-5	human GSC line obtained from a 85 year old male patient (Günther et al. 2008)	Neurobasal-A Medium
GS-5 GFP-Luc	human GSC line with stable expression of GFP/Luciferase (Linder et al. 2019)	Neurobasal-A Medium
GS-80	human GSC line obtained from a 60 year old male patient (Maire et al. 2021)	Neurobasal-A Medium
GS-86	human GSC line obtained from a 73 year old male patient with recurrent GBM (Maire et al. 2021)	Neurobasal-A Medium
GS-90	human GSC line obtained from a 61 year old female patient (Maire et al. 2021)	Neurobasal-A Medium
HEK-293T	human embryonal kidney cell line (Graham et al. 1977)	DMEM 10/1
LN-229	human GBM cell line established from a 60 year old female patient (ATCC CRL-2611) (Ishii et al. 1999)	DMEM 10/1
MZ-54	human glioma cell line (grade IV) derived from an explant of a secondary GBM (Hetschko et al. 2008)	DMEM 10/1
NCH421K	human GSC line obtained from 66 year old male patient (Campos et al. 2010)	Neurobasal-A Medium
NCH465	human GSC line (Campos et al. 2010)	Neurobasal-A Medium
NCH481	GBM patient-derived stem-like cell line (Gobin et al. 2019)	Neurobasal-A Medium
NCH644	human GSC line obtained from a 66 year old female patient (Podergajs et al. 2013)	Neurobasal-A Medium
U-251	human glioma cell line (Grade III/IV) isolated from a 75 year old male patient (Vaheri et al. 1976)	DMEM 10/1
U-87 MG	human glioma cell line grade III/IV, unknown origin, likely GBM (ATCC HTB-14) (Allen et al. 2016)	DMEM 10/1

Table 5. Stable CRISPR/Cas9 knockout cell lines. Cell lines were generated by a combination of two or three sgRNAs and the vectors PX458, PX459 or lentiCRISPRv2 expressing *Cas9* from *Streptococcus pyogenes*.

Cell line	sgRNA numbers (see Table 10)	Vector	Cell culture medium
LN-229 *ATG7* KO	2+4	pSpCas9(BB)-2A-Puro (PX459)	DMEM 10/1
MZ-54 *ATG5* KO	3+4	pSpCas9(BB)-2A-GFP (PX458)	DMEM 10/1
MZ-54 *ATG7* KO1	2+4	pSpCas9(BB)-2A-Puro (PX459)	DMEM 10/1
MZ-54 *ATG7* KO3	1+4	pSpCas9(BB)-2A-Puro (PX459)	DMEM 10/1
U-251 *ATG5* KO1	1+3+4	lentiCRISPRv2	DMEM 10/1, 1 µg/ml puromycin

Cell line	sgRNA numbers (see Table 10)	Vector	Cell culture medium
U-251 *ATG5* KO2	1+3+4	lentiCRISPRv2	DMEM 10/1, 1 µg/ml puromycin
U-251 *ATG5* KO3	1+3+4	lentiCRISPRv2	DMEM 10/1, 1 µg/ml puromycin
U-251 *ATG7* KO1	2+3+4	lentiCRISPRv2	DMEM 10/1, 1 µg/ml puromycin
U-251 *ATG7* KO2	2+3+4	lentiCRISPRv2	DMEM 10/1, 1 µg/ml puromycin
U-251 sgEGFP (con)	1+2+3	lentiCRISPRv2	DMEM 10/1, 1 µg/ml puromycin

Table 6. Cell culture medium contents.

Medium	Contents	Company	Catalog Number
DMEM 10/1	500 ml DMEM high glucose (+ 4.5 g/l glucose, + L-glutamine, - pyruvate)	Gibco/Life Technologies; Carlsbad, California, USA	61965026
	50 ml fetal calf serum (FCS, 10 %)	Gibco/Life Technologies; Carlsbad, California, USA	10270106
	5 ml penicillin-streptomycin (P/S) solution 10,000 U/ml (final conc. 100 U/ml)	Gibco/Life Technologies; Carlsbad, California, USA	15140122
DMEM/F12 OTC-Medium	500 ml DMEM/F12	Gibco/Life Technologies; Carlsbad, California, USA	31331028
	10 ml B-27 (50x), minus Vitamin A (2 %)	Gibco/Life Technologies; Carlsbad, California, USA	12587010
	5 ml N-2 Supplement (1 %)	Gibco/Life Technologies; Carlsbad, California, USA	1750248
	5 ml P/S 10,000 U/ml (final conc. 100 U/ml)	Gibco/Life Technologies; Carlsbad, California, USA	15140122
Freezing medium	80 % FCS, 20 % Dimethyl sulfoxide (DMSO)		
Neurobasal-A Medium	500 ml Neurobasal Medium, without glutamine	Gibco/Life Technologies; Carlsbad, California, USA	10888022
	10 ml B-27 (50x), minus Vitamin A (2 %)	Gibco/Life Technologies; Carlsbad, California, USA	12587010
	5 ml GlutaMAX (100x) (1 %)	Gibco/Life Technologies; Carlsbad, California, USA	35050038
	500 µl FGF_2 (0.1 %)	Peprotech; Hamburg, Deutschland	AF-100-18B
	500 µl EGF (0.1 %)	Peprotech	AF-100-15
	5 ml P/S 10,000 U/ml (final conc. 100 U/ml)	Gibco/Life Technologies; Carlsbad, California, USA	15140122
Opti-MEM	Reduced serum medium: + L-glutamine, - phenol red	Gibco/Life Technologies; Carlsbad, California, USA	11058021

Table 7. Bacterial strains.

Bacterial strain	Genotype	Company	Catalog Number
E.coli - Stbl3	*F-mcrB mrrhsdS20(rB-, mB-) recA13 supE44 ara-14 galK2 lacY1 proA2 rpsL20(StrR) xyl-5 λ-leumtl-1*	Invitrogen/Thermo Fisher Scientific; Waltham, Massachusetts, USA	C7373-03

Table 8. Medium and agar for bacteria.

Name	Usage	Company	Catalog number
LB agar	20 g agar powder; filled up to 500 ml with MilliQ water, pH 7.5	Carl Roth; Karlsruhe, Germany	X969.1
LB medium	22.5 g LB medium powder; filled up to 900 ml with MilliQ water, pH 7.5	Carl Roth; Karlsruhe, Germany	X968.1
S.O.C. medium	2 % tryptone, 0.5 % yeast extract, 10 mM NaCl, 2.5 mM KCl, 10 mM $MgCl_2$, 10 mM $MgSO_4$, 20 mM glucose	Invitrogen/Thermo Fisher Scientific; Waltham, Massachusetts, USA	15544034

Table 9. Antibiotic solutions.

Name	Concentration	Company	Catalog number
Ampicillin	100 µg/ml	Sigma-Aldrich; St. Louis, Missouri, USA	10044

3.2. Oligonucleotides

Table 10. Oligonucleotides for stable CRISPR/Cas9 knockouts.

Target gene	sgRNA number	Sense (S)/ antisense (AS)	Sequence	Company
ATG5	1	AS	aaacCACATCTCGAAG CACATCTTC	Eurofines Scientific, Luxembourg, Luxembourg
ATG5	1	S	CACCGAAGATGTGCT TCGAGATGTG	Eurofines Scientific, Luxembourg, Luxembourg
ATG5	3	AS	aaacTTTCAGTTATCT CATCCTGAC	Eurofines Scientific, Luxembourg, Luxembourg
ATG5	3	S	CACCGTCAGGATGA GATAACTGAAA	Eurofines Scientific, Luxembourg, Luxembourg
ATG5	4	AS	aaacCTGAGTGGTAG CATTAGAGGC	Eurofines Scientific, Luxembourg, Luxembourg
ATG5	4	S	CACCGCCTCTAATGC TACCACTCAG	Eurofines Scientific, Luxembourg, Luxembourg
ATG7	2	AS	aaacCCGTAGCTGCC GCCATTATTC	Eurofines Scientific, Luxembourg, Luxembourg
ATG7	2	S	CACCGAATAATGGCG GCAGCTACGG	Eurofines Scientific, Luxembourg, Luxembourg

Target gene	sgRNA number	Sense (S)/ antisense (AS)	Sequence	Company
ATG7	3	AS	aaacATACTCGTTCAG CTTCTTCTC	Eurofines Scientific, Luxembourg, Luxembourg
ATG7	3	S	CACCGAGAAGAAGC TGAACGAGTAT	Eurofines Scientific, Luxembourg, Luxembourg
ATG7	4	AS	aaacCCAGTATAGTGT CAGCTTTC	Eurofines Scientific, Luxembourg, Luxembourg
ATG7	4	S	CACCGAAAGCTGACA CTATACTGG	Eurofines Scientific, Luxembourg, Luxembourg
EGFP (FSFKK-C29.1)	1	S	GGAGCGCACCATCTT CTTCA	Addgene 51763 (Shalem et al. 2014); Massachusetts, USA
EGFP (FSFKK-C29.2)	2	S	GGCCACAAGTTCAGC GTGTC	Addgene 51762 (Shalem et al. 2014); Massachusetts, USA
EGFP (FSFKK-C29.3)	3	S	GGGCGAGGAGCTGT TCACCG	Addgene 51760 (Shalem et al. 2014); Massachusetts, USA

Table 11. siRNA oligonucleotides for transient knockdowns.

Name	Target gene	Number	Company
siBNIP3 #1	*BNIP3*	SASI_Hs01_00131554	Sigma-Aldrich; St. Louis, Missouri, USA
siBNIP3 #2	*BNIP3*	SASI_Hs01_00131555	Sigma-Aldrich; St. Louis, Missouri, USA
siBNIP3L #1	*BNIP3L*	SASI_Hs01_00030000	Sigma-Aldrich; St. Louis, Missouri, USA
siBNIP3L #2	*BNIP3L*	SASI_Hs01_00030001	Sigma-Aldrich; St. Louis, Missouri, USA
siNDRG1 #1	*NDRG1*	SASI_Hs01_00034471	Sigma-Aldrich; St. Louis, Missouri, USA
siNDRG1 #2	*NDRG1*	SASI_Hs01_00034472	Sigma-Aldrich; St. Louis, Missouri, USA
siRNA Universal Negative Control		SIC001	Sigma-Aldrich; St. Louis, Missouri, USA

3.3. Plasmids

Table 12. Plasmids for stable transfection or lentiviral transduction.

Plasmid	Catalog number	Company	Purpose
lentiCRISPRv2	52961	Addgene (Sanjana, Shalem and Zhang 2014); Massachusetts, USA	Lentiviral expression of *Cas9* from *S. pyogenes* and a cloning backbone for sgRNA to generate CRISPR/Cas9 knockouts

Plasmid	Catalog number	Company	Purpose
pCHAC-mt-mKeima	72342	Addgene (Lazarou et al. 2015); Massachusetts, USA	Mammalian expression of mt-mKeima for mitophagic flux analysis
pCMV-dr8.91		(Zufferey et al. 1997)	gag/pol packaging plasmid
pGIPZ control vector	RHS4349	Open BioSystems Inc; Huntsville, USA	Control vector for shRNA-mediated KD with the pGIPZ plasmid
pGIPZ shRB1CC1 KD1	RHS4430-101,100,096	Open BioSystems Inc; Huntsville, USA	shRNA-mediated KD of depicted gene
pGIPZ shRB1CC1 KD2	RHS4430-101,103,887	Open BioSystems Inc; Huntsville, USA	shRNA-mediated KD of depicted gene
pLKO.1 non-target shRNA control	SHC016-1EA	Sigma-Aldrich; St. Louis, Missouri, USA	Control vector for shRNA-mediated KD with the pLKO.1 plasmid
pLKO.1 shATG14 142849 (KD1)	SHCLNG-NM_014924	Sigma-Aldrich; St. Louis, Missouri, USA	shRNA-mediated KD of depicted gene
pLKO.1 shATG14 144080 (KD2)	SHCLNG-NM_014924	Sigma-Aldrich; St. Louis, Missouri, USA	shRNA-mediated KD of depicted gene
pLKO.1 shATG5 151963	SHCLNG-NM_004849	Sigma-Aldrich; St. Louis, Missouri, USA	shRNA-mediated KD of depicted gene
pLKO.1 shATG7 7584	SHCLNG-NM_006395	Sigma-Aldrich; St. Louis, Missouri, USA	shRNA-mediated KD of depicted gene
pLKO.1 shCYBB 64590 (KD1)	SHCLNG-NM_000397	Sigma-Aldrich; St. Louis, Missouri, USA	shRNA-mediated KD of depicted gene
pLKO.1 shCYBB 64591 (KD2)	SHCLNG-NM_000397	Sigma-Aldrich; St. Louis, Missouri, USA	shRNA-mediated KD of depicted gene
pLKO.1 shRUBCN 21540 (KD1)	SHCLNG-XM_032901	Sigma-Aldrich; St. Louis, Missouri, USA	shRNA-mediated KD of depicted gene
pLKO.1 shRUBCN 21541 (KD2)	SHCLNG-XM_032901	Sigma-Aldrich; St. Louis, Missouri, USA	shRNA-mediated KD of depicted gene
pLV[Exp]-CMV>Tet3G/Hygro	VB180123-1018bxq	Vectorbuilder; Neu-Isenburg, Germany	Regulator plasmid for inducible expression using doxycycline
pLV[Exp]-EGFP/Puro-CMV>Stuffer300	VB181209-1075efx	Vectorbuilder; Neu-Isenburg, Germany	Mammalian expression of EGFP for OTC experiments
pLV[Exp]-EGFP:T2A:Bsd-CMV>ORF_Stuffer	VB900142-6037fdr	Vectorbuilder; Neu-Isenburg, Germany	Mammalian expression of EGFP for OTC experiments
pLV[Exp]-Puro-TRE3G>hATG7	VB200302-1037hrd	Vectorbuilder; Neu-Isenburg, Germany	Inducible re-expression of *ATG7* in mammalian cells

Plasmid	Catalog number	Company	Purpose
pmCherry-Gal3	85662	Addgene (Papadopoulos et al. 2017); Massachusetts, USA	Mammalian expression of LGALS3-mCherry to measure/visualize lysosomal damage
pMD2.G	12259	Addgene (was a gift from Didier Trono); Massachusetts, USA	VSV-g envelope
pMRX-IP-GFP-LC3-RFP-LC3ΔG	84572	Addgene (Kaizuka et al. 2016); Massachusetts, USA	Mammalian expression of GFP-LC3-RFP-LC3ΔG to measure autophagic flux
psPAX2	12260	Addgene; Massachusetts, USA	Empty backbone/packaging vector
pSpCas9(BB)-2A-Puro (PX459)	48139	Addgene (Ran et al. 2013); Massachusetts, USA	Mammalian expression of *Cas9* from *S. pyogenes* and a cloning backbone for sgRNA to generate CRISPR/Cas9 knockouts
pSpCas9(BB)-2A-GFP (PX458)	48138	Addgene (Ran et al. 2013); Massachusetts, USA	Mammalian expression of *Cas9* from *S. pyogenes* and a cloning backbone for sgRNA to generate CRISPR/Cas9 knockouts

3.4. Chemicals

Table 13. Treatment reagents. Stocks were prepared with fresh DMSO or sterile H_2O and stored at -20 °C or -80 °C.

Substance	Abbr.	Company	Catalog Number	Function
2-deoxyglucose	2-DG	Sigma-Aldrich; St. Louis, Missouri, USA	D8375	Glycolysis inhibitor
ABT-737	-	Santa Cruz Biotechnology; Dallas, Texas, USA	sc-207242	Bcl-2 inhibitor/apoptosis inducer
Actinomycin D	ActD	Sigma-Aldrich; St. Louis, Missouri, USA	A1410	RNA-polymerase I inhibitor; inducer of nucleolar stress
Bafilomycin A1	BAF	LC Laboratories; Woburn, Massachusetts, USA	B-1080	H^+-ATPase inhibitor
CB-839	-	MedChemExpress; Monmouth Junction, New Jersey, USA	HY-12248	Inhibition of glutaminase
Cholesterol-methyl-β-cyclodextrin	CHOL	Sigma-Aldrich; St. Louis, Missouri, USA	C4951	Extracellular addition of cholesterol
Dimethyl sulfoxide	DMSO	Carl Roth; Karlsruhe, Germany GmbH	A994	Negative control, solvent

Substance	Abbr.	Company	Catalog Number	Function
Doxycycline hyclate	DOX	Sigma-Aldrich; St. Louis, Missouri, USA	D9891	Used for inducible gene expression
Iron(II)-chloride	$FeCl_2$	Sigma-Aldrich; St. Louis, Missouri, USA	372870	Extracellular addition of iron
Iron(III)-chloride	$FeCl_3$	Sigma-Aldrich; St. Louis, Missouri, USA	157740	Extracellular addition of iron
Etoposide	ETO	Enzo Life Science; Lausen, Switzerland	BML-GR307	Topoisomerase II inhibitor/apoptosis inducer
Gamitrinib TPP	GTPP	MedChemExpress; Monmouth Junction, New Jersey, USA	HY-102007	Hsp90 (HSP90AA1, heat shock protein 90 alpha family class A member 1) inhibitor
Imipramine hydrochloride	IM	Sigma-Aldrich; St. Louis, Missouri, USA	I0899	Tricyclic antidepressant; inhibits the serotonin and norepinephrine transporters; adenylate cyclase activator
Loperamide hydrochloride	LOP	Enzo Life Science; Lausen, Switzerland	ALX-550-253	Non-selective Ca^{2+} channel blocker; binds to opioid μ-receptors.
Pimozide	PIMO	Sigma-Aldrich; St. Louis, Missouri, USA	P1793	Dopamine and serotonin receptor antagonist
Rotenone	-	Sigma-Aldrich; St. Louis, Missouri, USA	R8875	ETC inhibitor; ROS-inducer
Ticlopidine hydrochloride	TIC	Sigma-Aldrich; St. Louis, Missouri, USA	T6654	$P2Y_{12}$ inhibitor
U18666A	-	Abcam; Cambridge, UK	ab133116	Cholesterol transport inhibitor
VLX600	-	Cayman Chemical; Ann Arbor, Michigan, USA	17192	OXPHOS inhibitor; iron chelator
Z-Val-Ala-DL-Asp-fluoromethylketone (Z-VAD-FMK)	z-VAD	Bachem Holding; Bubendorf, Switzerland	4026865	Caspase/Apoptosis inhibitor

Table 14. All other chemicals.

Substance	Company	Catalog number
0.1 M Dithiothreitol (DTT)	Invitrogen/Thermo Fisher Scientific; Waltham, Massachusetts, USA AG	707265ML
10 % NP-40	Abcam; Cambridge, UK	ab142227
2-Chloroacetamide (CAA)	Sigma-Aldrich; St. Louis, Missouri, USA	SLBV4943

Substance	Company	Catalog number
5x First Strand Buffer	Thermo Fisher Scientific; Waltham, Massachusetts, USA	Y02321
Accutase	Sigma-Aldrich; St. Louis, Missouri, USA	A6964
Acrylamide/Bis Solution 37.5:1 (40 % w/v) (PAA)	Serva Electrophoresis; Heidelberg, Germany	10681
Agarose	Serva Electrophoresis; Heidelberg, Germany	11406.02
Agarose Low Melt	Carl Roth; Karlsruhe, Germany	6351
Albumin Fraction V (BSA)	Carl Roth; Karlsruhe, Germany	8076
Amersham Protran 0.2 NC 300mm×4m	Cytiva; Freiburg, Germany	10600001
Ammoniumperoxodisulfat (APS)	Carl Roth; Karlsruhe, Germany	9592
Aprotinin	Applichem; Darmstadt, Germany	A2132
Bacteriostatic Concentrate Solution	BD Biosciences; Franklin Lakes, New Jersey, USA	653156
Bromphenol Blue Sodium Salt	Sigma-Aldrich; St. Louis, Missouri, USA	B8026
Calciumchlorid-Dihydrat	Merck; Darmstadt, Germany	1023821000
Cleaning Solution Concentrate	BD Biosciences; Franklin Lakes, New Jersey, USA	653157
D(+)-Sucrose	Applichem; Darmstadt, Germany	A2211
Diethylpyrocarbonat (DEPC)-treated H_2O	Carl Roth; Karlsruhe, Germany	T143.1
Digitonin	Sigma-Aldrich; St. Louis, Missouri, USA	D141
DNA Gel Loading Dye (6x)	Thermo Fisher Scientific; Waltham, Massachusetts, USA	R0611
dNTP-Mix 10 mM	Invitrogen/Thermo Fisher Scientific; Waltham, Massachusetts, USA AG	18427089
Dulbecco's Phosphate-Buffered Saline (DPBS)	Gibco/Life Technologies; Carlsbad, California, USA	14190094
Ethanol ≥99.8 %	Sigma-Aldrich; St. Louis, Missouri, USA	32221-M
Ethidiumbromide solution 1 % (10 mg/ml)	Carl Roth; Karlsruhe, Germany	2218
Ethylene glycol-bis(β-aminoethyl ether)-N,N,N′,N′-tetraacetic acid (EGTA)	Applichem; Darmstadt, Germany	A0878
Ethylenediaminetetraacetic acid (EDTA)	Applichem; Darmstadt, Germany	A2937
Extended Flow Cell Clean Solution	BD Biosciences; Franklin Lakes, New Jersey, USA	653159
FastDigest Esp3I	Thermo Fisher Scientific; Waltham, Massachusetts, USA	FD0454
FastDigest Green Buffer (10x)	Thermo Fisher Scientific; Waltham, Massachusetts, USA	B72
FastStart Universal Probe Master (Rox)	Roche; Basel, Switzerland	4913957001

Substance	Company	Catalog number
FuGENE HD Transfection Reagent	Promega; Madison, Wisconsin, USA	E2311
GeneRuler 100 bp DNA Ladder	Thermo Fisher Scientific; Waltham, Massachusetts, USA	SM0243
Geneticin disulfate (G418)-solution 50 mg/ml	Carl Roth; Karlsruhe, Germany	CP11.1
Glycerol	Sigma-Aldrich; St. Louis, Missouri, USA	G5516
Glycine	Applichem; Darmstadt, Germany	A1067
HBSS, calcium, magnesium, no phenol red	Gibco/Life Technologies; Carlsbad, California, USA	14025
HEPES	Applichem; Darmstadt, Germany	A1069
Hoechst 33342	Sigma-Aldrich; St. Louis, Missouri, USA	14533
Hydrochloric Acid (HCl), 32 %	Thermo Fisher Scientific; Waltham, Massachusetts, USA	H/1100/PB15
Hygromycin B (50 mg/ml)	Invitrogen/Thermo Fisher Scientific; Waltham, Massachusetts, USA AG	10687010
Isopropanol/2-propanol	Sigma-Aldrich; St. Louis, Missouri, USA	33539
KCl (Potassium chloride)	Honeywell; Charlotte, North Carolina, USA	60130
KH_2PO_4 (Potassium dihydrogen phosphate)	Carl Roth; Karlsruhe, Germany	3904
Leupeptin - Hemisulfat	Applichem; Darmstadt, Germany	A2183
Lipofectamine 3000 Transfection Reagent	Thermo Fisher Scientific; Waltham, Massachusetts, USA	L3000008
Methanol	Sigma-Aldrich; St. Louis, Missouri, USA	32213-M
Milk powder	Carl Roth; Karlsruhe, Germany	T145
Molecular weight marker: Precision Plus Protein™ All Blue Standards	Bio-Rad Laboratories; Hercules, California, USA	1610373
Mounting medium Fluoroshield with DAPI	Sigma-Aldrich; St. Louis, Missouri, USA	F6057
Mounting medium mountant PermaFluor without DAPI	Thermo Fisher Scientific; Waltham, Massachusetts, USA	12695925
MTT-solution 5 mg/ml in DPBS	Sigma-Aldrich; St. Louis, Missouri, USA	M5655
Na_2HPO_4 (Di-sodium hydrogen phosphate)	Carl Roth; Karlsruhe, Germany	P030
NaCl (Sodium chloride)	Sigma-Aldrich; St. Louis, Missouri, USA	31434
Oligo dT20 Primer	Genaxxon bioscience; Ulm, Germany	M3039.0151
Paraffin oil (vaseline)	VWR; Radnor, Pennsylvania, USA	301440ZK
Paraformaldehyde Solution 4 % in PBS (PFA)	Santa Cruz Biotechnology; Dallas, Texas, USA	sc-281692
PBS buffer (1x, Dulbecco's) - Powder	Applichem; Darmstadt, Germany	A0964
Phenylmethansulfonylfluorid (PMSF)	Carl Roth; Karlsruhe, Germany	6367
Phosphatase Inhibitor Cocktail (PhosSTOP)	Roche; Basel, Switzerland	04 906 837 001

Substance	Company	Catalog number
Polybrene (Hexadimethrine bromide)	Sigma-Aldrich; St. Louis, Missouri, USA	107689
Protamine Sulfate	Sigma-Aldrich; St. Louis, Missouri, USA	P3369
Protease inhibitor cocktail	Sigma-Aldrich; St. Louis, Missouri, USA	P8340
Puromycin dihydrochloride	Santa Cruz Biotechnology; Dallas, Texas, USA	SC-108071
QuickExtract DNA Extraction Solution	Biozym Scientific; Hessisch Oldendorf, Germany	101094
Random Hexamer Primer N6	Genaxxon bioscience; Ulm, Germany	M3038.0125
RNaseZAP	Sigma-Aldrich; St. Louis, Missouri, USA	R2020
SDS pellets (Sodium dodecyl sulfate)	Carl Roth; Karlsruhe, Germany	CN30
Sodium hypochlorite solution	Carl Roth; Karlsruhe, Germany	9062
Spherotech 6-Peak Validation Beads (FL4)	BD Biosciences; Franklin Lakes, New Jersey, USA	653145
Spherotech 8-Peak Validation Beads (FL1 - FL3)	BD Biosciences; Franklin Lakes, New Jersey, USA	653144
SuperScript III Reverse Transcriptase 200 U/µl	Thermo Fisher Scientific; Waltham, Massachusetts, USA	56575
T4 DNA Ligase	New England Biolabs; Ipswich, Massachusetts, USA	M0202
T4 DNA Ligase Reaction Buffer	New England Biolabs; Ipswich, Massachusetts, USA	B0202S
T4 Polynucleotide Kinase	New England Biolabs; Ipswich, Massachusetts, USA	M0201
TAE Buffer (50x)	Applichem, Darmstadt, Germany	A1691,0500
Taq DNA Polymerase + Standard Taq Buffer	New England Biolabs; Ipswich, Massachusetts, USA	M0273L
TEMED	Applichem; Darmstadt, Germany	A1148
Tris-(2-carboxyethyl)phosphin hydrochloride (TCEP)	Sigma-Aldrich; St. Louis, Missouri, USA	MKCF4259
Triton X-100	Sigma-Aldrich; St. Louis, Missouri, USA	T8787
Trizma-Base	Sigma-Aldrich; St. Louis, Missouri, USA	T1503
Trypan blue solution (0.4 %)	Sigma-Aldrich; St. Louis, Missouri, USA	T8154
Trypsin-EDTA (0.25 %)	Sigma-Aldrich; St. Louis, Missouri, USA	T4049
Tween 20	Applichem; Darmstadt, Germany	A4974
β-Mercaptoethanol	Sigma-Aldrich; St. Louis, Missouri, USA	M6250

3.5. Buffers and solutions

Table 15. Buffer for flow cytometry analysis.

Name	Composition
HEPES buffer for FACS (annexin V staining)	10 mM HEPES, 140 mM NaCl, 5 mM $CaCl_2$, pH 7.4; short before use add 0.8 µl annexin/well and 0.8 µl propidium iodide/well

Table 16. Buffers for protein analysis.

Name	Composition
10x phosphate buffered saline (PBS)	95.5 g PBS powder; filled up to 1 l with H_2O
1x electrophoresis transfer buffer for SDS-PAGE	25 mM Tris, 192 mM Glycine; freshly added: 20 % Methanol
1x gel elecrophoresis running buffer for SDS-PAGE	25 mM Tris, 192 mM Glycine, 0.1 % SDS
1x TBS (tris buffered saline)	150 mM NaCl, 50 mM Tris, pH 7.5
1x TBS-Tween-20 (TBS-T)	1x TBS with 0.05 % Tween-20
2x SDS-Page lysis buffer	137 mM Tris/HCl pH 6.8, 4 % SDS, 20 % Glycerol; freshly added: 1:10 phosphatase inhibitor and 1:100 protease inhibitor
5 % stacking gel for SDS-PAGE	5 % PAA, 120 mM Tris/HCl pH 6.8, 0.1 % SDS, 0.1 % APS, 0.05 % Temed
5x SDS loading sample buffer for SDS-PAGE	250 mM Tris/HCl pH 6.8, 10 % SDS, 30 % Glycerol, 0.02 % bromphenolblue; short before use add 5 % β-Mercaptoethanol
8 – 15 % separation gel for SDS-PAGE	8 – 15 % PAA, 375 mM Tris/HCl pH 8.8, 0.1 % SDS, 0.1 % APS, 0.05 % Temed

Table 17. Buffer for proteome analysis.

Name	Composition
lysis buffer	2 % SDS, 50 mM Tris/HCl pH 8.5, 40 mM 2-Chloroacetamide (CAA), 10 mM Tris-(2-carboxyethyl)phosphid (TCEP), 1 tablet Protease and Phosphatase inhibitors in 10 ml

Table 18. Buffers for separation of cytosol and organelle fraction containing intact mitochondria.

Name	Composition
Cytosol Extract Buffer	250 mM sucrose, 70 mM KCl, 137 mM NaCl, 4.3 mM Na_2HPO_4, 1.4 mM KH_2PO_4 pH 7.2; freshly added: 100 µM PMSF, 10 µg/ml Leupeptin, 2 µg/ml Aprotinin, 200 µg/ml Digitonin
Mitochondria Lysis Buffer	50 mM Tris-HCl pH 7.4, 150 mM NaCl, 2 mM EDTA, 2 mM EGTA, 0.2 % Triton X-100, 0.3 % NP-40; freshly added: 10 µg/ml Leupeptin, 2 µg/ml Aprotinin, 100 µM PMSF

Table 19. Buffer for transfection.

Name	Composition
2x HEPES-buffered saline (2x HBS)	274 mM NaCl, 10 mM KCl, 1.4 mM Na_2HPO_4, 42 mM HEPES, 11.1 mM glucose

3.6. Commercial Kits

Table 20. Commercial kits.

Kit	Cat No	Company
Cholesterol assay kit	ab133116	Abcam; Cambridge, UK
EndoFree Plasmid Maxi Kit	12362	Qiagen; Hilden, Germany
ExtractMe Total RNA Kit	EM09.1	Blirt; Gdańsk, Poland
Mitophagy detection kit	MD01-10	Dojindo EU GmbH; Munich, Germany
Pierce BCA Protein Assay Kit	23225	Thermo Fisher Scientific; Waltham, Massachusetts, USA
QIAprep Spin Miniprep Kit	27104	Qiagen; Hilden, Germany
QIAquick gel extraction kit	28704	Qiagen; Hilden, Germany

3.7. Fluorophores for flow cytometry

Table 21. Fluorescent dyes for flow cytometry.

Fluorescent dye	Company	Catalog number
APC Annexin V	BD Biosciences; Franklin Lakes, New Jersey, USA	550474
BioTracker ATP-Red Live Cell Dye	Sigma-Aldrich; St. Louis, Missouri, USA	SCT045
MitoSOX, mitochondrial superoxide indicator	Thermo Fisher Scientific; Waltham, Massachusetts, USA	M36008
Propidium iodide solution (PI)	Sigma-Aldrich; St. Louis, Missouri, USA	P4864
Tetramethylrhodamine (TMRM)	Thermo Fisher Scientific; Waltham, Massachusetts, USA	T668

3.8. Antibodies

Table 22. Primary antibodies for western blot. All antibodies (except for ATG7 and BNIP3) were diluted in 5 % BSA-TBST. ATG7 and BNIP3 were diluted in 5 % milk-TBST.

Antibody	Company	Catalog Number	Species	MW [kDa]	Dilution
ATG5 (D5F5U)	Cell Signaling Technology; Danvers, Massachusetts, USA	12994	Rabbit	55	1:1000
ATG7 (D12B11)	Cell Signaling Technology; Danvers, Massachusetts, USA	8558	Rabbit	78	1:500
BNIP3	Abcam; Cambridge, UK	ab10433	Mouse	30	1:250
BNIP3L/NIX	Cell Signaling Technology; Danvers, Massachusetts, USA	12396	Rabbit	38	1:1000
COX4I1 (3E11)	Cell Signaling Technology; Danvers, Massachusetts, USA	4850	Rabbit	17	1:1000
GAPDH (6C5)	Merck; Darmstadt, Germany	CB1001	Mouse	36	1:10,000
H3K4me2	Cell Signaling Technology; Danvers, Massachusetts, USA	9725	Rabbit	17	1:1000
H3K4me3	Cell Signaling Technology; Danvers, Massachusetts, USA	9751	Rabbit	17	1:1000
H3K9me2	Cell Signaling Technology; Danvers, Massachusetts, USA	4658	Rabbit	17	1:1000

Antibody	Company	Catalog Number	Species	MW [kDa]	Dilution
H3K9me3	Abcam; Cambridge, UK	ab8898	Rabbit	17	1:1000
HIF1A	BD Pharmingen; San Diego, California, USA	610959	Mouse	120	1:1000
Histone 3 (H3)	Cell Signaling Technology; Danvers, Massachusetts, USA	3638	Mouse	17	1:1000
HSPD1 (D6F1)	Cell Signaling Technology; Danvers, Massachusetts, USA	12165	Rabbit	60	1:1000
MAP1LC3B/LC3B	Thermo Fisher Scientific; Waltham, Massachusetts, USA	PA1-16930	Rabbit	14-16	1:1000
NDRG1	Proteintech; Rosemont, Illinois, USA	26902-1-AP	Rabbit	43	1:3000
pRPS6 (Ser240/244)	Cell Signaling Technology; Danvers, Massachusetts, USA	2215	Rabbit	32	1:1000
RB1CC1	Proteintech; Rosemont, Illinois, USA	17250-1-AP	Rabbit	200	1:1000
RPS6	Cell Signaling Technology; Danvers, Massachusetts, USA	2317	Mouse	32	1:1000
TOMM20 (FL-10)	Santa Cruz Biotechnology; Dallas, Texas, USA	sc-17764	Mouse	20	1:250
VDAC1	Abcam; Cambridge, UK	ab15895	Rabbit	31	1:1000

Table 23. Secondary antibodies for western blot. All secondary antibodies were diluted in 3 % BSA-TBST.

Antibody	Conjugate	Company	Catalog Number	Dilution
Goat Anti-mouse	IRDye 680RD	Li-cor Biosciences GmbH; Bad Homburg, Germany	926-68070	1:10,000
Goat Anti-rabbit	IRDye 800CW	Li-cor Biosciences GmbH; Bad Homburg, Germany	926-32211	1:10,000

Table 24. Primary antibodies for immunofluorescence. All antibodies were diluted in 4 % BSA-PBST.

Antibody	Company	Catalog Number	Species	MW [kDa]	Dilution
BNIP3L (D4R4B)	Cell Signaling Technology; Danvers, Massachusetts, USA	12396	Rabbit	38	1:100
LAMP1 (H4A3)	DSHB; Iowa City, Iowa, USA	H4A3-s	Mouse	120	1:25
NPM1 (FC-61991)	Invitrogen/Thermo Fisher Scientific; Waltham, Massachusetts, USA	32-5200	Mouse	37	1:200
TOMM20 (FL-10)	Santa Cruz Biotechnology; Dallas, Texas, USA	sc-11764	Mouse	20	1:50

Table 25. Secondary antibodies for immunofluorescence. All secondary antibodies were diluted in PBST.

Antibody	Company	Catalog Number	Species	Dilution
Alexa Fluor 488 anti-mouse	Invitrogen/Thermo Fisher Scientific; Waltham, Massachusetts, USA	A11029	Goat	1:500
Alexa Fluor 594 anti-rabbit	Invitrogen/Thermo Fisher Scientific; Waltham, Massachusetts, USA	A11037	Goat	1:500
Alexa Fluor 594 F(ab')2 fragment anti-mouse	Invitrogen/Thermo Fisher Scientific; Waltham, Massachusetts, USA	A11020	Goat	1:500

3.9. Primers for qRT-PCR and PCR

Table 26. FAM-MGB qRT-PCR Primers.

Primer name	Target gene	Company
Hs00166163_m1	*CYBB*	Thermo Fisher Scientific; Waltham, Massachusetts, USA
Hs00208732_m1	*ATG14*	Thermo Fisher Scientific; Waltham, Massachusetts, USA
Hs00395301_m1	*SLC45A1*	Thermo Fisher Scientific; Waltham, Massachusetts, USA
Hs00427620_m1	*TBP*	Thermo Fisher Scientific; Waltham, Massachusetts, USA
Hs00943570_m1	*RUBCN*	Thermo Fisher Scientific; Waltham, Massachusetts, USA

Table 27. PCR Primers.

Primer name	Sequence	Company
GAPDH Forward	5'-CCTGACCTGCCGTCTAGAAA-3'	Eurofines Scientific, Luxembourg, Luxembourg
GAPDH Reverse	5'-TTACTCCTTGGAGGCCATGT-3'	Eurofines Scientific, Luxembourg, Luxembourg
SLC45A1 Forward	5'-AGGTCCCCATGGGATTGAGT-3'	Eurofines Scientific, Luxembourg, Luxembourg
SLC45A1 Reverse	5'-GCACAATTGACAGCTGGGTC-3'	Eurofines Scientific, Luxembourg, Luxembourg

3.10. Laboratory Equipment

Table 28. Laboratory Equipment.

Item	Company
96 Fast PCR Plate half skirt	Sarstedt; Nümbrecht, Germany
Agarose gel chamber	Bio-Rad Laboratories; Hercules, California, USA
Amersham Protran Western-Blotting-Membrane, nitrocellulose	Cytiva; Freiburg, Germany
Autoclave Systec 2540 EL	Systec GmbH & Co. KG; Linden, Germany
Autoclave Varioklav	Biomedis; Gießen, Germany
BD Accuri C6 Flow Cytometer	BD Biosciences; Franklin Lakes, New Jersey, USA

Item	Company
BD Plastipak 10 ml Hypodermic Syringe	BD Biosciences; Franklin Lakes, New Jersey, USA
BL1500S Analytical Balance TE313S	Sartorius; Goettingen, Germany
Camera for agarose gel images: Herolab easy B-1228-3U5N	Herolab, Wiesloch, Germany
Cell Chip adapter	Tecan Group; Mannedorf, Switzerland
Cell Chips for cell counting	Tecan Group; Mannedorf, Switzerland
Cell culture dish (6 cm, 10 cm)	Greiner Bio-One; Kremsmunster, Austria
Cell scraper	Sarstedt; Nümbrecht, Germany
Cellstar 96-well, u-Shaped-Bottom Microplate	Greiner Bio-One; Kremsmunster, Austria
Cellstar Cell culture flask (25 cm^2, 75 cm^2, 175 cm^2)	Greiner Bio-One; Kremsmunster, Austria
Cellstar Cell culture plate (6-well, 12-well, 24-well, 96-well)	Greiner Bio-One; Kremsmunster, Austria
Confocal microscope: Nikon Eclipse TE2000-E	Nikon; Minato, Tokio, Japan
Dispensertips Combitips advanced	Eppendorf; Hamburg, Germany
Electrophoresis system: Mini PROTEAN system	Bio-Rad Laboratories; Hercules, California, USA
Erlenmeyer flask	Schott AG; Mainz, Germany
Falcon tubes: 15 ml and 50 ml	Greiner Bio-One; Kremsmunster, Austria
Flow cytometer 1-year maintenance kit	BD Biosciences; Franklin Lakes, New Jersey, USA
Fluorescence microscope: Nikon Eclipse TE2000-S microscope	neoLab Migge; Heidelberg, Germany
FluoroDish Cell Culture Dish - 35 mm	World Precision Instruments; Sarasota, Florida, USA
Freezer -20 °C	Liebherr comfort or Bosch economic
Freezer -80 °C: Thermo Electron Hera freeze	Heraeus; Hanau, Germany
Freezing container: Mr. Frosty	Thermo Fisher Scientific; Waltham, Massachusetts, USA
Gel Blotting Paper GB005, 58x58 cm: Whatman paper	neoLab Migge; Heidelberg, Germany
Heraeus Centrifuge Biofuge Stratos	Thermo Fisher Scientific; Waltham, Massachusetts, USA
Heraeus Microcentrifuge Fresco 21	Thermo Fisher Scientific; Waltham, Massachusetts, USA
Hettich Universal 320/320R centrifuge	Sigma-Aldrich; St. Louis, Missouri, USA
Horizontal shaker: KM-2	Edmund Bühler; Bodelshausen, Germany
Incubator for bacteria	Heraeus; Hanau, Germany
Incubator for cell culture	Binder; Tuttlingen, Germany
Incubator for cell culture (S2) MCO-18AIC	Sanyo; Moriguchi Osaka, Japan
Incubator for cell culture Hera Cell	Thermo Fisher Scientific; Waltham, Massachusetts, USA
Infrared imaging system: Li-Cor Odyssey-Scanner	Li-cor Biosciences GmbH; Bad Homburg, Germany
Laboratory bottles	VWR; Radnor, Pennsylvania, USA
Laminar Flow Cabinet	Esco Lifesciences; Friedberg, Germany

Item	Company
Lids for 96-well plates	Greiner Bio-One; Kremsmunster, Austria
Light microscope: Nikon Eclipse TS100	Nikon; Minato, Tokio, Japan
Liquid nitrogen tank: CBS Cryosystems 6000 series	CBS Cryosystems; L'Aigle, France
Magnetic stirrer and heat plate Variomag Powertherm	IKA-Werke; Staufen, Germany
Microcentrifuge Minispin	Eppendorf; Hamburg, Germany
Microscope cover glass	neoLab Migge; Heidelberg, Germany
Millex-LH syringe filter 0.45 µM	Merck; Darmstadt, Germany
Millicell cell culture inserts PICM0RG50	Merck; Darmstadt, Germany
Multipette E3/Multipette E3x - Electronic Multi-Dispenser Pipette	Eppendorf; Hamburg, Germany
Multipette M4 - Multi-Dispenser Pipette	Eppendorf; Hamburg, Germany
Nalgene Cryogenic vials 2.0 ml	Thermo Fisher Scientific; Waltham, Massachusetts, USA
Nunc Lab-Tek Chamber Slides (8-well)	Thermo Fisher Scientific; Waltham, Massachusetts, USA
Overhead tumbler Roto-Shake Genie	Scientific Industries; Bohemia, New York, USA
Oxo Dish OD24	PreSens - Precision Sensing GmbH; Regensburg, Germany
Parafilm "M" 10 cm x 38 m	Pechiney Plastic Packaging; Chicago, Illinois, USA
Pasteur capillary pipets 230 mm	WU; Mainz, Germany
PCR Optical Adhesive Film	Sarstedt; Nümbrecht, Germany
Petri dish	Greiner Bio-One; Kremsmunster, Austria
pH-Meter Lab850	Schott AG; Mainz, Germany
Pipette tips/Filter tips	Starlab; Hamburg, Germany
Pipettes: 2 µl, 10 µl, 100 µl, 1000 µl	Eppendorf; Hamburg, Germany
Pipettes: 2 µl, 10 µl, 20 µl, 200 µl, 1000 µl	Gilson; Middleton, Wisconsin, USA
Pipetting device: Easypet	Eppendorf; Hamburg, Germany
Pipetting device: Pipetus	Hirschmann Laborgeräte; Eberstadt, Germany
Polystrene round bottom tubes for FACS analysis	Corning; Corning, New York, USA
PowerPac HC High-Current Power Supply	Bio-Rad Laboratories; Hercules, California, USA
Q-Gard 1 Ultrapure Water Purification System	Merck; Darmstadt, Germany
Refrigeator 4 °C	Liebherr comfort or Bosch economic
Roller mixer RM5	Hecht Assistent; Sondheim vor der Rhön, Germany
Roller mixer SRT9D	Stuart (Bibby Scientific Limited); Stone, Staffordshire, UK
SDS-PAGE running chamber and accessoires (Mini-PROTEAN)	Bio-Rad Laboratories; Hercules, California, USA
Semi-dry blotter: Bio Rad Transblot SD Semi-dry-Transfer-Cell	Bio-Rad Laboratories; Hercules, California, USA

Item	Company
Serological Pipettes: 5 ml, 10 ml, 25 ml (Costar Stripette)	Corning; Corning, New York, USA
Shaking incubator for bacteria	New Brunswick Scientific; Edison, New Jersey, USA
Spark® Multimode Microplate Reader	Tecan Group; Mannedorf, Switzerland
StepOnePlus Real-Time PCR System	Applied Biosystems; Waltham, Massachusetts, USA
Stereo microscope: Nikon SMZ25 equipped with a P2-SHR Plan Apo 2x objective	Nikon; Minato, Tokio, Japan
Stereo microscope: Nikon SMZ645 Binocular	Nikon; Minato, Tokio, Japan
Sterile Bench: 2F120-II GS	Integra Biosciences; San Carlos, California, USA
Sterile Bench: Biological safety cabinets class II	Nuaire; Plymouth, Fernbrook, USA
Sterile Bench: HeraSafe	Heraeus; Hanau, Germany
Suspension culture flask (25 cm^2, 75 cm^2)	Greiner Bio-One; Kremsmunster, Austria
TE313-DS precision balance	Sartorius; Goettingen, Germany
Thermocycler	Eppendorf; Hamburg, Germany
Thermomixer Comfort	Eppendorf; Hamburg, Germany
Tubes: 0.2, 0.5, 1.5 and 2 ml and 5 ml	Eppendorf; Hamburg, Germany
Ultrasonic Homogenizer UW/HD 2070	Bandelin electronic GmbH & Co. KG; Berlin, Germany
Vacuum pump Sonorex RK 100 H	Bandelin electronic GmbH & Co. KG; Berlin, Germany
Vibratome VT1000	Leica, Wetzlar, Germany
Vortexer: Vortex-Genie 2	Scientific Industries; Bohemia, New York, USA
Water bath	Köttermann GmbH; Uetze, Germany

3.11. Software

Table 29. Software.

Software	Company
BD Accuri C6 Software V1.0.264.21	BD Biosciences; Franklin Lakes, New Jersey, USA
Benchling	San Francisco, California, USA
Cell Profiler 4.2.1	Broad Institute; Cambridge, Massachusetts, USA
Citavi V6.3	Swiss Academic Software GmbH; Wädenswil, Switzerland
CorelDRAW 2019 V21.3.0.755	Corel Corporation; Ottawa, Canada
GraphPad Prism 7/9	GraphPad Software; Boston, Massachusetts, USA
Image Studio 3.1	Li-cor Biosciences GmbH; Bad Homburg, Germany Biosciences
Image Studio Lite V5.2.5	Li-cor Biosciences GmbH; Bad Homburg, Germany Biosciences
ImageJ Fiji V1.52p	National Institutes of Health (NIH); Bethesda, Maryland, USA
Microsoft Excel 2016	Microsoft; Redmond, Washington, USA
Microsoft Power Point 2016	Microsoft; Redmond, Washington, USA

Software	Company
Microsoft Word 2016	Microsoft; Redmond, Washington, USA
NEB Tm calculator	New England Biolabs; Ipswich, Massachusetts, USA
NIS-Elements Viewer V4.20	Nikon; Minato, Tokio, Japan
Perseus 1.6.15.0	Computational Systems Biochemistry under Prof. Jürgen Cox, Martinsried, Germany (Tyanova et al. 2016)
Smart Servier Medical Art	Les Laboratoires Servier, Suresnes, France
Snapgene Viewer	GSL Biotech LLC; Chicago, Illinois, USA
STRING V11.5	STRING consortium 2019 (Szklarczyk et al. 2019)

4. Methods

4.1. Cell culture

4.1.1. Culture conditions of adherent cell lines

All cell culture work was performed under sterile conditions using a sterile bench and sterile plastic ware. The glioblastoma (GBM) cell lines MZ-54, LN-229, U-251 and U-87 MG, the human embryonal kidney cell line HEK-293T as well as the CRISPR/Cas9 knockout (KO) cell lines MZ-54 *ATG5* and *ATG7* KO and LN-229 *ATG7* KO cells were cultured in DMEM GlutaMAX supplied with 10 % fetal calf serum (FCS) and 1 % penicillin/streptomycin (P/S) solution at 37 °C and 5 % CO_2. The U-251 *ATG5* and *ATG7* KO cell lines, the U-251 sgEGFP control cell line, cell lines with small hairpin RNA (shRNA)-mediated knockdowns (KDs) and cell lines expressing the pMRX-IP-GFP-LC3-RFP-LC3ΔG plasmid were cultured together with the selection antibiotic puromycin with a final concentration of 1 µg/ml. MZ-54 *ATG7* KO cells re-expressing *ATG7* were cultured with 1 µg/ml puromycin and 125 µg/ml hygromycin and cell lines expressing the pmCherry-Gal3 plasmid together with 1 mg/ml G418. All cell lines were tested monthly for mycoplasma and cells were passaged twice a week to prevent overgrowing. For passaging, the culture medium was fully removed and cells were washed with 1xDPBS. Cells were detached from the flask using trypsin-EDTA incubated for about 3 – 5 minutes (min) at 37 °C and subsequently collected in cell culture medium. An appropriate amount of cells was returned into the flask and fresh medium was added.

4.1.2. Culture conditions of suspension cell lines

The glioma stem-like cell (GSC) lines NCH644, GS-5, GS-5 GFP-Luc, NCH481, GS-90, GS-86, NCH465, GS-80 and NCH421K were cultured in Neurobasal-A Medium supplied with 2 % B-27, 1 % GlutaMax, 0.1 % FGF_2 (fibroblast growth factor 2) and EGF (epidermal growth factor) and 1 % P/S. GS-5 GFP-Luc cells were generated by Dr. Bushra Rais and Stephan Müller (working group of Prof. Dr. Evelyn Ullrich, Pediatric Stem Cell Transplantation and Immunology, Goethe University Hospital Frankfurt/Main, Germany). NCH644 *ATG5* and *ATG7* KD cell lines were cultured in addition with 2 µg/ml puromycin and the GFP^+ (green fluorescent protein) spheres in combination with 1.25 µg/ml blasticidin. $NCH644^{GFP+}$ and $NCH421K^{GFP+}$ spheres (both generated by Caterina Roth and Julia Gerstmeier (Experimental Neurosurgery, Goethe University, Frankfurt/Main, Germany) (Gerstmeier et al. 2021)) were cultured with 2 µg/ml or

1 µg/ml puromycin, respectively. For passaging, spheres were collected in falcons and the flasks were rinsed with 1xDPBS. Cells were centrifuged at 195 x g for 3 min and the supernatant was aspirated. Cells were divided by mechanical dissociation using a pipette. An appropriate amount of cells was returned into the flask and fresh medium was added. For determination of cell number cells were dissociated by incubation with accutase for about 10 min at 37 °C.

4.1.3. Cryopreservation and thawing of cells

Cell lines were stored short term in the -80 °C freezer or for long term in the nitrogen tank. For adherent cell lines, the cell suspension was combined 1:1 with freezing medium and for suspension cell lines the culture medium was mixed with dimethyl sulfoxide (DMSO) to a final concentration of 10 %. 1 ml of each mix was pipetted into cryo vials and incubated in special freezing boxes (Mr Frosty), containing isopropanol ensuring slow cooling. The freezing box was stored at least overnight in the -80 °C freezer and finally cryo vials were stored in the nitrogen tank.

For thawing of cell lines, the respective cryo vials were directly warmed up in the water bath until the ice started to move. Then pre-warmed medium was added into the vial and transferred into a falcon with prepared warm medium. The cell suspension was spinned down at 195 x g for 3 min in order to fully remove the DMSO. The supernatant was aspirated, an appropriate amount of cell culture medium was added and cells were transferred into a cell culture flask. On the next day, the medium was changed in order to remove dead cells.

4.1.4. Determination of cell number, cell seeding and treatment

Cells were harvested as described above. The cell number was determined automatically using the Spark Multimode Microplate Reader. For this, 50 µl of the harvested cell suspension was mixed 1:1 with trypan blue solution (0.4 %) (staining of dead cells) and 10 µl of this was pipetted onto the cell chips for cell counting. For seeding, an appropriate amount of cells was taken to prepare a cell suspension with a defined cell concentration and added to the respective plates. The next day, cells were treated as described in the following. First, the treatment medium was prepared containing a defined concentration of the drugs of interest. For adherent cell lines, the medium was aspirated and the medium containing the drugs was pipetted onto the cells. When treating suspension cell lines the treatment medium was directly added (with the same volume) without aspirating the culture medium and containing

the twofold drug concentration. Cells were incubated for a defined period and then subsequent experiments were performed.

4.2. MTT (Cell viability) Assay

The MTT (3-(4,5-dimethylthiazol-2-yl)-2,5-diphenyltetrazolium bromide) assay depends on the water soluble MTT, which is metabolized by viable cells to the colored, water-insoluble formazan salt. Thereto, the amount of formed formazan corresponds to the metabolic activity of the cells (Mosmann 1983). At the end of the treatment period, 40 µl MTT-solution (5 mg/ml) was pipetted to the 200 µl medium in the 96-wells to get a final concentration of 0.83 mg/ml. After incubation of 3 hours (h) at 37 °C and 5 % CO_2, the plate was centrifuged for a few seconds (sec) in order to pelletize the suspension cells. As much as possible of the supernatant was removed without disturbing the cell pellets. Further, 150 µl isopropanol/HCl solution (25:1) was added and incubated for about 15 min at room temperature on a shaker until all of the formazan was solubilized. Finally, the absorbance at 560 nm was measured with the Spark Multimode Microplate Reader, which is indicative for the amount of viable and metabolic active cells.

4.3. Protein analysis

4.3.1. Whole cell lysates

In order to analyse proteins in a sample, protein lysates were prepared. For this, 120,000 cells were seeded out in 6-well plates and treated the next day. After treatment, the supernatant was collected, adherent cells were trypsinized and suspension cells were directly collected. The supernatant as well as the cell suspension were united in falcons and centrifuged at 195 x g for 3 min. The supernatant was aspirated and cell pellets were transferred with 1 ml cold 1xDPBS into 1.5 ml tubes. Cells were centrifuged at 1,358 x g for 3 min and the supernatant was aspirated. Cell pellets were frozen on dry ice and stored at -80 °C until further processing. Finally, an appropriate volume of the 2x sodium dodecyl sulfate polyacrylamide gel electrophoresis (SDS-PAGE) lysis buffer was added and cells were sonicated in order to destroy the cell membranes (2 x 10 ultrasonic beats with 5 min rest on ice in between to avoid warming). Protein lysates were frozen at -20 °C.

4.3.2. Mitochondrial fractionation

For the purpose of analysing mitochondrial proteins, the mitochondria were isolated from whole cell pellets. For this, cells were seeded out in a T75 flask with 1.3 x 10^6 cells per flask and treated on the next day. The cells should not exceed a confluence of 70 % at the time of harvest. Cells were detached from the flask with trypsin-EDTA as described before. The cell pellet was carefully resuspended in 600 µl cold DPBS followed by the addition of 600 µl cytosol extract buffer and an incubation for 20 min on an overhead turner. After centrifugation at 1,047 x g for 5 min and 4 °C, the supernatant was collected in a fresh tube and the cell pellet was saved for later. The supernatant was further centrifuged for 30 sec at 2,404 x g and the new supernatant, which contains the cytosolic fraction, was pipetted into a fresh tube. The pellet of the first centrifugation was now again centrifuged shortly to remove remaining supernatant. Then the pellet was resuspended with 400 µl mitochondria lysis buffer and incubated for 5 min at room temperature. Afterwards, this was centrifuged at 4 °C by 10,399 x g for 10 min and the supernatant was pipetted into a fresh tube. This was again centrifuged for 30 sec at 9,615 x g and the new supernatant was collected in a fresh tube, which contains the mitochondrial fraction.

4.3.3. BCA-assay (Protein quantification for SDS-Page)

In order to analyse the protein concentration in the cell lysates, the colorimetric bicinchoninic acid (BCA)-assay was performed. The colorimetric reaction consists of the biuret reaction that is the reduction of Cu^{2+} to Cu^{1+} by proteins in an alkaline medium and the subsequent formation of a BCA/copper complex, which exhibits a strong linear absorbance at about 560 nm with increasing protein amounts (Smith et al. 1985). The assay was performed in a 96-well plate and for every sample 150 µl NaCl solution (0.9 %) was prepared. The protein standard (0 – 12 µg), the lysis buffer (2 µl) and the samples (2 µl) were pipetted in duplicates followed by the addition of 150 µl BSA-solution (50:1, Reagent A:B) and 30 – 45 min incubation at 37 °C to let the reaction proceed. Finally, the absorbance at 560 nm was measured with the Spark Multimode Microplate Reader. The protein concentration (µg/µl) was calculated by subtracting the lysis buffer and dividing through the slope of the standard curve and sample volume.

4.3.4. Sodium dodecyl sulfate polyacrylamide gel electrophoresis (SDS-Page)

For separation of proteins, depending on their molecular weight, a SDS-Page was performed. A 10 % to 15 % separating gel (depending on the molecular weight of the protein of interest) and a 5 % stacking gel were used for all experiments. An appropriate amount of protein (35 µg – 60 µg) of each sample was mixed with 5x SDS loading sample buffer in a 1:5 dilution followed by boiling up at 95 °C for 5 min. After assembling the SDS-Page running chamber, this was filled up fully with 1x gel electrophoresis running buffer and samples were loaded onto the stacking gel including the molecular weight marker (2.5 µl). A voltage of 85 V was applied for the first 30 min until all proteins run through the stacking gel and then the voltage was increased up to 125 - 135 V until the loading dye run out of the separation gel (60 – 90 min).

4.3.5. Semidry-blot

During the semidry-blot the separated proteins from the SDS-gel were transferred onto a nitrocellulose membrane to allow their detection via antibodies. First, the membrane and the whatmann paper were equilibrated in 1x electrophoresis transfer buffer for a few minutes and afterwards placed into the semi-dry blotter in the following order: whatman paper, nitrocellulose membrane, SDS-gel, whatman paper. After removing all air bubbles and excess fluidics, the transfer was running for 35 min at 15 V constant.

4.3.6. Western blot detection

Transferred proteins were detected using an antibody-based approach. First, the membrane was blocked using either 5 % BSA/TBST or 5 % milk/TBST for 45 to 60 min at room temperature to prevent any nonspecific binding of antibodies to the surface of the membrane. If the primary antibody was diluted in a different buffer as the blocking buffer, the membrane was washed three times with 1xTBST. Otherwise the primary antibody was directly added onto the membrane diluted in the respective buffer and incubated overnight at 4 °C on a rolling shaker. On the next day, the primary antibody solution was removed and the membrane was washed three times for 10 min with 1xTBST followed by incubation with the secondary antibody diluted in 3 % BSA/TBST for 1 h at room temperature. After three washing steps with 1xTBST for 10 min, the detection of the secondary antibody was performed with the Li-Cor Odyssey-Scanner. As a loading control the housekeeping gene GAPDH (glyceraldehyde 3-phosphate dehydrogenase) was detected, too. Membranes were stored in 1xPBS at 4 °C for short time periods or were dried and stored at room temperature in aluminium foil up to 1 year.

4.4. Flow cytometry

Flow cytometry enables the measurement of single cells by their size (forward scatter) and granularity (side scatter), but also after staining with fluorescent dyes or the expression of fluorescent proteins. Lasers with a defined wavelength excite the fluorescent dyes or proteins followed by the emission of light with a particular wavelength, which is detected by specific filters. For all flow cytometry measurements, cells were seeded out in 12- or 24-well plates with 50,000 – 100,000 or 30,000 – 65,000 cells/well, respectively, and treated the following day. For every sample, 5,000 – 10,000 cells were measured with the BD Accuri C6 flow cytometer unless otherwise stated. The flow cytometer is equipped with two lasers with excitations at 488 nm and 640 nm and four optical filters for emission detection: FL1: 533/30 nm, FL2: 585/40 nm, FL3: > 670 nm and FL4: 675/25 nm.

4.4.1. Annexin V/propidium iodide staining

Cell death was measured via annexin V (excitation (ex)/emission (em) maxima: 488/518 nm) binding and propidium iodide (PI; ex/em maxima: 535/617 nm) uptake. Annexin V binds to phosphatidylserine (PS) that is externalized during early apoptosis but also during cell necrosis. Therefore annexin V stains cells in early apoptosis and necrosis (Vermes et al. 1995). PI is a DNA intercalating substance that cannot pass intact cell membranes and therefore is used as a general marker for cell death since PI can enter the cell (Ormerod et al. 1993). After the treatment period, the supernatants were collected in FACS tubes and cells were washed with DPBS. Adherent cells were trypsinized with trypsin-EDTA and collected with DPBS into the FACS tubes. Tubes were centrifuged at 195 x g for 3 min and the supernatants decanted carefully. Suspension cell lines were collected in FACS tubes, the wells were washed out with DPBS and cells were spinned down at 234 x g for 4 min. Cells were separated using accutase for about 5 – 7 min at 37 °C. Afterwards, DPBS was added and tubes were again centrifuged at 234 x g for 4 min. For analysis of cell death, 50 µl FACS buffer + 0.8 µL APC annexin V + 0.8 µl PI solution was added per sample and incubated for 10 min at room temperature. Measurements were performed in the FL3 (PI) and FL4 (annexin V) channels (Figure 10).

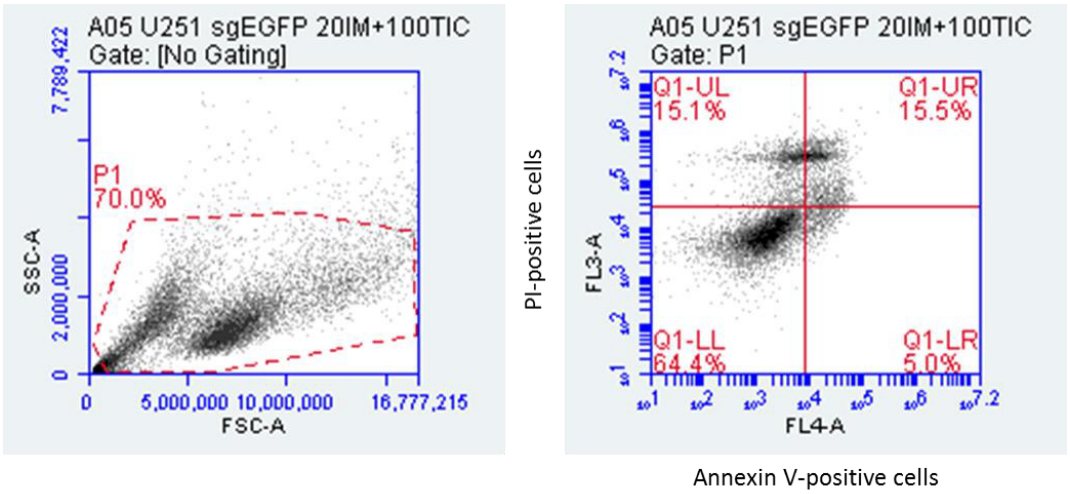

Figure 10. Gating strategy for the determination of cell death. On the left cells were gated using forward scatter (FSC) vs side scatter (SSC) in order to exclude debris and to define the cell population of interest. This population was further distinguished on the right by annexin V and PI staining, detecting negative (viable cells, LL), annexin V-only positive (LR), PI-only positive (UL) and double positive (UR) cell populations as depicted in each quarter in percent. Those percentages were used for further calculations.

4.4.2. Autophagic flux analysis using the pMRX-IP-GFP-LC3-RFP-LC3ΔG plasmid

Autophagic flux analysis was performed using cells transfected with the pMRX-IP-GFP-LC3-RFP-LC3ΔG plasmid. MZ-54 cells stably expressing the pMRX-IP-GFP-LC3-RFP-LC3ΔG plasmid were generated by Svenja Zielke (working group of Prof. Dr. Simone Fulda, Experimental Cancer Research in Pediatrics, Goethe University Hospital, Frankfurt/Main, Germany). The GFP-LC3-RFP-LC3ΔG tandem construct is cleaved into equimolar amounts of GFP-LC3 and RFP-LC3ΔG by endogenous ATG4. GFP-LC3 is degraded during autophagy, while RFP-LC3ΔG cannot be lipidated and therefore remains in the cytosol as an internal control. The reduction in the EGFP (enhanced green fluorescent protein)/mRFP1 (monomeric red fluorescent protein 1) ratio is therefore a sign for an increase in autophagic flux (Figure 11) (Kaizuka et al. 2016). After treatment, cells were collected into FACS tubes as described above, pelletized by centrifugation (195 x g, 3 min) and the supernatant was decanted carefully. After the addition of 50 µL DPBS, cells were measured at the flow cytometer in the FL2 (EGFP) and FL3 (mRFP1) channels.

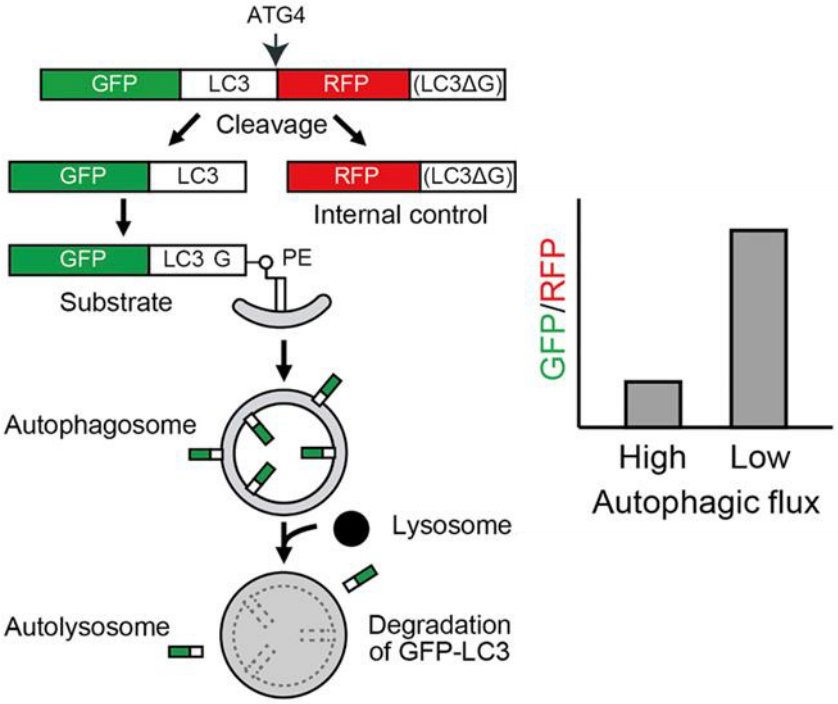

Figure 11. Assessment of autophagic flux using the pMRX-IP-GFP-LC3-RFP-LC3ΔG plasmid. Image showing the cleavage of the pMRX-IP-GFP-LC3-RFP-LC3ΔG and subsequent degradation of EGFP-LC3, while RFP-LC3ΔG remains in the cytosol. The EGFP/mRFP1 ratio relates to the amount of autophagic flux and is measured via flow cytometry (modified from Kaizuka et al. (2016)).

4.4.3. Mitophagic flux analysis using the mt-mKeima plasmid

The mitophagic flux analysis as well as the transfection of cells with the pCHAC-mt-mKeima plasmid was performed by Süleyman Bozkurt (working group of Dr. Christian Münch, Institute of Biochemistry II, Goethe University Hospital Frankfurt/Main, Germany) as described in Reisbeck et al. (2023). Keima is a coral-derived acid-stable fluorescent protein that changes its excitation wavelength in a pH-dependent manner from 488 nm (pH 7) to 561 nm (pH 4) (Figure 12). Calculating the 561 nm:488 nm ratio allows to calculate the delivery of mitochondria to lysosomes (mitophagy) (Katayama et al. 2011). Briefly, after treatment cells were trypsinized, washed with medium and resuspended in 1 ml chilled DPBS. During the measurement the cell suspensions were kept on ice and 10,000 cells per sample were measured with the BD LSRFortessa (BD Biosciences) flow cytometer.

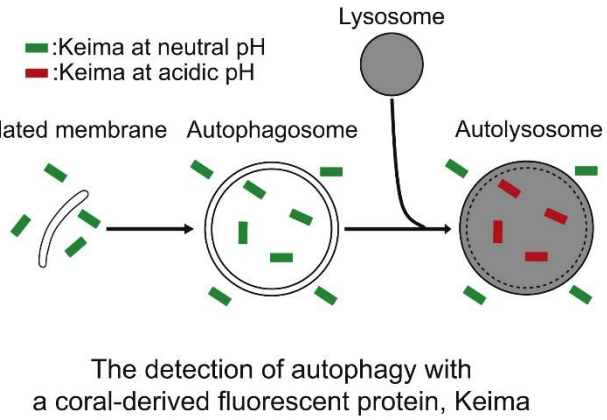

Figure 12. Analysis of mitophagic flux using the pCHAC-mt-mKeima plasmid. Image showing the membrane bound Keima that excites a green fluorescence at a neutral pH, which is changed after fusion with a lysosome to a red excitation wavelength at an acidic pH. Adapted from Katayama et al. (2011).

4.4.4. Measurement of ATP using the BioTrackerATP dye

BioTracker is a live cell dye that specifically detects ATP in the mitochondria of living cells. In the absence of ATP the probe is non-fluorescent because it forms a closed ring structure. In the presence of the negatively charged ATP it breaks the covalent bonds between boron and ribose opening the ring and producing fluorescence (Figure 13) (Wang et al. 2016b). After treatment, cells were stained with the BioTracker dye by adding it directly to the cell culture medium to a final concentration of 10 µM for 15 min at 37 °C. Afterwards, cells were harvested as described above and after centrifugation and decanting 50 µL DPBS were added for measurement at the flow cytometer in the FL2 channel.

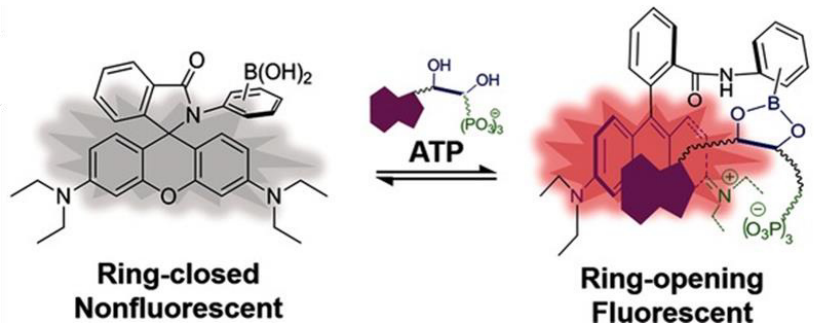

Figure 13. BioTracker ATP dye mechanism. In the absence of ATP the ATP probe forms a closed ring structure that is non-fluorescent (left side). In the presence of ATP the covalent bonds between boron and ribose break, which opens up the ring, producing fluorescence (right side). Adapted from Wang et al. (2016b).

4.4.5. Analysis of mitochondrial superoxide using MitoSOX

MitoSOX (ex/em maxima: 510/580 nm) is a red mitochondrial superoxide indicator that detects superoxide in the mitochondria of live cells. At the end of the treatment, the medium was collected in FACS tubes and 200 µl of 5 µM MitoSOX reagent in HBSS was added to the cells and incubated for 15 min at 37 °C. Afterwards, the MitoSOX reagent was removed, cells

were washed with 800 µl DPBS, trypsinized with 200 µl trypsin-EDTA, collected with 800 µl DPBS into FACS tubes and pelletized at 195 x g for 3 min. The supernatant was carefully decanted and 50 µl DPBS was added for the FACS measurement. The MitoSOX was measured in the FL2 channel.

4.4.6. Measurement of mitochondrial membrane potentials

The tetramethylrhodamine (TMRM; ex/em maxima: 553/576 nm) dye accumulates in healthy mitochondria depending on their membrane potential and therefore negatively correlates with mitochondrial membrane depolarization. At the end of the treatment, the TMRM staining solution was given to the cells at a final concentration of 30 nM and incubated for 20 min at 37 °C. Afterwards, cells were harvested as described above and the TMRM signal was measured in the FL2 channel.

4.5. Fluorescence microscopy

The intracellular localization of proteins was analysed using immunofluorescence stainings based on antibodies or dyes as well as transfection of fluorescence reporter plasmids followed by subsequent analysis under the fluorescence microscope.

For immunofluorescence stainings, 12,000 – 16,000 cells were seeded into chamberslides and treated the next day. After treatment, the cell culture medium was removed and cells were fixed with 4 % paraformaldehyde (PFA) for 10 min followed by ice-cold methanol for 5 min. Cells were washed three times with DPBS + 0.1 % Tween-20 (DPBST) and permeabilized with 0.5 % Triton X-100 in DPBS for 5 min. After another three washing steps, cells were blocked with 4 % BSA in DPBS for 1 h at room temperature followed by the addition of the primary antibody overnight at 4 °C diluted in blocking solution. The next day, cells were washed again and the secondary antibody was applied for 1 h at room temperature followed by three washing steps. Finally, cover glasses were fixed using mounting medium with DAPI and the slides were sealed with nail polish. For analysing reporter plasmids, cells were seeded, treated, fixed and directly mounted as described above. Microscope images were taken with the Nikon Eclipse TE2000-S microscope or the Nikon Eclipse TE2000-E confocal microscope at 60x magnification and processed with the NIS Elements AR 3.2 software. The overlay of the different fluorescent channels and further image processing was performed with ImageJ.

4.5.1. Monitoring lysosomal membrane permeabilization using the pmCherry-Gal3 plasmid

The pmCherry-Gal3 plasmid consists of mCherry as fluorescent reporter bound to galectin 3 (LGALS3/Gal3), which translocates to the lysosomal membrane upon its rupture and can therefore be used as a marker for lysosomal damage (Papadopoulos et al. 2017). For this, cells were prepared as described above. Additionally, cells were stained with the primary antibody against LAMP1 as a lysosomal marker, which was detected using the Alexa Fluor 488 anti-mouse secondary antibody. Finally, slides were mounted with the mounting medium Fluoroshield with DAPI. For washout experiments, the medium was changed after 16 h of drug treatment followed by additional 24 h of culturing.

4.5.2. Cholesterol staining with filipin III

The cholesterol staining was performed using a cholesterol assay kit containing filipin III according to the manufacturer's instructions. Filipin is a naturally fluorescent polyene antibiotic and its interaction with cholesterol alters the absorption and fluorescence spectrum of filipin III allowing the visualization of cholesterol under the fluorescence microscope (Robinson and Karnovsky 1980). Cells were seeded out as described above and treated on the next day. After treatment, the medium was removed and cells were fixed with 4 % PFA for 15 min. Afterwards, the PFA was removed and cells were washed three times with DPBST. The filipin III staining solution was added 1:100 in DPBS for 1 h at room temperature followed by three washing steps with DPBST. Permeabilization, blocking and antibody staining were performed as described above. The primary antibody against LAMP1 was used as a lysosomal marker and detected with the secondary antibody Alexa Fluor 594 F(ab')2 fragment together with filipin III staining solution. Finally, the microscope slide was mounted with the mounting medium mountant PermaFluor without DAPI.

4.5.3. Monitoring mitophagy using the Mtphagy Detection Kit

Microscopic assessment of mitophagy was performed using the mtphagy detection kit according to the manufacturer's instructions. The mtphagy dye accumulates in healthy mitochondria and changes its fluorescence characteristic according to the pH. At a neutral pH the mtphagy dye exerts only a weak fluorescence, but under acidic conditions the emitted fluorescence increases and can be visualized with a fluorescence microscope (Iwashita et al. 2017) (Figure 14). Therefore, the mtphagy dye can be used as a mitophagy reporter. For

additional validation, lysosomes were stained with the lyso dye to directly monitor the fusion of mitochondria-containing autophagosomes with lysosomes. For this, 100,000 cells were seeded out in live cell dishes and stained with the mtphagy dye on the next day before the start of the treatment. The mtphagy dye working solution (100 nM) was prepared in serum-free medium, added for 30 min at 37 °C followed by the addition of the treatment solutions. At the end of the treatment, medium was aspirated and the lyso dye working solution (1 µM in serum-free medium) was added for 30 min at 37 °C. Afterwards, nuclei were stained using Hoechst 33342 at a final concentration of 1 µg/ml for 10 min at room temperature. Between each step cells were washed twice with serum-free medium. After one more washing step, the cells were analysed under the fluorescence microscope in DPBS.

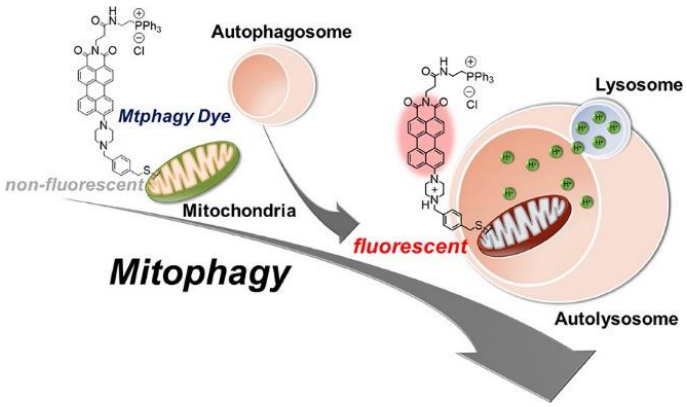

Figure 14. Mechanism of the mtphagy dye staining. The mtphagy dye is immobilized in healthy mitochondria and accumulates, exerting only a weak fluorescence at the neutral pH. During mitophagy, mitochondria-containing autophagosomes fuse with lysosomes, resulting in a decrease in the pH and subsequent increase of the fluorescence intensity of the mtphagy dye (adapted from Iwashita et al. (2017)).

4.5.4. NPM1 staining for analysing nucleolar stress

The translocation of the nucleolar protein nucleophosmin 1 (NPM1) into the nucleoplasm is a marker of nucleolar stress (Yung, Yang and Bor 1991). The NPM1 antibody staining was performed as described in Sutton et al. (2019). Briefly, after treatment, cells were washed twice with DPBS followed by 20 min fixation with 4 % PFA, 20 min permeabilization with 0.5 % Triton X-100 and two times blocking with 1 % BSA/DPBST for 10 min all performed at room temperature. The NPM1 primary antibody was incubated for 1 h as well as the secondary antibody. Between each step slides were washed three times for 5 min with DPBST and finally mounted with ProLong™ Diamond Antifade Mountant with DAPI. The coefficient of variation (CV) for individual nuclei, defined as the standard deviation in pixel intensity divided by the mean pixel intensity (see below), was calculated from the NPM1 images using Cell Profiler (Stirling et al. 2021).

$$CV = \frac{standard\ deviation\ of\ pixel\ intensity}{mean\ pixel\ intensity}$$

4.6. Immunohistochemistry

The cells were collected directly after treatment from culturing flasks, centrifuged at 195 x g for 3 min, the supernatant was removed and cells were incubated with 4 % PFA overnight. Further processing was done by Dr. Katharina J. Weber (Neurological Institute (Edinger Institute), Goethe University Hospital, Frankfurt/Main, Germany) as described in Reisbeck et al. (2023). Pictures were taken with the Nikon Eclipse TE2000-S microscope at 20x magnification, processed with the NIS Elements AR 3.2 software and further image processing was performed with ImageJ. The 300- or H-score was calculated by multiplying the percentages of stained cells (0 to 100 %) with 1, 2 or 3 depending on the respective intensities of staining (weak, moderate or strong, respectively) and subsequent summation of obtained values from all three groups (Goulding et al. 1995). The scoring was repeated twice by independent raters.

4.7. RNA isolation

In order to analyse messenger RNA (mRNA) expression levels, RNA was isolated using the ExtractMe total RNA kit according to the manufacturer's instructions. For this, 120,000 – 1,000,000 cells were seeded out in 6-well plates and harvested after 24 h as described before. The lysis of the cells was performed using 620 µL of the R-lys buffer (freshly added: 1:100 β-

Mercaptoethanol + AF (20 µL for each sample)) and mixed by vortexing for 1 min. After centrifugation for 2 min at 15,000 x g, the supernatant was transferred into a new tube and 600 µl 70 % ethanol was added and resuspended. This was transferred to a RNA purification column and centrifuged for 15 sec at 15,000 x g. The column was washed with 600 µl RW1 and then two times with 500 µl RW2. For washing, the column was centrifuged for 15 sec at 15,000 x g and the flow-through was removed. After the last washing step, the column was centrifuged again to remove remaining wash buffer and transferred into a new RNAase-free tube. The RNA was eluted using 40 – 50 µl REB-Buffer and centrifuged at 15,000 x g for 1 min. RNA concentration was measured using the Spark Multimode Microplate Reader.

4.8. cDNA synthesis of mRNA

The isolated RNA was transcribed into complementary DNA (cDNA) that can be further used for quantitative real time polymerase chain reaction (qRT-PCR). For cDNA-synthesis, 2 µg RNA of each sample was pipetted together with 1 µl oligo dT20 primer (50 µM), 1 µl random hexamer primer N6 (3 µg/µl), 1 µl dNTP mix (10 mM) and filled up with DEPC-H_2O to a total volume of 14 µl. The mixture was boiled up to 65 °C for 5 min and then cooled down on ice for at least 1 min. Tubes were centrifuged and then 4 µl 5x first strand buffer, 1 µl 0.1 M DTT and 1 µl superscript III reverse transcriptase (100 U/µl) were added. This was again heated up to 25 °C for 5 min, to 50 °C for 60 min and 70 °C for 15 min. Finally, the cDNA was diluted with up to 180 µl DEPC-H_2O.

4.9. Quantitative real-time polymerase chain reaction (qRT-PCR)

To quantify gene expression the qRT-PCR was performed using mRNA that was translated into cDNA (4.8) and TaqMan reagents. The TaqMan probe contains a specific oligonucleotide that is complementary to the target cDNA, a fluorescent reporter dye bound to the 5’ end and a quencher on the 3’ end that reduces the fluorescence emitted by the reporter dye while the probe is intact. During each elongation cycle the 5’ nuclease activity of the Taq DNA polymerase cleaves the fluorescent reporter, resulting in a fluorescence signal that is proportional to the amount of amplified cDNA (Bustin 2000). After reaching a certain threshold, this cycle is defined as the threshold cycle (C_T), which is inversely related to the starting amount of target DNA (Livak and Schmittgen 2001). For this, 1 µl TaqMan primer, 10 µl FastStart universal probe master (ROX), 4 µl DEPC-H_2O and 5 µl cDNA were mixed and transferred into a 96-well qRT-PCR plate. The following reactions were performed using the

StepOnePlus Real-Time PCR System: 50 °C for 2 min, 95 °C for 10 min, followed by 40 cycles of 15 sec at 95 °C and 60 sec at 60 °C. Data was analysed using the comparative C_T method. Therefore, the fold difference of the gene of interest was normalized to the amplification value of the endogenous control gene TBP (TATA-box binding protein) (ΔC_T) (Livak and Schmittgen 2001). Values outside of the detection range were set to 0 for data analysis.

4.10. Genomic DNA isolation and PCR for detection of *SLC45A1*

In order to identify the *SLC45A1* (solute carrier family 45 member 1) gene in different cell lines, cells were pelletized and resuspended with 200 µl Quick extract DNA solution per 200,000 cells. The DNA solution was incubated for 6 min shaking at 65 °C followed by 15 sec vortexing and 2 min at 98 °C. Finally, DNA extracts were stored at -80 °C.

The following reagents were mixed for the PCR reaction and filled up with DEPC-H_2O to 20 µl:

Table 30. Reagents and volumes for the PCR reaction.

Reagent	Volume
10x Taq Buffer	2 µl
200 µM dNTPs	0.4 µl
0.2 µM Primer forward	0.4 µl
0.2 µM Primer reverse	0.4 µl
0.5 u Taq Polymerase	0.1 µl
Template or negative control (H_2O)	1 µl

PCR reactions were performed with the following PCR program:

Table 31. PCR program for detection of SLC45A1.

Temperature	Time	Repeats
95°C	5 min	1x
95°C	30 sec	35x
54°C	30 sec	
68°C	13 sec	
68°C	2 min	1x

The annealing temperature was adjusted to the melting temperature of the primers, which is based on the primer sequence, concentration and the utilized DNA polymerase. Therefore, the melting temperature calculator tool from NEB was used. The elongation time was adjusted to the size of the template using about 1 min per kilo base.

Subsequently, the samples were separated on a 2 % agarose gel, which was prepared with TAE buffer together with ethidiumbromide. After the gel was polymerized, the gel chamber was prepared and filled up with TAE buffer. PCR samples were mixed with 4 µl loading buffer and loaded onto the gel together with a 100 bp DNA ladder. The gel was running at 110 V for about 30 – 45 min and DNA-bands were detected under a UV-light. GAPDH was used as a loading control.

4.11. Plasmid preparation

4.11.1. Bacterial culture

Plasmids used for transfection or transduction into cells were multiplied using bacteria. When using glycerol stocks they were directly used to start a bacterial culture. For this, some of the glycerol stock was scratched up, added into 500 µl LB-medium without antibiotics and incubated at 37 °C for 30 min in the shaker. 25 – 50 µl of this was spread out onto a LB-Agar plate supplied with ampicillin (100 µg/ml) to select only bacteria that contain the plasmid. The plate was incubated overnight for about 15 – 20 h at 37 °C. At least one of the grown bacterial colonies was picked up and transferred into 5 ml LB-Medium with 100 µg/ml ampicillin and incubated for about 16 h at 37 °C in the shaking incubator followed by plasmid isolation.

4.11.2. Plasmid isolation, Miniprep

Plasmids from bacterial overnight cultures were isolated using the QIAprep Spin Miniprep Kit according to the manufacturer's instructions. Overnight cultures were pelletized in 1.5 ml tubes at 6,800 x g for 3 min and some of the culture was stored at 4 °C as a backup. The pellet was further resuspended in 250 µl buffer P1 (+ RNase A) followed by the addition of 250 µl buffer P2, which was mixed through inverting 4 – 6 times. This mix was incubated not longer than 5 min and then buffer N3 was added and directly mixed through inverting again 4 – 6 times. After centrifugation at 17,900 x g for 10 min, the supernatant was added to the QIAprep 2.0 spin column followed by centrifugation at 17,900 x g for 30 – 60 sec. The flow-through was discarded and the column was washed with 0.5 ml buffer PB and again centrifuged for 30 – 60 sec. The column was washed with 0.75 ml buffer PE (+ ethanol) and centrifuged for 30 – 60 sec. Afterwards, the column was again centrifuged for 1 min to remove remaining wash buffer and the column was transferred into a new 1.5 ml tube. The DNA was eluted using 50 µl buffer EB that was incubated for 1 min and then centrifuged for 1 min. The DNA concentration

was measured with the Spark Multimode Microplate Reader. In order to verify the plasmid sequence, the plasmid DNA was sent to Microsynth Seqlab GmbH.

4.11.3. Plasmid purification, Maxiprep

If bacteria were positive for the plasmid of interest, the stored backup of the bacterial culture used for the Miniprep was directly used to start a new overnight culture for the Maxiprep in 150 ml LB-medium with 100 µg/ml ampicillin. The overnight culture was incubated for about 16 h at 37 °C and 250 rpm shaking. The purification of the plasmid was performed with the EndoFree Plasmid Maxi Kit (QIAGEN) according to the manufacturer's instructions. Therefore, the overnight culture was cooled down for 15 min on ice and then pelletized at 6,000 x g for 15 min. The supernatant was carefully decanted and the pellet was resuspended in 10 ml buffer P1 (+ RNase). For cell lysis, 10 ml buffer P2 was added, inverted and incubated not longer than 5 min at room temperature. To neutralize the mixture 10 ml buffer P3 was added and inverted. The lysate was then added to the QIAfilter cartridge and incubated for 10 min at room temperature. Then the cap of the QIAfilter cartridge was removed and the lysate was filtered into a 50 ml falcon. To remove endotoxins 2.5 ml ER-buffer was added, 10 times inverted and incubated on ice for 30 min. During the incubation time the QIAGEN-tip was equilibrated with 10 ml buffer QBT. Afterwards, the lysate was added to the QIAGEN-tip and let flow-through. Then the QIAGEN-tip was washed two times with 30 ml buffer QC. The DNA was eluted with 15 ml buffer QN in a 50 ml falcon. For DNA precipitation, 10.5 ml isopropanol was added, thoroughly vortexed and directly centrifuged at 1,160 x g for 60 min. Afterwards, the supernatant was carefully decanted and the DNA pellet was washed two times with 70 % ethanol and centrifuged at 16,249 x g for 5 min. At the end, as much as possible of the ethanol was removed and the DNA pellet was air-dried for about 5 – 15 min. The DNA pellet was then diluted in 100 µl TE buffer and the DNA concentration measured with the Spark Multimode Microplate Reader.

4.12. Generation of lentiCRISPR/Cas9 knockouts

4.12.1. Vector design

The single guide RNA (sgRNA) design was done by Dr. Nina Meyer (Meyer 2019; Meyer*, Henkel* et al. 2021) and sgRNAs were ordered at Eurofins. The sgRNAs were cloned into the pLentiCRISPRv2 vector in order to generate lentiviral particles for CRISPR/Cas9 KOs.

4.12.2. Digestion of the lentiCRISPRv2 vector

For the digestion of the lentiCRISPRv2 vector, 3 µg of the vector was mixed with 2 µl 10x FastDigestGreen Buffer, 1 µl DTT (20 mM), 1.5 µl ESP3I and filled up with water to 20 µl. After incubation at 37 °C for 4 h and for 20 min at 65 °C, the digested vector was cleaned up using the QIAquick gel extraction kit. For this, 60 µl buffer QG and 20 µl isopropanol were added to the digested vector and the sample was added to a QIAquick spin column followed by centrifugation for 1 min at 10,000 x g. The flow-through was discarded and 0.5 ml buffer QG was added followed by centrifugation of the column for 1 min. Further, 0.75 ml buffer PE was added and incubated for 4 min at room temperature with subsequent centrifugation for 1 min. The flow-through was discarded and the QIAquick column was transferred to a new 1.5 ml tube. DNA elution was performed with 50 µl buffer EB and centrifugation for 1 min.

4.12.3. Annealing and phosphorylation of the guides

Before the antisense and sense strands of each sgRNA can be cloned into the plentiCRISPRv2 vector they need to be annealed and phosphorylated. For this, 3.5 µl of the sense and antisense guide (100 µM stock) were mixed with 3.5 µl 10x T4 ligation buffer and 1.75 µl T4 polynucleotide kinase, filled up with MilliQ water to 35 µl and incubated for 30 min at 37 °C and 5 min at 95 °C. The annealed oligonucleotides were serial diluted up to 1:500.

4.12.4. Ligation of sgRNAs and the plentiCRISPRv2 vector

For ligation of the annealed sgRNAs and the digested plentiCRISPRv2 vector, 50 ng of the digested vector was mixed with 1.5 µl 10x T4 ligation buffer, 1 µl T4 ligase, 2 µl of the 1:500 diluted oligonucleotides and filled up with MilliQ water to 15 µl. The mixture was incubated for 2 h at 21 °C.

4.12.1. Transformation

The ligated vector was further transformed into Stbl3 bacteria in order to multiply the plasmid. For this, the one shot Stbl3 chemically competent *E.coli* were used. The Stbl3 bacteria were thawed one ice and 5 µl of the ligation mix was added and carefully mixed not resuspended followed by an incubation on ice for 30 min. Afterwards, a heat shock was performed by heating up the bacteria for 45 sec to 42 °C. Then bacteria were cooled down directly on ice for 2 min followed by the addition of 250 µl pre-warmed S.O.C. medium and subsequent incubation on the shaker for 1 h at 37 °C and 300 rpm. 200 µl of the transformation mix was spread out on a LB-Agar plate with ampicillin (100 µg/ml) and incubated overnight at 37 °C.

Grown bacterial clones were picked for overnight cultures followed by a mini prep as described above. Positive clones, containing the ligated vector that was proved by sequencing, were further multiplied with a maxi prep as described above.

4.12.2. Stable lentiviral transduction of the lentiCRISPR sgRNAs

Transduction was performed with all three sgRNA vectors for each gene. For this, viral particles were generated in the human embryonic kidney cell line HEK-293T that harbours the SV40 large T antigen, which enables them to produce recombinant proteins within plasmid vectors containing the SV40 promoter (Graham et al. 1977). For this, 1,000,000 cells were seeded out in 10 cm plates and transfection was performed on the next day. Cells were carefully washed with DPBS and DMEM with 10 % FCS but without P/S was added. The DNA- and the Fugene HD-Mix were prepared as followed:

Table 32. Preparation of the DNA- and the Fugene HD Mix for transfection of HEK-293T cells.

DNA-Mix	Fugene HD Mix
13 µg sgRNA plasmid	39 µl Fugene HD
9.75 µg psPAX2	
3.25 µg pMD2.G	
In 375 µl Opti-MEM	In 187.5 µl Opti-MEM

Both components were thoroughly mixed by pipetting, united and incubated for 30 min at room temperature. Afterwards, the transfection mix was added dropwise to the plate, which was carefully shaked meanwhile. The cells were incubated with the transfection mix for about 6 to 7 h. At the end the medium was removed, cells were carefully washed with DPBS and new DMEM 10/1 was added. After about 16 h, the supernatant that now contains the viral particles was collected in falcon tubes and new DMEM 10/1 was added. After another 24 h, the supernatant was collected in the falcon tubes, too and viral particles were filtered with a 0.45 µm filter. For short times, the viral particles were stored at 4 °C but for longer periods they were frozen at -80 °C. For transduction, 350,000 U-251 cells were seeded out in T25 flasks and on the next day transduced with the virus-containing supernatant diluted in DMEM and 3 µg/ml polybrene. The medium was changed after 24 h and after an additional 24 h cells stably expressing the plasmids were selected with 1 µg/ml puromycin. A second transfection was performed after 1 week of puromycin selection. Afterwards, stably transduced cells were seeded out in 96-well plates in order to generate single cell clones. Single cell clones were expanded and the KO was validated by immunoblot analysis.

4.13. Generation of shRNA-mediated knockdowns

4.13.1. Transfection using the pLKO.1 plasmid system

Lentiviral particles used for shRNA-mediated KDs were produced in HEK-293T cells as described above using Fugene HD (4.12.1). If lentiviral particles were produced for suspension cell lines, the medium was changed to Neurobasal medium after transfection of the HEK-293T cells.

4.13.2. Transfection using the pGIPZ plasmid system

Similarly to the transfection using the pLKO.1 system, HEK-293T cells were used for lentiviral particle production using the pGIPZ vector. In contrast, all three plasmids (7.5 µg shRNA plasmid, 12.5 µg pCMV-dr8.91 and 1 µg pMD2.G) were directly diluted in 450 µl H_2O and 50 µM $CaCl_2$ (2.5 M). Further, 500 µl of 2xHBS was prepared in a 15 ml falcon and the DNA/$CaCl_2$ solution was added drop-wise while blowing air bubbles through a pipette. During the incubation period of 15 – 20 min the medium of the cells was changed into medium containing 25 µM chloroquine. Finally, the DNA was added dropwise to the cells and incubated for 6 – 8 h followed by a medium change into fresh medium. After 24 h and 48 h the supernatant containing the viral particles was harvested, filtered and stored as described above.

4.13.3. Transduction of viral particles

For transduction of adherent cell lines, 350,000 cells were seeded out in T25 flasks and on the next day transduced with the virus-containing supernatant diluted 1:1 in DMEM plus 3 µg/ml polybrene. The medium was changed after 24 h and after an additional 24 h cells stably expressing the plasmids were selected with 1 µg/ml puromycin and KDs were verified via western blot or qRT-PCR of the targeted protein or gene, respectively.

For transduction of suspension cell lines, 50,000 cells were seeded out in 24-well plates and the virus-containing supernatant was added in different dilutions (1:1, 1:4, 1:10) in Neurobasal medium with the addition of 4 µg/ml protamine sulfate. Transduction was performed for 72 h and afterwards the medium was changed. After 24 h, the selection of cells stably expressing the shRNA plasmids was started with 1 µg/ml puromycin and after additional 48 h switched to 2 µg/ml puromycin. Wells containing viable spheroids under antibiotic selection were pooled, expanded and the KD was confirmed via immunoblot analysis.

4.14. Generation of GFP-positive cells

Generation of viral particles using HEK-293T cells, the pLV[Exp]-EGFP:T2A:Bsd-CMV>ORF_Stuffer plasmid or the pLV[Exp]-EGFP/Puro-CMV>Stuffer300 and Fugene HD mix as well as transduction of spheroids was performed as described above (4.12.1 + 4.13.3). Cells expressing the pLV[Exp]-EGFP:T2A:Bsd-CMV>ORF_Stuffer plasmid were selected with 1.25 µg/ml blasticidin and cells expressing the pLV[Exp]-EGFP/Puro-CMV>Stuffer300 with 1 or 2 µg/ml puromycin.

4.15. Re-expression of *ATG7* in *ATG7* KO cells

For the re-expression of *ATG7* in *ATG7* KO cells, an inducible plasmid that only allows expression of *ATG7* in the presence of doxycycline (DOX) was used. MZ-54 *ATG7* KO cells were first transduced with the plasmid containing the *hATG7* sequence (pLV[Exp]-Puro-TRE3G>hATG7) and in a second step transduced with the regulator plasmid (pLV[Exp]-CMV>Tet3G/Hygro). Virus particles were generated in HEK-293T cells using Fugene HD and transduction was performed as described above. The selection of cells containing the plasmids was performed using 1 µg/ml puromycin and 125 µg/ml hygromycin. Re-expression was confirmed by immunoblot analysis.

4.16. Transfection using Lipofectamine

Stable transfection of plasmids was performed using lipofectamine 3000 transfection reagent according to the manufacturer's instructions. Corresponding to this, 3.75 µl lipofectamine per 6-well was diluted in Opti-MEM and united with 2.5 µg DNA and 3.75 µl P3000 reagent diluted in Opti-MEM as well. After 10 – 15 min incubation at room temperature, the DNA-lipid complex was added dropwise to the cells and incubated for 24 h. Stable transfected cells were selected with antibiotics.

4.17. Transient knockdown using siRNA

Small interfering RNA (siRNA) was used to introduce a transient KD. Therefore, the double-stranded RNA molecule binds to its complementary region of the target mRNA and causes its degradation. For this, cells were transfected with siRNA complexed with lipofectamine 3000 at about 50 – 70 % confluence. The siRNA (1 nM – 5 nM) was diluted in Opti-MEM and united with lipofectamine 3000 that was diluted in Opti-MEM as well (5 µl in 250 µl Opti-MEM per 6-well or 1.5 µl in 50 µl Opti-MEM per 24-well). This was incubated for 10 – 15 min at room

temperature and then added dropwise to the cells. After 16 h, the medium was changed and treatments were performed.

4.18. Oxygen consumption rate

The oxygen consumption rate was measured in the group of Prof. Steinbach (Dr. Senckenberg Institute of Neurooncology, Goethe University, Frankfurt/Main, Germany). For this, 30,000 cells per well were seeded out in 24-well plates with integrated oxygen sensor and treated the next day. Directly after treating, the wells were covered with sterile paraffin oil to provide airtight conditions. Measurements were performed for 48 h (the first 60 min oxygen concentration was measured every minute and afterwards every 15 min) and the oxygen consumption rate was determined by calculating the reciprocal and normalizing the data to t0.

4.19. Adult organotypic brain tissue slice culture and *ex vivo* tumor growth assay

Adult mice brains from 8 – 12 week old C56BL/6JOlaHsd mice were collected by Dr. Benedikt Linder or Alicia Haydo (Experimental Neurosurgery, Goethe University, Frankfurt/Main, Germany) and organotypic brain tissue slice culture (OTC) was carried out as described in Gerstmeier et al. (2021). Accordingly, the brains were embedded in 2 % low-melting agarose and cut into evenly 150 µM thick transverse sections using a Vibratome with low speed and high vibration until evenly sections were not possible anymore. Brain sections were transferred with a small brush into 6-well plates containing Millicell cell culture inserts and OTC-specific medium without FCS. For the *ex vivo* tumor growth assay, 2,500 cells/well NCH644^{GFP+}, NCH421K^{GFP+} or 3,000 cells/well GS-5 GFP-Luc were seeded out in u-shaped 96-well plates at least 2 days before in order to form large spheres. Several spheres were carefully spotted with a pipette on each brain section and allowed to attach for one day. The treatment was performed as indicated and refreshed three times a week by changing the medium. At the end of the treatment period, OTC slices were stained with PI in order to exclude severe tissue damage through prolonged culturing or drug treatment. For this, 0.8 µg/ml PI solution in DPBS was added directly on to the brain slice and incubated for 10 min followed by washing with DPBS. Pictures were taken with a SMZ25 stereomicroscope equipped with a P2-SHR Plan Apo 2x objective in the group of PD Dr. Stefan Liebner (Neurological Institute (Edinger Institute), Goethe University Hospital, Frankfurt/Main, Germany) and operated with the NIS-Elements Software. The tumor area was quantified and processed with ImageJ Fiji.

4.20. Proteomics

Analysis of the whole proteome of U-251 wt, sgEGFP and *ATG5* KO cells after VLX600 treatment was performed using a combination of liquid chromatography and mass spectrometry (LC-MS/MS). For this, cells were seeded out in 6 cm dishes with 250,000 cells per dish and treated the next day. After treatment, the medium was removed and cells were washed thoroughly three times with pre-warmed DPBS to remove the FCS. On ice 400 µl proteomic lysis buffer was added, cells were detached using a cell scrapper and transferred into 2 ml tubes. The lysates were resuspended up to 20 times to reduce viscosity and then boiled up to 95 °C for 10 min. Protein lysates were stored at -80 °C and further prepared by Dr. Georg Tascher (working group of Dr. Christian Münch, Institute of Biochemistry II, Goethe University Hospital Frankfurt/Main, Germany) as described in Reisbeck et al. (2023). All mass spectrometry proteomics data have been deposited to the Proteo-meXchange Consortium (Deutsch et al. 2017) via the PRIDE partner repository (Perez-Riverol et al. 2019) with the dataset identifier PXD041246 (Username: reviewer_pxd041246@ebi.ac.uk, Password: xiniDuAC). GO term analysis was performed with String (string-db.org; (Szklarczyk et al. 2019); version 11.5, last accessed on: 08-April-2022).

4.21. Statistics

For statistical analysis, GraphPad Prism 7 or 9 was used. First, a Shapiro Wilk normality test was performed in order to determine if the data set is well-modelled by a normal distribution. In case of normally distributed data a one- or a 2way ANOVA was performed. For non-normally distributed data a Kruskal-Wallis test was used. Changes were considered as statistically significant if $p \leq 0.05$ and depicted as: $p \leq 0.05$: *, $p \leq 0.01$: **, $p \leq 0.001$ ***, $p \leq 0.0001$: **** or ns: not significant between control and treated cells or as indicated with brackets.

5. Results

5.1. Pimozide and loperamide induce an autophagy-dependent type of cell death in glioblastoma cells

The antipsychotic agent pimozide (PIMO) that antagonizes D(2)/(D(3) dopamine receptors (DRD2/3) and the HTR7/5-HT7 serotonin receptor (5-hydroxytryptamine receptor 7) and the opioid receptor antagonist loperamide (LOP) that inhibits voltage-gated P/Q-type Ca^{2+} channels have been previously shown to induce autophagy-dependent cell death (ADCD) in glioblastoma (GBM) cells (Zielke et al. 2018). However, the underlying pathways were not fully elucidated and needed further investigation. Building on the previous work from Dr. Nina Meyer published in her dissertation "*Molecular targeting of autophagy in glioblastoma*" (Meyer 2019) as well as in our joint publication (Meyer*, Henkel* et al. 2021) I validated the ADCD induction by PIMO and LOP observed in MZ-54 GBM cells in additional cell models as a starting point. Therefore, LN-229 wildtype (wt) and CRISPR/Cas9 *ATG7* knockout (KO) cells (generated by Svenja Zielke (working group of Prof. Dr. Simone Fulda, Experimental Cancer Research in Pediatrics, Goethe University Hospital, Frankfurt/Main, Germany) (Zielke et al. 2018)) were treated with different concentrations of PIMO and LOP for 48 h and cell death induction was measured using the annexin V/PI staining with subsequent flow cytometric analysis. This revealed a concentration-dependent increase in cell death in both cell lines, while the cell death was significantly reduced in the *ATG7* KO cells (Figure 15). The prominent induction of autophagy after PIMO and LOP treatment was already shown in our group for MZ-54 cells using the MAP1LC3B-I/II switch (Zielke et al. 2018), which is frequently used as a gold standard for autophagy induction. However, the accumulation of the membrane bound MAP1LC3B-II does not discriminate between an increased autophagic flux or a block in autophagosome clearance (Klionsky et al. 2016). Thereto, I analysed the induction of autophagic flux by using the bicistronic reporter plasmid pMRX-IP-GFP-LC3-RFP-LC3ΔG, consisting of EGFP-LC3 that is incorporated into the autophagosomal membrane during autophagy and gets degraded, while mRFP1-LC3ΔG that cannot be lipidated remains in the cytosol as an internal control. Accordingly, a decrease in the EGFP/mRFP1 ratio indicates an increase in autophagic flux and can be measured via flow cytometry (Kaizuka et al. 2016). Therefore, PIMO and LOP treatment of the GBM cell line MZ-54 resulted in an increased autophagic flux that was significantly inhibited in the *ATG5* and *ATG7* KO cells (Figure 16). The

combinatorial treatment of imipramine (IM) and ticlopidine (TIC) served as a positive control for autophagy activation (Shchors, Massaras and Hanahan 2015) and treatment with the autophagy inhibitor bafilomycin (BAF) blocked the autophagic flux. In light of the controversial discussion on autophagy as a pro-death mechanism (Kroemer and Levine 2008) it was essential to validate the autophagy-dependency of the PIMO- and LOP-induced cell death as faithfully as possible and thereto a re-expression experiment was performed. For this, a doxycycline (DOX) inducible plasmid was transduced into the MZ-54 *ATG7* KO3 cell line (Figure 17), which allows gene expression only when DOX is present. DOX treatment consistently induced the gene expression of *ATG7* in the *ATG7* KO3 cell line compared to no expression without DOX (Figure 17A). As a control the ATG7 protein level in the MZ-54 wt cells was concomitantly analysed showing that *ATG7* is re-expressed to a physiological level. MZ-54 *ATG7* KO3 cells expressing the inducible ATG7 plasmid were further analysed for cell death induction after IM + TIC, PIMO and LOP treatment. This revealed a significant increase in cell death when *ATG7* is re-expressed under DOX treatment compared to the *ATG7* KO3 cells without the addition of DOX (Figure 17B), underlining the previous findings that PIMO and LOP indeed induce an ATG5/7-dependent cell death (Meyer 2019; Meyer*, Henkel* et al. 2021).

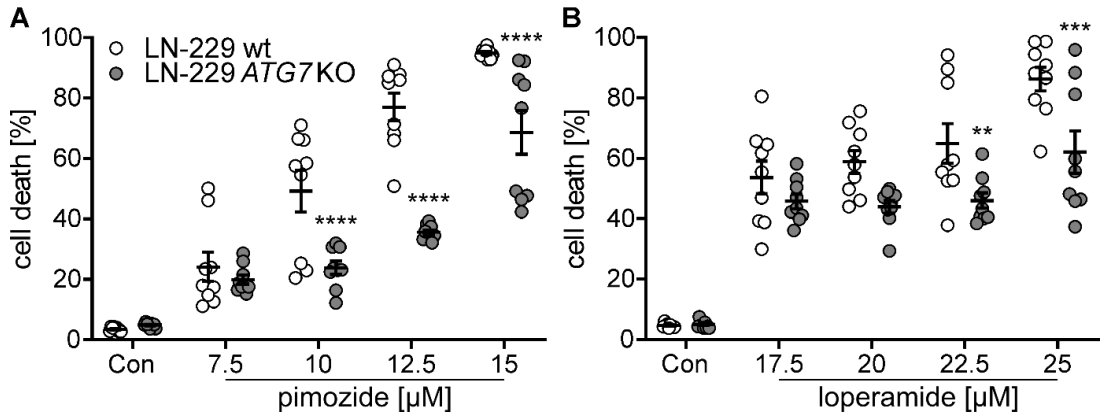

Figure 15. Pimozide and loperamide induce an autophagy-dependent cell death in LN-229 glioblastoma cells. Determination of cell death by flow cytometric analysis of APC-annexin V binding and propidium iodide (PI) uptake. LN-229 wt and *ATG7* KO cells were treated with pimozide **(A)** or loperamide **(B)** for 48 h with the indicated concentrations. Shown are annexin V only-positive, PI only-positive and double-positive cells. Data represent means ± SEM of three independent experiments with three replicates and 5,000 – 10,000 cells measured in each sample. Statistical significances were calculated with a 2way ANOVA (asterisks indicate difference between wt and *ATG7* KO cells). Figure adapted partly from Meyer*, Henkel* et al. (2021).

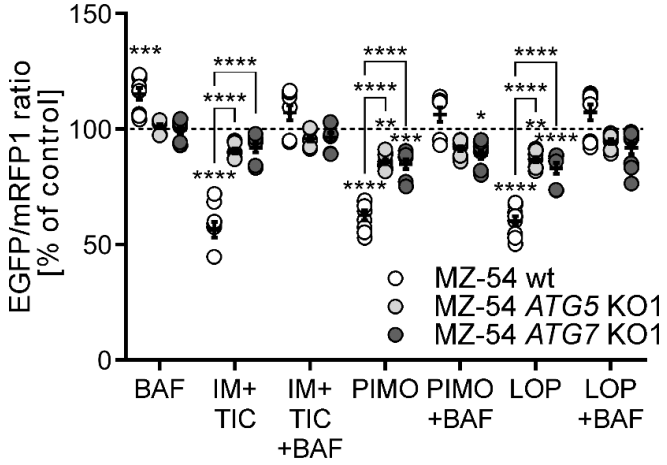

Figure 16. Pimozide and loperamide increase autophagic flux in MZ-54 glioblastoma cells. Measurement of autophagic flux using the fluorescence probe pMRX-IP-GFP-LC3-RFPΔG. MZ-54 wt, *ATG5* and *ATG7* KO1 cells were treated with 20 µM imipramine (IM) + 100 µM ticlopidine (TIC), 15 µM pimozide (PIMO) or 15 µM loperamide (LOP) with or without the addition of 10 nM bafilomycin (BAF) for 16 h. The EGFP and mRFP1 signals were measured by flow cytometry and the ratio was calculated and normalized to the solvent control. Data represent means ± SEM of three independent experiments with three replicates and 5,000 – 10,000 cells measured in each sample. Statistical significances were calculated with a 2way ANOVA (dashed line indicates respective solvent controls, which were normalized to 100 %. Asterisks indicate difference to the respective solvent control or as indicated). Figure modified from Meyer*, Henkel* et al. (2021).

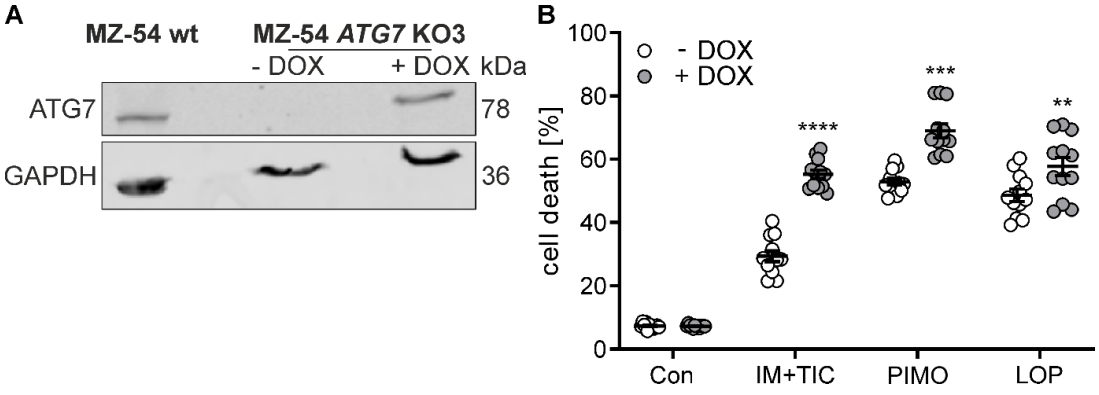

Figure 17. Re-expression of *ATG7* in *ATG7* KO3 cells enhances cell death induced by pimozide and loperamide. MZ-54 *ATG7* KO3 cells were transduced with a plasmid for *ATG7* re-expression under the control of a doxycycline (DOX) sensitive reporter. **A)** Validation of the re-expression of *ATG7* in the *ATG7* KO3 cells after 1 µg/ml DOX treatment for 24 h by western blot. The experiment was repeated two times. **B)** MZ-54 *ATG7* KO3 cells expressing the pLV[Exp]-Puro-TRE3G>hATG7 and the pLV[Exp]-CMV>Tet3G/Hygro plasmids were pre-incubated with or without the addition of 1 µg/ml DOX for 24 h in order to induce *ATG7* expression and subsequently treated with 20 µM imipramine (IM) + 100 µM ticlopidine (TIC), 12.5 µM pimozide (PIMO), 12.5 µM loperamide (LOP) or dimethyl sulfoxide (DMSO, Con) for 48 h. Next, cell death was analysed by annexin V staining and PI uptake. Shown is the total cell death (annexin V only-, PI only- and double-positive cells). Data represent means ± SEM of four independent experiments with three replicates and 5,000 – 10,000 cells measured in each sample. Statistical significances were calculated with a 2way ANOVA and asterisks indicate difference to the respective treatment without DOX. Figure partly adapted from Meyer*, Henkel* et al. (2021).

While genetic models with depletion of ATGs are the best approach to study the role of autophagy in cell death (Galluzzi et al. 2018), it cannot be completely ruled out that autophagy-independent roles of ATGs affect the obtained experimental results. During the course of this study, Heckmann and Green (2019) reported about a non-canonical function of several autophagy proteins that are involved in LC3-associated phagocytosis (LAP), which

plays a key role in immune regulation and inflammatory responses. LAP uses parts of the autophagic machinery, including ATG5 and ATG7, to conjugate LC3 family proteins to phagosome membranes. Accordingly, the autophagy proteins ATG5 and ATG7 are not solely specific for autophagy. To better distinguish between autophagy and LAP further knockdown (KD) models were used. In the study by Heckmann and Green (2019) the authors described ATG14 and RB1CC1/FIP200 as specific for autophagy and RUBCN (rubicon autophagy regulator) and CYBB/NOX2 (cytochrome b-245 beta chain) as specific for LAP. Knockdowns of those four proteins were generated (Figure 18) and cell death was analysed after IM + TIC, PIMO and LOP treatment (Figure 19). Knockdowns were performed using two different shRNAs for each gene (KD1 and KD2) and validated using either qRT-PCR (Figure 18A, C, D) or western blot (Figure 18B). All of the used shRNAs resulted in a significant reduction of the targeted gene or protein although to different extents. Subsequent cell death analysis revealed that the KDs of the autophagy specific genes *ATG14* and *RB1CC1* decreased IM + TIC-, PIMO- and LOP-induced cell death in contrast to the KDs of the LAP specific genes *RUBCN* and *CYBB* that do not evoke a decrease in cell death induction or at least to a much lesser extent (Figure 19) (Meyer*, Henkel* et al. 2021). These results underscore that induction of autophagy but not LAP is the primary mechanism of cell killing following treatment with PIMO and LOP in GBM cells.

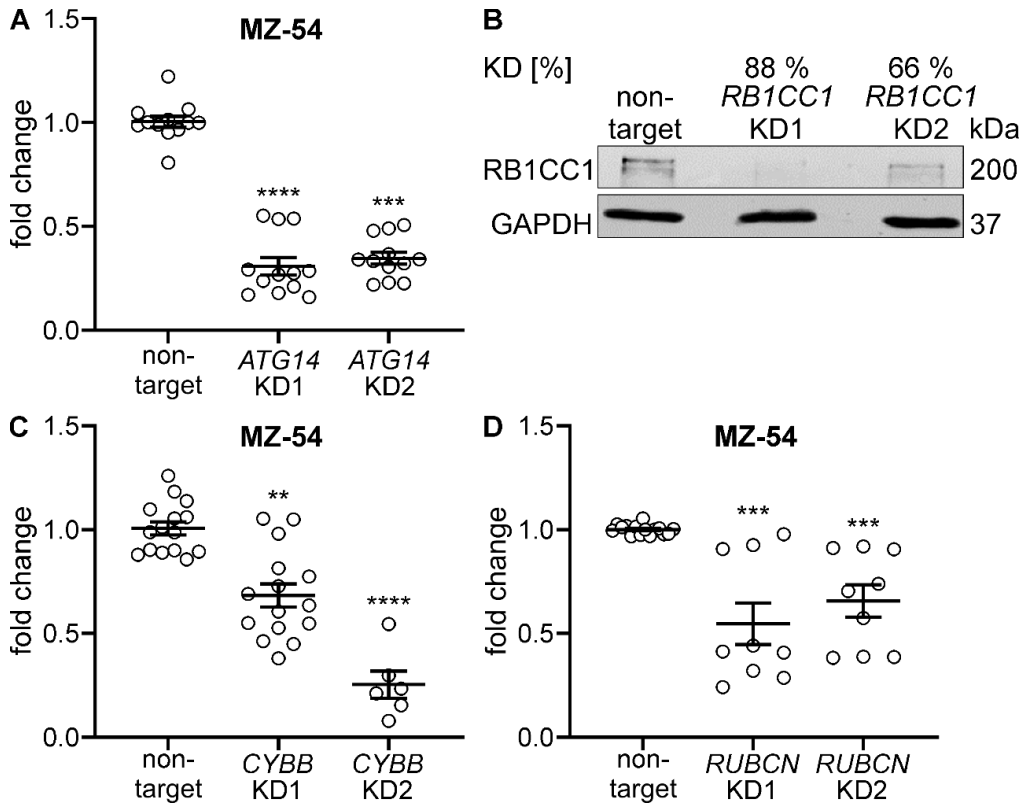

Figure 18. Knockdown validation of the autophagy-specific genes *ATG14* and *RB1CC1* and the LC3-associated phagocytosis-specific genes *CYBB* and *RUBCN*. MZ-54 wt cells were transduced with two different shRNAs for each gene against the autophagy-specific genes *ATG14* **(A)** and *RB1CC1* **(B)** and the LC3-associated phagocytosis (LAP)-specific genes *CYBB* **(C)** and *RUBCN* **(D)** in order to generate KDs. KDs were validated either by qRT-PCR **(A, C, D)** or western blot **(B)**. **A, C, D)** Shown is the fold change compared to the respective shRNA control (non-target). Data represent means ± SEM of at least two independent experiments with three replicates. Statistical significances were calculated with a Kruskal-Wallis test (asterisks indicate difference from non-target control). **B)** The experiment was repeated two times. Figure adapted from Meyer*, Henkel* et al. (2021).

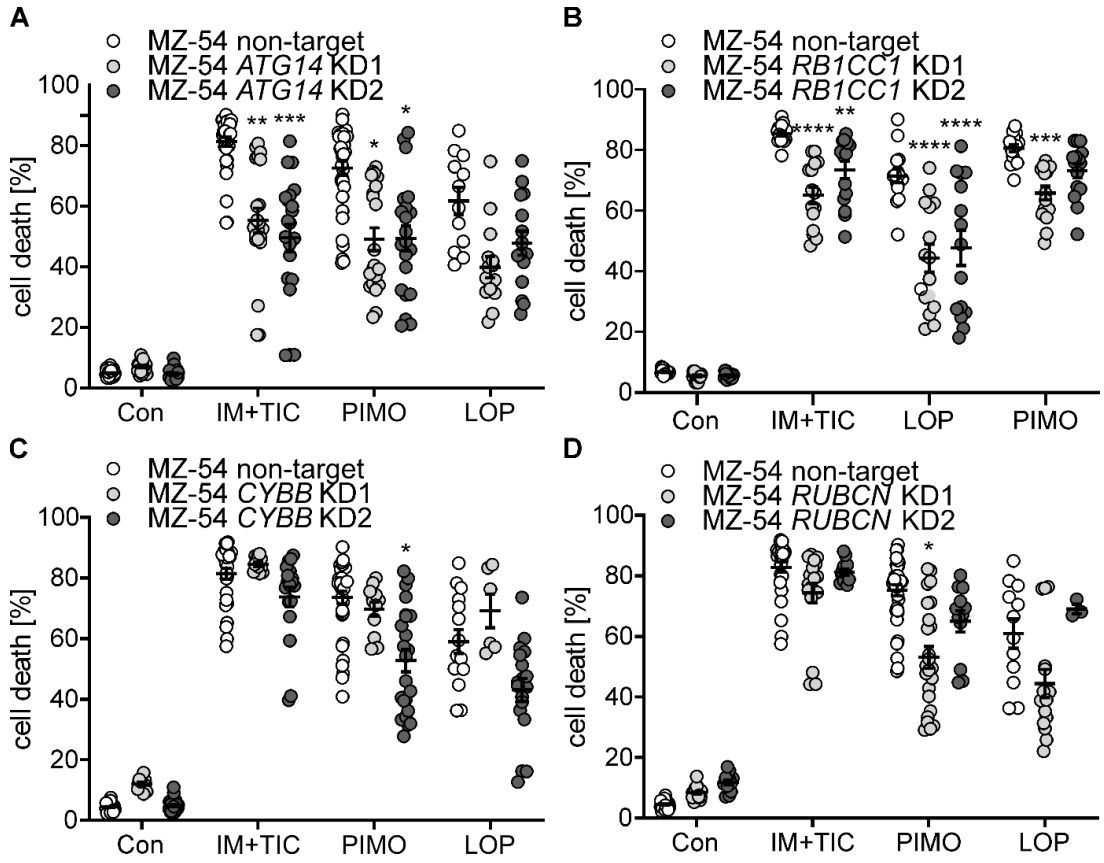

Figure 19. Cell death induced by pimozide and loperamide is inhibited by knockdown of the autophagy-specific genes *ATG14* and *RB1CC1*, but not by knockdown of the LC3-associated phagocytosis-specific genes *CYBB* and *RUBCN*. Measurement of cell death by flow cytometric analysis of annexin V binding and PI uptake. MZ-54 cells with either knockdown in the autophagy-specific genes *ATG14* **(A)** and *RB1CC1* **(B)** or the LC3-associated phagocytosis (LAP)-specific genes *CYBB* **(C)** and *RUBCN* **(D)** were treated with 20 µM imipramine (IM) + 100 µM ticlopidine (TIC), 12.5 µM pimozide (PIMO) or 12.5 µM loperamide (LOP) for 48 h. Shown are annexin V only-, PI only- and annexin V/PI double-positive cells. Data represent means ± SEM of at least two independent experiments with three replicates and 5,000 – 10,000 cells measured in each sample. Statistical significances were calculated with a Kruskal-Wallis test (asterisks indicate difference from non-target control). Figure modified from Meyer*, Henkel* et al. (2021).

5.2. Pimozide and loperamide induce lipotoxicity and lysosomal membrane permeabilization in glioblastoma cells

In order to further investigate the underlying mechanisms of the PIMO- and LOP-induced cell death in GBM, a whole proteome analysis of PIMO and LOP treated MZ-54 cells was previously performed by Dr. Nina Meyer (Meyer 2019; Meyer*, Henkel* et al. 2021). This approach revealed a strong increase in proteins associated with cholesterol metabolism and lipid metabolic processes, possibly related to the mechanisms of autophagy and cell death induction by these drugs. To further analyse the metabolic changes induced by PIMO and LOP treatment, I stained intracellular cholesterol using filipin III in combination with the lysosomal marker LAMP1. After PIMO and LOP treatment of LN-229 cells, I observed a massive accumulation of cholesterol in the lysosomes shown by a colocalization of filipin III and LAMP1

similarly to the positive control U18666A (Figure 20), suggestive of a disruption of cholesterol transport. This was previously also shown for MZ-54 cells (Meyer 2019; Meyer*, Henkel* et al. 2021). Since it is known that cholesterol levels may also influence mTOR signalling and thereto autophagy (Xu et al. 2010) I analysed the phosphorylation of the mTOR downstream target RPS6 (ribosomal protein S6) with or without the addition of extracellular cholesterol (CHOL) (Figure 21). Phosphorylation of RPS6 is mediated by the S6 kinase that in turn is regulated via mTOR and therefore an increase in phosphorylation of RPS6 indicates mTOR activation and autophagy inhibition (Dufner and Thomas 1999; Hay and Sonenberg 2004). Treatment of MZ-54 cells with IM + TIC, PIMO and LOP resulted in a decrease of RPS6 phosphorylation (p-RPS6), while the RPS6 protein amount was unchanged, suggesting inhibition of mTOR and activation of autophagy (Figure 21A). The extracellular addition of cholesterol rescued the decrease in p-RPS6 indicating autophagy inhibition (Figure 21B). Similarly, a decrease in the MAP1LC3B-I/II switch after the addition of cholesterol to the IM + TIC, PIMO and LOP treated MZ-54 cells was previously shown (Meyer 2019; Meyer*, Henkel* et al. 2021). Together this suggests that PIMO and LOP interfere with the cholesterol transport, resulting in the lysosomal accumulation of cholesterol and therefore reduced cytosolic cholesterol levels, which may contribute to increased autophagy activation.

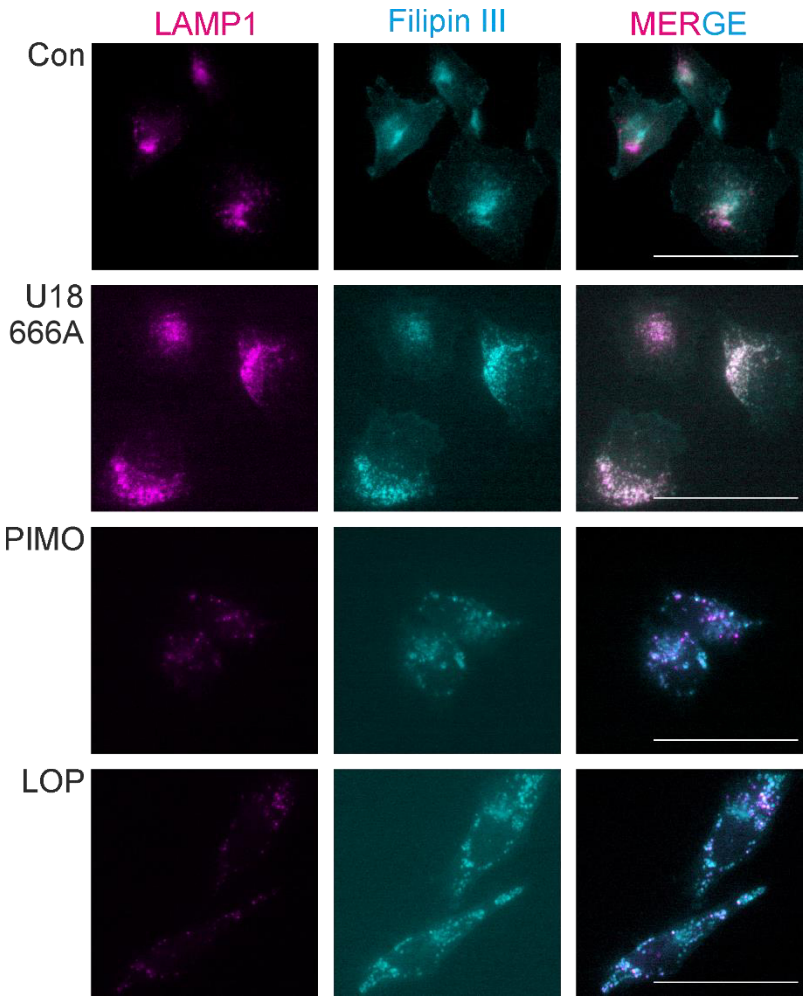

Figure 20. Colocalization of cholesterol and lysosomes in LN-229 glioblastoma cells treated with pimozide and loperamide using LAMP1 and filipin III staining. LN-229 wt cells were treated with 12.5 µM pimozide (PIMO), 22.5 µM loperamide (LOP), the positive control U18666A (1.25 µM) or with the solvent control (DMSO, Con) for 18 h. Pictures were taken at 60x magnification and the experiment was repeated four times with at least three pictures taken for each experiment (scale bar = 50 µM).

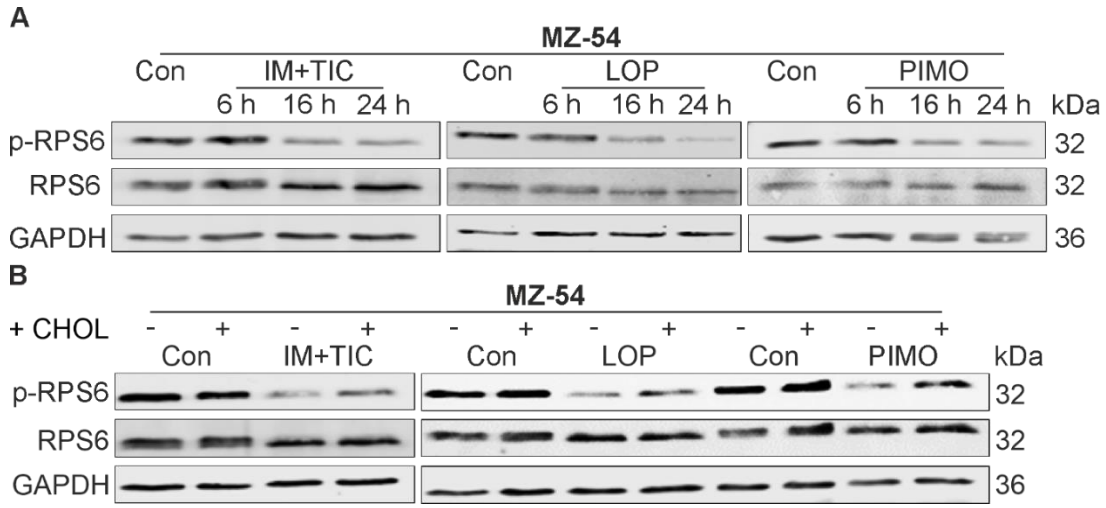

Figure 21. Ribosomal protein S6 phosphorylation after pimozide and loperamide treatment in MZ-54 glioblastoma cells. MZ-54 cells were treated with 20 µM imipramine (IM) + 100 µM ticlopidine (TIC), 15 µM pimozide (PIMO) or 15 µM loperamide (LOP) for the indicated time periods **(A)** or with the addition of 10 µg/ml cholesterol–methyl-β-cyclodextrin (CHOL) for 16 h **(B)** followed by immunoblot analysis of the ribosomal protein S6 (RPS6) and phospho-RPS6 (p-RPS6, Ser240/244). DMSO was used as a control (Con) and GAPDH as a housekeeper. The experiment was repeated at least two times. Figure adapted from Meyer*, Henkel* et al. (2021).

Furthermore, PIMO and LOP were previously shown to increase cellular ceramides investigated by lipidomic analysis as well as to increase lipid peroxidation in MZ-54 cells (Meyer 2019; Meyer*, Henkel* et al. 2021). Both are well-known inducers of lysosomal membrane permeabilization (LMP) (Serrano-Puebla and Boya 2016) and therefore this was further analysed. I investigated LMP induction using LN-229 GBM cells expressing the pmCherry-Gal3 (galectin 3, LGALS3) plasmid. LGALS3 translocates to the lysosomal membrane upon its rupture and is therefore used as a marker for LMP (Maejima et al. 2013). Treatment of the LN-229 wt cells with PIMO and LOP induced the formation of LGALS3 puncta located at the lysosomal membrane shown by simultaneous LAMP1 staining. Washout of the drugs for 24 h rescued LGALS3 puncta formation (Figure 22A, B), indicating the degradation of damaged lysosomes by autophagy (lysophagy). In contrast, LN-227 *ATG7* KO cells treated with PIMO and LOP showed no LGALS3 puncta formation (Figure 22C, D), suggesting that LMP is an autophagy-driven process (Meyer*, Henkel* et al. 2021). Similar results were previously reported when using MZ-54 wt, *ATG5* and *ATG7* KO cells (Meyer 2019; Meyer*, Henkel* et al. 2021). Furthermore, it was previously shown that cathepsin B (CTSB) and cathepsin D (CTSD) are involved in the PIMO- and LOP-induced cell death (Meyer 2019; Meyer*, Henkel* et al. 2021). CTSB and CSTD are thought to be released after LMP resulting in the degradation of cytosolic material and proteins. Additionally, lysophagy seems to play a protective role in this context since the siRNA-mediated KD of the lysophagy receptor VCP was previously shown to

further increase the PIMO- and LOP-induced cell death (Meyer 2019; Meyer*, Henkel* et al. 2021). In summary, PIMO and LOP induce autophagy and lipotoxicity that synergize to induce LMP and finally cell death.

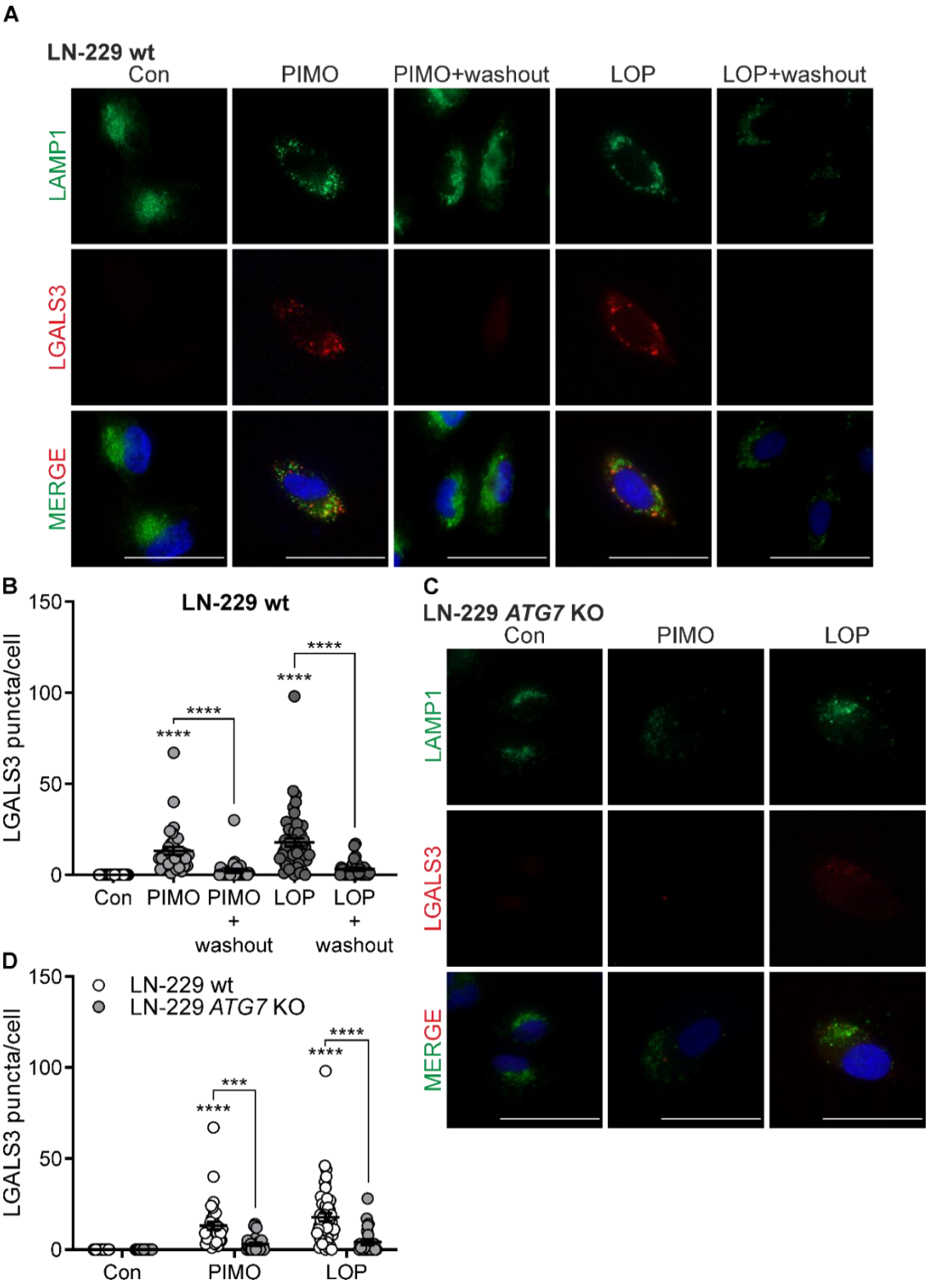

Figure 22. Lysosomal membrane permeabilization in LN-229 glioblastoma cells after pimozide and loperamide treatment. LN-229 wt and *ATG7* KO cells expressing the pmCherry-Gal3 plasmid were treated with 12.5 µM pimozide (PIMO), 22.5 µM loperamide (LOP) or the solvent control (DMSO, Con) for 16 h. For washout, the medium containing the drugs was removed after 16 h and exchanged with fresh medium without drugs for

additional 24 h. Pictures were taken at 60x magnification (scale bar = 50 µM). **A, C)** Representative pictures of three experiments with at least three pictures taken per condition. **B, D)** Quantification of LGALS3 puncta per cell with 12 – 21 pictures analysed per condition. Data represent means ± SEM and statistical significances were measured with a Kruskal-Wallis test (asterisks represent difference to the respective solvent control or as indicated). Figure modified from Meyer*, Henkel* et al. (2021).

5.3. Pimozide reduces cell viability and tumor growth of glioma stem-like cells

Furthermore, PIMO was analysed for its translational impact using glioma stem-like cells (GSCs), which often resist standard therapies and are therefore thought to be one of the major reasons for tumor recurrence (Singh et al. 2003). Cell viability was measured using the colorimetric MTT assay after PIMO treatment of NCH644 and NCH421K GSC lines (Figure 23), revealing a time- and dose-dependent reduction of cell viability. Already after 24 h of 10 µM PIMO treatment or after 5 µM PIMO treatment for 72 h, cell viability was reduced to about 50 %, which was even more pronounced after longer treatment periods or higher concentrations of PIMO. For example, after 72 h of 7.5 µM PIMO treatment almost no MTT activity could be measured. Thereby, reduction in cell viability by PIMO was at most time points highly significant. This results suggest that PIMO is able to completely block cell proliferation in the GSC lines NCH644 and NCH421K. To further analyse the drug response in an authentic brain environment, the NCH644 and NCH421K GSC lines were used in an *ex vivo* model. Organotypic mouse brain slices were cultured on special inserts in 6-well plates and the NCH644^{GFP+} and NCH421K^{GFP+} tumor spheres were grown on top and monitored via fluorescence microscopy during the PIMO treatment (Figure 24A). NCH644^{GFP+} tumor spheres showed a mean growth increase in the control treated group of about 18-fold after 14 days, which was significantly reduced to an only 6-fold increase in the PIMO treated group (Figure 24A, B). In general PIMO-treated NCH644^{GFP+} tumor spheres seem to grow slower compared to the control group. In contrast, NCH421K^{GFP+} tumor spheres not only showed a block in tumor growth after PIMO treatment, but also seem to reduce their size indicating the induction of cell death (Figure 24A, C). While NCH421K^{GFP+} spheres in the control group doubled their size after 14 days of treatment, the PIMO-treated tumors decreased in size by about 30 %. In summary, PIMO not only shows a strong cell death inducing ability *in vitro*, but also is able to reduce cell viability of GSCs and more intriguingly to inhibit their tumor growth *ex vivo*, making PIMO an interesting candidate for future therapeutic options.

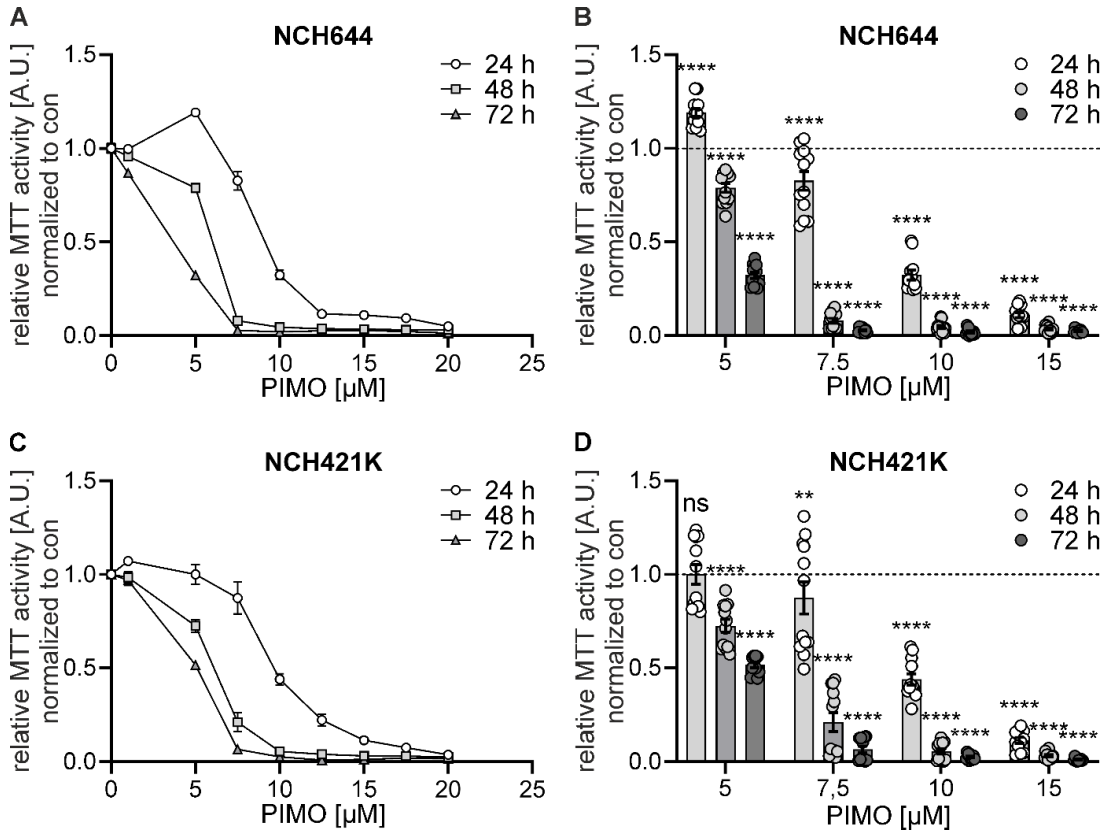

Figure 23. Cell viability measurement of NCH644 and NCH421K glioma stem-like cells after pimozide treatment. NCH644 **(A, B)** and NCH421K **(C, D)** cells were treated with different concentrations of pimozide (PIMO) as indicated for 24 h, 48 h and 72 h followed by cell viability measurement via MTT. On the left side all tested PIMO concentrations are shown and on the right side only a selected number of PIMO concentrations for a better comparison. Data represent means ± SEM of two independent experiments with six replicates. **B, D)** Statistical significances were measured with a 2way ANOVA and asterisks indicate difference from solvent control. Dashed line indicates the control treatment (Con, DMSO), which was normalized to one.

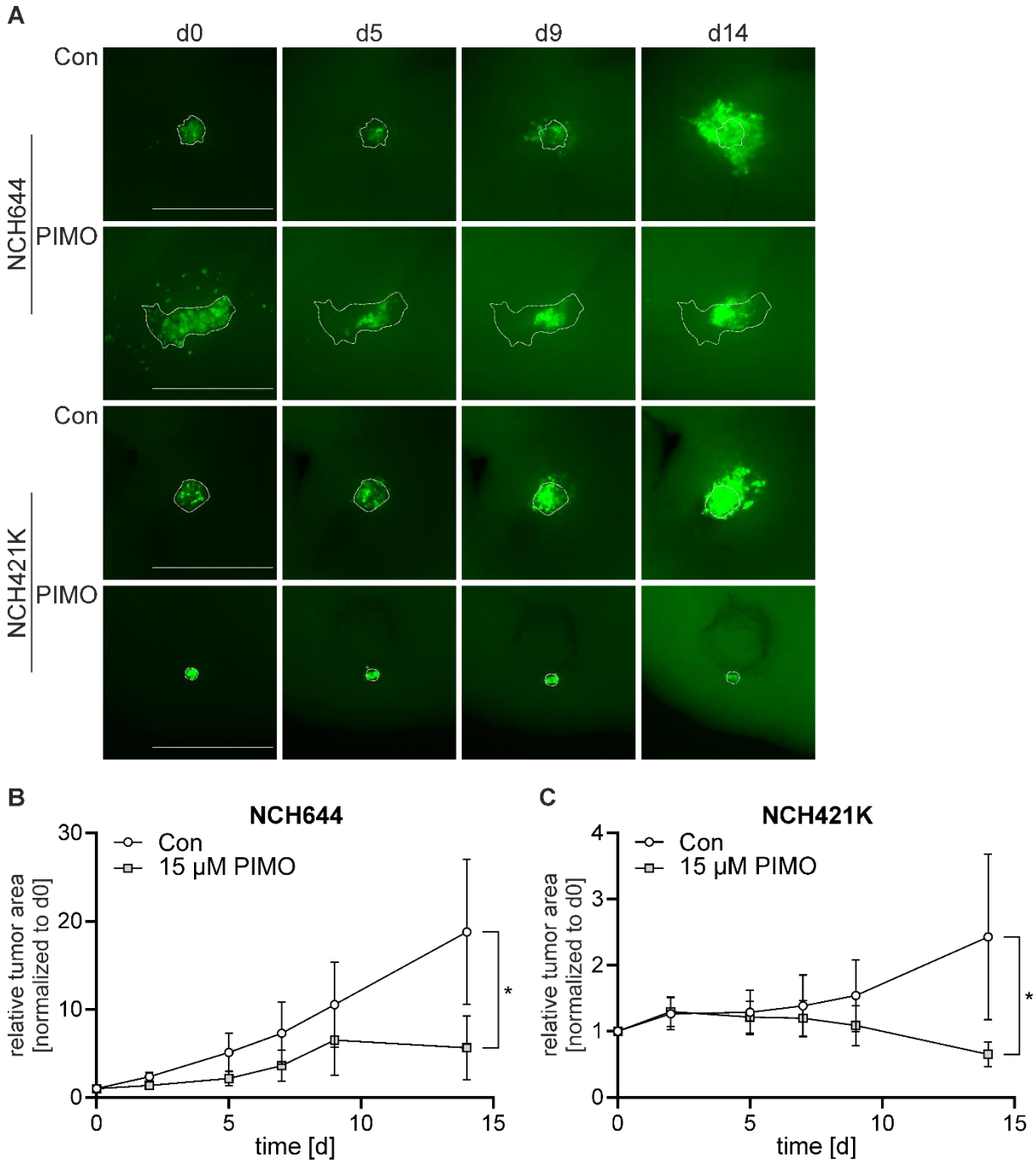

Figure 24. Pimozide reduces NCH644 and NCH421K tumor growth in an *ex vivo* brain transplantation model. NCH644^{GFP+} and NCH421K^{GFP+} tumor spheres were treated with 15 µM pimozide (PIMO) for a total of 14 days and tumor growth was monitored via fluorescence microscopy. **A)** Representative pictures of NCH644^{GFP+} and NCH421K^{GFP+} tumor spheres for selected days. Dotted circles indicate the respective tumor on day 0 and the scale bar is 1000 µM. **B, C)** Quantification of the tumor areas from NCH644^{GFP+} **(B)** and NCH421K^{GFP+} **(C)** tumor spheres over the whole time period. Data represent means ± SEM of five and eight or seven and ten tumors for DMSO (Con) and PIMO treated NCH644^{GFP+} or NCH421K^{GFP+} tumor spheres, respectively. Statistical significances were calculated with a 2way ANOVA.

5.4. The iron chelator and OXPHOS inhibitor VLX600 induces an autophagy-dependent type of cell death in glioblastoma cells

Depending on the cellular context and mode of drug action organelle-specific types of autophagy may differentially contribute to cell demise (Linder and Kögel 2019). Thereto, the second part of my thesis was aimed at investigating mitophagy as well as mitophagic cell death (MCD) in GBM using the iron chelator and oxidative phosphorylation (OXPHOS) inhibitor VLX600. VLX600 was reported to induce mitochondrial dysfunction with subsequent tumor cell death in colon carcinoma cells *in vitro* as well as *in vivo* (Zhang et al. 2014). Interestingly, VLX600 was already used in a phase I study for refractory advanced solid tumors and was reported to be reasonably well tolerated (Mody et al. 2019). However, the underlying mechanisms of the VLX600-induced tumor cell demise were not fully elucidated and to date there was no study investigating VLX600 in GBM. Therefore, I analysed VLX600 in U-251 GBM cells as well as a couple of GSC lines. First, I generated lentiCRISPR-mediated U-251 *ATG5* and *ATG7* KO cell lines, which were validated by immunoblot analysis (Figure 25A, B). Out of 12 single cell clones for *ATG5* and four clones for *ATG7* three or two clones were selected for each gene, respectively. Selection was decided on the mean cell death rescue of all KO clones after 20 µM IM and 100 µM TIC treatment (positive control for ADCD (Shchors, Massaras and Hanahan 2015)) in order to pick those that best represent the polyclonal KO population. As a control U-251 cells transduced with single guides against EGFP (sgEGFP) were used and cultivated as a bulk culture. I started to analyse the cell death inducing ability of VLX600 in GBM cells as well as the possible involvement of autophagy. Therefore, the U-251 sgEGFP, *ATG5* and *ATG7* KO cell lines were treated with different concentrations of VLX600 for 48 h followed by flow cytometric analysis of annexin V binding and PI uptake (Figure 25C, D). As expected, the positive control for ADCD, IM + TIC, resulted in a medium induction of cell death of about 30 – 40 % in the U-251 sgEGFP cells that was significantly inhibited in all of the *ATG5* as well as *ATG7* KO clones, validating the functional KO of autophagy in those cell lines. Treatment with VLX600 resulted in cell death induction of about 40 – 60 % in the control cell line that similarly to IM + TIC was rescued significantly in almost all of the *ATG5* (Figure 25C) and all of the *ATG7* (Figure 25D) KO clones. This indicates a dependency of autophagy in the VLX600-induced cell death in U-251 GBM cells (Reisbeck et al. 2023). In order to validate autophagic flux activation, U-251 and MZ-54 cells with stable expression of the reporter plasmid pMRX-IP-GFP-LC3-RFP-LC3ΔG were treated with VLX600 followed by flow cytometric

analysis whereby a decrease in the EGFP/mRFP1 ratio indicates an increase in autophagic flux (Figure 26). Again, the IM + TIC treatment served as a positive control and consequently resulted in a strong decrease in the EGFP/mRFP1 ratio in the MZ-54 wt cells, indicating a huge increase in autophagic flux (Figure 26B). Similarly, VLX600 treatment resulted in a significant decrease of the EGFP/mRFP1 ratio from 100 % in the control treatment to about 80 % or 60 % after VLX600 treatment in the U-251 (Figure 26A) or MZ-54 wt cells (Figure 26B), respectively. This indicates an increase in autophagic flux. In addition, the supplementary addition of the late stage autophagy inhibitor BAF (Figure 26A, B) completely rescued the increased autophagic flux after VLX600 treatment in the U-251 and MZ-54 cells and furthermore no increase in autophagic flux was seen in the MZ-54 *ATG5* KO cells after VLX600 treatment (Figure 26C) (Reisbeck et al. 2023). To further validate the autophagy KO as well as the increased autophagy after VLX600 treatment, the MAP1LC3B-I/II switch was analysed since lipidation of MAP1LC3B-I into MAP1LC3B-II is one of the crucial parts during autophagy for generating functional autophagosomes and therefore the accumulation of MAP1LC3B-II is indicative for autophagy activation. The U-251 sgEGFP, *ATG5* and *ATG7* KO clones were treated with IM + TIC or VLX600 followed by immunoblot analysis of MAP1LC3B (Figure 27). This revealed a pronounced increase of MAP1LC3B-II after IM + TIC and also after VLX600 treatment in the U-251 sgEGFP cells, which was completely absent in the *ATG5* or *ATG7* KO clones, confirming inhibition of functional autophagy (Reisbeck et al. 2023). Together my results highly support the hypothesis that VLX600 increases autophagic flux and induces ATG5/7-dependent cell death.

In order to analyse if apoptosis is activated after VLX600 treatment, the pan-caspase inhibitor Z-Val-Ala-DL-Asp-fluoromethylketone (z-VAD) that blocks apoptosis (Zhu, Fearnhead and Cohen 1995) was used in combination with VLX600 (Figure 28). As a positive control for apoptosis induction the combinatorial treatment of 1 µM ABT-737 (Oltersdorf et al. 2005) and 100 µM etoposide (ETO) (Sawada et al. 2000) was used. The ABT-737 + ETO treatment strongly induced cell death of about 80 % in the U-251 cells that was drastically reduced to about 30 % when z-VAD was added additionally. In contrast, VLX600 in combination with z-VAD did not resulted in any change of cell death induction compared to VLX600 alone, suggesting no involvement of apoptosis in the VLX600-induced cell death in U-251 cells (Reisbeck et al. 2023).

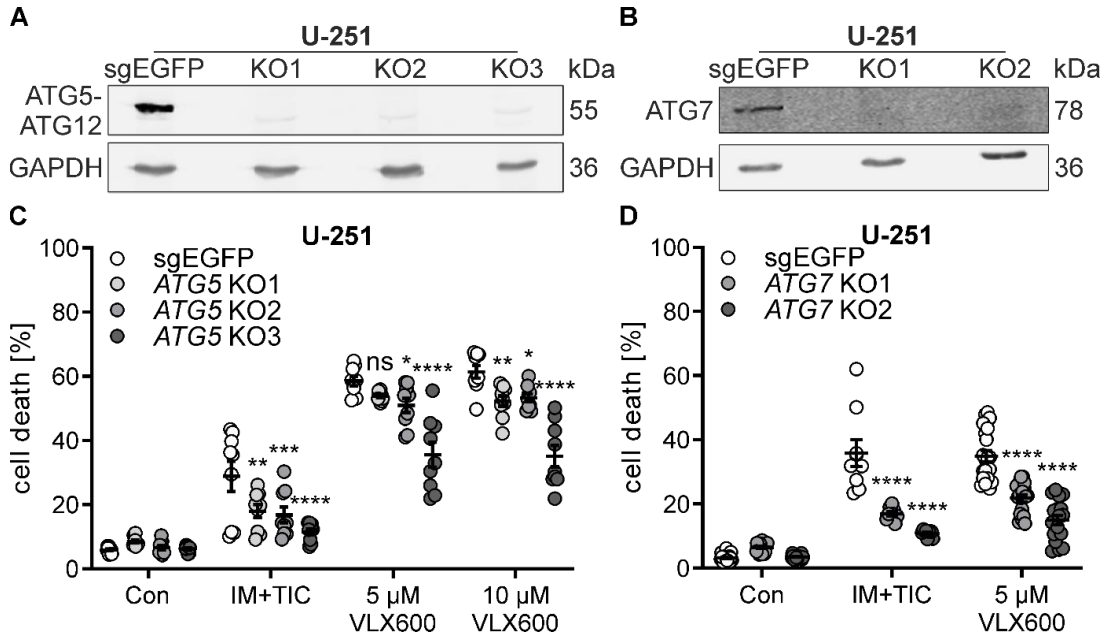

Figure 25. VLX600 induces an autophagy-dependent type of cell death in U-251 glioblastoma cells. A, B) *ATG5* **(A)** and *ATG7* **(B)** KOs were generated in the U-251 GBM cell line using the lentiCRISPR approach and positive KO clones were identified by immunoblot analysis. The experiments were repeated at least four times. **C, D)** Flow cytometric analysis of annexin V binding and PI uptake for cell death measurement. U-251 control (sgEGFP) and *ATG5* **(C)** or *ATG7* **(D)** KO cells were treated with 20 µM imipramine (IM) + 100 µM ticlopidine (TIC) or VLX600 for 48 h. Shown are annexin V only-, PI only- and double-positive cells. Data represent means ± SEM of at least three independent experiments with three replicates and 5,000 – 10,000 cells measured in each sample. Statistical significances were calculated with a 2way ANOVA (asterisks indicate difference from U-251 sgEGFP cells). Figure adapted from Reisbeck et al. (2023).

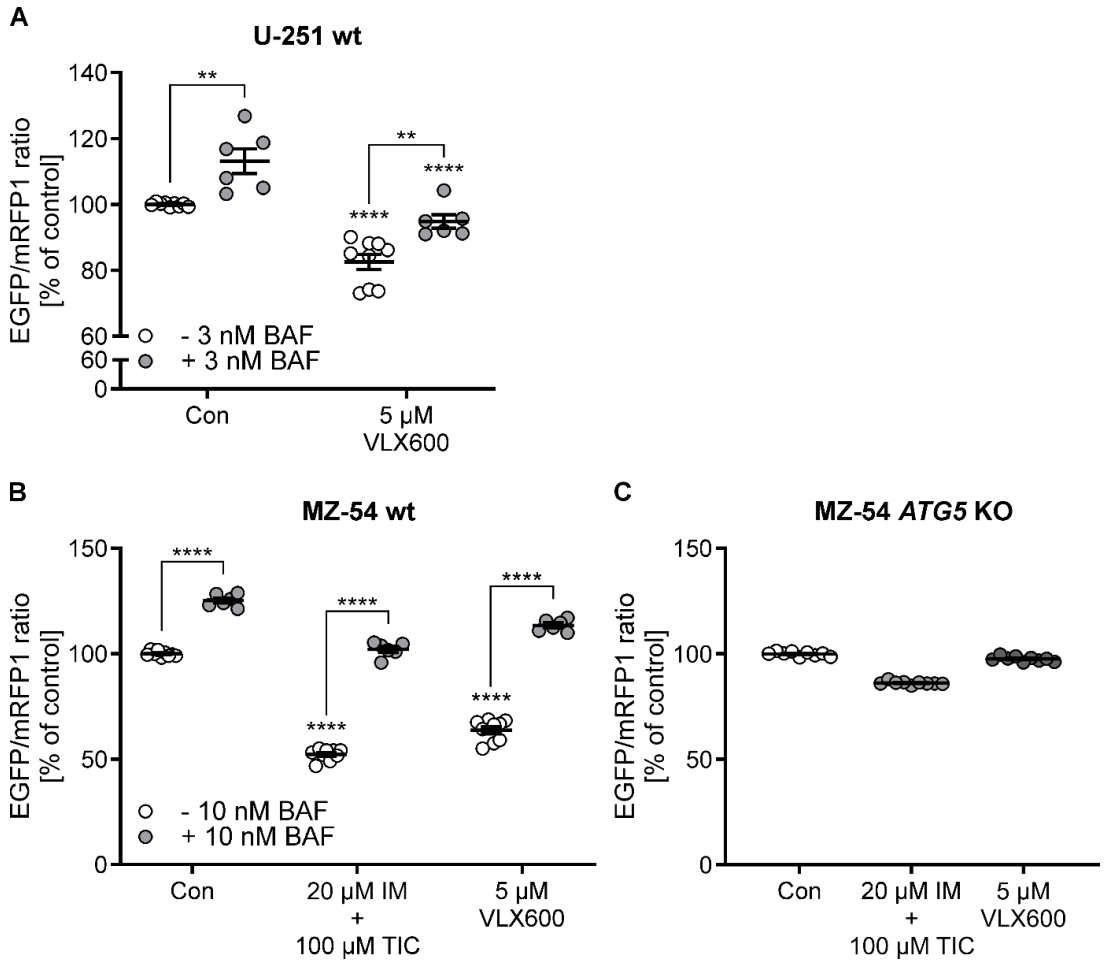

Figure 26. Increased autophagic flux in VLX600-treated U-251 and MZ-54 glioblastoma cells. U-251 **(A)** or MZ-54 wt **(B)** and *ATG5* KO **(C)** cells with stable expression of the pMRX-IP-GFP-LC3-RFPΔG plasmid were treated with 20 µM imipramine (IM) + 100 µM ticlopidine (TIC) (only B and C), 5 µM VLX600, 3 or 10 nM bafilomycin (BAF, where indicated) or DMSO as solvent control (Con) for 24 h and were subsequently analysed by flow cytometry. A decrease in the EGFP/mRFP1 ratio indicates increased autophagic flux. Data represent means ± SEM of at least two experiments with three replicates and 5,000 – 10,000 cells measured in each sample. Statistical significances were calculated with a 2way ANOVA (asterisks indicate difference from solvent control or as indicated). Figure partly adapted from Reisbeck et al. (2023).

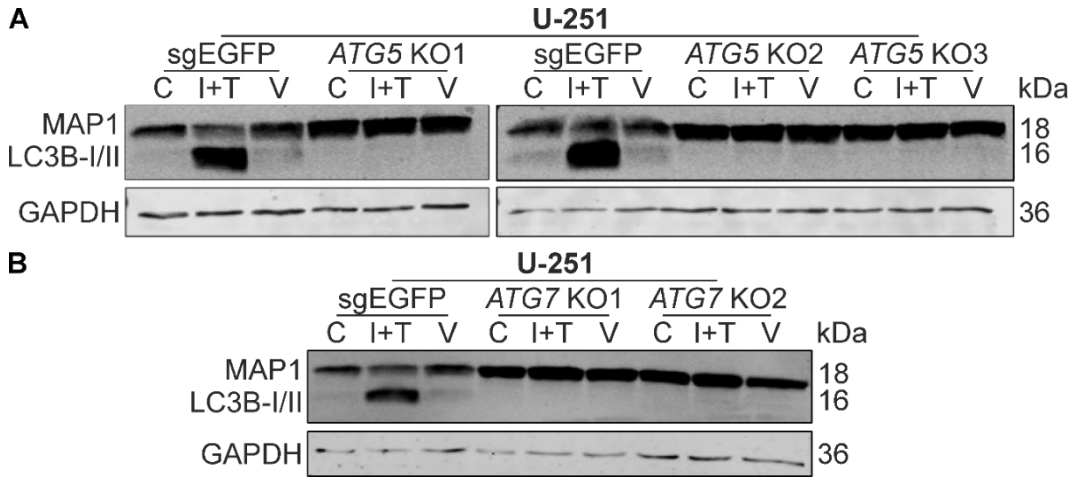

Figure 27. MAP1LC3B-switch is absent in autophagy-deficient cells. U-251 sgEGFP, *ATG5* **(A)** and *ATG7* **(B)** KO cells were treated either with DMSO (C), 20 µM imipramine + 100 µM ticlopidine (I+T) or with 1 µM VLX600 (V) for 24 h followed by immunoblot analysis of MAP1LC3B and GAPDH, which served as a housekeeper. The experiment was repeated three times. Figure modified from Reisbeck et al. (2023).

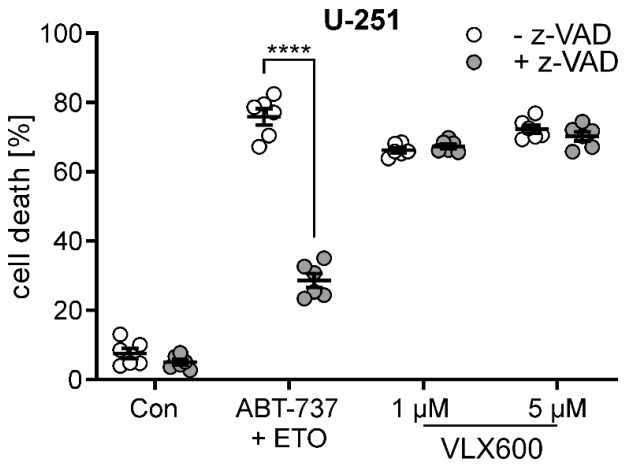

Figure 28. Cell death after VLX600 treatment is caspase-independent. Flow cytometric analysis of annexin V binding and PI uptake for cell death measurement. U-251 wt cells were treated with 1 µM ABT-737 + 100 µM etoposide (ETO) for 24 h or VLX600 for 70 h in combination with 20 µM z-VAD (1 h prior other treatments). Shown are annexin V only-, PI only- and double-positive cells. Data represent means ± SEM of at least two independent experiments with three replicates and 5,000 – 10,000 cells measured in each sample. Statistical significance was calculated with a 2way ANOVA. Figure adapted from Reisbeck et al. (2023).

Furthermore, an additional cell model was included to investigate if VLX600 is also effective against GSCs since there are thought to be involved in GBM recurrence as well as therapy resistance (Singh et al. 2003). For this, I generated NCH644 *ATG5* and *ATG7* KD cell lines using shRNAs against the respective genes and as a control shRNA against no known target in the human genome (non-target). The KDs were validated by immunoblot analysis, revealing a strong reduction of both targeted proteins (Figure 29A, B). Similar to the U-251 cells, the NCH644 non-target, *ATG5* and *ATG7* KD cells were treated with VLX600 for 48 h with subsequent analysis of cell death induction (Figure 29C). This revealed a 6-fold increase of cell death after 2 µM VLX600 treatment in the NCH644 control cell line that was significantly reduced in the *ATG5* and *ATG7* KD cell lines to about 5- and 3-fold, respectively (Reisbeck et al. 2023). Further, the MAP1LC3B-I/II switch was analysed after IM + TIC and VLX600 treatment for additional KD validation (Figure 30). Again, IM + TIC as well as VLX600 induced a prominent increase in the MAP1LC3B-II band indicative of autophagy activation, which was strongly reduced in the *ATG5* and *ATG7* KD cells proofing efficient autophagy inhibition (Reisbeck et al. 2023).

In conclusion, VLX600 induced a prominent amount of cell death in the adherent GBM cell line U-251 as well as in the GSC line NCH644, which was strongly inhibited in the respective *ATG5* and *ATG7* KOs or KDs, respectively. Further, autophagic flux was significantly increased after treatment, which was absent in the autophagy-deficient cell lines and cell death induced by VLX600 does not include the induction of caspase-dependent apoptosis since z-VAD was not

able to block the VLX600-induced cell death. In summary, this indicates that VLX600 induces an autophagy-dependent type of cell death in glioblastoma cells.

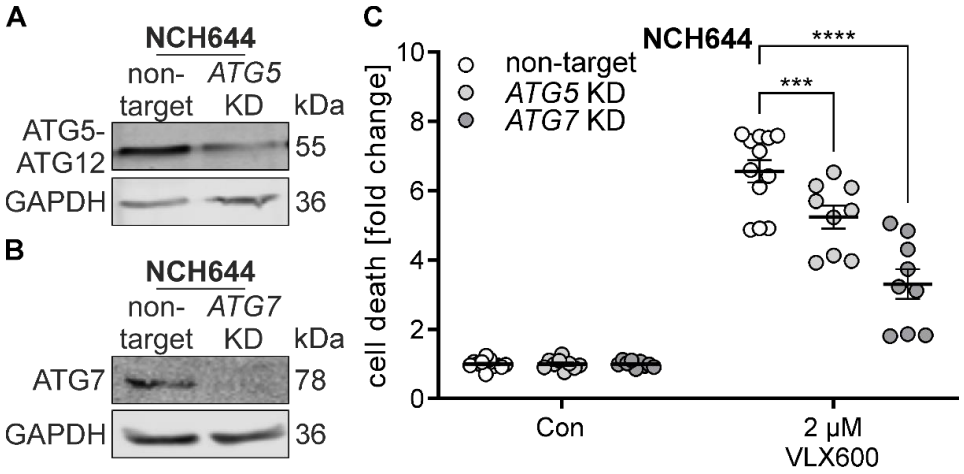

Figure 29. VLX600 induces an autophagy-dependent type of cell death in NCH644 glioblastoma stem-like cells. A, B) *ATG5* **(A)** and *ATG7* **(B)** KDs were generated in the GSC line NCH644 using shRNAs against the respective genes. KDs were validated via immunoblot analysis. The experiments were repeated at least four times. **C)** Cell death analysis of NCH644 non-target (control), *ATG5* and *ATG7* KD cells after 2 µM VLX600 treatment for 48 h. Shown is the fold change of total cell death (annexin V only-, PI only- and double-positive cells) compared to the DMSO control (Con). Data represent means ± SEM of at least three experiments with three replicates and 5,000 – 10,000 cells measured in each sample. Statistical significances were calculated with a 2way ANOVA. Figure modified from Reisbeck et al. (2023).

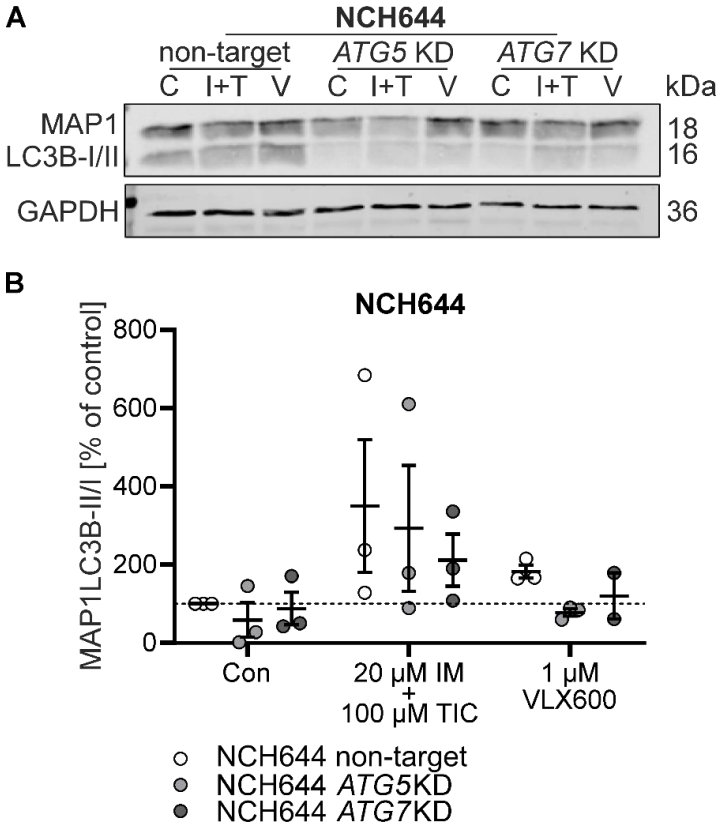

Figure 30. MAP1LC3B switch in NCH644 GBM cells. NCH644 non-target, *ATG5* and *ATG7* KD cells were treated either with DMSO (C), 20 µM imipramine + 100 µM ticlopidine (I+T) or 1 µM VLX600 (V) for 24 h with subsequent immunoblot analysis of MAP1LC3B and GAPDH, which served as a loading control. **A)** Representative blot of three experiments. **B)** Quantification of the MAP1LC3B-I/II switch. Data represent means ± SEM of three

experiments and was normalized to the NCH644 non-target con (dashed line). Figure modified from Reisbeck et al. (2023).

5.5. VLX600 inhibits oxidative phosphorylation in glioblastoma cells

VLX600 was described as an OXPHOS inhibitor in colon carcinoma cells (Zhang et al. 2014) and therefore this was also validated in GBM cells. When analysing the oxygen consumption of the U-251 sgEGFP and *ATG5* KO cells during VLX600 treatment (Figure 31) I observed a decrease in the oxygen consumption rate already after 14 h (Figure 31A). Finally, after 24 h of treatment, the difference to the vehicle treated condition was much more prominent and also significant (Figure 31B) (Reisbeck et al. 2023). In contrast, the U-251 *ATG5* KO cells showed a less eminent decrease in the oxygen consumption rate after treatment compared to the control cell line (Figure 31B). When OXPHOS is inhibited the resulting lack in ATP may increase glycolysis as a compensatory mechanism as it was shown in colon carcinoma cells (Zhang et al. 2014). To test this possibility, I treated the U-251 cells with VLX600 in combination with different concentrations of the glycolysis inhibitor 2-deoxyglucose (2-DG) followed by flow cytometric analysis of cell death as described before. VLX600 induced cell death of about 30 % (1 µM VLX600) and 35 % (5 µM VLX600) that remained unchanged when 2-DG was added (Figure 32), suggesting that glycolysis is not increased as a protective mechanism during VLX600-mediated OXPHOS inhibition in U-251 GBM cells. Of course also other catabolic pathways may be upregulated to ensure proper energy supply for the cells. For example, glutaminolysis where glutamine is catabolized into the tricarboxylic acid (TCA) cycle to produce ATP and anabolic carbons for the synthesis of amino acids, nucleotides and lipids is suggested to be upregulated in certain tumor cells. Thereto, glutaminolysis could also provide cellular energy during OXPHOS inhibition (Jin, Alesi and Kang 2016). To investigate this idea, the glutaminolysis inhibitor CB-839 was used that inhibits the glutaminase, which catalyses the initial deamination of glutamine into glutamate (Jin, Alesi and Kang 2016). The addition of different concentrations of CB-839 consistently increased the VLX600-induced cell death in the U-251 GBM cells in a concentration-dependent manner (Figure 33). For example, when treating the U-251 cells with 1 µM VLX600 this resulted in about 40 % cell death that was increased to about 60 % when 20 µM CB-839 was added additionally. This suggests that glutaminolysis at least partly protects the U-251 tumor cells from VLX600-induced cell death although this could depend strongly on the respective tumor/cell line.

The inhibition of OXPHOS, which is the main producer of ATP (Mitchell 1961), may result in a huge energy lack, which was further investigated. In order to analyse the amount of ATP after VLX600 treatment, U-251 cells were stained with the ATP biotracker, which was measured by flow cytometry (Figure 34). Already after 6 h of VLX600 treatment, a decrease in the ATP amount was seen that further decreased during longer treatment periods up to halve of the control. The withdrawal (w/o) of glucose served as a positive control and also resulted in a significant decrease in ATP (Reisbeck et al. 2023). Therefore, OXPHOS inhibition resulted in a huge bioenergetic dyshomeostasis, which cannot be counteracted by the upregulation of other ATP-producing pathways.

Reactive oxygen species (ROS) are constantly produced during OXPHOS at low levels, which are counteracted by the cellular antioxidant defence, but may also serve as intracellular signaling molecules (Brand 2016). However, during disturbance of the electron transport chain (ETC), like the inhibition of OXPHOS, ROS generation may increase to a point where certain ROS species are harmful for the cell, resulting in further mitochondrial damage and maybe also cell death. Therefore, I used the MitoSOX reagent, which specifically detects mitochondrial superoxide that is the main ROS species produced by the ETC, to analyse ROS production after VLX600 treatment. Subsequent flow cytometric analysis after 24 h of VLX600 treatment revealed a significant increase in mitochondrial ROS of about 2-fold (for 5 µM VLX600) compared to the solvent control in the U-251 cell line, similarly to the ETC inhibitor rotenone (Figure 35).

In summary, this indicates that VLX600 inhibits OXPHOS in U-251 GBM cells, resulting in a huge cellular energy depletion corresponding to strongly reduced amounts of ATP, which cannot be rescued by augmented glycolysis or glutaminolysis and which is accompanied by increased mitochondrial ROS.

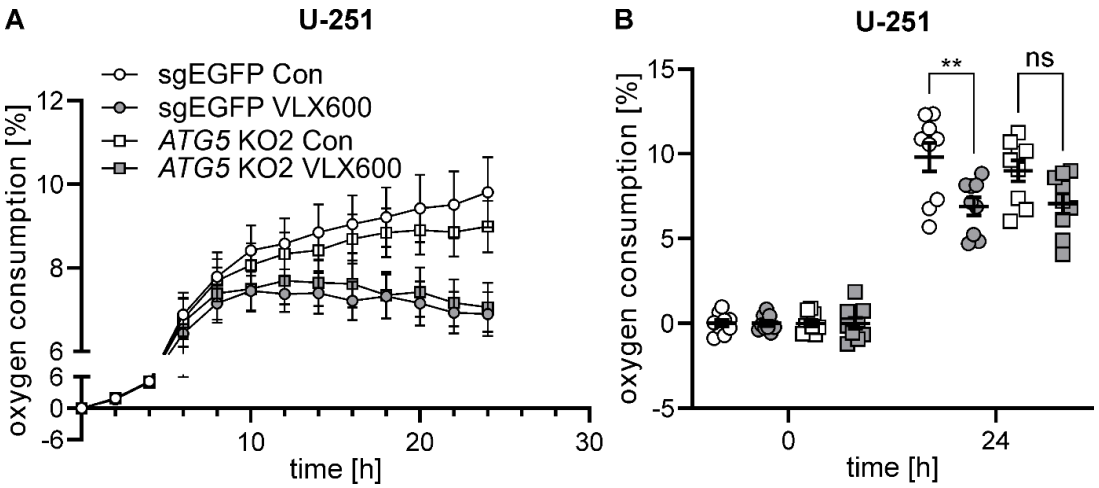

Figure 31. Oxygen consumption is disturbed after VLX600 treatment in U-251 glioblastoma cells. U-251 sgEGFP and *ATG5* KO2 cells were seeded out in special 24-well plates with integrated oxygen sensors and treated with 5 µM VLX600 for a total of 24 h. The amount of oxygen in the media was measured over the whole treatment period with measurements for the first 60 min every minute and afterwards every 15 min. Data represent means ± SEM of three experiments with three replicates. Statistical significances were measured with a 2way ANOVA. **A)** Depiction of oxygen consumption over the whole treatment period. **B)** Oxygen consumption after 24 h of treatment. Figure partly adapted from Reisbeck et al. (2023).

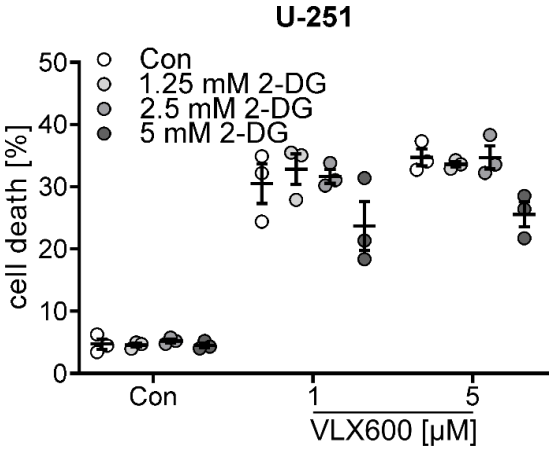

Figure 32. Cell death after VLX600 treatment is not rescued by upregulation of glycolysis in U-251 glioblastoma cells. U-251 wt cells were treated with 1 and 5 µM VLX600 with or without the addition of the glycolysis inhibitor 2-deoxyglucose (2-DG) as indicated for 48 h. Cell death was analysed by flow cytometry analysis of annexin V binding and PI uptake (cell death indicates only annexin V-, only PI- and double-positive cells). Data represent means ± SEM of one experiment with three replicates and 10,000 cells measured in each sample.

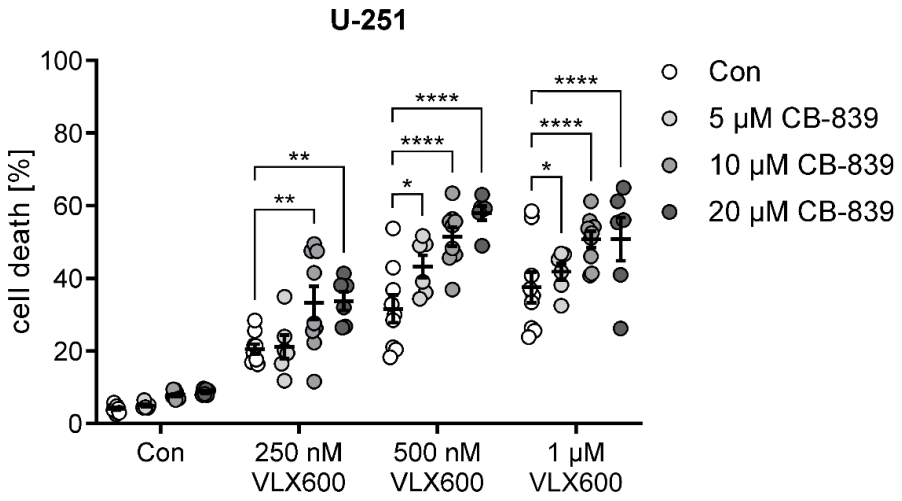

Figure 33. The glutaminolysis inhibitor CB-839 further increased the VLX600-induced cell death in U-251 glioblastoma cells. U-251 cells were treated with different concentrations of VLX600 as indicated with or without the addition of 5, 10 or 20 µM CB-839 for 48 h. Subsequently, cell death was analysed by annexin V binding and PI uptake followed by flow cytometric measurement. Displayed is the total cell death consisting of annexin V only-, PI only- and double-positive cells. Data represent means ± SEM of at least two experiments with three replicates and 5,000 – 10,000 cells measured in each sample. Statistical significances were measured with a 2way ANOVA.

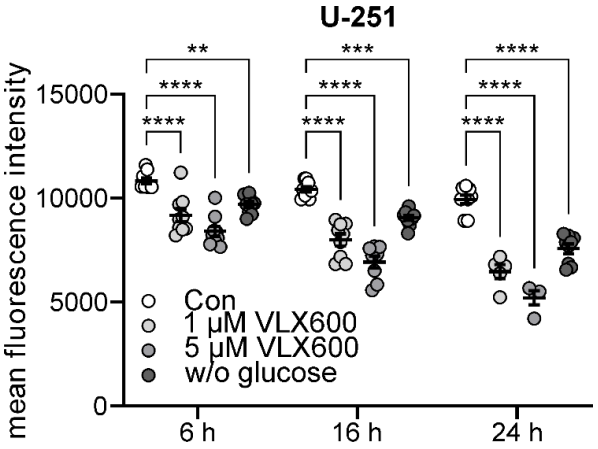

Figure 34. Measurement of ATP after VLX600 treatment in U-251 glioblastoma cells. U-251 wt cells were treated with 1 and 5 µM VLX600 or glucose was withdrawn (w/o glucose) for the indicated time periods. Afterwards, ATP amounts were measured using the BioTracker ATP dye and flow cytometry. Data represent means ± SEM of three experiments with one – three replicates and 10,000 cells measured in each sample. Statistical significances were measured with a 2way ANOVA. Figure adapted from Reisbeck et al. (2023).

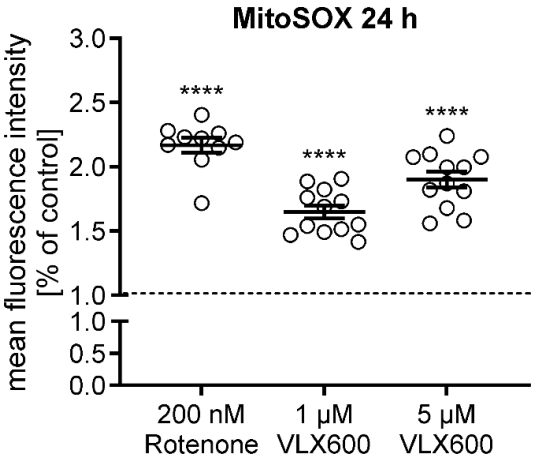

Figure 35. Mitochondrial ROS is increased in U-251 cells after VLX600 treatment. U-251 control (sgEGFP) cells were seeded out in 12-well plates and treated with 200 nM Rotenone or 1 and 5 µM VLX600 for 24 h. Subsequently, cells were stained with the MitoSOX reagent that detects mitochondrial superoxide, which was measured by flow cytometry. Data represent means ± SEM of at least three experiments with three replicates and 5,000 – 10,000 cells measured in each sample. Statistical significances were measured with a 2way ANOVA. The dashed line indicates the solvent control, which was normalized to one. Asterisks indicate difference from solvent control.

5.6. VLX600 induces mitophagy in glioblastoma cells

VLX600 inhibited OXPHOS in U-251 cells resulting in increased mitochondrial ROS production, which may further disrupt mitochondrial homeostasis. In order to analyse mitochondrial function/dysfunction after VLX600 treatment in GBM cell lines, I started to examine the mitochondrial membrane potentials since this is a good readout for the overall mitochondrial condition. Therefore, U-251 cells were stained with the TMRM dye after VLX600 treatment for 24 h and subsequently analysed by flow cytometry whereby the TMRM signal intensity correlates with the mitochondrial membrane potentials (Figure 36). This revealed a highly significant concentration dependent decrease in the mitochondrial membrane potentials, indicating mitochondrial damage (Reisbeck et al. 2023). Additionally, immunofluorescence analysis of mitochondria using an antibody against the outer mitochondrial membrane (OMM) protein TOMM20 (translocase of outer mitochondrial membrane 20) further promotes the idea that VLX600 induces mitochondrial damage since the mitochondrial network was strongly disrupted already after 16 h of 5 µM VLX600 treatment, which was even more severe after 48 h of treatment (Figure 37).

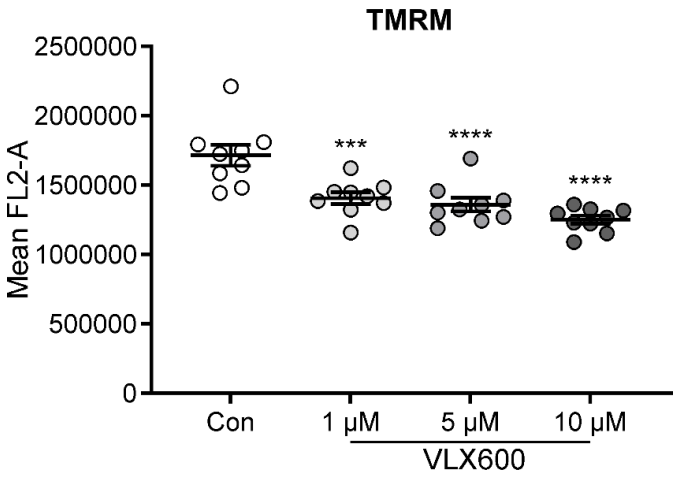

Figure 36. Decrease of mitochondrial membrane potentials in U-251 cells after VLX600 treatment. U-251 cells were treated with VLX600 or DMSO (Con) as indicated for 24 h followed by TMRM staining and subsequent flow cytometric analysis. Data represent means ± SEM of three independent experiments with three replicates and 10,000 cells measured. Statistical significances were calculated with a one-way ANOVA. Asterisks indicate difference from Con. Figure adapted from Reisbeck et al. (2023).

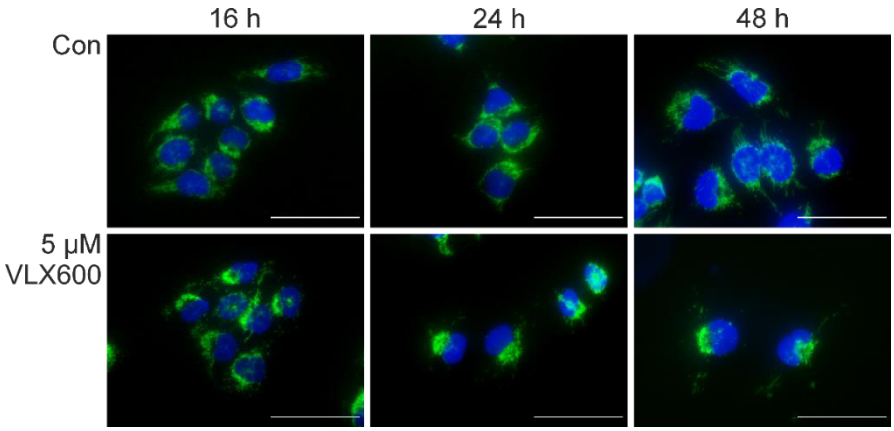

Figure 37. Mitochondrial morphology after VLX600 treatment. U-251 cells were treated with 5 µM VLX600 for the indicated time periods followed by immunofluorescence staining of the mitochondrial marker protein TOMM20 as well as DAPI to stain the nuclei. Representative pictures of two independent experiments with at least two pictures taken per treatment. Pictures were taken at 60x magnification and the scale bar is 50 µM.

Damaged mitochondria may be degraded by mitophagy in order to protect the cells from harmful consequences including cell death. A first hint of increased mitophagy is the decrease of mitochondrial proteins like COX4I1 (cytochrome c oxidase subunit 4I1), TOMM20, VDAC1 and HSPD1, which were subsequently analysed after VLX600 treatment. U-251 GBM cells were treated with 1 and 5 µM VLX600 for different time periods followed by immunoblot analysis of the mitochondrial marker proteins (Figure 38). All of the mitochondrial proteins were decreased after VLX600 treatment in a time-dependent manner with the most prominent decrease after 48 h of treatment. The quantification of the western blots revealed that the reduction was highly significant at least for COX4I1 and TOMM20 with only about 20 % protein amount left (for 1 µM VLX600) (Figure 38B – D) or slightly significant for HSPD1 with about 25 % protein amount left after 48 h of 5 µM VLX600 treatment (Figure 38E) (Reisbeck et al.

2023). In addition, a similar experiment was performed with the GSC line NCH644 to validate the results obtained in the U-251 cells. NCH644 cells were treated with 1 and 2 µM VLX600 for the same time periods, which similarly resulted in a decrease of the mitochondrial proteins although to a lesser extent when compared to the U-251 cells (Figure 39). In the NCH644 cells the protein level of COX4I1 was reduced by about 40 % after 24 h, TOMM20 by about 50 % and VDAC1 was only slightly reduced (Figure 39B – D) (Reisbeck et al. 2023). However, as the decrease is clearly visible for COX4I1 and TOMM20 this underscores the previous results obtained in the U-251 cells, suggesting the induction of mitochondrial dysfunction and possibly also mitophagy.

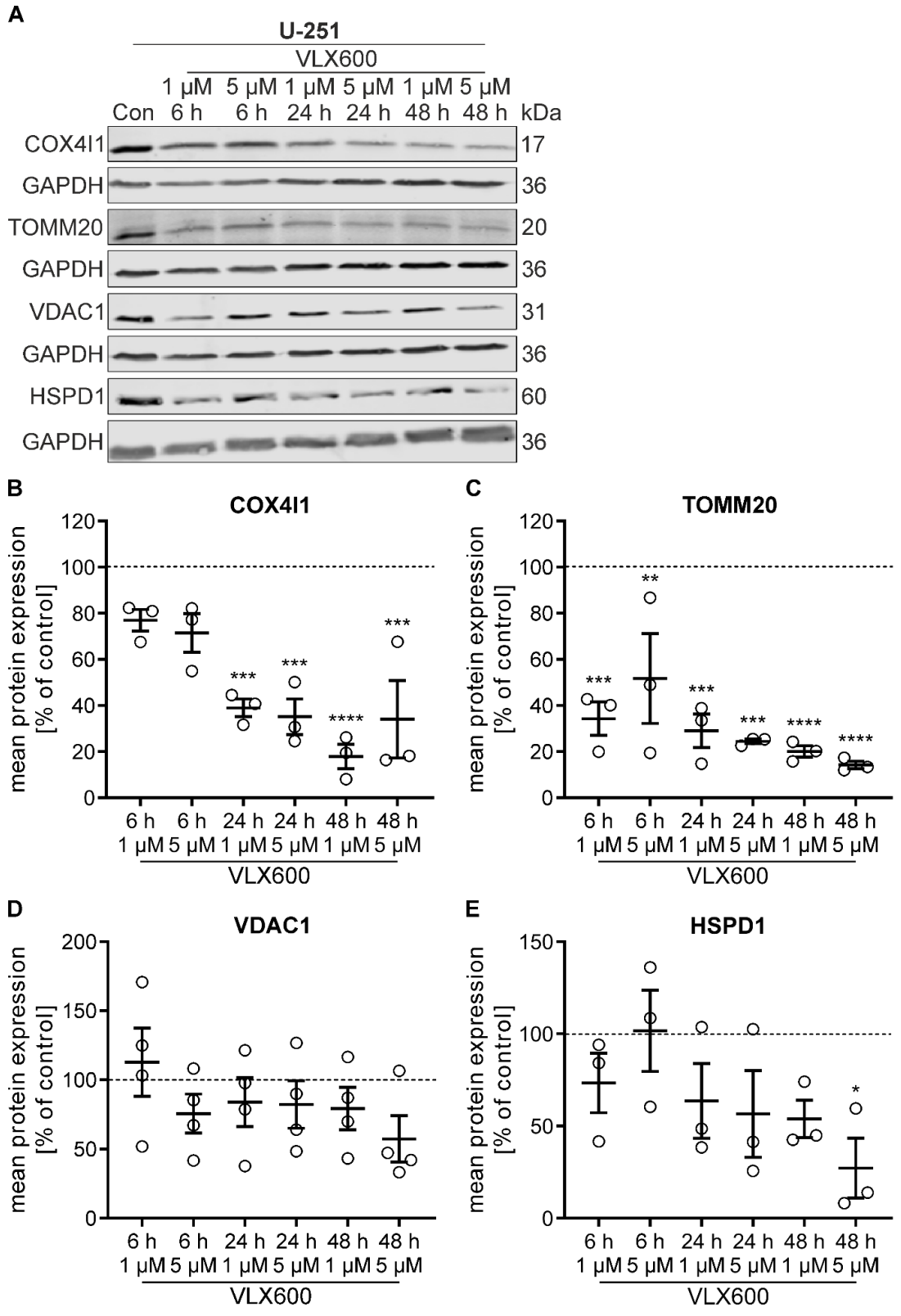

Figure 38. Reduced levels of mitochondrial proteins after VLX600 treatment in U-251 glioblastoma cells. Evaluation of the protein amounts of the mitochondrial proteins COX4I1 **(A, B)**, TOMM20 **(A, C)**, VDAC1 **(A, D)** and HSPD1 **(A, E)** by immunoblot analysis in U-251 cells. GAPDH was used as housekeeper. U-251 cells were treated with 1 and 5 µM VLX600 for 6 h, 24 h and 48 h. DMSO was used as control (Con). **B – E)** Quantification of the mitochondrial proteins seen in A. Data represent means ± SEM of at least three independent experiments. Statistical significances were calculated with a one-way ANOVA and asterisks indicate difference from Con (dashed line indicates DMSO control, which was normalized to 100 %). Figure partly adapted from Reisbeck et al. (2023).

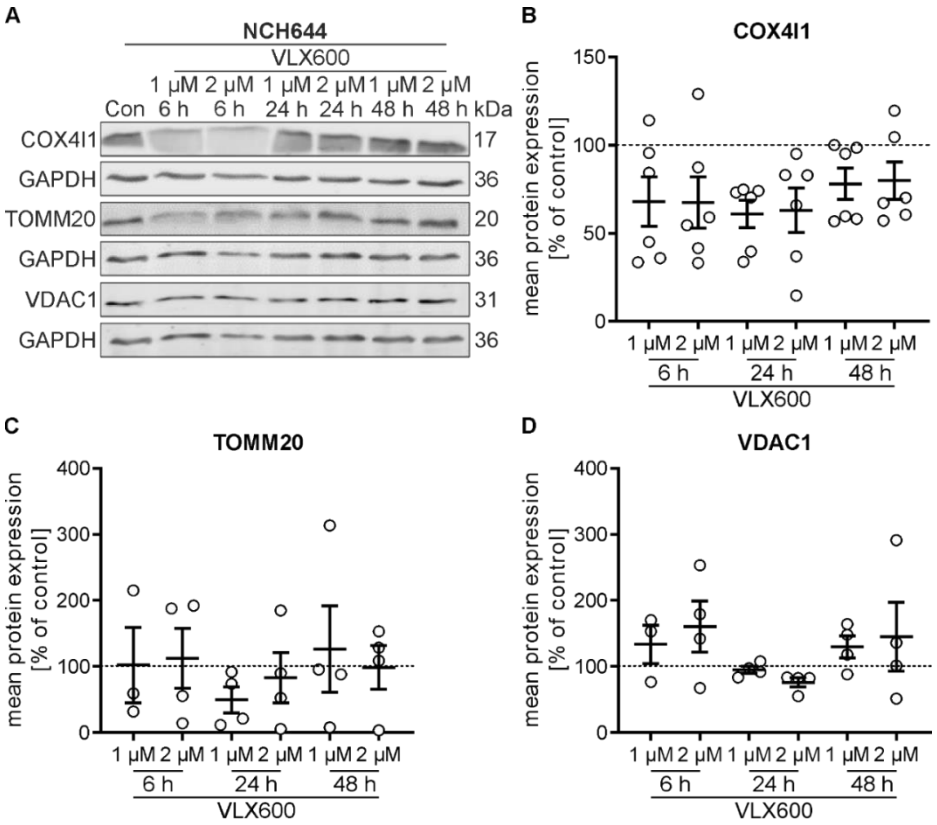

Figure 39. Investigation of mitochondrial proteins after VLX600 treatment in NCH644 glioblastoma stem-like cells. The mitochondrial protein levels of COX4I1 **(A, B)**, TOMM20 **(A, C)** and VDAC1 **(A, D)** were analysed by immunoblot analysis after VLX600 treatment (1 and 2 µM for 6 h, 24 h and 48 h) in NCH644 wt cells. DMSO was used as a solvent control (Con) and GAPDH as a housekeeper. **B – D)** Quantification of the mitochondrial proteins seen in A. Data represent means ± SEM of at least three independent experiments (dashed line indicates DMSO control that was normalized to 100 %). Figure partly adapted from Reisbeck et al. (2023).

Furthermore, the involvement of autophagy in the VLX600-induced mitophagy was analysed by performing a rescue experiment. Therefore, the mitochondrial protein level in the autophagy-deficient cell lines was analysed. U-251 sgEGFP, *ATG5* and *ATG7* KO cells were treated with 1 µM VLX600 for 24 h and once more immunoblot analysis of the mitochondrial proteins was performed. Again, the protein level of COX4I1 and TOMM20 was reduced by about 40 % and 60 % in the control cell lines, respectively (Figure 40A – C). In contrast, in the *ATG5* and *ATG7* KO cell lines the COX4I1 protein level remained unchanged after treatment and the TOMM20 protein amount was reduced to a lesser extent in the *ATG7* KO cells (about 50 %) compared to the sgEGFP cells (about 60 %) (Reisbeck et al. 2023). In all three cell lines the VDAC1 protein level was hardly changed at all (Figure 40D). Further, the NCH644 non-target, *ATG5* and *ATG7* KD cells were treated with 1 and 2 µM VLX600 for 24 h and subsequent immunoblot analysis showed a strong decrease in the COX4I1 protein level and a slight decrease in the TOMM20 and VDAC1 protein amount after VLX600 treatment (at least for 2 µM) in the non-target control cells (Figure 41). The decreased COX4I1 protein level was

almost completely rescued in the *ATG5* and *ATG7* KD cells and even significantly in the *ATG7* KD cells after 2 µM VLX600 treatment (Figure 41B) (Reisbeck et al. 2023). In the *ATG5* KD cells the protein amount of TOMM20 and VDAC1 was also almost unchanged after treatment and in the *ATG7* KD cells the TOMM20 protein level was fully rescued (Figure 41C). The VDAC1 protein amount was rescued at least after 1 µM VLX600 treatment (Figure 41D).

In summary, the obtained data suggest that VLX600 disturbs mitochondrial homeostasis as shown by mitochondrial membrane depolarization and disruption of the mitochondrial network, possibly resulting in increased mitophagy shown by a reduction of mitochondrial proteins that is partially blocked in *ATG5* and *ATG7* KO and KD cell lines.

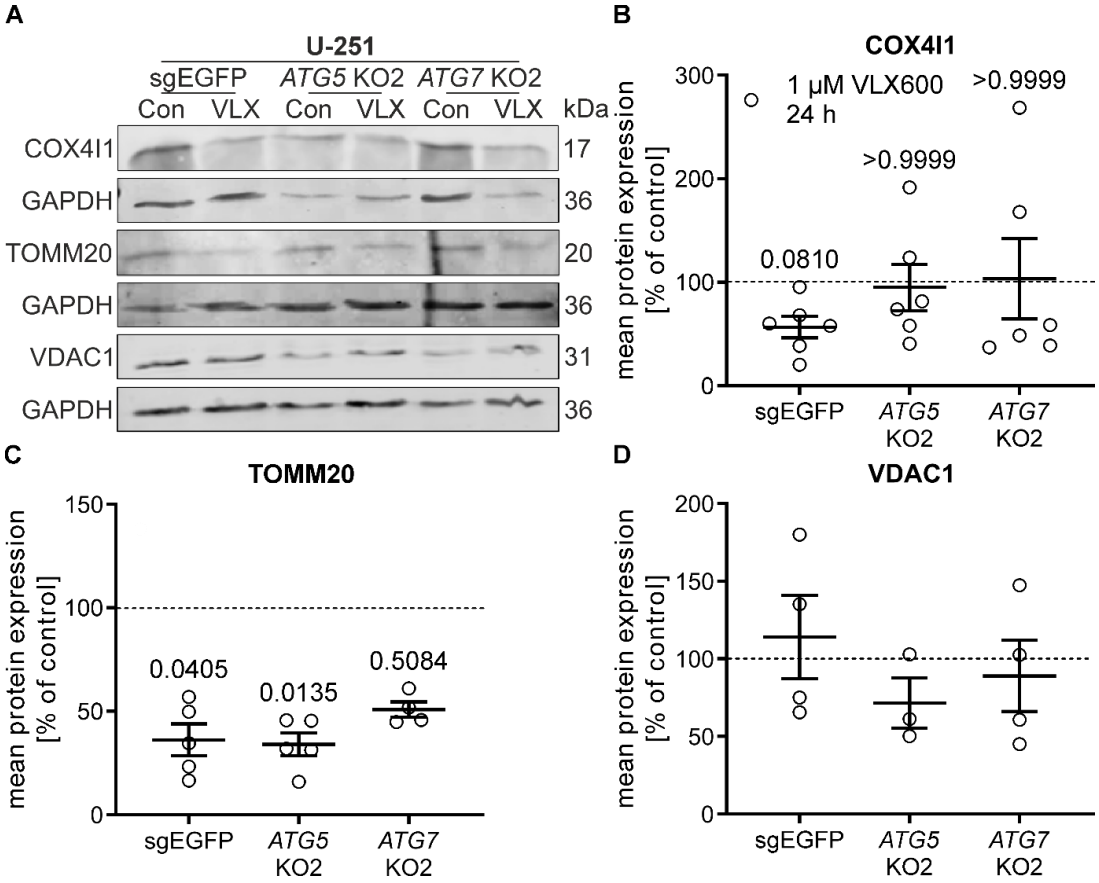

Figure 40. Reduction of mitochondrial proteins after VLX600 treatment is partially rescued in *ATG5* and *ATG7* KO cells. The mitochondrial proteins COX4I1 **(A, B)**, TOMM20 **(A, C)** and VDAC1 **(A, D)** were analysed by western blot after 1 µM VLX600 treatment for 24 h in U-251 *ATG5* and *ATG7* KO cells. DMSO served as a solvent control (Con) and GAPDH as a housekeeper. **B – D)** Quantification of the proteins seen in A. Data represent means ± SEM of at least three experiments. Statistical significances were calculated with a Kruskal-Wallis test (dashed line indicates DMSO control that was normalized to 100 %; numbers represent the p-values). Figure partly adapted from Reisbeck et al. (2023).

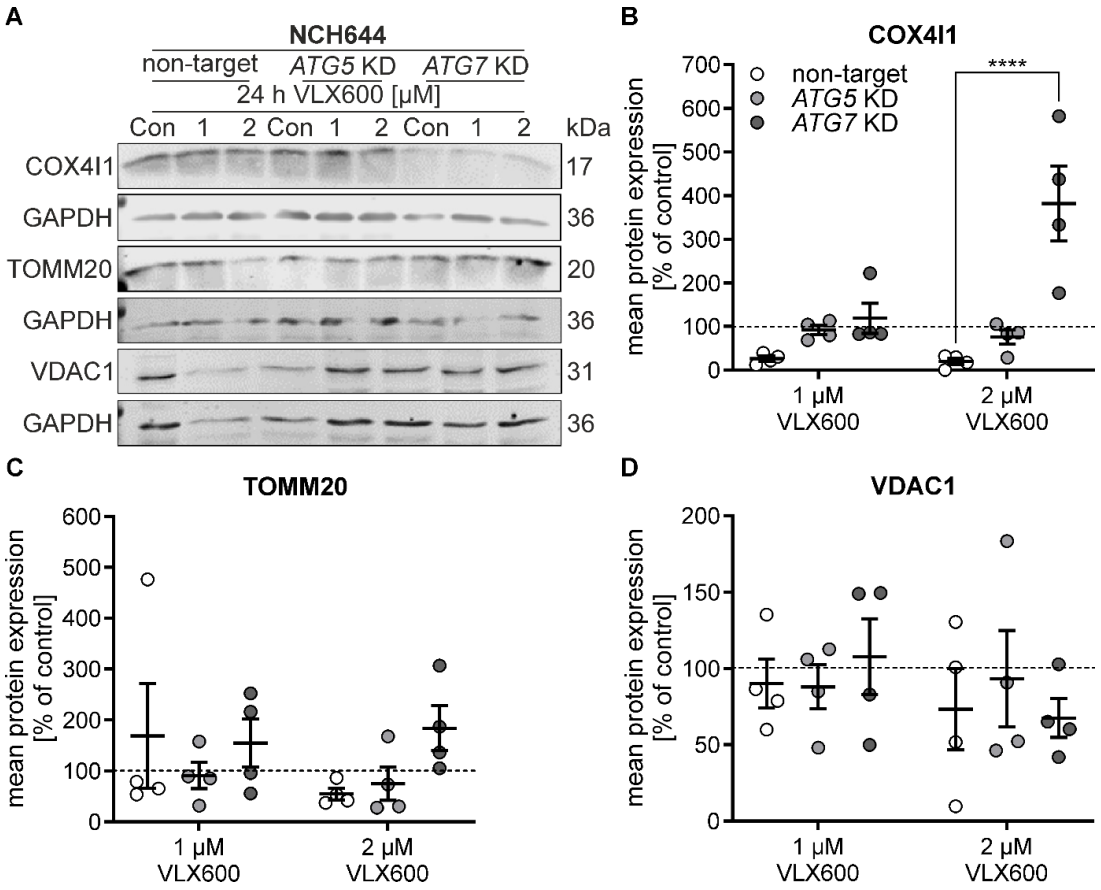

Figure 41. Analysis of mitochondrial proteins after VLX600 treatment in NCH644 *ATG5* and *ATG7* KD cells. The mitochondrial proteins COX4I1 **(A, B)**, TOMM20 **(A, C)** and VDAC1 **(A, D)** were analysed by western blot after 1 and 2 µM VLX600 treatment for 24 h in NCH644 *ATG5* and *ATG7* KD cells. DMSO served as a solvent control (Con) and GAPDH as a housekeeper. **B – D)** Quantification of the proteins seen in A. Data represent means ± SEM of four experiments. Statistical significance was calculated with a 2way ANOVA (dashed lines indicate the DMSO control, which was normalized to 100 %). Figure partly adapted from Reisbeck et al. (2023).

Reduced mitochondrial proteins may indicate the induction of mitophagy. In order to validate this idea, the mitochondrial Keima reporter plasmid (pCHAC-mt-mKeima) was used that changes its emission wavelength depending on the pH and therefore is used as a mitophagy reporter (Lazarou et al. 2015) (the mt-mKeima experiment was performed by Süleyman Bozkurt (working group of Dr. Christian Münch, Institute of Biochemistry II, Goethe University Hospital Frankfurt/Main, Germany)). U-251 sgEGFP and *ATG5* KO cells stably expressing the mt-mKeima reporter plasmid were treated with 5 µM VLX600 followed by flow cytometry (Figure 42). A change in the fluorescence wavelength from 488 nm to 561 nm correlates with the induction of mitophagy. VLX600 induced mitophagy of about 60 % in the U-251 sgEGFP cells, but only of about 50 % in the U-251 *ATG5* KO cells (Figure 42B), underlining the assumption of mitophagy induction after VLX600 treatment and suggesting that the inhibition of autophagy also partially blocks the induction of mitophagy (Reisbeck et al. 2023).

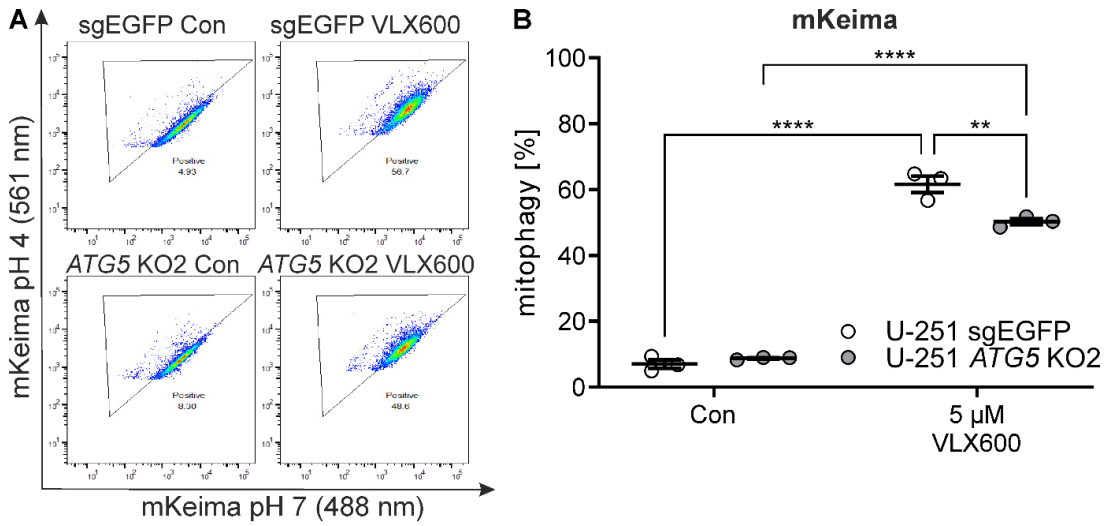

Figure 42. Mitophagy is induced in U-251 glioblastoma cells after VLX600 treatment. U-251 control (sgEGFP) and *ATG5* KO2 cells expressing the mitophagy reporter pCHAC-mt-mKeima were treated with 5 µM VLX600 for 24 h and subsequently analysed by flow cytometry. A shift from 488 nm to 561 nm indicates the induction of mitophagy. **A)** Representative experiment. **B)** Comparison of mitophagy (561 nm positive cells) induced in the sgEGFP and the *ATG5* KO2 cells. Data represent means ± SEM of three replicates. Statistical significances were analysed with a 2way ANOVA. This experiment was performed by Süleyman Bozkurt (working group of Dr. Christian Münch, Institute of Biochemistry II, Goethe University Hospital Frankfurt/Main, Germany). Figure modified from Reisbeck et al. (2023).

To further confirm the induction of mitophagy at the single cell level, I used the mtphagy dye that similar to Keima changes its fluorescence emission depending on the pH, but can directly be given to the cell culture medium without prior transfection or transduction. An augmented mtphagy dye signal is already indicative for increased mitophagy, but additionally the fusion of mitochondria-containing autophagosomes with lysosomes can be monitored by using a lysosomal staining (lyso dye), too. U-251 sgEGFP, *ATG5* and *ATG7* KO cells were treated with 5 µM VLX600 for 24 h, stained with the lyso and mtphagy dyes and were subsequently analysed under the fluorescence microscope (Figure 43A). While almost no mtphagy dye signal was visible in the vehicle treated cells, a strong signal was seen in the U-251 sgEGFP cells after 24 h of VLX600 treatment. Further, I observed many mitophagosomes (mitochondria-containing autophagosomes) colocalizing with lysosomes (indicating fusion of mitophagosomes and lysosomes; orange colour, depicted by arrows) representing ongoing mitophagy. In contrast, no mtphagy dye signal increase was seen in the *ATG5* and *ATG7* KO cells after VLX600 treatment. The quantification of the double positive dots further confirmed the significant rescue of colocalized dots in the autophagy-deficient cell lines compared to the control cell line (Figure 43B). As a control for mitophagy induction I also used the Hsp90 (HSP90AA1, heat shock protein 90 alpha family class A member 1) inhibitor Gamitrinib-TPP (GTPP) in a similar setting. U-251 cells were treated with 5 and 10 µM GTPP for 24 h resulting

in a strong increase in the mtphagy dye signal and the formation of double positive dots, which was also highly significant after 10 µM GTPP treatment (Figure 44). In summary, I could show that VLX600 induces mitochondrial dysfunction in GBM cells that finally culminates in mitophagy induction, which is partially rescued by *ATG5* and *ATG7* deficiency.

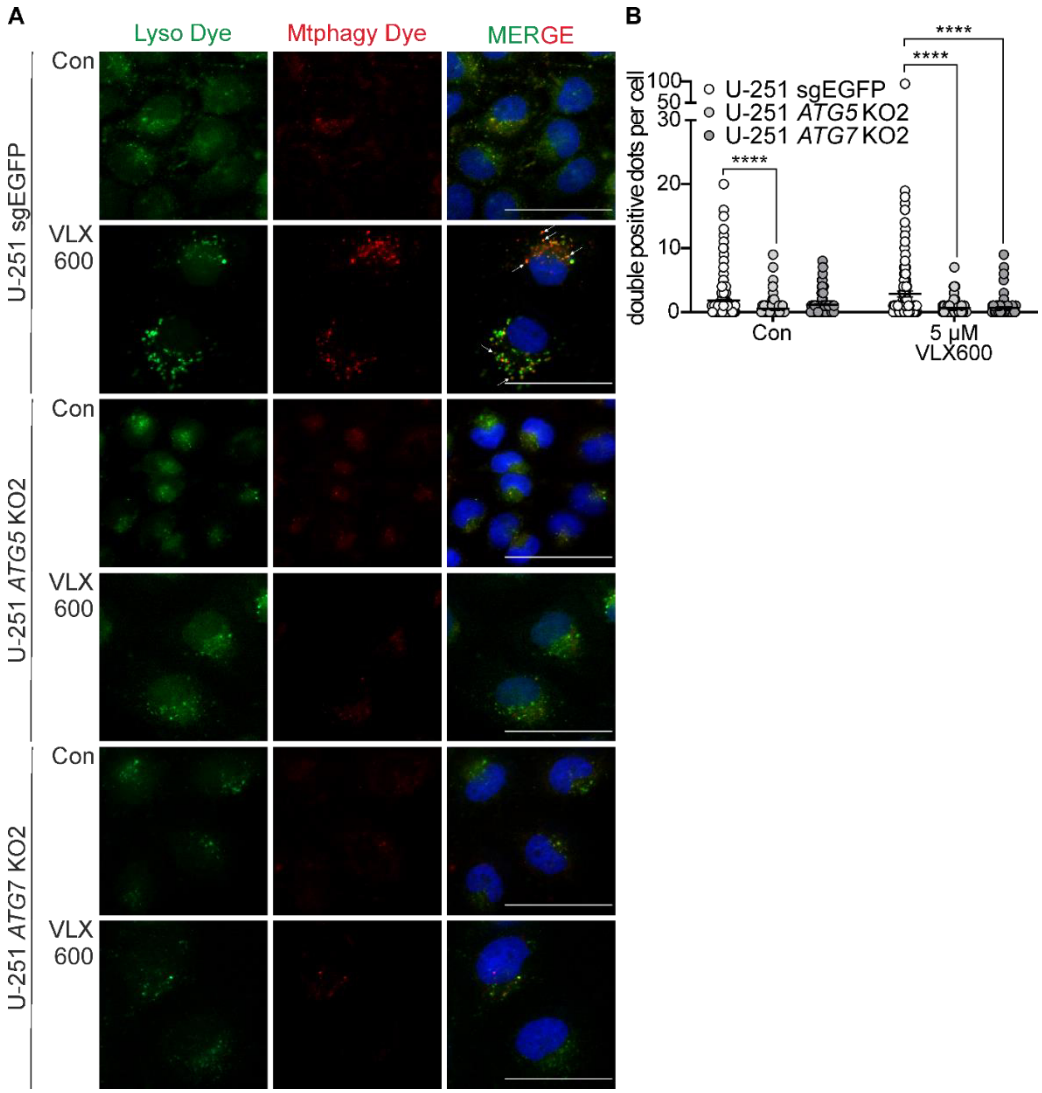

Figure 43. VLX600 induced mitophagy that is partially blocked in *ATG5* and *ATG7* KO cells. A) Assessment of mitophagy using the mtphagy and lyso dyes, which stain mitochondria undergoing mitophagy and lysosomes, respectively. U251 sgEGFP, *ATG5* and *ATG7* KO cells were treated with 5 µM VLX600 for 24 h. DMSO was used as a control (Con). Nuclei were stained with Hoechst 33342 and images were taken at 60x magnification. The scale bar is 50 µm. Shown are representative images of three experiments with overall 9 – 33 images taken per treatment. **B)** Quantification of the double positive dots. Data represent means ± SEM of a total of 79 – 360 cells measured per treatment. Statistical significances were measured with a Kruskal-Wallis test.

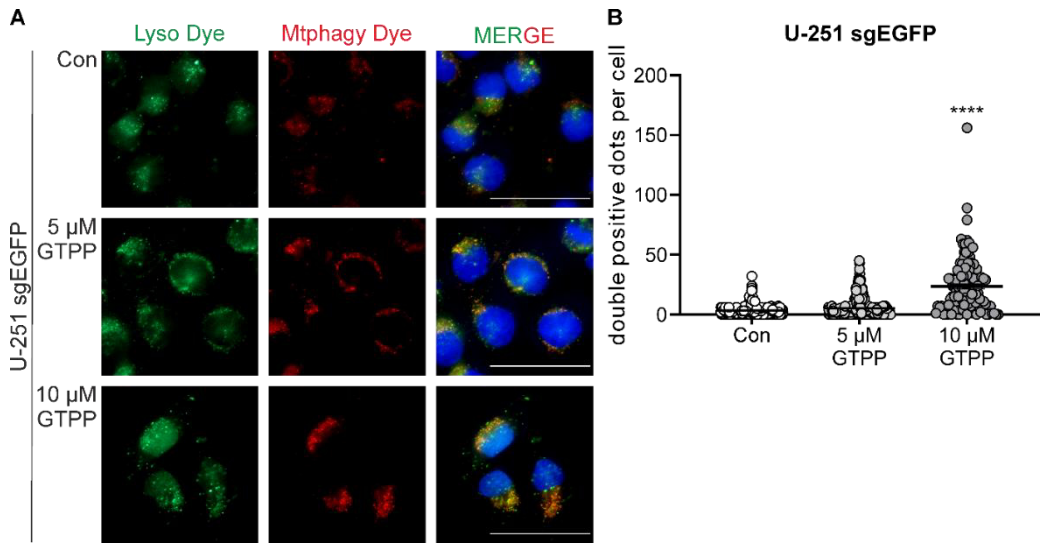

Figure 44. The mitophagy inducer Gamitrinib-TPP induced mitophagy in U-251 glioblastoma cells. A) Representative images of U-251 cells treated for 24 h with 5 and 10 µM Gamitrinib-TPP (GTPP) or DMSO (Con) followed by staining with the mtphagy and lyso dyes in order to analyse mitophagy induction. Nuclei were stained with Hoechst 33342 and images were taken at 60x magnification. The experiment was repeated five times with at least three images taken per treatment. The scale bar indicates 50 µm. **B)** Quantification of the dots positive for the mtphagy and the lyso dye as seen in A. Data represent means ± SEM of a total of 118 – 409 cells per treatment. Statistical significance was measured with a Kruskal-Wallis test and asterisk indicates difference from Con.

5.7. VLX600 induces BNIP3- and BNIP3L-dependent mitophagy

So far, I had shown that VLX600 induces ADCD and mitophagy in GBM cells, which both can be rescued by *ATG5* or *ATG7* KO or KD, but the underlying mechanisms were still unclear. Mitophagy can be executed by a plethora of mitophagy receptors like BNIP3/BNIP3L, FUNDC1 and many more (Vara-Perez, Felipe-Abrio and Agostinis 2019). The PINK1/Parkin pathway plays only a minor role for GBM since Parkin is frequently mutated and hence not expressed or at least only at very low levels (Veeriah et al. 2010; Rouland et al. 2021). The mitophagy receptors BNIP3 and BNIP3L are known to facilitate mitophagy during hypoxia that is mediated via the hypoxia-inducible transcription factor HIF1A (Bellot et al. 2009). In line with this, I observed a huge upregulation of HIF1A protein already after 6 h of VLX600 treatment in the U-251 cells (Figure 45) (Reisbeck et al. 2023). Therefore, I further investigated the protein amount of the mitophagy receptors BNIP3 and BNIP3L after VLX600 treatment. After treatment, the cell pellets were fractionated into cytosolic and mitochondrial fractions, which were further analysed by western blot (Figure 46). This revealed a strong increase in the protein levels of both BNIP3 and BNIP3L already after 6 h, which was even more prominent after 24 h of treatment especially in the mitochondrial fractions. In addition, BNIP3 and BNIP3L were observed as homodimers, which were shown to be extremely stable also under denaturating conditions, migrate at 60 and 76 kDa, respectively, and are needed for proper

mitophagy initiation and progression (Sulistijo and MacKenzie 2006; Marinković, Šprung and Novak 2021) Additionally, the dimers were only seen in the mitochondrial fractions (Reisbeck et al. 2023). GAPDH served as a cytosolic marker and COX4I1 as a mitochondrial marker to validate prober fractionation (Figure 46). Furthermore, the microscopic analysis of BNIP3L together with the mitochondrial marker protein TOMM20 revealed a prominent increase of BNIP3L at mitochondria after 16 h and slightly already after 6 h of VLX600 treatment that was not seen in the vehicle treated cells (Figure 47) (Reisbeck et al. 2023). Altogether, the protein levels of BNIP3 and BNIP3L were highly upregulated after VLX600 treatment in U-251 cells most likely mediated via HIF1A.

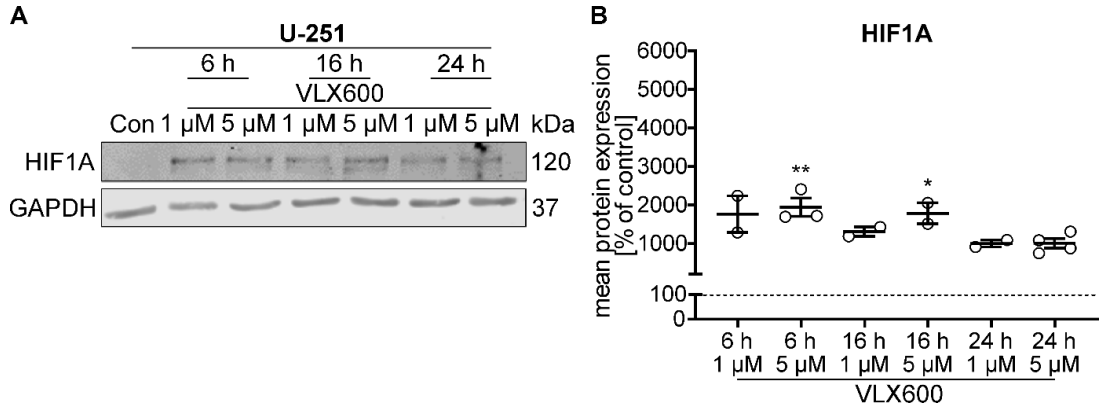

Figure 45. HIF1A protein level in U-251 glioblastoma cells after VLX600 treatment. U-251 cells were treated with 1 and 5 µM VLX600 or DMSO (Con, 24 h) for the indicated time periods with subsequent immunoblot analysis of HIF1A. **A)** Representative immunoblot. The experiment was repeated two to four times. **B)** Quantification of the western blot seen in A. Data represent means ± SEM of two to four experiments. The dashed line indicates the DMSO control that was normalized to 100 %. Statistical significances were measured with a Kruskal-Wallis test and asterisks indicate difference from Con. Figure adapted from Reisbeck et al. (2023).

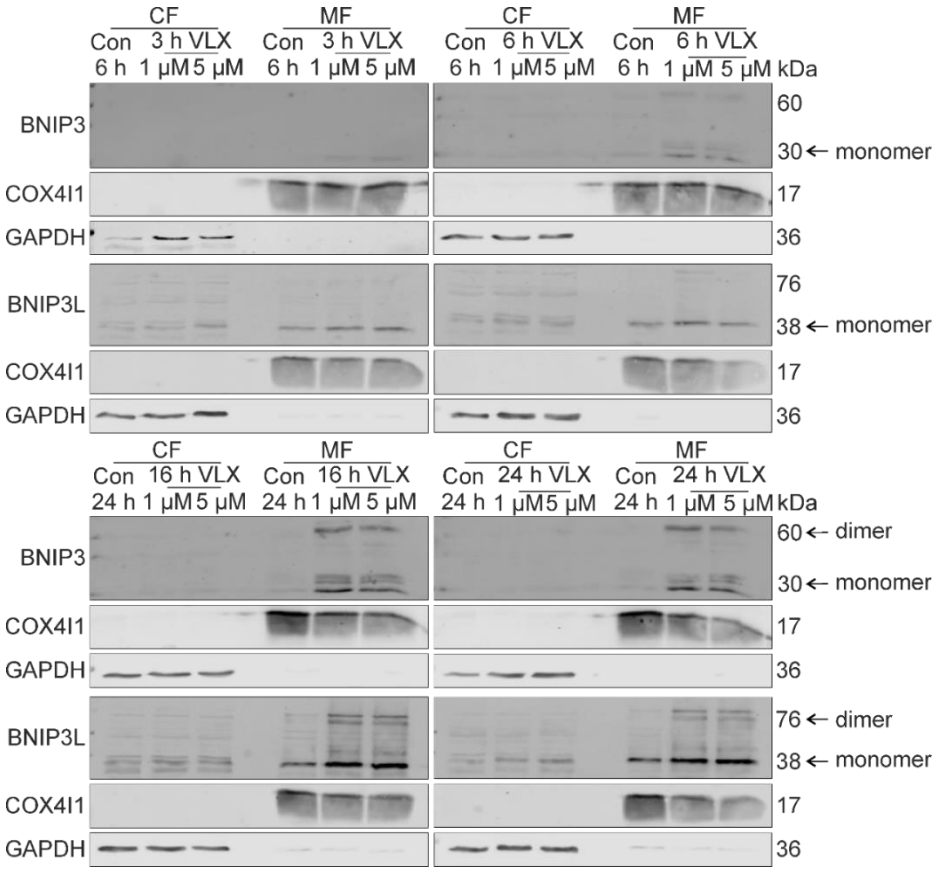

Figure 46. Immunoblot analysis of the mitophagy receptors BNIP3 and BNIP3L after VLX600 treatment. U-251 glioblastoma cells were treated with 1 and 5 µM VLX600 for the indicated time periods followed by fractionation into cytosolic (CF) and mitochondrial fractions (MF). Both were analysed for their BNIP3 and BNIP3L protein amounts via western blot. Monomers and dimers are indicated with arrows. DMSO was used as a solvent control (Con). GAPDH served as a marker for the cytosolic fraction and COX4I1 as a marker for the mitochondrial fraction. The experiment was repeated three times. Figure partly adapted from Reisbeck et al. (2023).

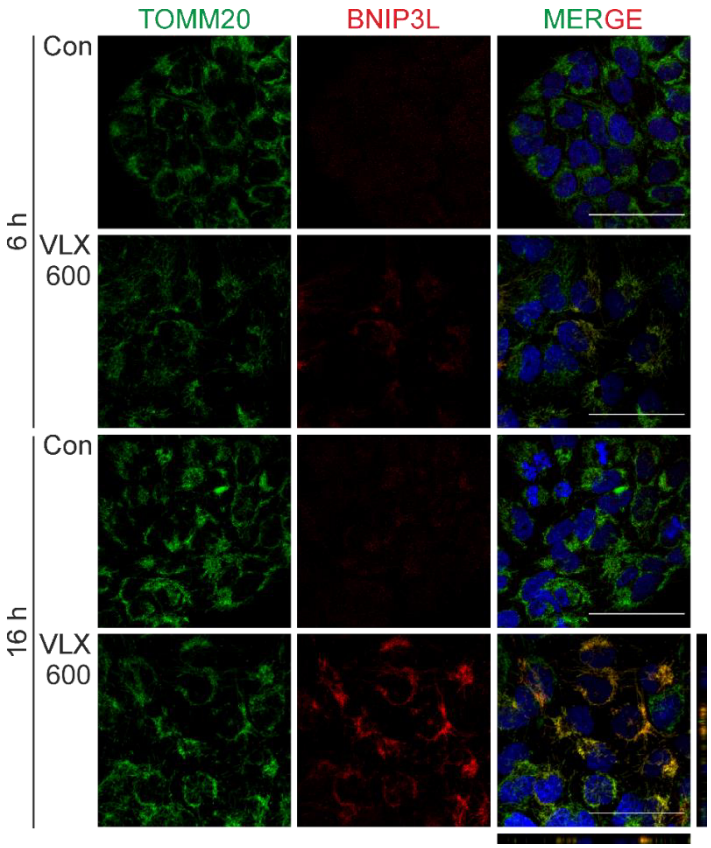

Figure 47. Microscopic analysis of TOMM20 and BNIP3L in U-251 glioblastoma cells. U-251 cells were treated with 5 µM VLX600 for 6 h and 16 h followed by immunofluorescence staining of the OMM protein TOMM20 and the mitophagy receptor BNIP3L. DAPI was used as a nuclear staining and DMSO as a solvent control (Con). Shown are representative pictures taken with a confocal microscope at 60x magnification. Three to eight images were taken per treatment. The scale bar is 50 µm. For 16 h VLX600 treatment, the xz- and yz-orthogonal views are shown for the merged picture. Figure partly adapted from Reisbeck et al. (2023).

In order to further evaluate the involvement of BNIP3 and BNIP3L in the VLX600-induced cell death and/or mitophagy, I performed siRNA experiments. For this, two different siRNAs against *BNIP3* and *BNIP3L* or the control siRNA were used in U-251 cells. The KDs were confirmed by immunoblot analysis after VLX600 treatment, showing a reduction in the protein levels of both proteins although the BNIP3 protein amount was reduced to a lesser extent (Figure 48A). Cell death induction was analysed in the siRNA treated U-251 cells after 5 µM VLX600 treatment for 48 h. VLX600 induced cell death in the siCon treated cells of about 60 % that remained unchanged in the siBNIP3 (B) and siBNIP3L (N) treated cells (Figure 48B), suggesting that the VLX600-induced cell death is not dependent on BNIP3 or BNIP3L (Reisbeck et al. 2023). Furthermore, I analysed if the VLX600-induced mitophagy is dependent on BNIP3 or BNIP3L. Therefore, U-251 cells treated with the siRNAs against *BNIP3* and *BNIP3L* were treated with 1 µM VLX600 and subsequently the protein levels of the mitochondrial marker proteins COX4I1, TOMM20 and VDAC1 were analysed via western blot (Figure 49). The immunoblot analysis revealed a reduction of all three proteins after VLX600 treatment in the

mock (lipofectamine control) and siCon treated cells, but not or to a lesser extent in the siBNIP3 and siBNIP3L treated cells (Reisbeck et al. 2023). This not only proofs the block in mitophagy after siRNA treatment, but also encourages the idea that BNIP3 and BNIP3L mediate the VLX600-induced mitophagy. In conclusion, my results suggest that the VLX600-induced cell death is not dependent on BNIP3 and BNIP3L hence mitophagy induction mediated by BNIP3 and BNIP3L has no discernible net effect on cell death.

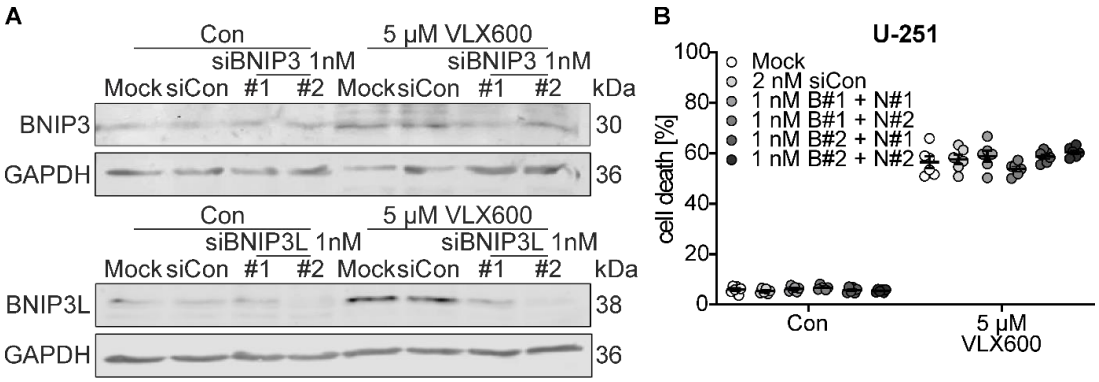

Figure 48. Analysis of VLX600-induced cell death after knockdown of the mitophagy receptors *BNIP3* and *BNIP3L*. U-251 GBM cells were treated with 1 nM of siRNAs against *BNIP3* (B) and *BNIP3L/NIX* (N) for 16 h with subsequent VLX600 treatment for 48 h. Mock served as the lipofectamine control and siCon as the siRNA control. DMSO was used as a vehicle control (Con). **A)** Knockdown after siRNA treatment was validated via immunoblot analysis. The experiment was repeated four times. **B)** Flow cytometric analysis of cell death (only annexin V-, only PI- and double-positive cells) after 5 µM VLX600 treatment for 48 h with prior siRNA-mediated knockdown of *BNIP3* (B) and *BNIP3L* (N). Data represent means ± SEM of two experiments with three replicates and 5,000 – 10,000 cells measured in each sample. Figure modified from Reisbeck et al. (2023).

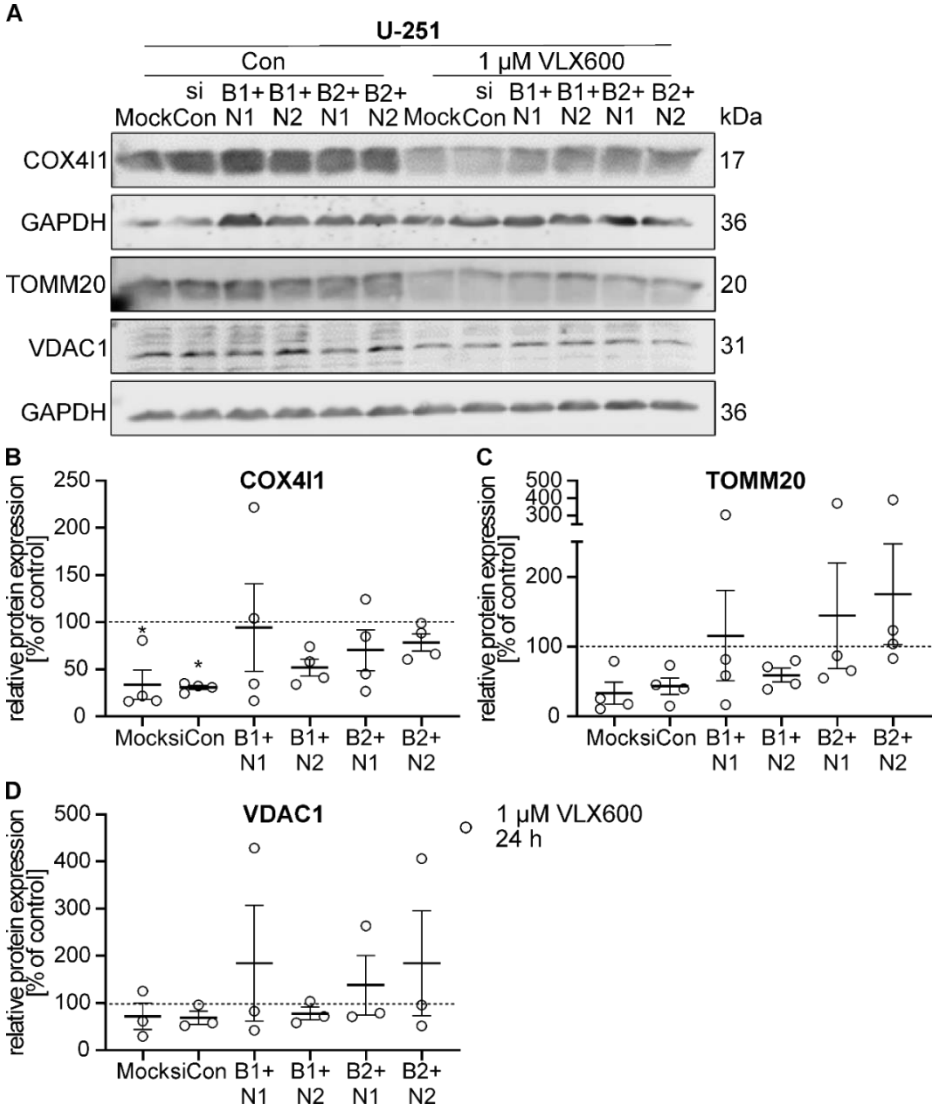

Figure 49. Analysis of mitochondrial marker proteins after knockdown of *BNIP3* and *BNIP3L*. U-251 GBM cells were treated with 1 nM of siRNAs against *BNIP3* (B) and *BNIP3L/NIX* (N) for 16 h followed by treatment with 1 µM VLX600 for 24 h. Mock is the lipofectamine control and siCon the siRNA control. DMSO served as a vehicle control (Con). **A)** Representative images of the immunoblot analysis of the mitochondrial marker proteins COX4I1, TOMM20 and VDAC1. The experiment was repeated at least three times. **B – C)** Quantification of the protein amounts of COX4I1 **(B)**, TOMM20 **(C)** and VDAC1 **(D)**. Data represent means ± SEM of at least three experiments. The dashed line indicates the DMSO treated condition that was normalized to 100 %. Statistical significances were measured with a 2way ANOVA. Asterisks indicate statistical significance to the Con. Figure partly adapted from Reisbeck et al. (2023).

5.8. Expression of the glucose proton symporter *SLC45A1* is not indicative for VLX600 sensitivity

During my studies Garofano et al. (2021) characterized four different GBM subtypes depending on their intrinsic biological states using transcriptomic analysis of individual GBM cells via single-cell RNA sequencing as well as of bulk tumors. This revealed metabolically different as well as developmental phenotypes that were used for an additional GBM classification including proliferative/progenitor, neuronal, mitochondrial and glycolytic/plurimetabolic phenotypes. The mitochondrial phenotype was in general associated

with a better clinical outcome and relied exclusively on OXPHOS for energy production, leading to an increased vulnerability against inhibitors of OXPHOS. Further, deletion of the glucose-proton symporter *SLC45A1* was shown to be significantly associated with the mitochondrial GBM phenotype. Since VLX600 is an OXPHOS inhibitor I wanted to analyse if the *SLC45A1* expression can predict VLX600 sensitivity. First, a subset of GBM cells, mostly GSCs, were investigated for their expression of *SLC45A1* followed by the analysis of their VLX600-sensitivity using the annexin V/PI staining. PCR analysis of their genomes revealed that almost all of the analysed GBM cells harbour the *SLC45A1* gene except for the GSC line GS-80 (Figure 50A). The GSC lines NCH669 and NCH705 were not included in further experiments because their growth was not sufficient and also the adherent cell lines were excluded. Quantification of the *SLC45A1* mRNA by qRT-PCR confirmed the loss of any *SLC45A1* mRNA expression in the GS-80 cell line and revealed strong differences in the *SLC45A1* mRNA expression throughout the different GSC lines (Figure 50B). This made it possible to define two groups: the no/low and high *SLC45A1* expressing GSC lines.

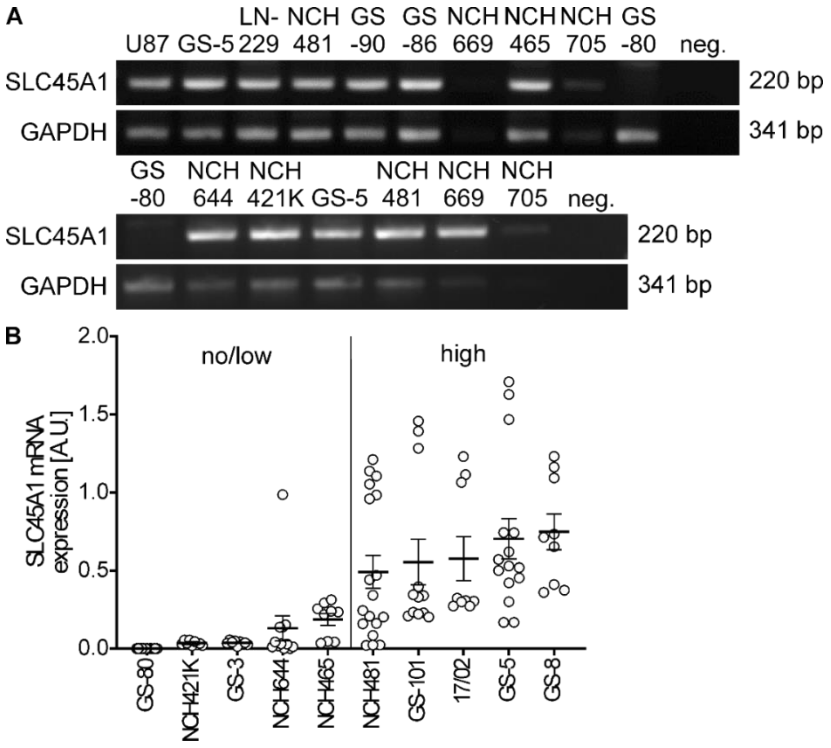

Figure 50. *SLC45A1* expression in a subset of glioblastoma cells. A) PCR analysis of different adherent and GS cell lines for their *SLC45A1* gene expression. The experiment was repeated one – two times. **B)** Quantitative analysis of the mRNA expression of *SLC45A1* in a subset of GSC lines using qRT-PCR. Data represent means ± SEM of at least three independent experiments with three replicates measured. The cut-off between the no/low and high group was set at 0.37.

Next, the GSC lines were treated with 1 and 2 µM VLX600 for 48 h (Figure 51, Figure 52A) and 72 h (Figure 52B) followed by cell death analysis as described before. Most of the GSC lines

responded highly sensitive to the VLX600 treatment resulting in cell death up to 80 % with 1 µM VLX600 treatment after 48 h for GS-101 and NCH421K cell lines (Figure 51). By summarizing all of the now/low or high *SLC45A1* expressing cell lines and calculating the fold change compared to the control treatment I observed that cell death was generally induced in a concentration dependent manner, which was slightly increased in the group of *SLC45A1* high expressing cell lines (Figure 52A, B). Correlation analysis showed a minor positive correlation between the *SLC45A1* mRNA expression and VLX600 sensitivity although not significantly (Figure 52C – F). In conclusion, the hypothesized vulnerability against OXPHOS inhibitors for *SLC45A1* low expressing cell lines was not confirmed and even a slightly higher sensitivity for *SLC45A1* high expressing cell lines was observed.

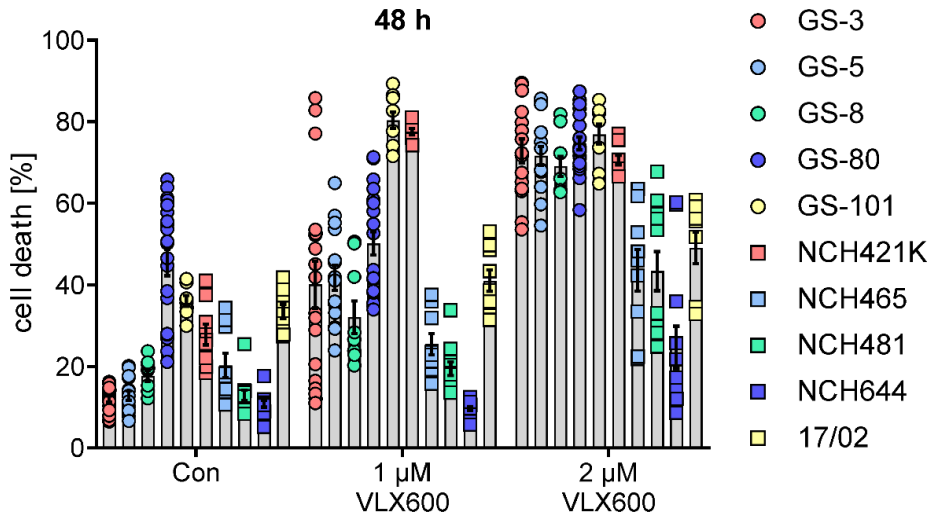

Figure 51. Glioblastoma stem-like cell lines were highly sensitive for VLX600-induced cell death. A large set of GSC lines was analysed after 48 h of 1 and 2 µM VLX600 treatment for cell death induction using the annexin V/PI staining and subsequent flow cytometric analysis. Displayed is the total cell death including only annexin V-, only PI- and double-positive cells. Data represent means ± SEM of at least three experiments with three replicates and 10,000 cells measured.

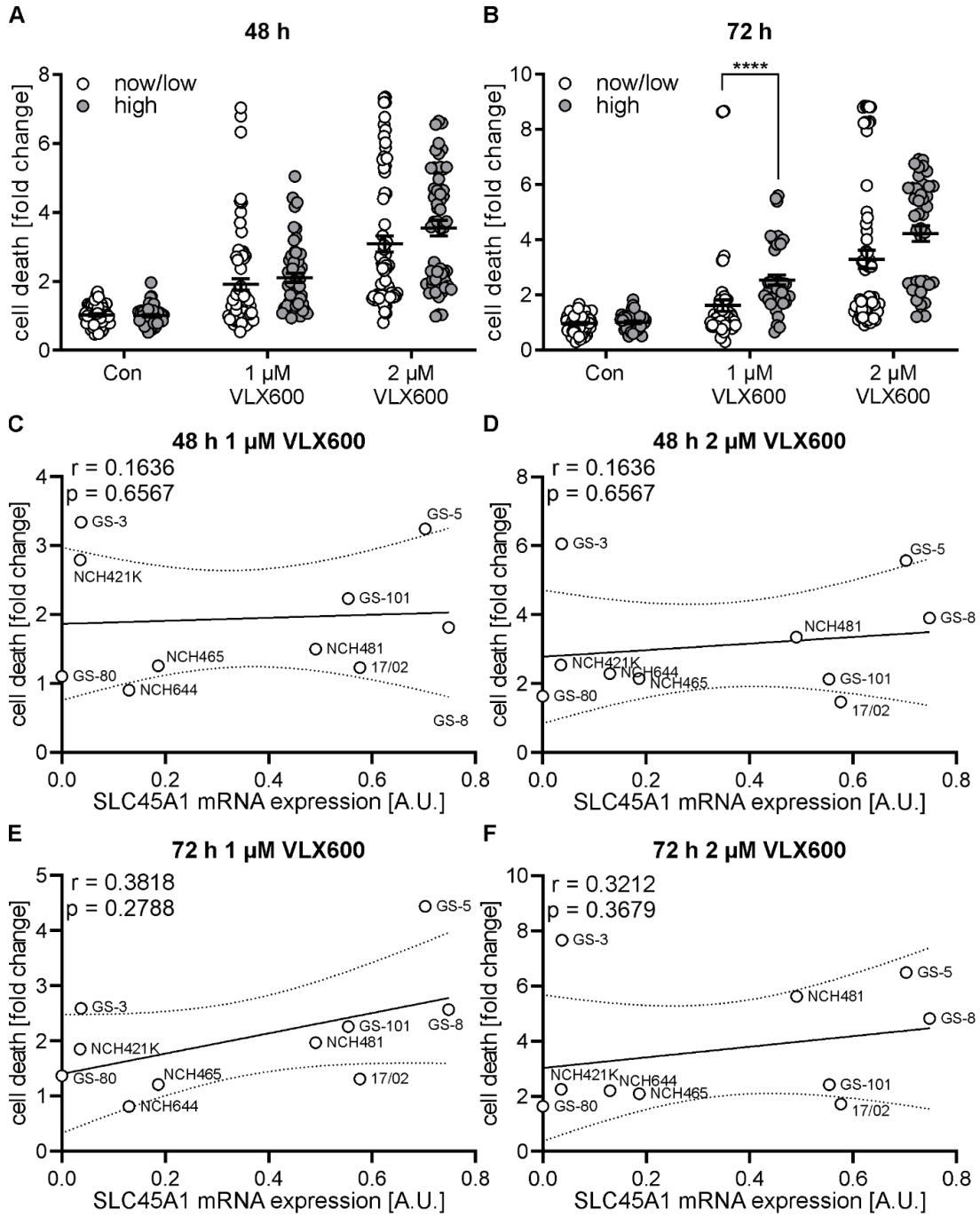

Figure 52. Correlation analysis of *SLC45A1* mRNA expression and VLX600 sensitivity. A subset of GSCs (also partly shown in Figure 51) were grouped into now/low or high expression of *SLC45A1* depending on the qRT-PCR data shown in Figure 50. Cell death was analysed after 1 and 2 µM VLX600 treatment for 48 h **(A)** and 72 h **(B)** using the annexin V/PI staining. **A, B)** Data represent means ± SEM of at least three independent experiments with three replicates and 10,000 cells measured in each sample. Statistical significance was measured with a Kruskal-Wallis test. **C – F)** Correlative analysis of the *SLC45A1* mRNA expression and the VLX600 induced cell death using Spearman correlation (r indicates the correlation coefficient; lines indicates linear regression line and the dashed lines indicate the 95 % confidence intervals).

5.9. VLX600 reduces tumor growth in an *ex vivo* brain transplantation model

In order to analyse VLX600 in a more translational setting, I used an *ex vivo* tumor growth model where mice brains were cut into 150 µm thick slices and tumor spheres consisting of GSCs (GS-5 GFP-Luc or NCH644^{GFP+}) were spotted on top. The brain slices with the tumor

spheres were cultured on special inserts in 6-well plates surrounded by special OTC culture medium and treatments were performed three times a week. First, I used the GSC line GS-5 that expresses GFP-Luc and treated the spheres for a total of nine days with 1, 5 and 10 µM VLX600 (Figure 53). The vehicle treated GS-5 tumor spheres showed only a slight increase in the tumor area after a total of nine days, however this fits to their growth behaviour *in vitro* (personal observation). In contrast, GS-5 tumor spheres treated with VLX600 showed already after a few days of treatment a reduced tumor area compared to the control (Figure 53B, C). At the end of the treatment period after nine days, all of the GS-5 tumor spheres treated with 10 µM VLX600 disappeared completely, suggesting the induction of tumor cell death by VLX600 treatment (Reisbeck et al. 2023).

For validation reasons and to include the autophagy aspect, the NCH644^{GFP+} non-target, *ATG5* and *ATG7* KD cells with stable expression of a GFP-plasmid were used in the *ex vivo* model, too. NCH644^{GFP+} cells were treated with 5 µM VLX600 for a total of 17 days (Figure 54, Figure 55). NCH644^{GFP+} non-target cells treated with DMSO showed a very strong tumor growth up to about 17,500 µm^2 after 17 days compared to about 5000 µm^2 at day 0, appropriate to their relatively fast proliferation *in vitro* (personal observation). More intriguingly, the treatment with VLX600 fully blocked the strong tumor growth of the NCH644^{GFP+} non-target cells, resulting in a complete inhibition of tumor area increase during the whole treatment period, suggesting a robust tumor growth inhibition induced by VLX600. In addition, the *ATG5* and *ATG7* KD cells were used in this experiment. The NCH644^{GFP+} *ATG5* KD cells showed a similar growth pattern in the vehicle treated group compared to the non-target cells (Figure 55A), but the NCH644^{GFP+} *ATG7* KD cells showed a reduced growth already at control treatment conditions (Figure 55B). When the autophagy-deficient tumor spheres were treated with VLX600 they also responded with a reduced tumor growth but to a lesser extend compared to the NCH644^{GFP+} non-target cells (Figure 55C). A strong difference was seen, for example, after 10 days of VLX600 treatment where the NCH644^{GFP+} non-target tumor spheres already showed a reduced tumor area of about 50 % and the *ATG5* and *ATG7* KD cells only of about 20 % and 10 %, respectively (Reisbeck et al. 2023). To exclude severe tissue damage of the brain sections through prolonged culturing or the treatment substances, a PI staining was performed in order to stain dead cells at the end of the experiment (Figure 56). This revealed only minor tissue damage especially at the cutting edges of the brain that most likely resulted from brain processing. Sometimes also the dead tumor cells after VLX600 treatment were

visible. In summary, VLX600 is able to not only inhibit tumor growth completely but also to induce tumor cell death *ex vivo*, underscoring the therapeutic potential for VLX600 in GBM treatment. Further, *ATG5* and *ATG7* KD tumor spheres were less affected by the VLX600 treatment, further supporting the autophagy-dependency of VLX600-induced cell death.

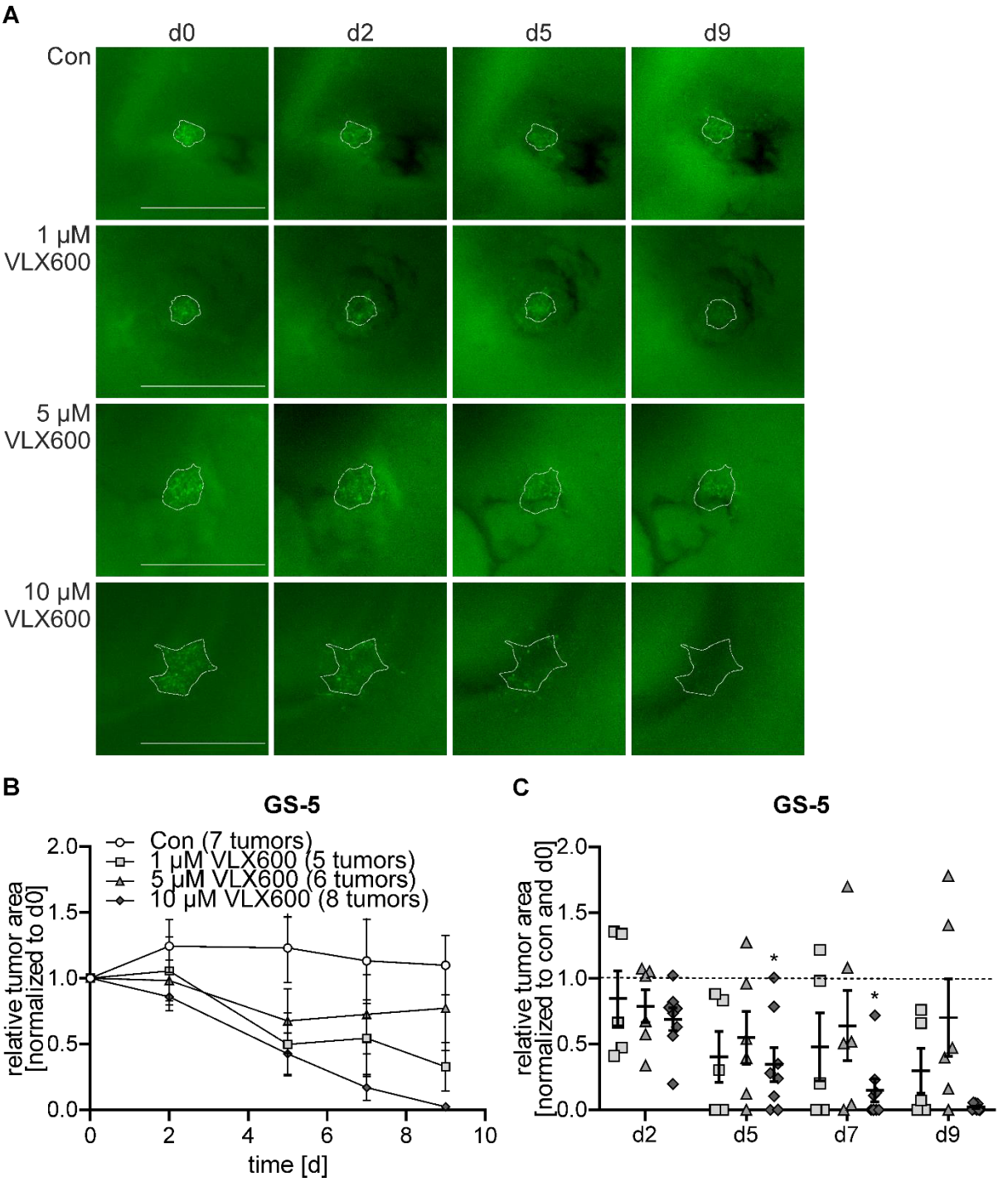

Figure 53. VLX600 reduces GS-5 tumor growth in an *ex vivo* brain transplantation model. GS-5 GFP-Luc cells were grown as spheres on organotypic brain slices and treated with 1, 5 and 10 µM VLX600 for a total of nine days. **A)** Representative images of the GS-5 tumor spheres at indicated days. DMSO served as a solvent control (Con). The dotted circles indicate the respective tumor at day 0. The scale bar is 1000 µm. The experiment was repeated three times with similar results **B, C)** Quantification of the tumor area normalized to d0 **(B)** or to the control treatment and d0 **(C)**. Data represent means ± SEM of five – eight tumors per treatment condition. **C)** The

dashed line indicates the DMSO control on all days as well as the d0 for all treatments that was normalized to one and statistical significances were measured with a one-way ANOVA (asterisks represent statistical significance compared to the respective control and day 0). Figure partly adapted from Reisbeck et al. (2023).

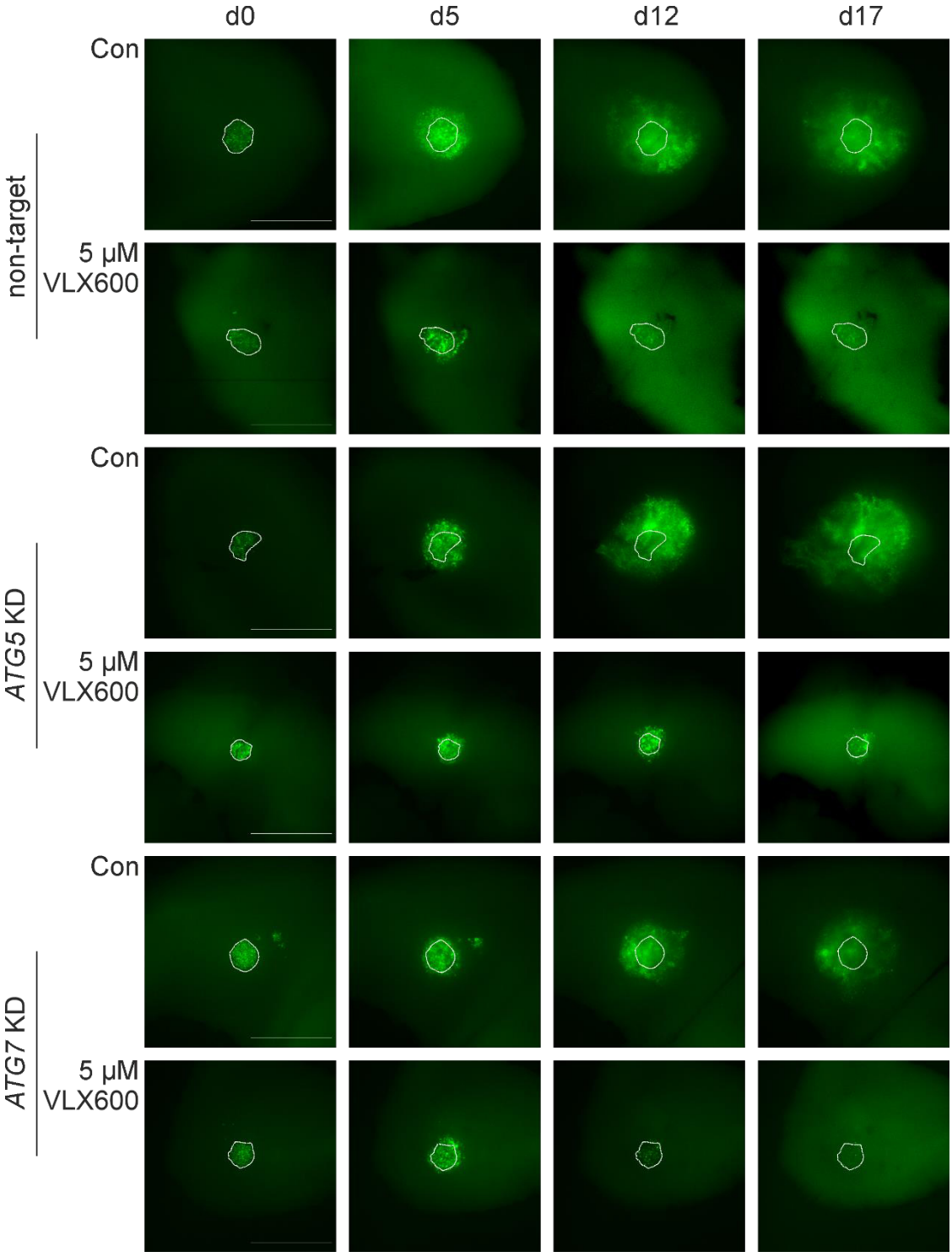

Figure 54. VLX600-induced growth restriction of NCH644 tumor spheres is partly dependent on *ATG5* and *ATG7*. NCH644^{GFP+} control (non-target), *ATG5* and *ATG7* KD cells were grown as spheres on organotypic mouse brain slices and treated with 5 µM VLX600 or the solvent control (Con) for a total of 17 days. Shown are representative images of 7 – 11 tumors per treatment. The dotted circles indicate the respective tumor on day 0. Figure partly adapted from Reisbeck et al. (2023).

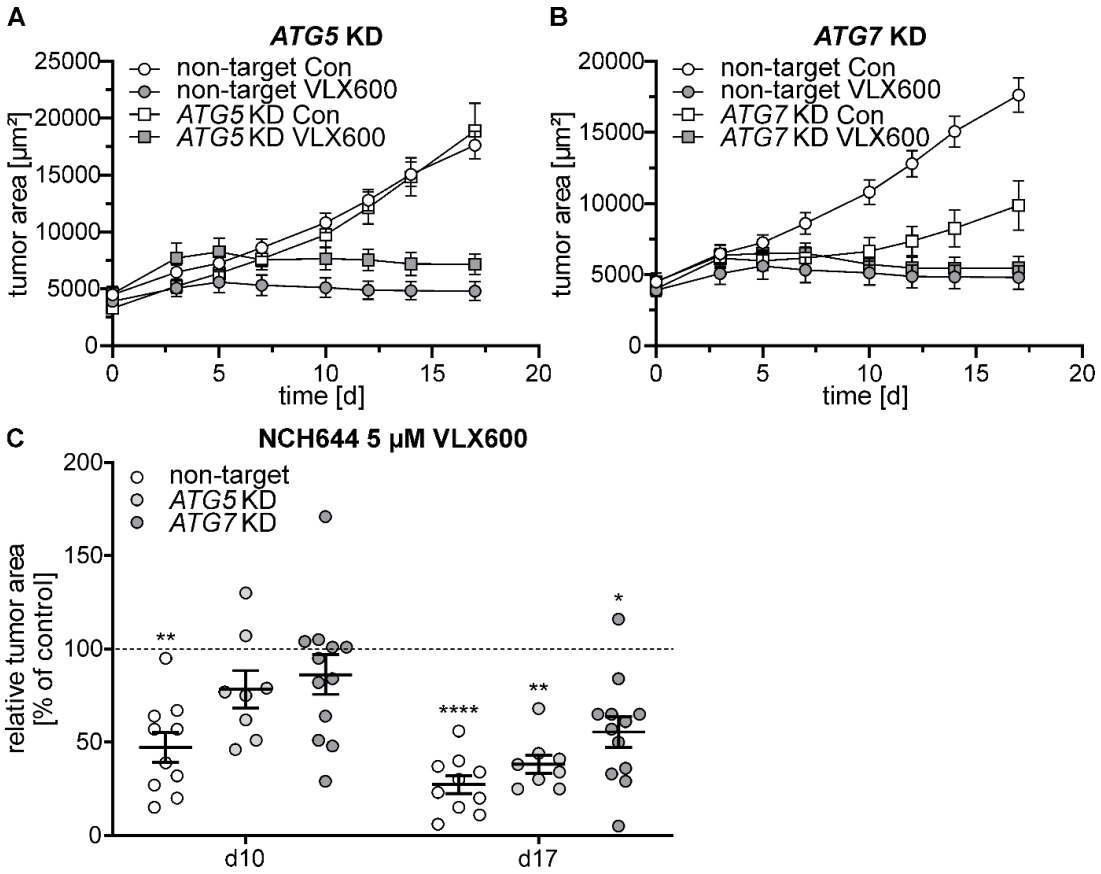

Figure 55. Analysis of the tumor area of NCH644 tumor spheres after VLX600 treatment. Quantification of the tumor area of NCH644^{GFP+} control (non-target), *ATG5* KD **(A)** and *ATG7* KD **(B)** cells after treatment with 5 µM VLX600 for a total of 17 days as seen in Figure 54. DMSO served as a solvent control (Con). The data of the NCH644 non-target cell line is the same in A and B. Data represent means ± SEM of 7 – 11 tumors. **C)** Additional representation for better comparison of the different cell lines for d10 and d17. The dashed line indicates the DMSO control treatment that was normalized to 100 %. Statistical significances were calculated with a 2way ANOVA. Asterisks indicate difference to Con. Modified from Reisbeck et al. (2023).

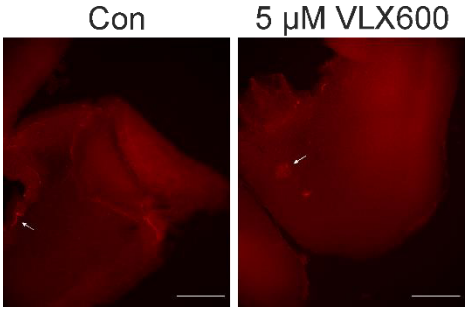

Figure 56. Tissue damage evaluation of the OTC brain sections using propidium iodide staining. Brain sections used in the OTC experiments were stained with PI at the end of the treatment period (day 17) of the NCH644 non-target tumor spheres to exclude severe tissue damage. Arrows indicate dead tumor cells or tissue damage and the scale bar is 1000 µM.

5.10. Extracellular addition of iron rescues VLX600-induced cell death and mitophagy

So far, I could show that VLX600 inhibits OXPHOS in GBM cells, possibly resulting in mitochondrial dysfunction and subsequent mitophagy including the involvement of the mitophagy receptors BNIP3 and BNIP3L, which finally culminates in ATG5/7-dependent cell death. However, knockdown of BNIP3 and BNIP3L was not able to rescue the VLX600-induced

cell death. Since VLX600 is also known to chelate iron I wanted to know if this may contribute to the induced cell death and/or mitophagy. Therefore, U-251 and NCH644 cells were treated with 1 or 2 µM VLX600, respectively, in combination with different amounts of $FeCl_2$ and $FeCl_3$ as indicated for 48 h (Figure 57). As expected, VLX600 induced cell death of about 50 % in the U-251 and about 70 % in the NCH644 cells, which was rescued by the addition of increasing amounts of $FeCl_2$ and $FeCl_3$. The combination of 2.5 or 3 µM $FeCl_2$ or $FeCl_3$ with VLX600 almost completely rescued the VLX600-induced cell death in the U-251 or NCH644 cells, respectively, suggesting that the iron chelation mediated by VLX600 is the key contributor to the VLX600-induced cell death (Reisbeck et al. 2023). To analyse if this is also the case for the VLX600-induced mitophagy, U-251 cells were treated with 1 µM VLX600 together with different concentrations of $FeCl_2$ and $FeCl_3$ for 24 h followed by immunoblot analysis of the mitophagy receptor BNIP3L and the mitochondrial marker proteins COX4I1, TOMM20 and VDAC1 (Figure 58). VLX600 alone significantly increased the BNIP3L protein level, which was rescued by the addition of 2 µM $FeCl_2$ or 1.5 and 2.5 µM FeCl3 (Figure 58A, B). The protein amount of COX4I1 was significantly reduced after VLX600 treatment as seen before and this was partially inhibited when 2 µM $FeCl_2$ or 1.5 and 2.5 µM $FeCl_3$ were added additionally (Figure 58C) (Reisbeck et al. 2023). The TOMM20 and VDAC1 protein amounts were only slightly and not significantly reduced after VLX600 treatment, but with the addition of 2 µM $FeCl_2$ or 2.5 µM $FeCl_3$ a minor rescue was seen for both proteins (Figure 58D, E). This suggests that mitophagy at least partly depends on iron depletion following VLX600 treatment. In summary, the iron-chelating ability of VLX600 seems to be important for VLX600-induced cell death as well as mitophagy.

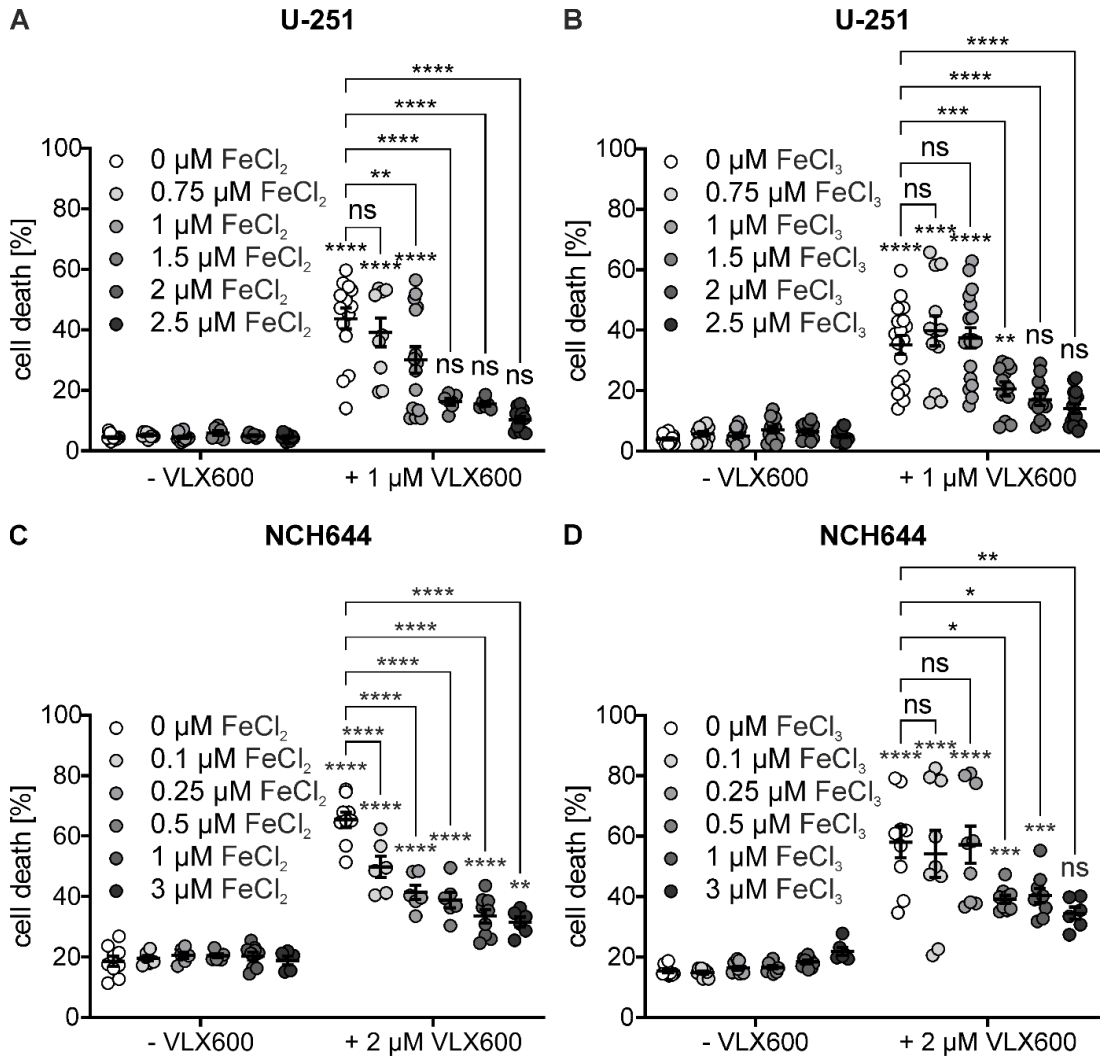

Figure 57. Extracellular addition of iron rescues the VLX600-induced cell death. U-251 **(A, B)** and NCH644 **(C, D)** GBM cells were treated with 1 or 2 µM VLX600 in combination with different concentrations of $FeCl_2$ **(A, C)** and $FeCl_3$ **(B, D)** as indicated for 48 h followed by flow cytometric analysis of cell death (only annexin V-, only PI- and double-positive cells). Data represent means ± SEM of two – six experiments with three replicates and 10,000 cells measured in each sample. Statistical significances were measured with a 2way ANOVA (asterisks indicate statistical significance compared to the $FeCl_2$ or $FeCl_3$ treatment without VLX600 or as indicated). Modified from Reisbeck et al. (2023).

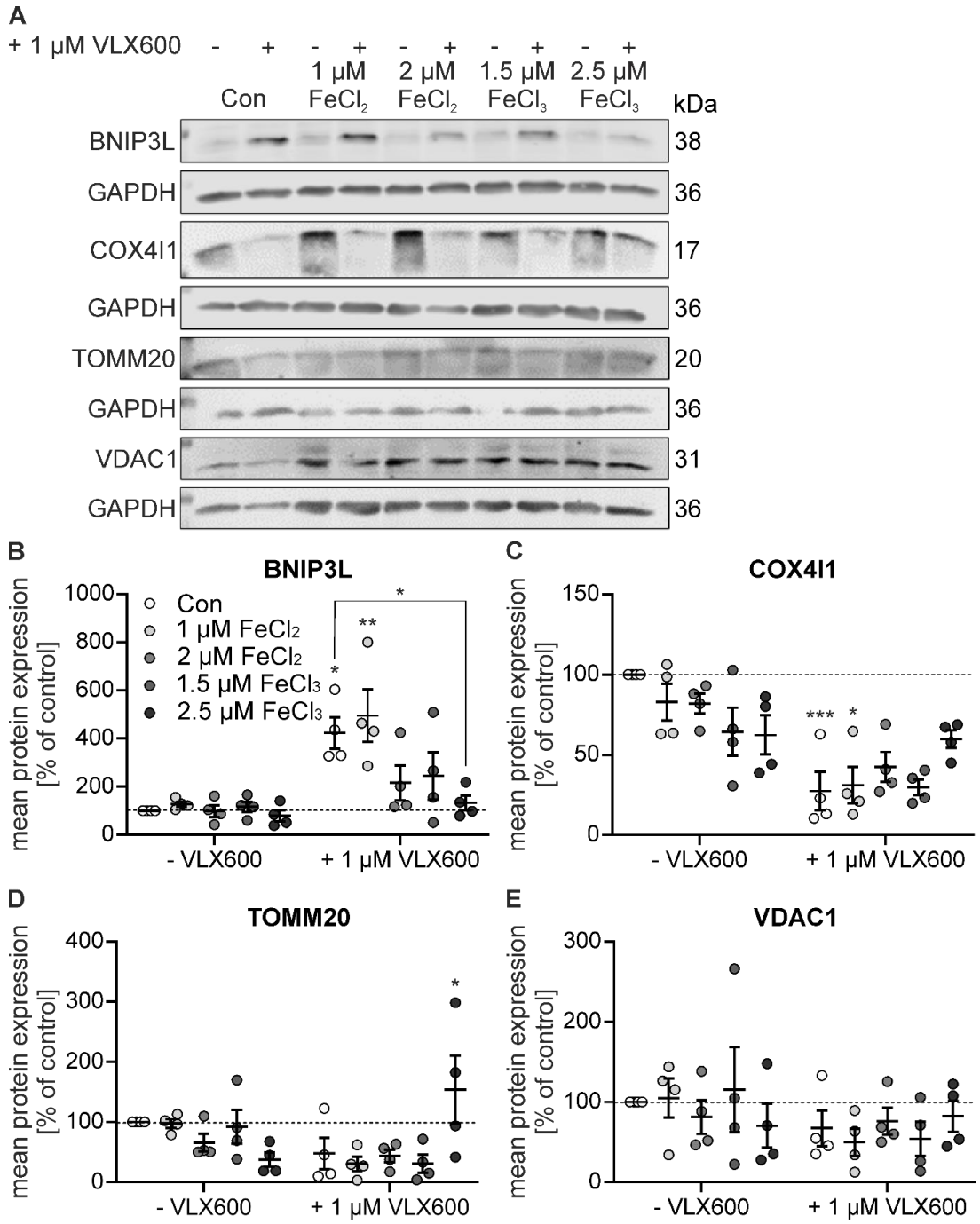

Figure 58. Extracellular addition of iron partially rescues the VLX600-induced mitophagy. U-251 GBM cells were treated with 1 µM VLX600 in combination with different amounts of $FeCl_2$ and $FeCl_3$ as indicated for 24 h. Subsequently, the protein amounts of the mitophagy receptor BNIP3L and the mitochondrial marker proteins COX4I1, TOMM20 and VDAC1 were analysed by western blot. **A)** Representative images of the immunoblot analysis. **B – E)** Quantification of the western blots shown in A. Data represent means ± SEM normalized to the control of four independent experiments (dashed line indicates the control that was normalized to 100 %). Statistical significances were measured with a 2way ANOVA and asterisks indicate significant difference to the respective treatment without VLX600 or as indicated. Partly adapted from Reisbeck et al. (2023).

5.11. Global proteomic analysis after VLX600 treatment revealed histone lysine methylation changes and the induction of ribosomal stress

In order to further clarify the underlying mechanisms of VLX600-induced cell death, a global proteomic analysis of U-251 wt, sgEGFP and *ATG5* KO cells after 24 h VLX600 treatment was performed (the proteomic analysis was performed by Dr. Georg Tascher (working group of Dr. Christian Münch, Institute of Biochemistry II, Goethe University Hospital Frankfurt/Main, Germany)). In total 6,757 proteins were quantified of which 1,262, 1,510 or 1,288 were significantly upregulated and 1,411, 1,475 or 1,398 significantly downregulated after VLX600 treatment in the U-251 wt, sgEGFP or *ATG5* KO cells, respectively (Figure 59) (Reisbeck et al. 2023). Proteins that were under the top 50 downregulated proteins (Table 33) in all three cell lines were for example CCNB1 (cyclin B1) that is important for cell cycle control and its knockdown was shown to trigger autophagy via AMPK-ULK1 (Xie et al. 2019) and FADS2 (Acyl-CoA 6-desaturase), which is a member of the fatty acid desaturase family and was shown to be upregulated in GBM tissue and GSCs compared to normal brain tissue. Further, *FADS2* KD inhibited cell proliferation and EGFR signaling (Affronti and Wellen 2019). The autophagy receptor SQSTM1 that is degraded during autophagy was under the top 50 downregulated proteins in the U-251 wt cells and also strongly reduced in the U-251 sgEGFP cells, but only slightly reduced in the U-251 *ATG5* KO cells after VLX600 treatment. Under the top 50 significantly upregulated proteins (Table 33) were BNIP3 that I already observed to be strongly increased in the immunoblot analysis (Figure 46), HK2 (hexokinase 2) that catalyses the first step of glycolysis and NDRG1 (N-myc downstream regulated 1) that is regulated via HIF1A (Salnikow et al. 2000) and is among other things described as a tumor suppressor (Kurdistani et al. 1998; Bandyopadhyay et al. 2003) (Figure 59). As a proof of concept, the NDRG1 protein level after VLX600 treatment in U-251 cells was analysed, revealing a time- and concentration-dependent increase of the NDRG1 protein level up to almost 5-fold after 24 h of 1 µM VLX600 treatment (Figure 60). Since NDRG1 was described as a tumor suppressor as well as to contribute to decreased cell proliferation, G1/S arrest and apoptosis (Fang et al. 2014) I wanted to know if it may also contribute to the VLX600-induced growth inhibition and/or cell death. Therefore, siRNA-mediated *NDRG1* KDs were generated using two different siRNAs, which resulted in a decrease of NDRG1 protein of 79 % when both siRNAs (50 nM) were combined (Figure 61). Further, the siRNA-mediated *NDRG1* KDs were treated with VLX600 and

cell death was subsequently measured (Figure 61). However, KD of *NDRG1* did not had any effect on the VLX600-induced cell death, suggesting no involvement of NDRG1 in this setting.

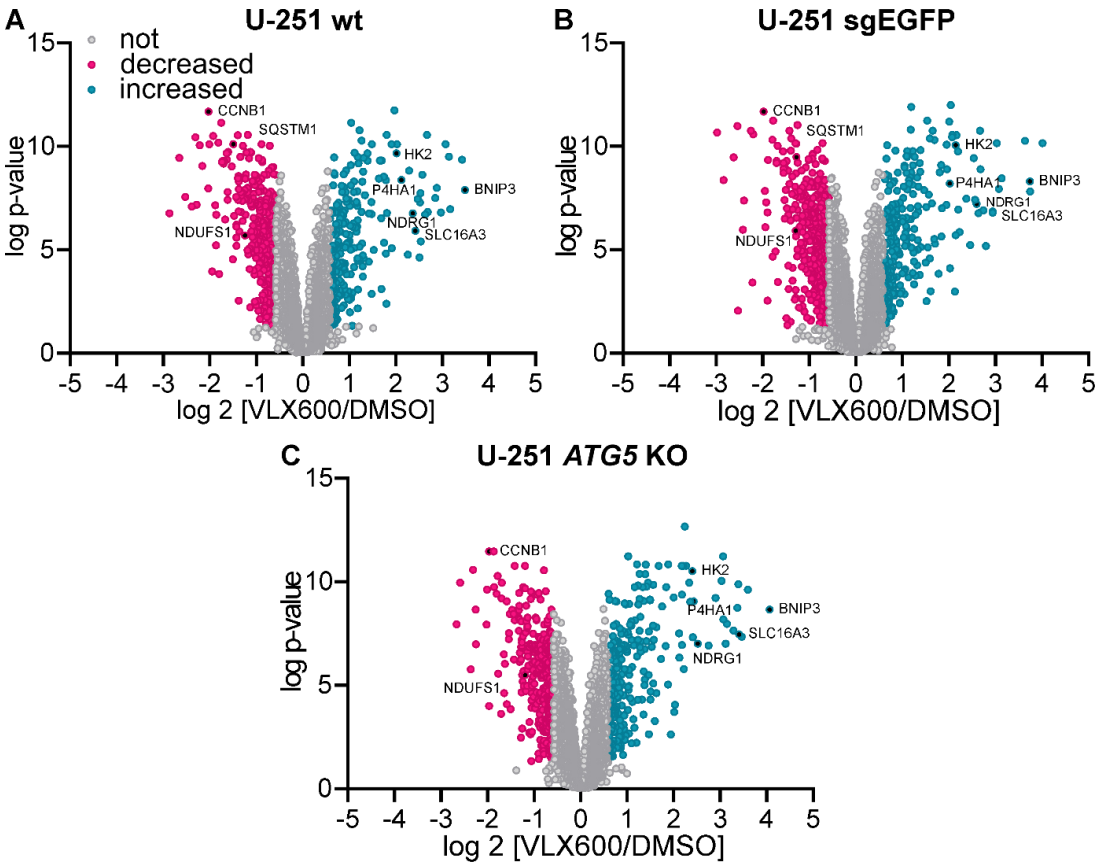

Figure 59. Global proteomic analysis after VLX600 treatment in U-251 cells. U-251 wt **(A)**, sgEGFP **(B)** and *ATG5* KO **(C)** cells were treated with 5 µM VL600 for 24 h followed by a whole proteome analysis. Volcano plots displaying the protein ratios (log2) of TMT-labelled proteome data as a function of the -log p-value. Experiments were performed in triplicates and a total of 6,757 proteins were quantified in all samples. Significantly down- or upregulated proteins with log p-value ≤ 0.05 and FC ≤ -0.58 or ≥ 0.58 are each depicted in purple or blue, respectively and proteins with no significant expression changes are shown in grey. This experiment was performed by Dr. Georg Tascher (working group of Dr. Christian Münch, Institute of Biochemistry II, Goethe University Hospital Frankfurt/Main, Germany). Partly adapted from Reisbeck et al. (2023).

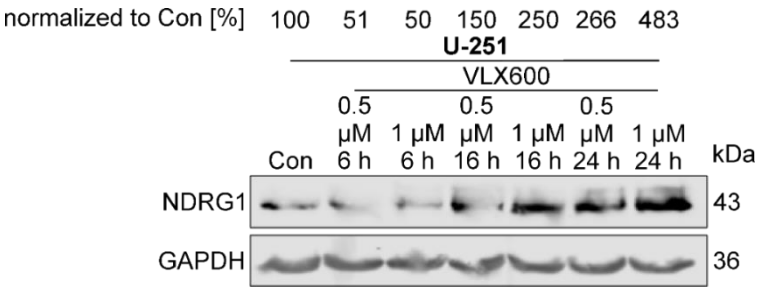

Figure 60. NDRG1 protein level after VLX600 treatment in U-251 cells. U-251 GBM cells were treated with different concentrations of VLX600 as indicated for 6 h, 16 h and 24 h followed by immunoblot analysis of NDRG1. DMSO served as a control (Con, 24 h) and the experiment was repeated two times with similar results.

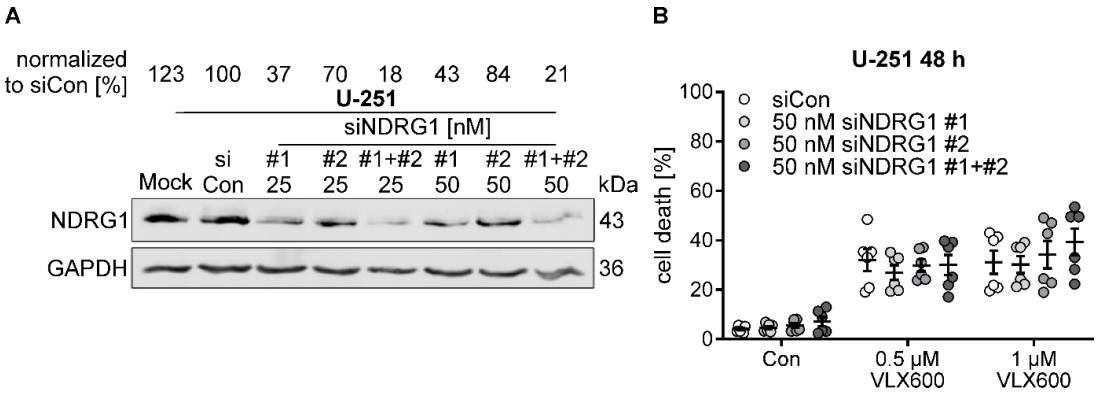

Figure 61. Cell death analysis of VLX600-treated U-251 cells after siRNA-mediated knockdown of *NDRG1*. **A)** U-251 cells were treated with 25 nM or 50 nM of two different siRNAs against *NDRG1* for 16 h followed by immunoblot analysis of NDRG1. Representative blot of three independent experiments with similar results. **B)** U-251 wt cells were treated for 16 h with two different siRNAs against *NDRG1* as indicated followed by treatment with 0.5 and 1 µM VLX600 for 48 h. Afterwards, cell death was measured by annexin V/PI staining and subsequent flow cytometry. Shown is the total cell death including annexin V only-, PI only- and double-positive cells. Data represent means ± SEM of two independent experiments with three replicates and 5,000 – 10,000 cells measured in each sample.

When comparing U-251 sgEGFP and *ATG5* KO cells either after solvent or VLX600 treatment (Figure 62) only 463 or 580 proteins were significantly regulated, respectively. Among them ATG5 was one of the most significantly downregulated proteins in the *ATG5* KO cells validating again the *ATG5* KO. Further, ATG16L1 that interacts with ATG12-ATG5 to mediate the conjugation of phosphatidylethanolamine (PE) to MAP1LC3 or RB1CC1 that is part of the ULK1/2 complex during autophagy were among the most significantly downregulated proteins in the *ATG5* KO cells compared to the sgEGFP cells. Among the most upregulated proteins were for example the autophagy receptor SQSTM1 and the Atg8 orthologous MAP1LC3B and GABARAPL2 (GABA type A receptor associated protein like 2).

All three cell lines investigated here showed similar patterns in the gene ontology (GO) term analysis after VLX600 treatment with only minor differences (Figure 63). Among the significantly downregulated GO terms was “oxidative phosphorylation”, supporting the OXPHOS inhibitory ability of VLX600. Further relevant downregulated processes were “cell cycle”, suggesting a block in cell proliferation, which fits to the reduced growth of cells during treatment and the complete growth inhibition of NCH644^{GFP+} tumor spheres (Figure 54 and Figure 55) and “ribosome biogenesis”, suggesting that VLX600 may somehow interfere with ribogenesis. In accordance to my previous results that VLX600 induces autophagy the GO term “autophagy” was significantly upregulated as well as “HIF-1 signaling pathway”, validating the observed increase in HIF1A protein level after VLX600 treatment (Figure 45). Further, the GO term “canonical glycolysis” was upregulated, suggesting a metabolic switch from OXPHOS to

glycolysis, which was however not observed in my previous experiments (Figure 32), but reported by Zhang et al. (2014) for colon carcinoma cells. In summary, the global proteomic analysis mostly underlines my previous results like the activation of HIF1A signaling or the OXPHOS inhibition (Reisbeck et al. 2023). Unexpectedly, no obvious major changes between the U-251 sgEGFP cells and the *ATG5* KO cells could be observed.

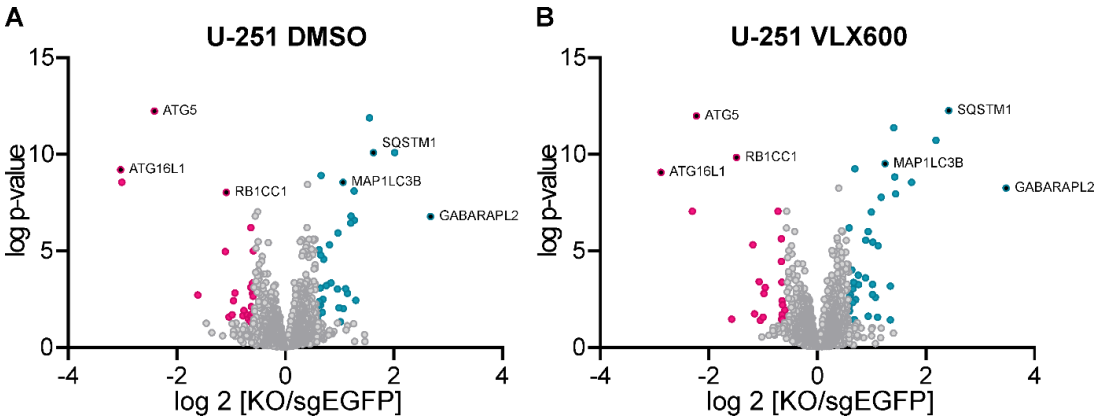

Figure 62. Global proteomic analysis after VLX600 treatment in U-251 cells. U-251 sgEGFP and *ATG5* KO cells were treated with 5 µM VL600 for 24 h followed by a whole proteome analysis. Volcano plots displaying the protein ratios (log2) of TMT-labelled proteome data as a function of the -log p-value. Comparison of DMSO- **(A)** or VLX600- **(B)** treated U-251 sgEGFP and *ATG5* KO cells. Experiments were performed in triplicates and a total of 6,757 proteins were quantified in all samples. Significantly down- or upregulated proteins with log p-value ≤ 0.05 and FC ≤ -0.58 or ≥ 0.58 are each depicted in purple or blue, respectively and proteins with no significant expression changes are shown in grey. This experiment was performed by Dr. Georg Tascher (working group of Dr. Christian Münch, Institute of Biochemistry II, Goethe University Hospital Frankfurt/Main, Germany).

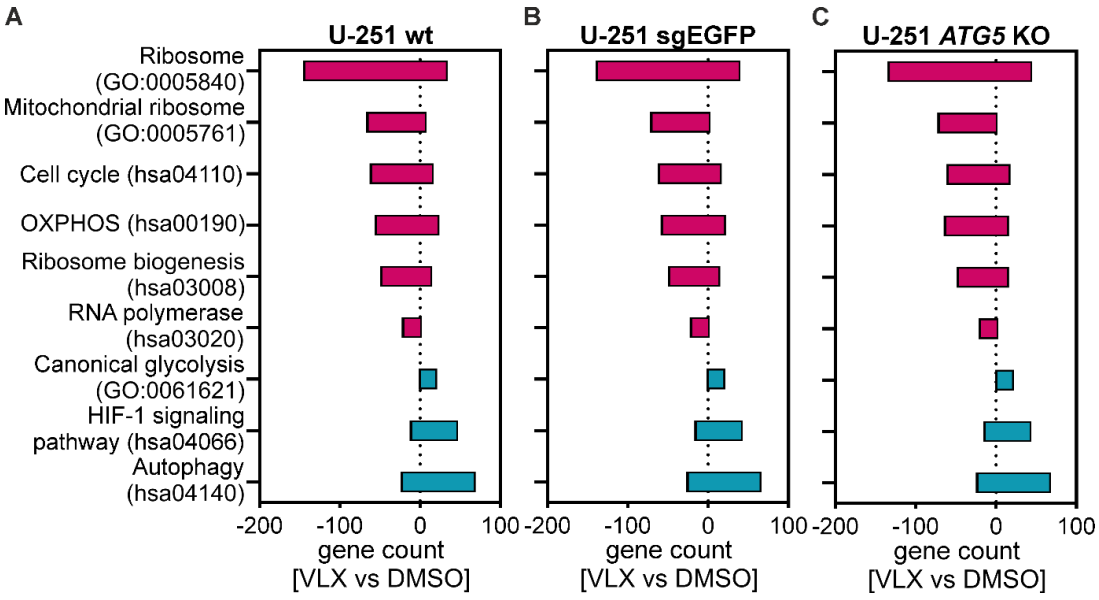

Figure 63. Bioinformatic analysis of the whole proteome analysis of U-251 glioblastoma cells treated with VLX600. Bioinformatic analysis of the global proteomic analysis of U-251 wt **(A)**, sgEGFP **(B)** and *ATG5* KO **(C)** cells, as shown in Figure 59 and Figure 62, using String (string-db.org; (Szklarczyk et al. 2019); version 11.5), revealed the significant reduction of the GO terms "ribosome" and "mitochondrial ribosome" as well as of the KEGG pathways "cell cycle", "oxidative phosphorylation (OXPHOS)", "ribosome biogenesis" and "RNA polymerase". Significantly increased was the GO term "canonical glycolysis" and the KEGG pathways "HIF-1 signaling" and "autophagy".

The upregulation of classical HIF1A gene markers, like SLC2A1 (GLUT1, solute carrier family 2 member 1) and HK2, were previously also associated with inhibition of the histone lysine demethylase KDM5A (lysine demethylase 5A), which harbours an iron-dependent Jumonji C (JmjC) domain. KDM5A specifically demethylates di- and tri-methyl groups from lysine 4 (K4) at histone 3 (H3) and was shown to be overexpressed in GBM promoting cell proliferation, self-renewal and drug resistance (Yang et al. 2021). Furthermore, previous reports also suggested a connection between iron chelation and histone modifications (Wang et al. 2013; Müller et al. 2020; Yang et al. 2021). Appropriate to this, the KDM5A protein level was significantly downregulated after VLX600 treatment in U-251 cells as well as KDM1A/B (lysine demethylase 1A/B) and JMJD1C (jumonji domain containing 1C) (Table 35). With the aim to further investigate possible histone methylation changes following VLX600 treatment, immunohistochemistry and immunoblot analysis of histone lysines methylation were performed (Figure 64). Immunohistochemistry revealed a continuous increase of tri-methylation of H3K9, H3K27 and H4K20 after VLX600 treatment with 300 scores of 247.5, 235 and 195 compared to the vehicle control with 300 scores of 140, 185 and 100, respectively (Figure 64A, B) (this experiment was performed by Dr. Katharina J. Weber (Neurological Institute (Edinger Institute), Goethe University Hospital, Frankfurt/Main, Germany)). Consistently, immunoblot analysis supported these findings since tri-methylation of H3K4 and H3K9 was increased after VLX600 treatment, while di-methylation of those histones was reduced (Figure 64C, D), underlining the notion that histone demethylases are inhibited by VLX600 (Reisbeck et al. 2023).

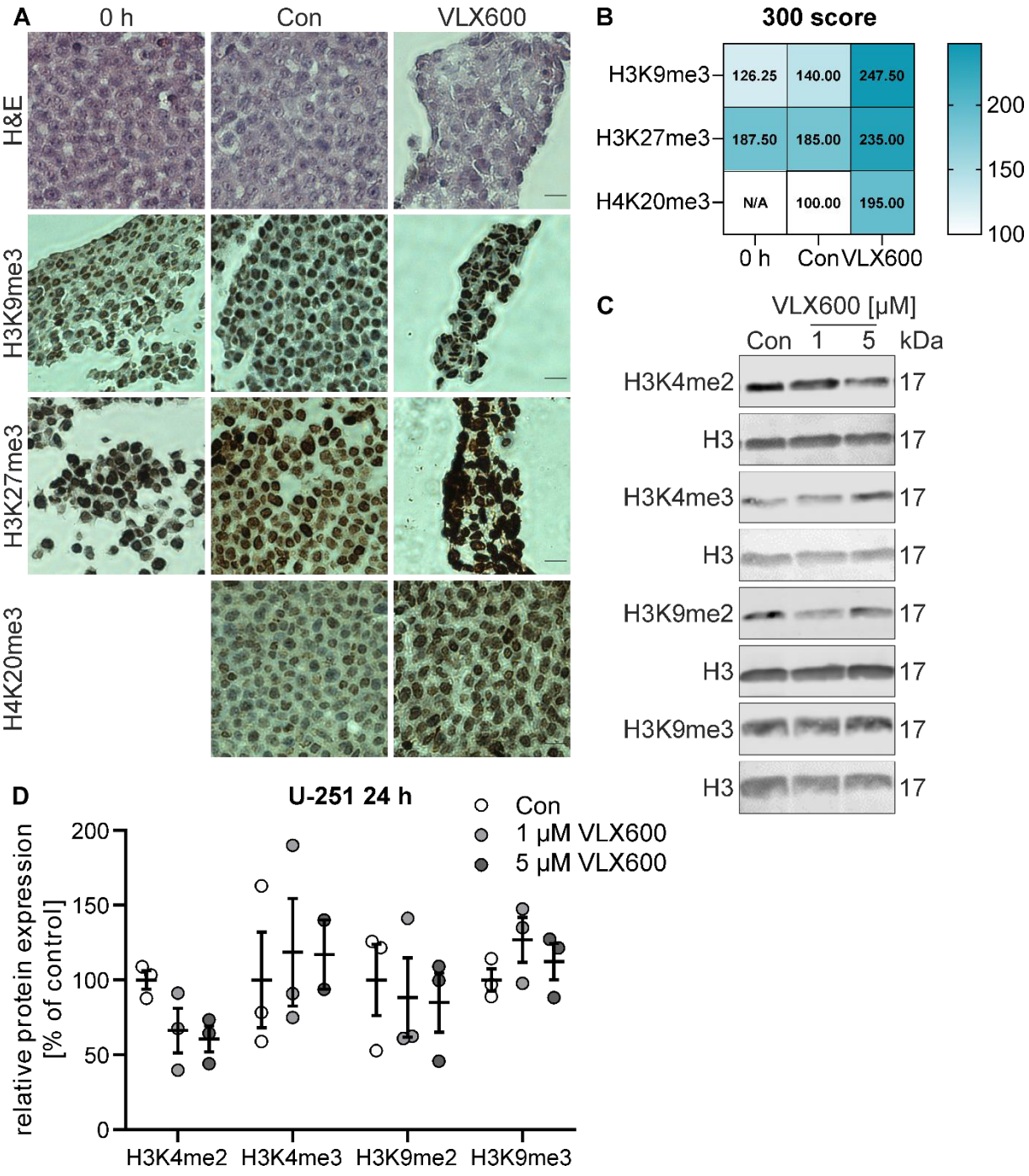

Figure 64. Immunohistochemistry and immunoblot analysis of histone H3 and H4 lysine methylation after VLX600 treatment in U-251 cells. A, B) U-251 cells were treated with 5 µM VLX600 or vehicle control for 24 h or left untreated followed by hematoxylin-eosin (H&E), H3K9me3, H3K27me3 and H4K20me3 staining. **A)** Representative pictures taken at 20x magnification (scale bar = 20 µM). The immunohistochemistry processing and staining was performed by Dr. Katharina J. Weber (Neurological Institute (Edinger Institute), Goethe University Hospital, Frankfurt/Main, Germany). **B)** Quantification of the antibody stainings shown in A using the 300 scoring. **C, D)** Western blot analysis of di- and tri-methylated lysine 4 and 9 at histone 3 after 1 and 5 µM VLX600 treatment for 24 h. **C)** Representative blots of three replicates. **D)** Quantification of the western blots seen in C of three independent experiments. Data represent means ± SEM. Adapted from Reisbeck et al. (2023).

Furthermore, among the significantly downregulated processes many were associated with ribosomes, like “mitochondrial ribosome” or “ribosome biogenesis”, linking VLX600 to the induction of ribosomal dysfunction. To further evaluate this idea, a NPM1 staining was

performed to analyse the induction of ribosomal stress. NPM1 is localized in the granular component of the nucleolus and the translocation of NPM1 to the nucleoplasm is a hallmark of nucleolar stress (Yung, Yang and Bor 1991). Actinomycin D (ActD) served as a positive control since it inhibits RNA-polymerase I and indeed after 24 h treatment resulted in a strong redistribution of NPM1. Similarly, treatment with VLX600 induced NPM1 translocation from the nucleolus to the nucleoplasm (Figure 65A). Calculation of the coefficient of variation as a value for the NPM1 redistribution (Sutton et al. 2019) revealed also a significant and slightly concentration-dependent NPM1 translocation after VLX600 treatment (Figure 65B) (Reisbeck et al. 2023).

In summary, I could show that VLX600 induces ADCD that is accompanied by major mitochondrial changes, which culminate in HIF1A-BNIP3-BNIP3L-mediated mitophagy. Further, my results suggest that the iron chelating ability plays a major role in the VLX600-induced cell death and histone lysine methylation changes as well as the induction of ribosomal stress. Of note, VLX600 is also effective in an *ex vivo* GBM model with limited toxicity in normal brain tissue, making it a promising compound for future therapeutic options.

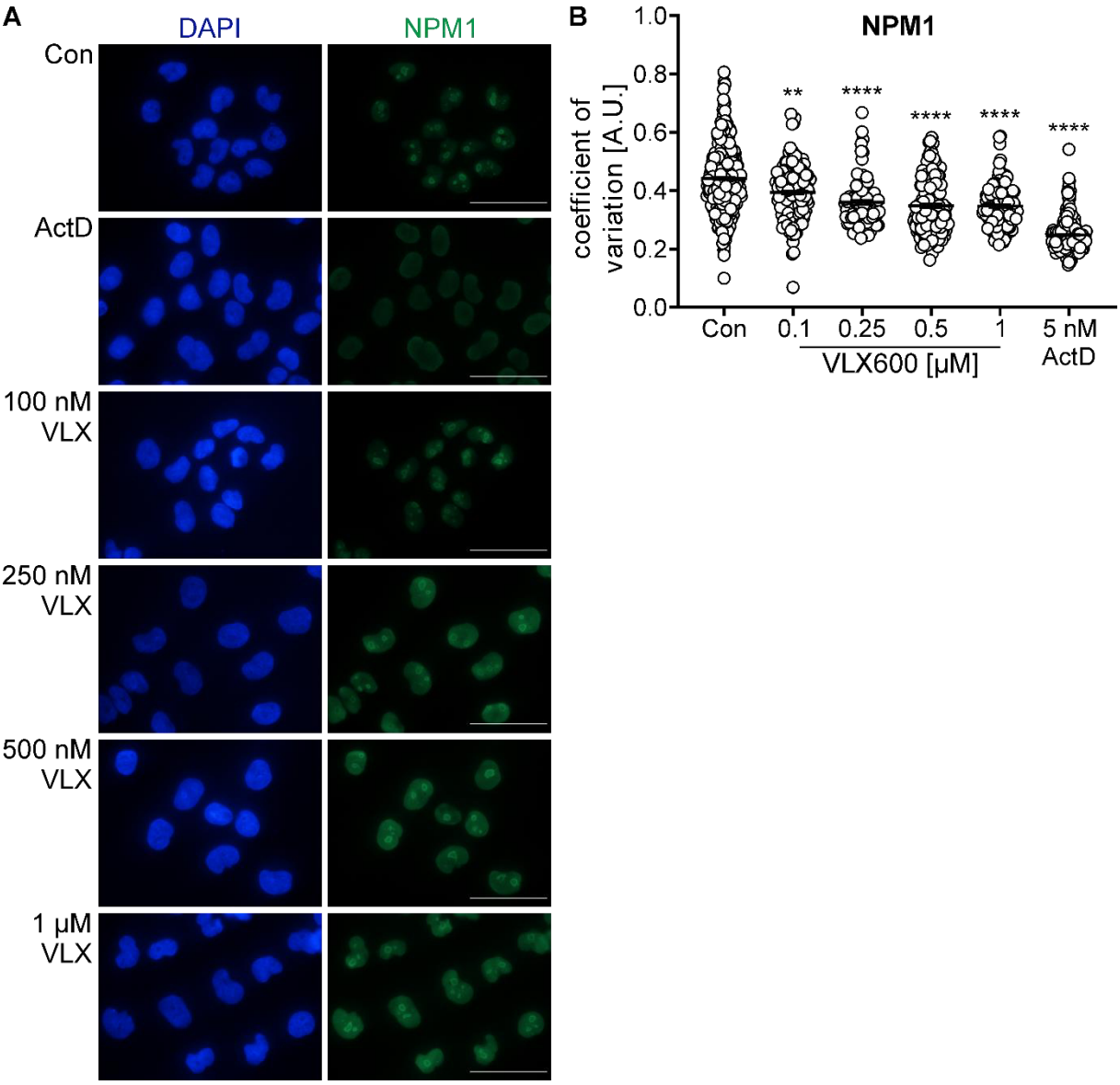

Figure 65. VLX600 induced nucleolar stress in U-251 glioblastoma cells. U-251 wt cells were treated with different concentrations of VLX600 as indicated, 5 nM actinomycin D (ActD) as positive control or DMSO as vehicle control (Con) for 24 h. Afterwards, cells were stained for the nucleolar protein NPM1 and DAPI to stain the nuclei. **A)** Representative pictures of two – four independent experiments and at least three images taken per treatment at 60x magnification. The scale bar is 50 µm. **B)** Quantification of the coefficient of variation indicating the translocation of NPM1 from the nucleolus into the nucleoplasm. Data represent means ± SEM of 61 – 345 cells analysed per treatment. Statistical significances were measured with a Kruskal-Wallis test and asterisks indicate difference to Con. Modified from Reisbeck et al. (2023).

6. Discussion

The importance of autophagy-dependent cell death (ADCD) for cancer therapy is highly acknowledged since it offers an alternative cell death pathway for apoptosis-resistant tumor entities like glioblastoma (GBM). ADCD is a form of programmed cell death that is characterized by increased autophagic flux and the involvement of the autophagic machinery that orchestrates cell demise. Thereby, the induction of ADCD in cancer cells using specific drugs was already shown by our and other studies (Kanzawa et al. 2005; Puissant et al. 2010; Shchors, Massaras and Hanahan 2015; Zielke et al. 2018; Meyer*, Henkel* et al. 2021; Reisbeck et al. 2023). For example, the combination of the tricyclic antidepressant imipramine (IM) and the anticoagulant ticlopidine (TIC) that inhibits the purinergic receptor $P2Y_{12}$ was shown to promote autophagy-associated cell death in glioma cells via the EPAC (RAPGEF3, Rap guanine nucleotide exchange factor 3) branch of the cAMP-signaling pathway (Shchors, Massaras and Hanahan 2015). Additionally, our group showed that AT 101, a natural compound from cotton seeds, induces lethal mitophagy via opening of the mitochondrial permeability transition pore, which results in mitochondrial membrane depolarization and BNIP3-BNIP3L-mediated mitophagy (Meyer et al. 2018). Of note, the induction of autophagy as well as of selective forms like lysophagy and mitophagy for tumor therapy needs to be carefully evaluated because both are frequently reported to have a dual role in cancer either promoting or suppressing tumor growth, which mostly depends on the tumor type as well as the tumor stage (Linder and Kögel 2019).

The first part of my thesis is a follow-up study on the piperidine derivative loperamide (LOP) that inhibits voltage-gated L-type calcium channels and the diphenylbutylpiperidine pimozide (PIMO) that targets the D2/D3 dopamine receptors and the HTR7/5-HT7 serotonin receptor, which were both shown to induce ADCD in GBM cells in a screen performed in our group (Zielke et al. 2018). Since the underlying mechanisms of ADCD were not fully elucidated in this publication I further analysed them using different GBM models and reporter assays.

In the second part, I focused on the iron chelator and oxidative phosphorylation (OXPHOS) inhibitor VLX600, which was reported to induce cell death in colon carcinoma cells accompanied by mitochondrial dysfunction. My aim was to investigate the cell death-inducing ability of VLX600 for GBM *in vitro* as well as *ex vivo* and to analyse the underlying mechanisms with a special emphasis on selective autophagy.

6.1. Pimozide and loperamide induce an autophagy-dependent type of cell death in glioblastoma cells

In connection to the previous work of Dr. Nina Meyer already published in her dissertation "*Molecular targeting of autophagy in glioblastoma"* (Meyer 2019) as well as in our joint publication (Meyer*, Henkel* et al. 2021) the concept of the PIMO- and LOP-induced ADCD in MZ-54 cells was further validated using additional cell models. This similarly revealed cell death induction by PIMO and LOP in the GBM cell line LN-229, which was significantly rescued by *ATG7* knockout (KO) as previously shown for MZ-54 cells (Meyer 2019; Meyer*, Henkel* et al. 2021). Further, I analysed autophagic flux using MZ-54 cells expressing the pMRX-IP-GFP-LC3-RFPΔG reporter that further underpinned the previous results (Meyer 2019; Meyer*, Henkel* et al. 2021), showing that PIMO and LOP induce autophagy and additionally confirms the induction of an ongoing autophagic flux (Galluzzi et al. 2018). As an additional and rigorous validation experiment, I performed re-expression of *ATG7* in MZ-54 *ATG7* KO3 cells, which consistently resulted in increased cell death after treatment. Therefore, PIMO and LOP induce ATG5- and ATG7-dependent autophagy with subsequent cell death. Interestingly, during my studies a report by Heckmann and Green (2019) described a non-canonical function for some autophagy proteins that are involved in LC3-associated phagocytosis (LAP). LAP uses parts of the autophagic machinery, like ATG5 and ATG7, to conjugate the family of MAP1LC3 proteins (MAP1LC3A, MAP1LC3B and MAP1LC3C) to phagosome membranes (Figure 66). LAP recognizes a variety of cargos including pathogens, dying cells, soluble ligands and protein aggregates and plays an important role for immune regulation and inflammatory responses (Heckmann and Green 2019). Obviously, this raised the question of the specificity of *ATG5* and *ATG7* KO cells in the context of ADCD since these KOs not only inhibit autophagy but could also block LAP. Therefore, I performed additional knockdown (KD) experiments to distinguish between those two pathways, revealing that only the KDs of the autophagy specific proteins *ATG14* and *RB1CC1* and not the KDs of the LAP-specific proteins *CYBB* and *RUBCN* were able to significantly rescue the PIMO- and LOP-induced cell death, underscoring the previous assumption that PIMO and LOP induce an autophagy-dependent type of cell death in GBM cells.

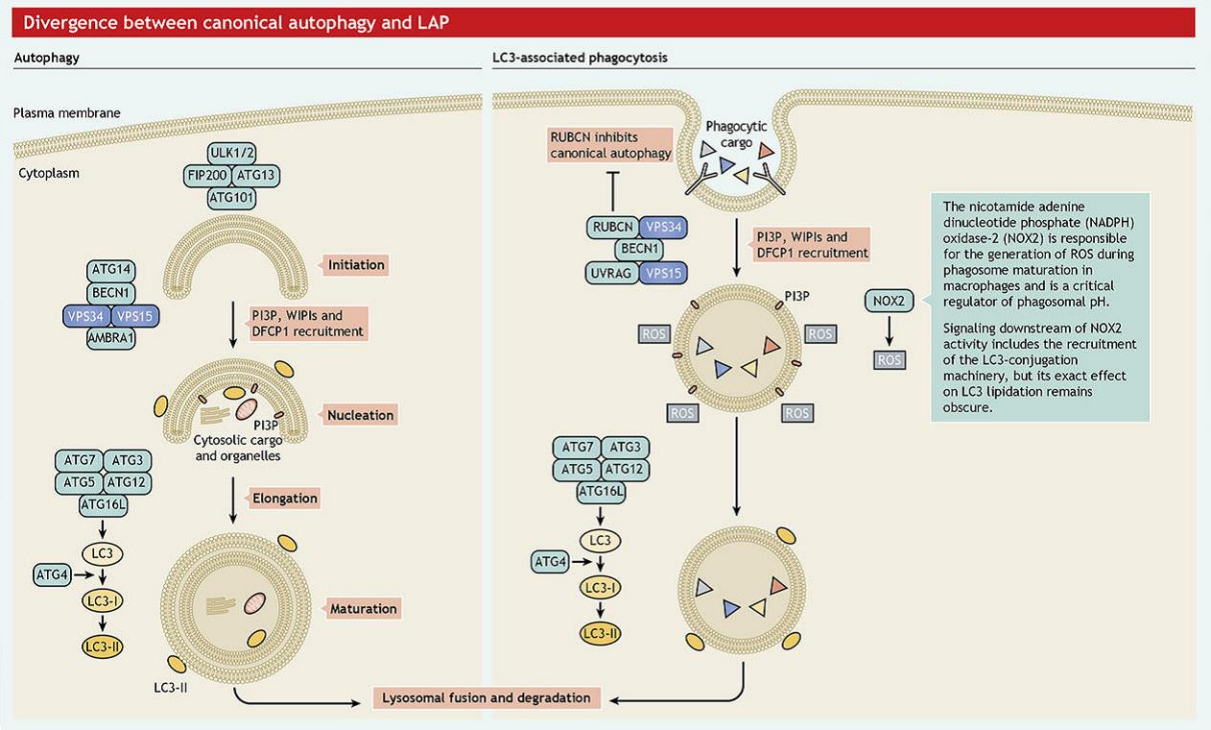

Figure 66. Autophagic pathway vs. LC3-associated phagocytosis. Autophagy (left side) starts with the initiation membrane or phagophore mediated by the ULK1 complex, followed by nucleation orchestrated by the PIK3C3 complex including ATG14, BECN1 and AMBRA1. Further elongation of the phagophore includes the two conjugation systems ATG5-ATG12-ATG16L and MAP1LC3 (LC3) that finally mediate the maturation of the double-membraned autophagosome containing the cargo. In contrast, LC3-associated phagocytosis (right side) starts with the phagocytic cargo, which stems from the exterior of the cells and the development of the phagosome cap with subsequent formation of the single-membrane phagosome. Similarly to autophagy, the next step is mediated by the PIK3C3 complex that however varies in certain components. Importantly, reactive oxygen species (ROS) are required at the phagosome membrane, which is produced by NOX2/CYBB. Finally, LC3 is, similarly to autophagy, ligated to the phagosome. Adapted from Heckmann and Green (2019).

6.2. Lipotoxicity and lysosomal membrane permeabilization synergize to induce autophagy-dependent lysosomal cell death

The previously performed proteomic analysis of MZ-54 cells after treatment with PIMO and LOP (Meyer 2019; Meyer*, Henkel* et al. 2021) revealed an unexpected upregulation of proteins involved in lipid and cholesterol metabolic processes like HMGCR (3-hydroxy-3-methylglutaryl coenzyme A reductase; the rate limiting enzyme in cholesterol biosynthesis) and LDLR (low-density lipoprotein receptor; cholesterol uptake) (Wiklund et al. 2010). Both are directly regulated by the transcription factor SREBP2 (sterol regulatory element binding protein 2), which regulates the gene expression of genes involved in cholesterol uptake and synthesis (Horton et al. 1998). Interestingly, SREBP2 was described to be highly activated during impaired lipid trafficking as a result of the decreased cytosolic cholesterol levels (Kristiana et al. 2010), suggesting a dysregulation of lipid homeostasis after PIMO and LOP treatment. Appropriate to this, I observed a massive accumulation of cholesterol in the

lysosomes of LN-229 cells after PIMO and LOP treatment, suggestive of impaired lipid trafficking. Of note, cancer cells are suggested to have a higher demand of cholesterol in order to meet their altered metabolic needs and to sustain their high proliferative capacity, which however may sensitize them for inhibitors of cholesterol biogenesis and trafficking (Wiklund et al. 2010; Kuzu et al. 2017). Especially the brain exhibits a distinct environment since cholesterol cannot be transported across the blood-brain barrier (BBB). While astrocytes are able to cover their cholesterol demands by *de novo* synthesis (Fagan et al. 1999), GBM cells rely on the exogenous uptake of cholesterol, suggesting that GBM cells may be particularly vulnerable for cholesterol shortage (Björkhem and Meaney 2004; Villa et al. 2016). PIMO as well as other antipsychotic agents were also shown by others to disturb cholesterol homeostasis and to upregulate the gene expression of key molecules involved in cholesterol metabolism (Wiklund et al. 2010). Moreover, decreased cytosolic cholesterol levels were associated with autophagy activation via mTOR, contributing to the induction of cell-lethal autophagy induced by PIMO and LOP (Xu et al. 2010).

Increased accumulation of lipids in the lysosomes is associated with increased oxidative stress, resulting in lipid peroxidation and finally lysosomal membrane permeabilization (LMP), disturbing prober lysosomal function (Serrano-Puebla and Boya 2016). Indeed, I could show that PIMO and LOP induce LMP in LN-229 cells ectopically expressing a pmCherry-Gal3 reporter plasmid. A disturbed lysosomal membrane function may further result in the release of lysosomal content e.g. lysosomal proteases (cathepsins) that may damage cytosolic contents, resulting in further cellular stress. Actually, it was previously shown that the cytosolic CTSB and CTSD levels were increased after PIMO and LOP treatment of MZ-54 cells as well as the cytosolic CTSB activity (Meyer 2019; Meyer*, Henkel* et al. 2021). Although cathepsins function only at an acidic pH some cathepsins like cathepsin B, D, and L remain active at a neutral pH (Serrano-Puebla and Boya 2016). In addition, it was previously shown that the inhibition of the cathepsin activity rescued the PIMO- and LOP-induced cell death, suggesting the induction of a lysosome-dependent cell death (LDCD) (Meyer 2019; Meyer*, Henkel* et al. 2021). Furthermore, I could show that the induction of LMP after PIMO and LOP treatment was absent in the autophagy-deficient cell lines and more interestingly was reversible after drug washout, suggesting the degradation of damaged lysosomes by lysophagy. Appropriate to this, it was previously shown that lysophagy in this context served as a pro-survival mechanism since siRNA-mediated KD of the lysophagy receptor VCP further

increased the drug-induced cell death in MZ-54 cells (Meyer 2019; Meyer*, Henkel* et al. 2021). In conclusion, PIMO and LOP induce detrimental “bulk” autophagy, paired with massive lysosomal damage resulting in mounting impairment of the lysosomal degradative function at later time points and causing the induction of an autophagy-dependent lysosomal cell death.

Interestingly, the induction of LMP as anti-tumor therapy was also suggested by others especially for apoptosis-resistant tumors (Groth-Pedersen and Jäättelä 2013). LMP was shown in particular to be induced by lysosomotropic agents, which can pass the lysosomal membrane because of their weakly basic properties. Inside the lysosomes they get protonated due to the acidic environment, which makes them non-diffusible, resulting in their lysosomal accumulation. After reaching a certain concentration threshold, those protonated forms can acquire detergent-like properties, inducing lethal lysosomal damage (Boya and Kroemer 2008). Of note, PIMO and LOP were reported to belong to this class of agents (Kornhuber et al. 2008; Kornhuber et al. 2011). The lysosomal accumulation of lysosomotropic agents was further reported to result in the detachment of SMPD1, an enzyme located at the lysosomal membrane, thereby inhibiting its activity. SMPD1 catalyzes the conversion of sphingomyelin to phosphorylcholine and ceramide and thereby inhibition results in the reduction of the *de novo* synthesis of ceramides, which could further contribute to lipid accumulation of sphingomyelin in the lysosomes. Therefore, this drugs are also termed functional inhibitors of acid sphingomyelinase (FIASMAs) (Kornhuber et al. 2008; Kornhuber et al. 2011). Indeed, SMPD1 activation was previously shown to be reduced by both compounds PIMO and LOP (Meyer 2019; Meyer*, Henkel* et al. 2021). Intriguingly, loss of function mutations in SMPD1 causes type A and B forms of the Niemann-Pick disease, a lysosomal storage disorder with inhibition of lysosomal cholesterol efflux (Kuzu et al. 2017), further underlining the idea of disturbed lipid trafficking out of the lysosomes induced by PIMO and LOP.

In summary, PIMO and LOP treatment results in disturbed lipid trafficking because of their lysosomotropic properties, resulting in the accumulation of lipids like cholesterol and sphingomyelin in the lysosomes. Lipid accumulation in the lysosomes further causes lipotoxicity, culminating in lysosomal damage and subsequent LMP that activates pro-survival lysophagy, which however cannot fully counteract the massive lysosomal damage and together with ongoing cell-lethal bulk autophagy result in an autophagy-dependent lysosomal cell death (Figure 67).

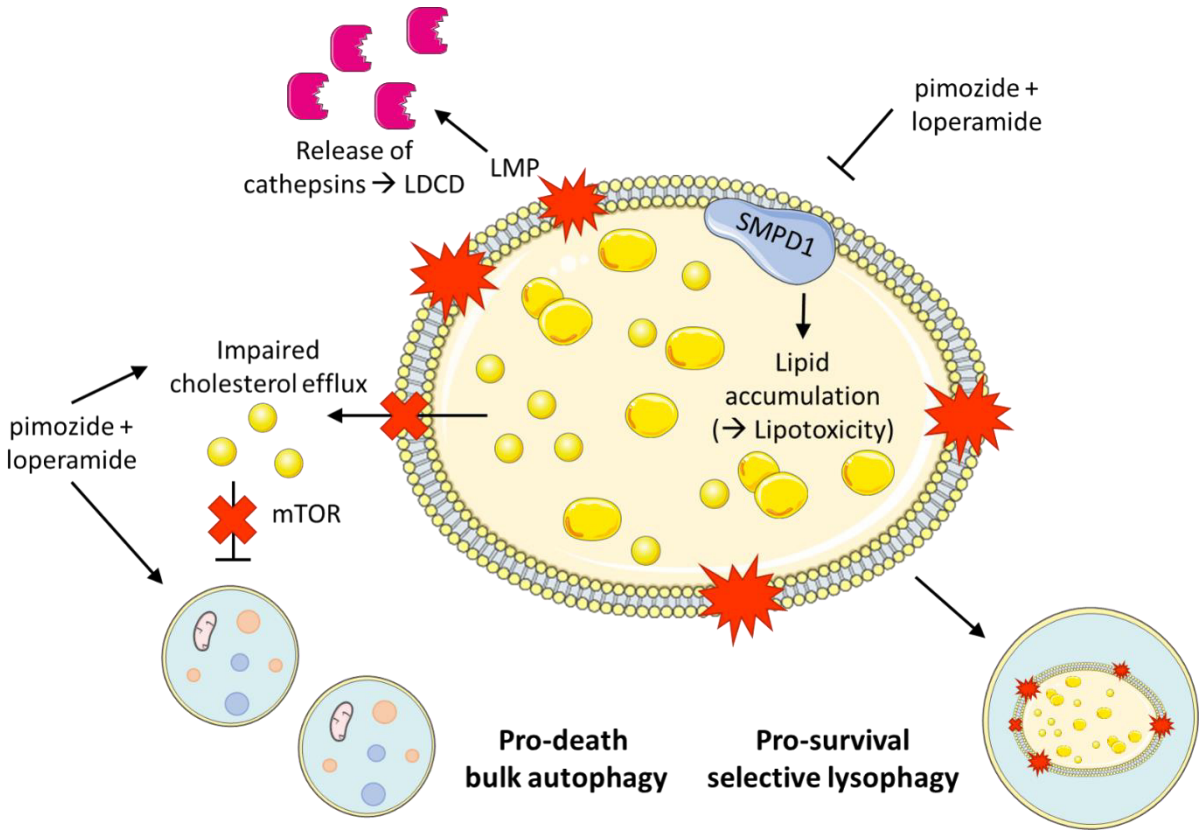

Figure 67. Proposed model of the pimozide- and loperamide-exerted effects in glioblastoma cells. My results together with the previous work from Dr. Nina Meyer (Meyer 2019; Meyer*, Henkel* et al. 2021) implicate that the induction of autophagy-dependent cell death by pimozide and loperamide is accompanied by impair lipid transport and the inhibition of SMPD1 function, resulting in lysosomal lipid accumulation and subsequent lipotoxicity as well as impaired cholesterol efflux out of the lysosomes. Lipotoxicity may further result in lysosomal membrane permeabilization (LMP) and the release of cathepsins, further disturbing the cellular integrity and resulting in lysosome-dependent cell death (LDCD). Reduced cytosolic cholesterol levels may further contribute to the induction of pro-death bulk autophagy induced by pimozide and loperamide. Pro-survival selective lysophagy is simultaneously activated in order to degrade the damaged lysosomes trying to ensure cellular survival. However, lysophagy cannot protect the cells from the excessive overactivation of autophagy and the massively damaged lysosomes, resulting in the induction of an autophagy-dependent lysosomal cell death. The Figure was partly generated using Servier Medical Art, provided by Servier, licensed under a Creative Commons Attribution 3.0 unported license (https://creativecommons.org/licenses/by/3.0/) and modified from Meyer (2019).

6.3. Translational significance of pimozide and loperamide for cancer therapy

In vitro models can only reflect the effectivity of a certain drug for cancer therapy to a limited extent because among other things the respective organ environment is absent. In order to imitate the specific brain environment, an *ex vivo* experiment was performed using mouse organotypic brain slices on which tumor spheres comprising of glioma stem-like cells (GSCs) were grown, treated and monitored. This revealed a huge tumor growth inhibitory ability of PIMO for NCH644 GSCs and also a tumor cell death-inducing ability for NCH421K tumor spheres. LOP is an antidiarrheal compound and the repurposing as an anticancer treatment for GBM is unfortunately hampered by the fact that LOP is not systemically bioavailable after

oral administration and does not cross the BBB. Nevertheless, there were attempts to use nanoparticles to improve LOP transport to the brain (Alyautdin et al. 1997) with the most pronounced effect using PVA (poly(vinyl alcohol))-stabilized PLGA (Poly(lactide-co-glycolide)) nanoparticles coated with poloxamer 188 (Gelperina et al. 2010). In contrast, the antipsychotic drug PIMO that antagonizes the dopamine receptor D2/D3 (DRD2/3) and the serotonin receptor HTR7 is indicated for neuropsychiatric disorders e.g. schizophrenia, paranoid personality disorder or the Tourette syndrome and has a highly traversing capability through the BBB (Elmaci and Altinoz 2018). Interestingly, HTR7 is commonly upregulated in GBM and the abnormal activation of HTR7 is associated with resistance to apoptosis and an increased proliferation through increased ERK1/2 (ERK1/MAPK3, mitogen-activated protein kinase 3; ERK2/MAPK1, mitogen-activated protein kinase 1) activation, IL6 (interleukin 6) synthesis and STAT3 (signal transducer and activator of transcription 3) activation (Kast 2010). Strikingly, it was previously shown that when using a HTR7 receptor agonist AS 19 this significantly inhibited the PIMO-induced cell death in MZ-54 cells (Meyer 2019; Meyer*, Henkel* et al. 2021), suggesting a contribution of the HTR7 receptor for the PIMO exerted effects. Similarly, also other HTR7 receptor antagonists like paliperidone and risperidone were shown to reduce GBM cell growth (Kast 2010; Liu et al. 2019; Liu et al. 2021). Furthermore, the anti-cancer effects exerted by those drugs were suggested to not only rely on their HTR7 inhibition, but also on their antagonistic effects against the DRD2 whose elevated expression (Li et al. 2014) as well as signaling, e.g. in patients with schizophrenia (Dalton et al. 2005; Lin et al. 2013), is associated with increased cancer risk (Liu et al. 2021). Appropriate to this, it was previously shown that the DRD2 antagonist DR4485 induced cell death in MZ-54 cells that was similarly like PIMO rescued by *ATG5* and *ATG7* KO (Meyer 2019; Meyer*, Henkel* et al. 2021). In summary, drug availability of LOP has to be further established for the brain since it's not able to pass the BBB by itself, but then it could be a promising treatment strategy for GBM. In contrast, the antipsychotic drug PIMO can pass the BBB effectively and most likely exerts its anti-cancer effects via HTR7 and DRD2 antagonism. The promising effects of dopamine receptor antagonists were already successfully shown, for example, in pancreatic cancer cells and orthotopic mouse models of pancreatic cancer (Jandaghi et al. 2016) or also in GBM models using oral administration of PIMO that had anti-tumor effects in *in vivo* experiments of intracranial implanted U-87 MG GBM cells (Ranjan, Kaushik and Srivastava 2020). Furthermore, the dopamine receptor antagonist ONC201 was shown to be well

tolerated in patients with refractory solid tumors (Stein et al. 2017). However, potential limitations of psychoactive compounds like PIMO are possible severe side-effects, e.g. arrhythmias, tardive dyskinesia and rarely but life-threatening the neuroleptic malignant syndrome (Zemrak and Kenna 2008; Elmaci and Altinoz 2018). Therefore, novel autophagy-inducing drugs with other modes of actions and limited side effects are searched. One promising compound is the iron chelator and OXPHOS inhibitor VLX600 that was already used in a phase I study for advanced solid tumors and was reasonably well tolerated by the patients (Mody et al. 2019). Thereto, in the second part of my thesis I focused on this drug and analysed the underlying mechanisms of the VLX600-induced cell death in GBM.

6.4. VLX600 triggers pro-death non-selective (bulk) autophagy in GBM cells

VLX600 was suggested to induce cell death in colon carcinoma cells (Zhang et al. 2014; Fryknäs et al. 2016), but the underlying mechanisms were not fully elucidated. In particular the therapeutic effects in GBM and the potential role of autophagy/mitophagy in drug action were largely unknown. VLX600 treatment of U-251 and NCH644 GBM cells induced cell death that was strongly rescued in *ATG5* and *ATG7* KO and KD cells, respectively. Additionally, autophagy was highly increased after VLX600 treatment as shown by increased autophagic flux, increased MAP1LC3B-I/II switch and increased amounts of proteins associated with autophagy as shown by global proteomic analysis. The effects of autophagy on tumor cell survival are known to be highly dependent on the extent and duration of autophagy as well as on the respective cellular context (Kögel, Fulda and Mittelbronn 2010; Fulda and Kögel 2015; Linder and Kögel 2019). Autophagy is robustly activated in tumor cells by several stressors, including starvation, hypoxia, growth factor deprivation, damaging stimuli and proteasome inhibition, trying to help the cells to survive (White 2012). In contrast, autophagy can be tumor suppressive through the elimination of oncogenic protein substrates and damaged organelles (White 2012) or the restriction of uncontrolled cell growth (Gozuacik and Kimchi 2004) and limitation of genomic instability (Nassour et al. 2019). In addition, there are several examples demonstrating that prolonged overactivation of autophagy can result in ADCD in GBM cells and GBM appears to be a tumor entity particularly prone to this type of cell death shown by our previous results (Meyer et al. 2018; Zielke et al. 2018; Meyer*, Henkel* et al. 2021; Reisbeck et al. 2023) as well as by others (Kanzawa et al. 2005; Puissant et al. 2010; Shchors, Massaras and Hanahan 2015). Since the VLX600-induced cell death was rescued by genetic KO and KD of autophagic pathway components (*ATG5*/*ATG7*), occurs independent of apoptosis

and autophagic flux was increased (Shen and Codogno 2011) I propose that VLX600 induces ADCD in the GBM cell lines U-251 and NCH644.

Still it has to be noted that the VLX600-induced cell death was not completely blocked in the autophagy-deficient cell lines, suggesting the possible simultaneous activation of other cell death modalities. Other forms of regulated cell death (RCD) include mitochondrial permeability transition-driven necrosis, resulting from severe oxidative stress and cytosolic Ca^{2+} overload, which depends on peptidylprolyl isomerase F (PPIF, CYPD) and the opening of the mitochondrial permeability transition pore (Izzo et al. 2016). However, proteomic analysis did not revealed any significant changes of proteins associated with mitochondrial permeability transition-driven necrosis like EPAC (RAPGEF3, Rap guanine nucleotide exchange factor 3) (Fazal et al. 2017) or pro- and anti-apoptotic BCL2 family members such as BAX, BAK1, and BID (Marzo et al. 1998; Zamzami et al. 2000; Karch et al. 2013) as well as BCL2 and BCL-x_L (BCL2L1, BCL2 like 1) (Shimizu, Narita and Tsujimoto 1999; Vander Heiden et al. 2001). Necroptosis is also classified as RCD that is independent of caspases and mediated by specific death receptors including FAS (Fas cell surface death receptor) and TNFR1 (TNFRSF1A, TNF receptor superfamily member 1A) (Holler et al. 2000; Degterev et al. 2005) as well as pathogen recognition receptors including TLR3 (toll like receptor 3), TLR4 (toll like receptor 4), and ZBP1 (Z-DNA binding protein 1) (Upton, Kaiser and Mocarski 2012; Kaiser et al. 2013). Further, necroptosis activation depends on the activation of RIPK3 (receptor interacting serine/threonine kinase 3) and MLKL (mixed lineage kinase domain like pseudokinase) (Murphy et al. 2013; Linkermann and Green 2014), which were also not detectable in the proteome analysis. Ferroptosis is a form of RCD initiated by oxidative perturbations of the intracellular microenvironment, depends on intracellular iron levels and can be inhibited by iron chelators (Dixon et al. 2012). Therefore, this form of cell death is unlikely since VLX600 is an iron chelator. Conclusively, this further underlines the notion that VLX600 induces cell-lethal bulk autophagy since no sign of activation of other RCDs was observed during my studies, which however might be investigated further using specific inhibitors and/or further KD/KO models.

6.5. Iron chelation by VLX600 mediates mitophagy via the HIF1A-BNIP3-BNIP3L axis and contributes to cell death

Furthermore, Zhang et al. (2014) reported the induction of mitochondrial dysfunction by VLX600 in colon carcinoma cells. Appropriate to this, VLX600 treatment resulted in mitochondrial dysfunction in GBM cells, too, associated with mitochondrial membrane depolarization, the decrease of mitochondrial proteins, as well as disturbance of the mitochondrial network. The TMRM staining revealed a significant reduction of the mitochondrial membrane potentials after VLX600 treatment, followed by the reduction of the mitochondrial proteins COX4I1, TOMM20, VDAC1 and HSPD1 indicative of ongoing mitophagy. COX4I1 is a subunit of complex IV of the electron transport chain (ETC) sitting in the inner mitochondrial membrane (IMM), while TOMM20 is located at the outer mitochondrial membrane (OMM) and regulates protein import into the mitochondria (Baker et al. 2007). VDAC1 facilitates the exchange of metabolites and ions across the OMM and therefore is located there, but VDAC1 can as well form channels in the plasma membrane (Benz 1994; Báthori et al. 2000; Pinto et al. 2010). HSPD1 belongs to the chaperonin family, is located in mitochondria and is essential for the folding and assembly of newly imported proteins into the mitochondria. In addition, HSPD1 is also associated with the mitochondrial unfolded protein response (UPRmt) in order to properly fold damaged proteins (O'Malley et al. 2020). Appropriate to this, the reduction of COX4I1 and TOMM20 proteins was the greatest compared with only a minor decrease in VDAC1 protein likely because VDAC1 is also present at the plasma membrane that is not affected by increased mitophagy.

Damaged mitochondria may be rescued by mitochondrial fission and fusion or the UPRmt, but if the damage is too severe mitochondria may be degraded by mitophagy (Ni, Williams and Ding 2015). The induction of mitophagy after VLX600-induced mitochondrial dysfunction was supported by the mt-mKeima as well as the mtphagy dye assay. Both assays rely on the change of the emission wavelength dependent on the pH that makes it possible to monitor ongoing mitophagy. After VLX600 treatment, both experiments revealed the induction of ongoing mitophagy, which was partly rescued in the autophagy-deficient cell lines, suggesting the induction of ATG5-/7-dependent mitophagy. Mitophagy is exerted via mitophagy receptors that facilitate the transport of the cargo to the MAP1LC3-II-decorated autophagosomes mostly via their LC3-interacting region (LIR)-motifs. The best studied mitophagy pathway consists of the PINK1 kinase and the ubiquitin ligase Parkin that ubiquitylates mitochondrial

proteins after induction of mitochondrial stress, resulting in the translocation of several mitophagy receptors (Vara-Perez, Felipe-Abrio and Agostinis 2019). However, Parkin expression is mostly lost in GBM, indicating only a minor or no role of this pathway for GBM cells (Veeriah et al. 2010). Therefore, I investigated the protein amounts of the mitophagy receptors BNIP3 and BNIP3L, which were reported to be activated during hypoxia and regulated via HIF1A (Rodger, McWilliams and Ganley 2018). Indeed, both proteins were highly increased after VLX600 treatment especially at mitochondria and homodimerization was observed in the western blot analysis, which was reported to be crucial for BNIP3- and BNIP3L-dependent activation of mitophagy (Sulistijo and MacKenzie 2006; Marinković, Šprung and Novak 2021). Additionally, siRNA-mediated KD of both genes resulted in a block in mitophagy, further supporting the idea that VLX600 induces BNIP3- and BNIP3L-dependent mitophagy. In contrast, treatment with siRNAs against *BNIP3* and *BNIP3L* had no discernible net effect on VLX600-triggered cell death, indicating the lack of a major pro-survival or pro-death function of mitophagy in the response of GBM cells to this drug (Meyer et al. 2018), further suggesting that VLX600 triggers pro-death non-selective (bulk) autophagy in GBM cells.

Interestingly, BNIP3 and BNIP3L were previously reported to be indispensable for iron chelation-mediated pexophagy (autophagic degradation of peroxisomes) in human-derived retinal pigment epithelial cells and to localize at peroxisomes after treatment with the iron chelator deferiprone (DFP). Thereby, *HIF1A* KO revealed that similar to mitophagy, BNIP3 and BNIP3L-mediated pexophagy can be regulated via hypoxia and/or HIF1A (Wilhelm et al. 2022). While the peroxisomal proteins PEX5 (peroxisomal biogenesis factor 5) and PMP70/ABCD3 (ATP binding cassette subfamily D member 3) were unchanged after VLX600 treatment, PEX19 (peroxisomal biogenesis factor 19) was significantly increased (logFC = 0.79, adj. p-value = 2.87) and CAT (catalase) was significantly decreased (logFC = -0.35, adj. p-value = 1.4) in my proteomic analysis. Therefore, the induction of pexophagy after VLX600 treatment possibly mediated via BNIP3 and BNIP3L seems unlikely, but could be further confirmed or refuted by additional KD/KO models or by using a pexophagy reporter (Wilhelm et al. 2022).

Furthermore, the transcription factor HIF1A, which regulates BNIP3 and BNIP3L, was strongly upregulated after VLX600 treatment. HIF1A is regulated by prolyl hydroxylases (PHDs) that depend on iron (Fe^{2+}) and oxygen (O_2) as cofactors and prime HIF1A for proteasomal degradation under normal oxygen levels (Infantino et al. 2021). In the absence of oxygen or iron HIF1A is no longer under control of the PHDs and therefore gets stabilized (Hara et al.

2020). Since oxygen levels remained unchanged the iron-chelating ability of VLX600 likely induced a “chemical hypoxia”, resulting in HIF1A-BNIP3-BNIP3L-mediated mitophagy. This is further emphasized by the fact that the extracellular addition of iron partly rescued mitophagy induction. The induction of mitophagy through iron chelators was also described by others. For example, Allen et al. (2013) reported the induction of PINK1/Parkin-independent mitophagy through several iron chelators with DFP having the strongest effect. They similarly observed stabilization of HIF1A, but no dependency on the mitophagy receptor BNIP3 for mitophagy induction. Since ATP levels were maintained after DFP treatment and ROS production was only slightly increased they concluded that mitophagy induction might not be a damage response but a recycling one to restore iron levels. Further, Sandoval-Acuña et al. (2021) showed the induction of lethal mitophagy by mitochondrial targeted deferoxamine (mitoDFO), accompanied by increased BNIP3 protein level and elevated mitochondrial ROS (mtROS) production after inhibition of mitochondrial respiration. Similarly, I also observed a decrease in the oxygen consumption rate and an increase in mtROS production after VLX600 treatment. This may also be explained by the iron chelating ability of VLX600 since it is widely known that iron plays important roles in many cellular components/functions including iron-sulfur (Fe-S) proteins or as cofactor for enzymatic reactions like in respiration (Lill and Mühlenhoff 2008). Fe-S proteins are present in multiple OXPHOS complexes and destabilisation through iron chelation might result in inhibition of mitochondrial respiration, increased ROS production and finally dysfunctional mitochondria that triggers the induction of mitophagy. ROS is mainly produced by mitochondria (Balaban, Nemoto and Finkel 2005) as by-products by electron leakage during OXPHOS reacting with oxygen to superoxide ($O_2^{\cdot-}$) and hydrogen peroxide (H_2O_2) (Freeman and Crapo 1982). ROS are highly reactive molecules that can damage cellular components, but also serve as signaling molecules at physiological levels, contributing to various cellular processes including proliferation, innate immunity and autophagy (Finkel 2011; Nikoletopoulou et al. 2013; Yun et al. 2020). However, upon chronic impairment of mitochondrial function, by e.g. mitochondria-targeting agents like VLX600 and the generation of extensive amounts of ROS, this may shift their role from bulk autophagy inducers into mitophagy inducers, representing a negative feedback loop eliminating the source of oxidative stress and protecting the cell from oxidative damage (Filomeni, Zio and Cecconi 2015). Therefore, increased mtROS may also contribute to VLX600-mediated mitophagy induction in GBM cells. In summary, here I revealed the novel ability of VLX600 to

induce mitophagy in GBM cells via the HIF1A-BNIP3-BNIP3L axis most likely because of increased HIF1A stability facilitated by iron chelation as well as increased mtROS production as a result of severely damaged mitochondria.

Furthermore, the extracellular addition of iron almost completely abrogated the VLX600-induced cell death in U-251 and NCH644 GBM cells, suggesting a key role for iron in the VLX600-induced cell death. Of note, cancer cells show higher demands for iron due to their increased proliferation and altered metabolic needs, making them more susceptible to iron withdrawal (Richardson et al. 2009). Increased amounts of iron have already been associated with an elevated risk for tumor formation as well as tumor growth (Poulsen et al. 2012; Oh et al. 2016) and therefore iron chelators were already been tested as possible anticancer agents, resulting in inhibition of cancer cell proliferation *in vitro* (Kovar et al. 1997) and delay of tumor growth *in vivo* (Lui et al. 2013; Harima et al. 2016). For example, the iron chelator deferasirox was shown to inhibit proliferation of lung carcinoma and neuroepithelioma cell lines and potently inhibited lung carcinoma xenograft growth in nude mice. Further, the metastasis and growth suppressor NDRG1 was upregulated and cell cycle was negatively regulated, resulting in a G_1/S arrest (Lui et al. 2013). Noteworthy, iron chelators are also under clinical investigation like the di-2-pyridylketone 4-cyclohexyl-4-methyl-3-thiosemicarbazone (DpC) that was used in a phase I study for patients with advanced solid tumors (NCT02688101). Further a phase II study was recently enrolled to evaluate the efficacy and safety of deferoxamine in combination with chemotherapy for patients with metastatic breast cancer (NCT05300958) and also VLX600 was investigated for its safety and tolerability in patients with refractory advanced solid tumors (NCT02222363, (Mody et al. 2019)). Those reports highlight the suitability and importance of iron chelators like VLX600 for cancer therapy.

6.6. Histone lysine methylation changes possibly mediated by VLX600

As already mentioned, iron is important for many cellular processes as well as a plethora of enzymes like the iron-dependent Jumonji C (JmjC) domain-containing (JMJD) family of histone demethylases. This protein family of more than 30 members harbours a ~170 amino acid long JmjC domain where the complexation with Fe^{2+} occurs. They demethylate histone lysines at different methylated states (Kme1, Kme2, and Kme3) using their Fe^{2+} and 2-oxoglutarate-dependent dioxygenase activity (Tsukada et al. 2006; Kooistra and Helin 2012; Manni et al. 2022). Thereto, iron is needed for proper binding and for activating the substrate molecule

(Young, Guha and Sidoli 2023). For example, deferoxamine was shown to prevent the demethylation of H3K9me2 in cancer cell lines and primary cancer cells (Müller et al. 2020) and intriguingly VLX600 was reported to inhibit the activity of KDM4 (lysine demethylase 4) demethylases in ovarian cancer cells, resulting in increased H3K9 tri-methylation and the disruption of homologous recombination (Ekstrom et al. 2021). Interestingly, KDM4A was shown to suppress autophagy, enhancing GBM survival and thereto *KDM4A* KD resulted in decreased GBM cell viability and increased expression of autophagy-related genes (Wang et al. 2016a). When I analysed several histone lysine methylation patterns I observed increased tri-methylation of H3K4, H3K9, H3K27 and H4K20, possibly triggered by inhibition of demethylation. H3K4 can be demethylated by KDM1A/B and KDM5A-D and is associated with transcriptionally active genes (Kouzarides 2007). KDM1A and B were reported to maintain GSC stemness, tumorigenicity and invasion and of note KDM1A was shown to be overexpressed particularly in GSCs (Singh et al. 2015). Further, KDM5A-D were suggested to be important in temozolomide (TMZ)-resistance in GBM (Young, Guha and Sidoli 2023). In contrast, H3K9 and H3K27 have been associated with transcriptionally inactive genes (Kouzarides 2007). H3K9 is demethylated by KDM1, KDM3 (lysine demethylase 3), KDM4 and KDM7 (lysine demethylase 7) and interestingly GSCs show reduced H3K9 methylation (Mallm et al. 2020). Further, KDM7 (lysine demethylase 7) was shown to prevent cell death in GBM (Young, Guha and Sidoli 2023). H3K27 is demethylated by KDM6A-C (lysine demethylase 6 A, B; KDM6C/UTY, ubiquitously transcribed tetratricopeptide repeat containing, Y-linked) (Santa et al. 2007), which were reported to regulate GBM drug tolerance (Young, Guha and Sidoli 2023). Demethylases of H4K20 have only been revealed for the mono-methylated but not the di- or tri-methylated states (Angerilli et al. 2023). Thereby increased tri-methylation of H4K20 was associated with a better outcome for patients with secondary GBM (Liu et al. 2010). Additionally, the aberrant expression of JMJD proteins was reported in certain cancer types having tumor suppressive as well as tumor promoting outcomes. For example, KDM3A was shown to suppress the proliferation of gastric cancer cells by regulating its target gene *RUNX3* (RUNX family transcription factor 3) (Ning et al. 2020), but on the over hand overexpression of KDM3A was reported to correlate with increased metastasis and unfavourable prognosis of colorectal (Peng et al. 2018) as well as gastric cancer (Yang et al. 2015). Of note, KDM5A was shown to be overexpressed in GBM and to promote cell proliferation, self-renewal and drug resistance of GBM by regulating *Hoxa9* and *10* (homeobox A9 and 10) and the transcription factor *FOXM1*

(forkhead box M1) in TMZ-resistant GBM cells (Banelli et al. 2015; Romani et al. 2019) and inhibition of KDM5A seems to be a promising target (Vinogradova et al. 2016; Yang et al. 2018; Yang et al. 2021). Inhibition of KDM5A was further shown to be associated with the upregulation of classical HIF1A gene markers like SLC2A1 and HK2 (Wang et al. 2013; Müller et al. 2020; Yang et al. 2021), which were also under the top 50 upregulated proteins after VLX600 treatment. Appropriate to this, KDM5A protein levels were downregulated after VLX600 treatment (Table 35). In summary, VLX600 indeed increased tri-methylation of certain histone lysines, while reducing di-methylation, suggestive of a block in histone lysine demethylases, which was earlier linked to autophagy regulation, possibly contributing to increased autophagy after VLX600 treatment (Wang et al. 2016a; Ambrosio, Ballabio and Majello 2019). However, histone lysine demethylase inhibition as well as the connection to autophagy should be further validated in future experiments, for example, by activity assays of certain demethylases and/or KD/KO experiments. In addition, increased methylation could also result from a block in acetylation (Latham and Dent 2007; Reynolds et al. 2012; Zhang, Cooper and Brockdorff 2015), which should also be investigated.

Strikingly, a plethora of JMJD inhibitors are under investigation for cancer therapy, underlining the clinical importance of this class of agents. For example, inhibition of KDM1A with NCL-1 or NCD-38 was found to significantly reduce neurosphere formation and cell viability in GSCs, accompanied by increased differentiation, endoplasmic reticulum (ER) stress and apoptosis (Sareddy et al. 2017). Furthermore, KDM6B inhibition with GSK-J4, resulting in increased H3K27me3 levels, was demonstrated to have antitumor activity both *in vitro* and *in vivo* (Hashizume et al. 2014; Grasso et al. 2015). Further, KDM6B was shown to regulate *OLIG2* expression that is a key transcription factor for GSCs and drives proliferation and invasion of GBM cells. Inhibition of KDM6B with GSK-J4 reduced *OLIG2* gene expression as well as OLIG2 protein content (Sui et al. 2022), which may contribute to its antitumor activity. Furthermore, the KDM1A inhibitor Tranylcypromine was already clinically investigated for acute myeloid leukemia (NCT02273102, NCT02717884), however although those studies were already completed no results were posted so far. All in all, histone demethylation inhibitors seem to be a promising target for certain cancers including GBM and maybe also VLX600 belongs to this kind of drugs.

6.7. VLX600 interferes with ribosome biogenesis resulting in nucleolar stress

Global proteomic analysis of U-251 cells further suggested changes in ribosome biogenesis after VLX600 treatment since this was one of the most decreased processes. Strikingly, a plethora of RNA polymerase I, II and III subunits (Table 34) as well as the KEGG pathway “RNA polymerase” (hsa03020) were downregulated after VLX600 treatment. RNA polymerase I transcribes rDNA into 47 S ribosomal RNA (rRNA), which is the pre-rRNA for the 18 S, 5.8 S and 28 S rRNAs. Only the 5 S rRNA is transcribed by the RNA polymerase III and finally all of the rRNAs are assembled to the 40 S and 60 S ribosomal subunits (Hua et al. 2022). A decrease in rRNA synthesis would therefore result in dysfunctional or less ribosomes, which are essential for cell proliferation by ensuring proper protein synthesis. As already noted, cancer cells are highly proliferative and therefore have a higher need for protein synthesis and thereto increased ribosome biogenesis, which is also a hallmark of cancer (Liao et al. 2021). Accordingly, VLX600 treatment resulted in increased translocation of the nucleolar protein NPM1 from the nucleolus to the nucleoplasm, which is a marker for nucleolar stress as it was also shown for the iron chelator deferoxamine in human leukemia cells (Yung, Yang and Bor 1991). Treatment with deferoxamine resulted in NPM1 translocation as well as inhibition of cell growth and DNA and RNA synthesis. More intriguingly, the extracellular addition of iron reversed completely the effects of deferoxamine, confirming that iron chelation is the primary mechanism of the deferoxamine induced blockade in cell growth. This is in line with that Fe-S clusters were also shown to be essential for ribosome biogenesis (Lill and Mühlenhoff 2008).

Induction of nucleolar stress was earlier shown to activate the tumor suppressor TP53/p53 by inhibition of MDM2 (MDM2 proto-oncogene) through binding of unassembled ribosomal proteins (Chakraborty, Uechi and Kenmochi 2011), resulting in cell cycle arrest and/or cell death (Pestov, Strezoska and Lau 2001; Yuan et al. 2005) although it should be mentioned that the U-251 GBM cells used in this study express mutant TP53 (Zhang et al. 1996). Interestingly, the existence of a TP53-independent nucleolar stress response was previously proposed in several studies (Li et al. 2009; Iadevaia et al. 2010; Donati et al. 2011; Russo et al. 2013). Given their partial functional redundancy the TP53 homologues TP63 (tumor protein p63) and TP73 (tumor protein p73) may theoretically also play a role in the nucleolar stress response. While TP63 (tumor protein p63) was not detected in the proteomic analysis after VLX600 treatment, I found a slight increase of TP73 in U-251 GBM cells (logFC = 0.40 and adj. p-value: 0.46). TP73 was shown to be stabilized under iron depletion (Laubach, Zhang and Chen 2021), to modulate

cancer cell viability via the NAD^+ salvage pathway (Sharif et al. 2016) and to possibly regulate autophagy by increasing *ATG5* transcription (He et al. 2013). Importantly, ribosomal dysfunction/nucleolar stress has previously been linked to autophagy (Pfister 2019). For example, Katagiri et al. (2015) reported that the inhibition of RNA polymerase I or RRN3/TIF-IA (RRN3 homolog, RNA polymerase I transcription factor (Grummt 2003; Yuan et al. 2005)) resulted in the induction of nucleolar stress and subsequent autophagy that could be blocked by inhibition of NPM1, revealing a probable upstream role of the nucleolar stress response for autophagy. Since, my proteome data analysis also revealed a strong reduction in RNA polymerase I subunits (Table 34) as well as of RRN3 (RRN3 homolog; logFC = -0.78, and adj- p-value = 1.76) that could be one possible explanation linking iron chelation with subsequent nucleolar stress to the induction of autophagy. However, if this mechanism is also required for ADCD has to be further elucidated.

6.8. Possible translational significance of VLX600 for glioblastoma therapy

Furthermore, new treatment perspectives for GBM may also include individualized therapies depending on the respective genomic alterations as well as the different metabolic phenotypes of tumors. For example, GSCs were found to have altered metabolic needs compared to the bulk tumor mass, which may be one of the reasons for their increased resistance against conventional chemotherapies, leading frequently to tumor recurrence. For example, GSCs were reported to have higher mitochondrial activities and to express higher levels of OXPHOS proteins (Kuramoto et al. 2020), making them more susceptible to mitochondria-targeted therapies, suggesting that the mitochondrial homeostasis still may play a key role for the sensitivity of a drug. In line with this, I observed that most of the GSC lines analysed here were highly sensitive to the mitochondria-targeting agent VLX600. Furthermore, during this study a publication by Garofano et al. (2021) classified four different metabolic and neurodevelopmental subtypes of GBM termed proliferative/progenitor, neuronal, mitochondrial and glycolytic/plurimetabolic. Interestingly, the authors claim that the mitochondrial GBM subtype relies exclusively on OXPHOS for energy production in contrast to the glycolytic phenotype that depends on aerobic glycolysis and amino acid and lipid metabolism. The deletion of the glucose-proton symporter *SLC45A1* was the most significantly alteration associated with the mitochondrial GBM phenotype, which were more vulnerable to inhibitors of OXPHOS. When I analysed a large set of GBM and GS cell lines I found marked differences in their *SLC45A1* mRNA expression and cell death analysis of the

GSC lines revealed a slight positive correlation of *SLC45A1* mRNA expression and sensitivity to VLX600 treatment, which is in contrast to the proposal by Garofano et al. that the deletion of *SLC45A1* is associated with the mitochondrial phenotype, resulting in a higher sensitivity to OXPHOS inhibition. However, here I compared different mRNA expressions, whereby Garofano et al. looked at gene deletions that are associated with the mitochondrial phenotype. Further, the *SLC45A1* deletion was rather described as a consequence of the lower intracellular pH in cells with a mitochondrial phenotype and not as a reason for this metabolic alteration. In this context, *SLC45A1* deletion protects the cancer cells from further pH decrease and of note reintroduction of *SLC45A1* increased the cellular acidification and impaired cell proliferation. Conclusively, GBM cell lines with *SLC45A1* gene deletion should be tested for their VLX600 sensitivity in comparison to GBM cell lines with an intact *SLC45A1* locus. Further, it is likely that the metabolic phenotype of certain cancer cells may not dependent on only one single gene deletion as well as differ between certain cancer entities and cell lines especially in the heterogeneous tumor GBM. Thereto, it is of great interest to define further genetic characteristics of different GBM phenotypes.

Moreover, also other metabolic pathways may play a role in the GBM cells after VLX600 treatment possibly as a result of impaired OXPHOS to restore the energy lack. Accordingly, Zhang et al. (2014) showed that inhibition of cell viability of colon carcinoma cells by VLX600 was even more reduced when access to glucose was restricted. However, when I used the glycolysis inhibitor 2-deoxyglucose (2-DG) in combination with VLX600 no increase in GBM cell death was visible. In contrast, my proteomic analysis revealed an enriched upregulation of proteins associated with the glycolytic pathway like HK2. Thereto, glycolysis seems to be upregulated after VLX600-mediated OXPHOS inhibition, but this does not contribute to protect the GBM cells from cell death. Importantly, Zhang et al. (2014) analysed cell viability of HCT116 colon carcinoma cells after VLX600 treatment in glucose-free medium, whereby I analysed cell death induction, which of course could lead to different results. Further, only one colon carcinoma cell line was tested by Zhang et al. (2014) and only one GBM cell line was analysed in this study. Thereto, cell viability as well as cell death of more GBM cell lines should be tested after VLX600 treatment in glucose-free medium and/or in combination with 2-DG to generate reliable results.

Furthermore, glutaminolysis could also possibly be upregulated as a response to OXPHOS inhibition, which is in line with the fact that certain cancer cells, including GBM, were shown

to be addicted to glutamine showing increased glutaminolysis, which was reported to contribute to increased tumor growth (DeBerardinis et al. 2007; Venneti et al. 2015; Jin, Alesi and Kang 2016). Interestingly, when I used the glutaminolysis inhibitor CB-839 in combination with VLX600 this significantly increased cell death in U-251 GBM cells, suggesting that at least partly glutaminolysis is upregulated to protect cells from energy deficiency and finally cell death although ATP levels were not maintained. Glutamine is not only catabolized for ATP production, but is also an important substrate for the synthesis of other macromolecules like nucleotides and proteins and glutaminolysis also plays an important role in regulating the redox balance, mTOR signaling, apoptosis and autophagy (Durán et al. 2012; Jin, Alesi and Kang 2016). Therefore, inhibition of glutaminolysis may also result in increased oxidative stress, autophagy activation and finally cell death (Durán et al. 2012; Jin et al. 2015; Gregory et al. 2019). In accordance with the upregulation of glutaminolysis in some cancer entities and the possible contribution to tumor growth, the development of a plethora of glutaminolysis inhibitors that target either the import of glutamine into the cells or the enzymatic processing of glutamine to α-ketoglutarate developed as a possible anti-cancer therapy (DeBerardinis et al. 2007; Venneti et al. 2015; Jin, Alesi and Kang 2016). For example, CB-839 or telaglenastat inhibits the glutaminase, which catalyses the first step of glutamine processing into glutamate and is already under clinical development. Single-use of CB-839 was shown to be well tolerated in patients with relapsed/refractory leukemia and to have some single-agent activity (Wang et al. 2015), but combination therapies seem to be more promising such as the combination of CB-839 with radiation therapy and TMZ for patients with IDH-mutated diffuse astrocytoma or anaplastic astrocytoma (NCT03528642) (Lemberg et al. 2022). Further, inhibition of the second deaminating enzyme GDH1 (GLUD1, glutamate dehydrogenase 1) that catalyses the conversion of glutamate into α-ketoglutarate with R162 resulted in disturbed redox homeostasis, leading to reduced cancer cell proliferation and tumor growth (Jin et al. 2015). In summary, glutaminolysis may be intrinsically upregulated in U-251 GBM cells, rendering these GBM cell line especially sensitive against glutaminolysis inhibitors at least in combination with other metabolic-targeting agents like VLX600. Of note, inhibition of glutaminolysis is well known to activate autophagy via mTORC1 inhibition and thereto could further contribute to the induction of bulk autophagy and subsequent ADCD (Villar et al. 2015).

Conclusively, the metabolic phenotypes of different GBM cells could be very important for the successful treatment of cancer patients and for decreasing therapy failure. However, the metabolic phenotypes may not only depend on one single gene deletion and thereto should be further distinguished by a subset of genetic alterations and/or metabolic modifications. VLX600 upregulates bulk autophagy, culminating in cell death and further affects OXPHOS and mitochondrial homeostasis thereby depriving cells of energy, which may be counteracted by the metabolic adaption of cancer cells. Surprisingly, inhibition of glycolysis has no net effect on cell death, but glutaminolysis upregulation may compensate for the energy loss induced by VLX600 in U-251 GBM cells since glutaminolysis inhibition further increased the VLX600-induced cell death. Additionally, glutaminolysis plays an important role in the cellular antioxidant defence mechanism, which may also contribute to increased cell death (Villar et al. 2015). Finally, my and other observations (Hoang-Minh et al. 2018; Garofano et al. 2021) implicate the importance to better understand the metabolic heterogeneity of tumors since several metabolic pathways may be dysregulated in cancer cells, underscoring the aim to better tailor individualized therapies and targeting tumor cell metabolism with agents such as VLX600.

Furthermore, the translational significance of VLX600 is underlined by the VLX600-induced reduction of tumor growth in colon carcinoma xenograft models (Zhang et al. 2014), the good toleration of VLX600 in a phase I study for refractory advanced solid tumors (Mody et al. 2019), the complete block in tumor growth of NCH644 tumor spheres and the induction of tumor cell death of GS-5 tumor spheres in the *ex vivo* model performed in this study. Dimethyl sulfoxide (DMSO) treated GS-5 tumor spheres served as control, but showed almost no increase in tumor area after nine days, which however fits to their behaviour *in vitro* where their also grow very slow (personal observation). Nevertheless, after nine days of 10 µM VLX600 treatment, all of the GS-5 tumor spheres were eliminated, supporting a role for VLX600 in tumor therapy. Further, the growth inhibitory effect for the NCH644 tumor spheres was partly dependent on ATG5 and ATG7, but especially after longer treatment periods the *ATG5* and *ATG7* KD tumor spheres showed also a reduced tumor growth after VLX600 treatment compared to the DMSO control treatment. Taking into account that here only polyclonal KD cells were used, which were not under antibiotic selection pressure during the *ex vivo* experiment, the possibility exists that cells not expressing the shRNA plasmid proliferate and increase in number, weakening the KD effects after longer treatment periods. Importantly,

the brain tissue on which the tumor spheres grew was not severely damaged by VLX600 treatment as shown by propidium iodide (PI) stainings of the brain sections at the end of the treatment period.

One important remaining question for the suitability of VLX600 in GBM therapy is the ability of VLX600 to pass the BBB. To my knowledge no study was performed testing the ability of VLX600 to pass the BBB. However, also if VLX600 would not be able to pass the BBB there are other possibilities to overcome this barrier. Invasive opportunities comprise of intracerebroventricular and intrathecal infusion where the therapeutic agents are directly injected into the ventricles (Pandit, Chen and Götz 2020), interstitial polymer wafers, which are placed into the resection cavity after surgery allowing localized administration of the drug (Azad et al. 2015) or also active disruption of the BBB using toxic agents, focused ultrasounds, radiation or hypertonic solutions, resulting in shrinkage and tight-junction dysfunction of the brain's endothelial cells (Zhang, Xu and Liu 2015; Da Wang et al. 2019). Since this are invasive methods that will possibly also damage the healthy brain the use of transport carriers are maybe the preferred method to increase drug delivery to the brain. Among them are nanoparticles, which are administered intravenously releasing the loaded drugs continuously (Zhang, Xu and Liu 2015), viral vectors that cross the BBB and deliver the therapeutic drug into the brain and exosomes, which normally circulate in virtually all body fluids (also the cerebrospinal fluid) and are able to cross the BBB (Khatami et al. 2023). So far only nanoparticles reached the phase of clinical studies (NCT04881032, NCT03020017) and some liposomal formulations have already been approved by the FDA (Food and Drug Administration) (Hao et al. 2015).

In summary, iron chelation mediated by VLX600 has profound effects that drive the cells into cell death. Elimination of iron inhibits the function of the PHDs, which regulate HIF1A stability, resulting in the increased expression of HIF1A target genes and the respective proteins like HK2 and NDRG1 as well as in the activation of the mitophagy receptors BNIP3 and BNIP3L. Further, iron chelation has intense effects on proteins that harbour Fe-S cluster like the protein complexes of the ETC or proteins of the ribosome biogenesis pathway. Together this results in major mitochondrial dysfunction and the induction of mitophagy as well as the disruption of ribosome biogenesis and increased nucleolar stress. Diminished mitochondrial function and the inhibition of OXPHOS with subsequent reduced amounts of ATP as well as enhanced ROS levels and possibly also the nucleolar stress response induce cell-lethal bulk

autophagy and finally all these cellular stress conditions induced by VLX600 acting in concert to synergistically drive cells into cell death (Figure 68).

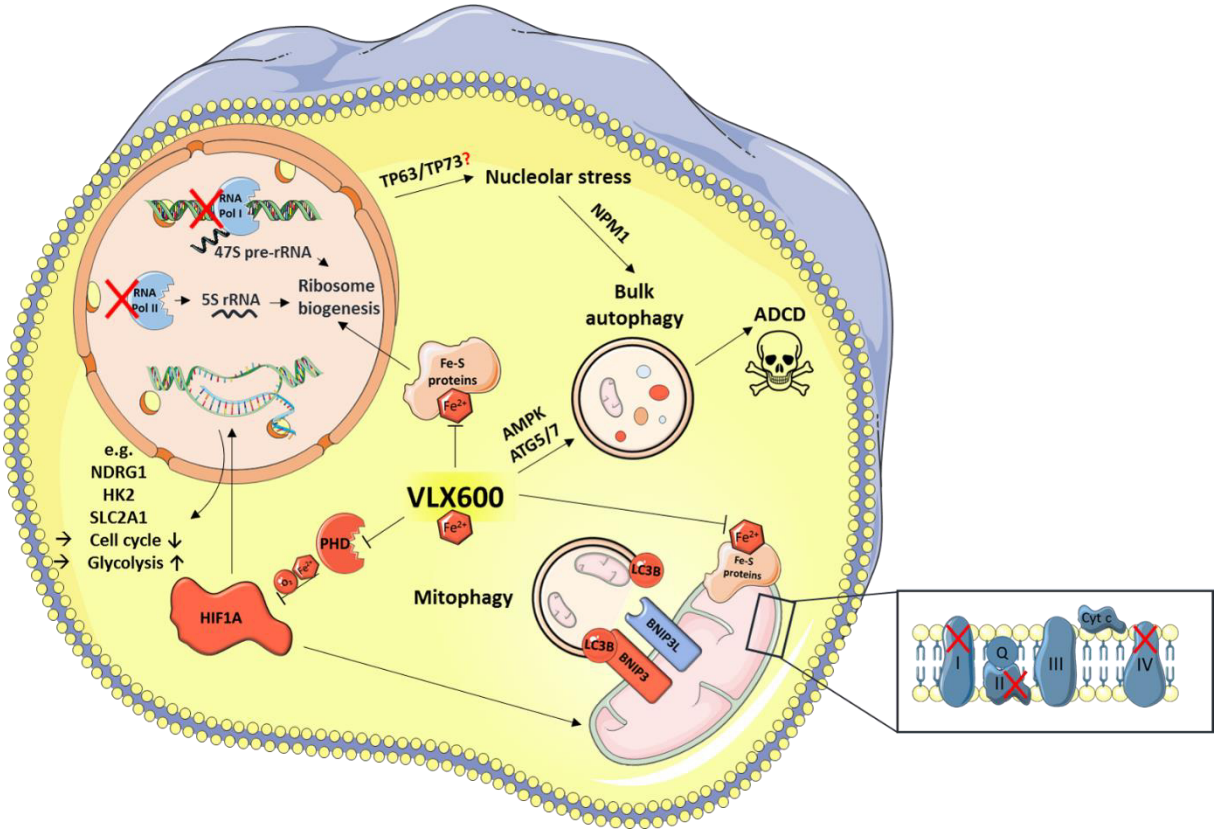

Figure 68. Proposed model of VLX600-induced mitophagy and autophagy-dependent cell death in U-251 glioblastoma cells. The iron chelating ability of VLX600 results in a plethora of events like the inhibition of PHDs and Fe-S proteins, resulting in the stabilization of the transcription factor HIF1A, inhibition of the electron transport chain and the disturbance of ribosome biogenesis, respectively. HIF1A may induce BNIP3- and BNIP3L-mediated mitophagy as well as cell cycle reduction and increase glycolysis. Additionally, VLX600 induced bulk autophagy with a possible involvement of NPM1 and the nucleolar stress response, finally culminating in autophagy-dependent cell death (ADCD). The Figure was partly generated using Servier Medical Art, provided by Servier, licensed under a Creative Commons Attribution 3.0 unported license (https://creativecommons.org/licenses/by/3.0/). Figure adapted from Reisbeck et al. (2023).

6.9. Conclusion

This thesis aimed to investigate new inducers of ADCD for GBM and to analyse the underlying mechanisms using different genetic models as well as several ADCD-inducing drugs.

Here I provide proof that the drugs PIMO and LOP (Zielke et al. 2018) induce ADCD in GBM, which was accompanied by increased autophagic flux. Depending on an earlier report (Heckmann and Green 2019) showing that some autophagy proteins, including ATG5 and ATG7, having functions outside of autophagy, e.g. in LAP, additional KD models were needed to distinguish between those two processes. However, this proofed that indeed PIMO and LOP

induce ADCD in GBM without the involvement of LAP and further highlights the great importance to carefully decipher which KO models are used for analysing ADCD.

Furthermore, PIMO and LOP impaired lipid trafficking, resulting in the lysosomal accumulation of lipids like cholesterol, increased lipid peroxidation and subsequent LMP. Importantly, GBM cells may be particularly sensitive to inhibitors of cholesterol trafficking since they rely on the extracellular import of cholesterol (Björkhem and Meaney 2004; Villa et al. 2016) and decreased cytosolic cholesterol levels may contribute to autophagy activation (Xu et al. 2010). Further, both drugs were earlier described to belong to a group of functional inhibitors of SMPD1 (FIASMAs) that accumulate in the lysosomes because of their lysosomotropic properties, resulting in the inhibition of the lysosomal enzyme SMPD1, which may further contribute to lysosomal lipid accumulation (Kornhuber et al. 2008; Kornhuber et al. 2011). Interestingly, cancer cells were reported to have an upregulated lysosomal function in order to fulfil their increased metabolic demands, suggesting that lysosomes could be a suitable target for cancer therapy (Kirkegaard and Jäättelä 2009; Perera et al. 2015; Yang et al. 2016). Strikingly, the induction of LMP was reversible by drug washout, suggesting the induction of lysophagy and accordingly the inhibition of lysophagy was previously shown to further exacerbate the PIMO- and LOP-induced cell death, suggesting the activation of pro-survival lysophagy in this context (Meyer 2019; Meyer*, Henkel* et al. 2021). The release of cathepsins into the cytosol after LMP may further damage cytosolic material, which is supported by previous results showing that the inhibition of CTSB and CTSD further increased the PIMO- and LOP-induced cell death (Meyer 2019; Meyer*, Henkel* et al. 2021). Thereto, PIMO and LOP induce cell-lethal bulk autophagy as well as pro-survival lysophagy in this respective cellular context, further emphasizing the dual role of bulk and selective autophagy. However, overactivated bulk autophagy together with massively damaged lysosomes cannot be rescued by lysophagy, still resulting in cell death induction with characteristics of both ADCD as well as LDCD (Galluzzi et al. 2018) and thereto the term autophagy-dependent lysosomal cell death may also be used.

Importantly, LOP is not able to pass the BBB (Alyautdin et al. 1997) and although the antipsychotic agent PIMO showed promising results in the *ex vivo* GSC model, was successfully used in *in vivo* experiments (Ranjan, Kaushik and Srivastava 2020) and is able to pass the BBB (Lee, Nam and Lee 2016; Elmaci and Altinoz 2018) possible limitations of repurposing antipsychotic agents may include severe side effects like arrhythmias or the neuroleptic

malignant syndrome (Zemrak and Kenna 2008; Elmaci and Altinoz 2018), underlining the need for novel drug candidates with different mode of actions. Thereto, in the second part of my thesis I focused on the investigation of the iron chelator and OXPHOS inhibitor VLX600. Treatment of GBM cells with VLX600 resulted in the induction of bulk autophagy, mitophagy and finally cell death. While mitophagy was dependent on the mitophagy receptors BNIP3 and BNIP3L, the VLX600-induced cell death was not, suggesting that mitophagy has no net effect on cell death in this context. Thereto, VLX600 induces lethal "bulk" autophagy in GBM cells, further contributing to the notion that bulk autophagy and selective forms, like mitophagy, can be activated simultaneously but still exerting different effects.

VLX600 is an iron chelator and iron is an essential cofactor for cellular homeostasis including Fe-S cluster that are part of many proteins like the ETC complexes. Thereto, it is not surprising that iron chelation mediated by VLX600 plays a key role in several effects exerted by VLX600 including cell death, mitophagy, histone methylation changes and ribosomal stress. Since iron chelation is particularly unspecific the use of iron chelators for cancer patients has to be carefully evaluated. Nevertheless, an ever increasing number of studies highlight the suitability of iron chelators for several tumor entities *in vitro* (Kovar et al. 1997) as well as *in vivo* (Lui et al. 2013; Harima et al. 2016) and strikingly also clinical studies were already performed (NCT02688101, NCT02222363). The suitability of iron chelators may rely on the fact that tumor cells have a higher need for iron due to their increased protein synthesis for cell proliferation and their higher metabolic demands (Richardson et al. 2009).

The translational significance of VLX600 is supported by its cell death inducing ability of GSC tumor spheres treated in the *ex vivo* tumor growth assay. GSCs are thought to be one of the major reasons for GBM drug-resistance and recurrence (Singh et al. 2003) and interestingly were reported to have different metabolic needs compared to the bulk tumor mass. Thereto, one possible GBM treatment strategy could include the untangling of specific metabolic phenotypes of tumors tailoring individualized therapies depending on the metabolic needs of the tumor cells (Hoang-Minh et al. 2018; Garofano et al. 2021). VLX600 could thereby be of special interest since it effectively inhibits OXPHOS, showed synergistic toxicity together with other metabolic-targeting agents and strikingly was already investigated in a phase I study, showing that VLX600 is well tolerated in patients. Nevertheless, it is not known whether VLX600 can pass the BBB, but the use of nanoparticles is already under clinical investigation (NCT04881032, NCT03020017) and could be useful to transport drugs like VLX600 across the

BBB. However, in future experiments VLX600 should also be investigated for its possibility to pass the BBB *in vivo* or using *in vitro* BBB models (Jagtiani et al. 2022)

Finally, my results further underline the heterogenic role of bulk and selective autophagy as well as the possibility of simultaneous activation of different forms of autophagy, which can be either pro-survival or pro-death depending on tumor type and stage (Fulda and Kögel 2015; Linder and Kögel 2019), which is supported by several other studies dealing with the dual role of autophagy (Degenhardt et al. 2006; Liu and Ryan 2012; Zielke et al. 2018). Consequently, it is of great importance to accurately select ADCD-inducing drugs depending on tumor characteristics.

7. Summary

The brain tumor glioblastoma (GBM) is the most invasive and deadliest glioma that is characterized by an infiltrative growth into the brain parenchyma, which makes a full surgical resection nearly impossible, resulting in frequent tumor relapse (Cuddapah et al. 2014; Wilson, Karajannis and Harter 2014; Yalamarty et al. 2023). Although new GBM therapies are extensively investigated only the tumor treating fields (TTF) therapy may be considered as adjuvant therapy, increasing the median overall survival up to 20.9 months (Stupp et al. 2017). GBM is further characterized by a high intra- and inter-tumoral heterogeneity, which is partly thought to depend on the glioma stem-like cells (GSCs) that were shown to mostly have altered metabolic needs compared to the differentiated bulk tumor mass and frequently resist standard chemoradiotherapy, resulting in tumor recurrence (Singh et al. 2003; Clarke et al. 2006; Bradshaw et al. 2016). Moreover, GBM was shown to be highly resistant against apoptotic cell death further hindering therapy progress (Steinbach and Weller 2004). To overcome this hurdles many research is done for alternative cell death therapies including the autophagy-dependent cell death (ADCD) (Zielke et al. 2018; Linder and Kögel 2019). This form of regulated cell death (RCD) is characterized by increased autophagic flux and depends on the autophagic machinery (Galluzzi et al. 2018). Autophagy normally serves as a pro-survival mechanism that ensures cell survival also under nutrient deprivation or oxygen shortage, providing the cells with energy and metabolic building blocks (Klionsky 2007) and damaged or superfluous organelles can be removed by selective autophagy like lysophagy or mitophagy (Vargas et al. 2023). Although autophagy is described as a pro-survival mechanism many studies implicate a dual role for autophagy in cancer development and progression having either a tumor promoting or a tumor suppressive function, which depends highly on the tumor type and stage as well as the respective cellular context. Nevertheless, the activation of drug-induced ADCD got highly acknowledged during the last years and our own studies as well as other highly emphasize this cell death modality as a future therapeutic option for GBM (Fulda and Kögel 2015; Shchors, Massaras and Hanahan 2015; Meyer*, Henkel* et al. 2021; Reisbeck et al. 2023).

In order to further understand the underlying mechanisms of drug-induced ADCD in GBM, several ADCD-inducing drugs were investigated in this study. First, the antipsychotic agent pimozide (PIMO) and the opioid receptor antagonist loperamide (LOP) have been previously shown to induce ADCD in GBM cells in a screen performed in our lab (Zielke et al. 2018). Here

I validated the ADCD-inducing ability in further cell models using autophagy-deficient LN-229 cells with *ATG7* knockout (KO) and MZ-54 cells ectopically expressing an autophagic flux reporter plasmid. This revealed that cell death is rescued in *ATG7* KO cells and that autophagic flux is significantly increased after PIMO and LOP treatment, while autophagic flux remained unchanged in MZ-54 *ATG5* and *ATG7* KO cells. Moreover, re-expression of *ATG7* in MZ-54 *ATG7* KO cells restores cell death induced by PIMO and LOP. During this thesis a study by Heckmann and Green (2019) highlighted the non-canonical function of some autophagic proteins, including ATG5 and ATG7, for LC3-associated phagocytosis (LAP), a pathway implicated in immune regulation and inflammatory responses. Thereto, additional knockdown (KD) models were established to distinguish between autophagy and LAP, revealing that only KD of the autophagy specific proteins is able to significantly rescue the PIMO- and LOP-induced cell death in GBM, suggesting the induction of ADCD without the involvement of LAP.

Furthermore, a global proteomic analysis after PIMO and LOP treatment previously revealed an unexpected alteration of proteins associated with cholesterol and lipid metabolism (Meyer 2019; Meyer*, Henkel* et al. 2021). Among them were several proteins known to be regulated by the transcription factor SREBP2 that was shown to be activated during impaired lipid trafficking (Kristiana et al. 2010). Indeed, cholesterol was strongly accumulated in the lysosomes indicative of impaired lipid transport out of the lysosomes, resulting in reduced cytosolic cholesterol levels. Appropriate to this, reduced cytosolic cholesterol levels were shown to regulate autophagy activation via mTOR (Xu et al. 2010) and indeed the extracellular addition of cholesterol inhibited autophagy shown by increased phosphorylation of the downstream mTOR target RPS6, underlining the idea that impaired cholesterol transport contributes to autophagy activation.

Increased amounts of lipids in the lysosomes after PIMO and LOP treatment were previously shown to result in lipotoxicity (Meyer 2019; Meyer*, Henkel* et al. 2021), which may further damage lysosomal integrity and subsequently result in lysosomal membrane permeabilization (LMP). When treating GBM cells ectopically expressing the pmCherry-Gal3 plasmid with PIMO and LOP this resulted in a massive induction of LGALS3 puncta indicative of LMP. Interestingly, LGALS3 formation was absent in autophagy-deficient cell lines and was reversible by drug washout, assuming the removal of damaged lysosomes by lysophagy. Since KD of the lysophagy receptor *VCP* was previously shown to further increase the PIMO- and LOP-induced

cell death (Meyer 2019; Meyer*, Henkel* et al. 2021) I conclude that lysophagy served as a pro-survival mechanism in this context.

Furthermore, LMP may result in the release of lysosomal contents like the cathepsins causing further cellular damage. Indeed, it was previously shown that PIMO and LOP treatment resulted in increased CTSB and CTSD levels in the cytosol and that inhibition of the cathepsins rescued the PIMO- and LOP-induced cell death, suggesting the induction of a lysosomal dependent cell death (LDCD) (Meyer 2019; Meyer*, Henkel* et al. 2021). In summary, PIMO and LOP induce lipotoxicity, LMP as well as pro-survival lysophagy, which however cannot rescue the devastating lysosomal damage resulting in the induction of an autophagy-dependent lysosomal cell death in GBM cells. Of note, only the antipsychotic agent PIMO is able to pass the blood-brain barrier (BBB) (Elmaci and Altinoz 2018) and although PIMO showed promising results in this study *in vitro* as well as in the *ex vivo* tumor growth assay and by others also *in vivo* (Ranjan, Kaushik and Srivastava 2020) the suitability may be hampered by severe side effects (Zemrak and Kenna 2008). Thereto, in the second part of my thesis I focused on an agent with a different mode of action, VLX600, which is an iron chelator and oxidative phosphorylation (OXPHOS) inhibitor and was previously reported to induce mitochondrial dysfunction and cell death in colon carcinoma cells (Zhang et al. 2014; Fryknäs et al. 2016). However, to my knowledge to date no study investigated VLX600 for its therapeutic suitability in GBM cells. Here, I revealed a novel ADCD-inducing ability of VLX600 for GBM cells since cell death was significantly rescued in *ATG5* and *ATG7* KO and KD cells but not by caspase inhibition and autophagic flux was increased. Further, I validated the inhibition of OXPHOS in GBM cells, which resulted in stringent reduction of ATP levels and increased mitochondrial reactive oxygen species (mtROS), resulting in mitochondrial dyshomeostasis including mitochondrial membrane depolarization and the reduction of mitochondrial proteins. Major mitochondrial damage may culminate in the degradation of damaged mitochondria, which was further validated by the mt-mKeima and the mtphagy dye assay. Both assays revealed a stringent activation of mitophagy after VLX600 treatment, which was partly rescued by *ATG5*/*7* KO. In order to further elucidate the underlying mechanisms of VLX600-induced mitophagy, the mitophagy receptors BNIP3 and BNIP3L were further analysed, revealing a huge increase in the protein amounts, an increased mitochondrial localization and homodimerization, which was shown to be important for BNIP3 and BNIP3L activation (Sulistijo and MacKenzie 2006; Marinković, Šprung and Novak 2021). Further, siRNA

experiments supported the notion that the VLX600-induced mitophagy is dependent on BNIP3 and BNIP3L, but this had no discernible net effect on cell death induced by VLX600, suggesting the induction of cell-lethal “bulk” autophagy in this context. The mitophagy receptors BNIP3 and BNIP3L are known to be activated during hypoxia and to be regulated by the transcription factor HIF1A (Vara-Perez, Felipe-Abrio and Agostinis 2019), which was actually strongly increased after VLX600 treatment, suggesting the induction of mitophagy via the HIF1A-BNIP3-BNIP3L axis. HIF1A is regulated via the prolyl hydroxylases (PHDs), which depend on oxygen and iron as cofactors (Hara et al. 2020; Infantino et al. 2021) and since oxygen levels remained unchanged I propose that the VLX600-induced iron chelation results in HIF1A stabilization inducing a “chemical hypoxia”. Appropriate to this, the extracellular addition of iron partially rescued mitophagy as well as completely abrogated cell death induced by VLX600. Several enzymes/components rely on iron as cofactor or for the formation of Fe-S clusters including the electron transport chain (ETC) complexes, the Jumonji C domain-containing (JMJD) family of proteins as well as proteins involved in ribosome biogenesis (Lill and Mühlenhoff 2008). Appropriate to this, the global proteomic analysis after VLX600 treatment further highlighted the inhibition of OXPHOS and induction of mitochondrial dysfunction, but also suggested major changes in histone methylation as well as in ribosomal biogenesis. Of note, the upregulation of several proteins associated with HIF1A signaling, including HK2 and SLC2A1, is associated with the inhibition of the histone demethylase KDM5A. KDM5A belongs to the iron-dependent JMJD family of histone lysine demethylases that demethylate histone lysines at different methylated states (Yang et al. 2021). Interestingly, treatment with VLX600 resulted in increased tri-methylation of H3K4, H3K9, H3K27 and H4K20, while di-methylation of H3K9 and H3K4 was decreased. Appropriate to this, KDM5A protein levels were significantly downregulated after VLX600, suggesting the inhibition of demethylation of tri-methylated histone lysines by VLX600, but this as well as the possible connection to autophagy (Ambrosio, Ballabio and Majello 2019) have to be further investigated by additional activity assays of specific demethylases and/or KD/KO models. Furthermore, the global proteomic analysis revealed a massive downregulation of proteins associated with ribosome biogenesis that was further investigated by analysing the translocation of the nucleolar protein NPM1 from the nucleolus to the nucleoplasm, which is a marker for nucleolar stress (Yung, Yang and Bor 1991). This revealed a constant NPM1 translocation after VLX600 treatment and appropriately, a plethora of RNA polymerase I, II

and III subunits as well as the KEGG pathway “RNA polymerase” (hsa03020) were downregulated after VLX600 treatment, suggesting the induction of nucleolar stress. In addition, a probable upstream role of the nucleolar stress response for autophagy was reported (Katagiri et al. 2015). These results further underline the notion that iron chelation is a key driver for the VLX600 exerted effects. Intriguingly, it was shown that cancer cells have a higher need for iron due to their augmented cell proliferation and that increased intracellular iron levels are associated with an increase in cancer risk (Richardson et al. 2009; Poulsen et al. 2012; Oh et al. 2016). Thereto, iron chelation could be a possible future treatment strategy for GBM, which is further acknowledged by other studies showing that iron chelation can reduce tumor growth and some iron chelators are already under clinical investigation (Lui et al. 2013; Harima et al. 2016) (NCT02688101).

Furthermore, the translational significance of VLX600 was investigated in an authentic brain environment using organotypic brain slices and GSC tumor spheres. This revealed a strong tumor growth inhibiting as well as cell death inducing ability of VLX600, which was partly dependent on ATG5 and ATG7, further supporting the autophagy dependency of the VLX600-induced cell death. As already mentioned, GBM is a highly heterogeneous tumor leading to continuously changing classifications depending on new genetic as well as metabolic characteristics. Accordingly, a study by Garofano et al. (2021) recently described four metabolically as well as developmental phenotypes of which the mitochondrial GBM subtype was described to rely exclusively on OXPHOS for energy production and was associated with the deletion of the glucose-proton symporter *SLC45A1.* Although I could not verify the hypothesis that *SLC45A1* expression correlates with VLX600 sensitivity in my cell models it is further of great interest to target the distinct metabolic phenotypes of tumor cells. This is further underlined by my results showing that glycolysis inhibition had no net effect on the VLX600-induced cell death, while inhibition of glutaminolysis synergistically increased the VLX600 toxicity. Since the sensitivity to metabolic-targeting agents may also depend on tumor type and cell line it is important to further decipher the genetic background of different metabolic phenotypes in order to better tailor individualized therapies and minimizing therapy failure.

In summary, here I showed that VLX600 induces cell-lethal bulk autophagy that is accompanied by major mitochondrial damage, culminating in HIF1A-BNIP3-BNIP3L mediated mitophagy as well as histone lysine methylation changes and ribosomal stress altogether

terminating in ADCD. The fact that VLX600 was already tested in a phase I study (Mody et al. 2019) makes it an interesting compound for future therapies. Although it is not known whether VLX600 can pass the BBB the use of nanoparticles could improve the delivery to the brain, but still this should be further investigated in future studies.

8. Zusammenfassung

Der Hirntumor Glioblastom (GBM) ist der invasivste und tödlichste Gliomtyp, der aufgrund seines infiltrativen Wachstums in das umliegende Hirngewebe nahezu unmöglich vollständig chirurgisch zu entfernen ist und daher nahezu unweigerlich zu Rezidiven führt (Cuddapah et al. 2014; Wilson, Karajannis and Harter 2014; Yalamarty et al. 2023). Obwohl neue Therapien für das GBM umfassend untersucht werden, konnte in den letzten Jahren nur die Verwendung von Tumortherapiefeldern als zusätzliche Therapie das mittlere Gesamtüberleben auf bis zu 20,9 Monate erhöhen (Stupp et al. 2017). Das GBM ist zudem durch eine hohe intra- und intertumorale Heterogenität gekennzeichnet, die teilweise durch die sogenannten gliomartigen Stammzellen hervorgerufen wird. Diese zeigen im Vergleich zur differenzierten Tumormasse meist veränderte metabolische Bedürfnisse, widerstehen daher häufig der Standardtherapie und tragen damit zur Rezidiv Entwicklung bei (Singh et al. 2003; Clarke et al. 2006; Bradshaw et al. 2016). Darüber hinaus behindert die häufige Apoptose Resistenz des GBMs den weiteren Therapiefortschritt (Steinbach and Weller 2004). Um diese Hindernisse zu überwinden wird in vielen Studien nach alternativen Zelltodtherapien geforscht, darunter auch der Autophagie-abhängige Zelltod (Zielke et al. 2018; Linder and Kögel 2019). Diese Form des regulierten Zelltods ist durch einen erhöhten autophagischen Flux und der Abhängigkeit von der autophagischen Maschinerie gekennzeichnet (Galluzzi et al. 2018). Autophagie spielt normalerweise eine überlebenswichtige Rolle um das Zellüberleben auch während eines Nährstoff- oder Sauerstoffmangels zu gewährleisten (Klionsky 2007) oder um beschädigte oder überflüssige Organellen durch selektive Autophagie wie der Lysophagie oder der Mitophagie abzubauen (Vargas et al. 2023). Obwohl Autophagie als ein überlebensfördernder Mechanismus beschrieben wird, deuten viele Studien auf eine duale Rolle der Autophagie bei der Tumorentstehung, -progression und -therapie hin, wobei Autophagie sowohl eine tumorfördernde als auch eine tumorsuppressive Rolle einnehmen kann. Dies kann jedoch stark vom Tumortyp und -stadium sowie dem jeweiligen zellulären Kontext abhängen. Trotzdem wurde der Autophagie-abhängige Zelltod, der durch gewisse Substanzen induziert werden kann, in den letzten Jahren vielfach untersucht und unsere eigenen Studien sowie Studien anderer Labore betonen diese Form des Zelltods als zukünftige therapeutische Option für das GBM (Fulda and Kögel 2015; Shchors, Massaras and Hanahan 2015; Meyer*, Henkel* et al. 2021; Reisbeck et al. 2023).

Um die zugrunde liegenden Mechanismen des durch Substanzen induzierten Autophagie-abhängigen Zelltods im GBM weiter zu entschlüsseln, habe ich in meiner Dissertation verschiedene Substanzen untersucht, die einen Autophagie-abhängigen Zelltod induzieren können. In einer zuvor in unserem Labor durchgeführten Studie konnte gezeigt werden, dass das Antipsychotikum Pimozid (PIMO) und der Opioidrezeptor Antagonist Loperamid (LOP) einen Autophagie-abhängigen Zelltod in GBM Zellen induzieren (Zielke et al. 2018). Darauf aufbauend habe ich mit Hilfe weiterer Zellmodelle wie den Autophagie-defizienten LN-229 Zellen mit *ATG7* Knockout (KO) und den MZ-54-Zellen, die ein autophagisches Flux Reporterplasmid exprimieren, die Fähigkeit zur Induktion des Autophagie-abhängigen Zelltods validiert. Diese Experimente konnten die Induktion eines Autophagie-abhängigen Zelltods bestätigen, da der Zelltod in den *ATG7* KO Zellen deutlich reduziert war. Zusätzlich konnte ich einen erhöhten autophagischen Flux in den Wildtyp Zellen nach PIMO und LOP Behandlung messen, während der autophagische Flux in den MZ-54 *ATG5* und *ATG7* KO Zellen unverändert blieb. Darüber hinaus konnte durch die Wiederexpression von *ATG7* in MZ-54 *ATG7* KO Zellen der durch PIMO und LOP induzierte Zelltod wiederhergestellt werden. Während meiner Dissertation hat eine Studie von Heckmann und Green (2019) die nichtkanonische Funktion einiger autophagischer Proteine, einschließlich ATG5 und ATG7, für die LC3-assoziierte Phagozytose (LAP) hervorgehoben. LAP ist ein Signalweg, der an der Immunregulation und an inflammatorischen Reaktionen beteiligt ist. Zusätzliche Knockdown (KD) Modelle wurden etabliert um zwischen Autophagie und LAP zu unterscheiden und konnten zeigen, dass nur der KD der Autophagie-spezifischen Proteine den PIMO- und LOP-induzierten Zelltod in GBM Zellen signifikant reduzieren kann. Dies weist darauf hin, dass die Induktion des Autophagie-abhängigen Zelltods ohne Beteiligung von LAP erfolgt.

Weiterhin konnte eine zuvor durchgeführte globale Proteomanalyse nach PIMO und LOP Behandlung eine unerwartete Veränderung von Proteinen, die mit dem Cholesterin- und Lipidstoffwechsel assoziiert sind, aufzeigen (Meyer 2019; Meyer*, Henkel* et al. 2021). Darunter waren mehrere Proteine, die durch den Transkriptionsfaktor SREBP2 reguliert werden. Dabei ist bekannt, dass der SREBP2-Signalweg insbesondere während eines gestörten Lipidtransports aktiviert wird (Kristiana et al. 2010). Passend dazu konnte ich eine starke Akkumulierung von Cholesterin in den Lysosomen nach PIMO und LOP Behandlung beobachten und demnach auf einen gestörten Lipidtransport aus den Lysosomen schließen. Ein gehemmter Cholesterintransport könnte weiterhin zu geringeren cytoplasmatischen

Cholesterinspiegeln führen und damit auch die Aktivierung der Autophagie über mTOR regulieren (Xu et al. 2010). Tatsächlich hemmte die extrazelluläre Zugabe von Cholesterin die PIMO- und LOP-induzierte Autophagie, welches ich durch eine erhöhte Phosphorylierung des nachgeschalteten mTOR-Zielproteins RPS6 zeigen konnte und weiterhin die Idee unterstreicht, dass der deregulierte Cholesterintransport zur Aktivierung der Autophagie beiträgt.

Erhöhte Mengen an lysosomalen Lipiden können zu einer Lipotoxizität führen, wie es bereits für PIMO und LOP in vorherigen Experimenten gezeigt wurde (Meyer 2019; Meyer*, Henkel* et al. 2021), dadurch die Lysosomenintegrität weiter beeinträchtigen und letztendlich zu einer lysosomalen Membranpermeabilisierung (LMP) führen. Dabei war die massive Schädigung der Lysosomen nach PIMO und LOP Behandlung deutlich in den Autophagie-defizienten Zelllinien reduziert und interessanterweise konnte die Schädigung durch Wegnahme der Substanzen Rückgängig gemacht werden. Dies deutet darauf hin, dass Lysosomen, die durch PIMO und LOP beschädigt wurden, durch Lysophagie abgebaut werden können. Da zuvor gezeigt wurde, dass der KD des Lysophagie-Rezeptors *VCP* den durch PIMO- und LOP-induzierten Zelltod weiter erhöht (Meyer 2019; Meyer*, Henkel* et al. 2021), schließe ich daraus, dass Lysophagie in diesem Kontext eine überlebensfördernde Rolle spielt.

Darüber hinaus könnte LMP zur Freisetzung von lysosomalen Inhalten wie den Cathepsinen und daher zu weiteren zellulären Schäden führen. Tatsächlich wurde zuvor gezeigt, dass die Behandlung mit PIMO und LOP zu erhöhten CTSB- und CTSD-Spiegeln im Cytoplasma führte und dass die Hemmung der Cathepsine den durch PIMO- und LOP-induzierten Zelltod reduzierte. Dies könnte auf die Induktion eines Lysosomen-abhängigen Zelltods hinweisen (Meyer 2019; Meyer*, Henkel* et al. 2021). Zusammenfassend konnte ich in meiner Dissertation gemeinsam mit den Vordaten der Dissertation von Dr. Nina Meyer (*Molecular targeting of autophagy in glioblastoma* (Meyer 2019)) zeigen, dass die Behandlung mit PIMO und LOP Lipotoxizität, LMP, sowie überlebensfördernde Lysophagie induziert, die jedoch nicht die schwerwiegenden lysosomalen Schäden ausgleichen kann und daher zur Induktion eines Autophagie-abhängigen lysosomalen Zelltods in GBM Zellen führt. Es ist zu beachten, dass nur das Antipsychotikum PIMO in der Lage ist die Blut-Hirn-Schranke zu überwinden (Elmaci and Altinoz 2018) und obwohl PIMO in dieser Studie vielversprechende Ergebnisse *in vitro* sowie im *ex vivo* Tumorwachstums Assay zeigte und auch in anderen Studien in *in vivo* Experimenten vielversprechende Ergebnisse erzielt wurden (Ranjan, Kaushik and Srivastava 2020), könnten

schwere Nebenwirkungen die Eignung von PIMO beeinträchtigen (Zemrak and Kenna 2008). Infolgedessen konzentrierte ich mich im zweiten Teil meiner Dissertation auf einen Wirkstoff mit einem anderen Wirkmechanismus. VLX600 ist ein Eisenchelator und Inhibitor der oxidativen Phosphorylierung (OXPHOS). Zwar konnte bereits gezeigt werden, dass VLX600 mitochondriale Dysfunktion und Zelltod in Kolonkarzinomzellen induziert (Zhang et al. 2014; Fryknäs et al. 2016), allerdings hat meines Wissens nach bisher noch keine Studie die therapeutische Eignung von VLX600 für GBM Zellen untersucht. Hier zeige ich eine zuvor noch nicht bekannte Autophagie-abhängige Zelltod-induzierende Fähigkeit von VLX600 für GBM Zellen auf, da der Zelltod signifikant in *ATG5* und *ATG7* KO und KD Zellen aber nicht durch Caspase Inhibitoren gehemmt wurde und der autophagische Flux erhöht war. Darüber hinaus konnte ich die Hemmung der OXPHOS in GBM Zellen bestätigen und eine starke Reduktion der ATP-Spiegel beobachten. Dies resultierte weiterhin in einer erhöhten Produktion von mitochondrialen reaktiven Sauerstoffspezies und mündete letztendlich in einer deregulierten mitochondrialen Homöostase einschließlich mitochondrialer Membrandepolarisation und der Reduktion von mitochondrialen Proteinen. Da schwere mitochondriale Schäden zur Degradation der beschädigten Mitochondrien durch Mitophagie führen können, habe ich die Induktion der Mitophagie mithilfe des mt-mKeima und des mtphagydye Assays weiter untersucht. Beide Experimente zeigten eine konstante Aktivierung der Mitophagie nach VLX600 Behandlung, die teilweise durch *ATG5*/*7* KO gehemmt wurde. Um die zugrunde liegenden Mechanismen der VLX600-induzierten Mitophagie weiter zu entschlüsseln, habe ich die Mitophagie Rezeptoren BNIP3 und BNIP3L weiter analysiert. Beide Proteine waren nach VLX600 Behandlung stark erhöht, zeigten eine vermehrte mitochondriale Lokalisierung und Homodimerisierung, die mit einer erhöhten Aktivierung von BNIP3 und BNIP3L assoziiert ist (Sulistijo and MacKenzie 2006; Marinković, Šprung and Novak 2021). Darüber hinaus unterstützen meine siRNA Experimente die Annahme, dass die VLX600-induzierte Mitophagie von BNIP3 und BNIP3L abhängig ist, aber dies hatte keinen erkennbaren Nettoeffekt auf den durch VLX600-induzierten Zelltod. Demnach induziert VLX600 eine letale "Bulk"-Autophagie in diesem spezifischen zellulären Kontext. Die Mitophagie Rezeptoren BNIP3 und BNIP3L werden durch den Hypoxie-regulierten Transkriptionsfaktor *HIF1A* reguliert (Vara-Perez, Felipe-Abrio and Agostinis 2019), der nach VLX600 Behandlung tatsächlich stark erhöht war und demnach auf eine Induktion von Mitophagie über die HIF1A-BNIP3-BNIP3L-Achse hindeutet. HIF1A wird über die Prolylhydroxylasen reguliert, die Sauerstoff und Eisen als

Kofaktoren benötigen (Hara et al. 2020; Infantino et al. 2021). Da die Sauerstoffzufuhr unverändert blieb, vermute ich, dass die durch VLX600 verursachte Eisenchelatierung zu einer Stabilisierung von HIF1A führt und eine "chemische Hypoxie" induziert. Passend dazu konnte ich zeigen, dass durch die extrazelluläre Zugabe von Eisen die Mitophagie teilweise gehemmt und der durch VLX600 verursachte Zelltod vollständig blockiert wurde. Viele Enzyme/Proteinkomplexe sind auf Eisen als Kofaktor oder für die Bildung von Fe-S-Clustern angewiesen darunter auch die Komplexe der Elektronentransportkette, die JMJD-Proteinfamilie sowie Proteine, die an der Ribosomenbiogenese beteiligt sind (Lill and Mühlenhoff 2008). Dementsprechend konnten in der hier durchgeführten globalen Proteomanalyse nach der Behandlung mit VLX600 die Hemmung der OXPHOS und die Induktion von mitochondrialer Dysfunktion bestätigt werden und zusätzlich gab es Hinweise auf Veränderungen in der Histonenmethylierung sowie in der Ribosomenbiogenese. Die Hochregulierung mehrerer Proteine, die mit der HIF1A-Signalgebung verbunden sind, einschließlich HK2 und SLC2A1, wurden mit der Hemmung der Histondemethylase KDM5A in Verbindung gebracht. KDM5A gehört zur eisenabhängigen JMJD-Familie von Histonlysin-Demethylasen, die methylierte Lysine demethylieren (Yang et al. 2021). Interessanterweise führte die Behandlung mit VLX600 zu einer erhöhten Tri-methylierung von H3K4, H3K9, H3K27 und H4K20, während die Di-methylierung von H3K9 und H3K4 abnahm. Passend dazu waren die KDM5A Proteinspiegel nach VLX600 Behandlung deutlich reduziert. Gemeinsam könnte dies auf eine Hemmung der De-methylierung von tri-methylierten Histonlysinen hinweisen. Die Hemmung von Demethylasen als auch die mögliche Verbindung zur Autophagie Regulation (Ambrosio, Ballabio and Majello 2019) sollte jedoch durch zusätzliche Aktivitätsassays spezifischer Demethylasen und/oder KD/KO-Modelle weiter untersucht werden. Weiterhin zeigte die globale Proteomanalyse eine massive Herabregulierung von Proteinen, die mit der Ribosomenbiogenese assoziiert sind. Passend dazu beobachtete ich weitere Hinweise auf eine Induktion von ribosomalen Stress, da zum einen das nukleäre Protein NPM1 vermehrt vom Nukleolus in das Nukleoplasma translozierte (Yung, Yang and Bor 1991) und zum anderem eine Vielzahl von Untereinheiten von RNA-Polymerase I, II und III sowie der KEGG-Weg "RNA-Polymerase" (hsa03020) nach VLX600 Behandlung herunterreguliert waren. Interessanterweise wurde eine Voranschaltung der nukleären Stressantwort vor die Autophagie berichtet und bietet damit einen möglichen Zusammenhang zwischen ribosomalen Stress und Autophagie (Katagiri et al. 2015). Diese Ergebnisse

unterstreichen weiterhin die Annahme, dass die Eisenchelatierung ein wesentlicher Treiber für die von VLX600 ausgeübten Effekte ist. Es wurde interessanterweise gezeigt, dass Krebszellen aufgrund ihrer erhöhten Zellproliferation einen höheren Bedarf an Eisen haben und dass erhöhte intrazelluläre Eisenspiegel mit einem erhöhten Krebsrisiko einhergehen (Richardson et al. 2009; Poulsen et al. 2012; Oh et al. 2016). Daher könnte die Eisenchelatierung eine mögliche zukünftige Behandlungsstrategie für das GBM sein. Dies wird bereits durch andere Studien unterstützt, die eine Reduktion des Tumorwachstums in Maus-Modellen nach Behandlung mit Eisenchelatoren zeigen konnten und zusätzlich werden einige Eisenchelatoren bereits klinisch untersucht (Lui et al. 2013; Harima et al. 2016) (NCT02688101).

Darüber hinaus wurde die translationale Bedeutung von VLX600 in einer authentischen Gehirnumgebung unter Verwendung von organotypischen Hirnschnitten und Tumorsphären bestehend aus den gliomartigen Stammzellen untersucht. Dies zeigte eine starke tumorhemmende Fähigkeit von VLX600, die teilweise von ATG5 und ATG7 abhing und unterstützt demnach die Autophagie Abhängigkeit für den durch VLX600 induzierten Zelltod. Da das GBM ein hochgradig heterogener Tumor ist, wird die Klassifikation kontinuierlich angepasst abhängig von neu identifizierten genetischen und/oder metabolischen Merkmalen. In diesem Zusammenhang beschrieb eine Studie von Garofano et al. (2021) kürzlich vier metabolische sowie entwicklungsbedingte Phänotypen unter denen der mitochondriale GBM-Subtyp ausschließlich auf OXPHOS zur Energieproduktion angewiesen war und mit der Deletion des Glukose-Protonen-Symporters *SLC45A1* assoziiert wurde. Obwohl ich die Hypothese, dass die Expression von *SLC45A1* mit der Empfindlichkeit gegenüber VLX600 korreliert, in meinen Zellmodellen nicht verifizieren konnte, ist es weiterhin von großem Interesse die unterschiedlichen metabolischen Phänotypen von Tumorzellen zu erforschen. Dies wird durch meine Ergebnisse weiter untermauert, da die Hemmung der Glykolyse keinen Nettoeffekt auf den durch VLX600 induzierten Zelltod hatte, während die Hemmung der Glutaminolyse die Toxizität von VLX600 synergistisch erhöhte. Dabei ist es wichtig zu beachten, dass dies von der Tumorart und Zelllinie abhängen kann und demnach sollten weiterhin die genetischen Hintergründe unterschiedlicher metabolischer Phänotypen weiter entschlüsselt werden um individualisierte Therapien besser anzupassen und ein Therapieversagen zu minimieren.

Zusammenfassend konnte ich in meiner Dissertation aufzeigen, dass VLX600 eine zelltödliche bulk Autophagie induziert, die von schweren mitochondrialen Schäden begleitet wird und in HIF1A-BNIP3-BNIP3L-vermittelter Mitophagie mündet. Weiterhin vermittelt die Eisenchelatierung von VLX600 Änderungen in der Histonlysinmethylierung, führt zu ribosomalen Stress und letztendlich zur Induktion eines Autophagie-abhängigen Zelltods. Die Tatsache, dass VLX600 bereits in einer Phase I Studie getestet wurde (Mody et al. 2019), macht VLX600 zu einem interessanten Wirkstoff für zukünftige Therapien. Obwohl nicht bekannt ist, ob VLX600 die Blut-Hirn Schranke passieren kann, könnte die Verwendung von Nanopartikeln den Transport an das Gehirn verbessern aber dies sollte dennoch in zukünftigen Studien weiter untersucht werden.

9. References

Abdrakhmanov A, Kulikov AV, Luchkina EA, Zhivotovsky B, Gogvadze V (2019). Involvement of mitophagy in cisplatin-induced cell death regulation. *Biol Chem* **2,** 161–170.

Affronti HC, Wellen KE (2019). Epigenetic Control of Fatty-Acid Metabolism Sustains Glioma Stem Cells. *Cancer Discov* **9,** 1161–1163.

Aita VM, Liang XH, Murty VV, Pincus DL, Yu W, Cayanis E, Kalachikov S, Gilliam TC, Levine B (1999). Cloning and genomic organization of beclin 1, a candidate tumor suppressor gene on chromosome 17q21. *Genomics* **1,** 59–65.

Aits S, Jäättelä M (2013). Lysosomal cell death at a glance. *J Cell Sci* **Pt 9** 1905–1912.

Allen GFG, Toth R, James J, Ganley IG (2013). Loss of iron triggers PINK1/Parkin-independent mitophagy. *EMBO Rep* **12,** 1127–1135.

Allen M, Bjerke M, Edlund H, Nelander S, Westermark B (2016). Origin of the U87MG glioma cell line: Good news and bad news. *Sci Transl Med* **354,** 354re3.

Alyautdin RN, Petrov VE, Langer K, Berthold A, Kharkevich DA, Kreuter J (1997). Delivery of loperamide across the blood-brain barrier with polysorbate 80-coated polybutylcyanoacrylate nanoparticles. *Pharm Res* **3,** 325–328.

Ambrosio S, Ballabio A, Majello B (2019). Histone methyl-transferases and demethylases in the autophagy regulatory network: the emerging role of KDM1A/LSD1 demethylase. *Autophagy* **2,** 187–196.

Angerilli A, Tait J, Berges J, Shcherbakova I, Pokrovsky D, Schauer T, Smialowski P, Hsam O, Mentele E, Nicetto D, et al. (2023). The histone H4K20 methyltransferase SUV4-20H1/KMT5B is required for multiciliated cell differentiation in Xenopus. *Life Sci Alliance* **7,**

Ashkenazi A, Dixit VM (1998). Death receptors: signaling and modulation. *Science* **5381,** 1305–1308.

Ashton TM, McKenna WG, Kunz-Schughart LA, Higgins GS (2018). Oxidative Phosphorylation as an Emerging Target in Cancer Therapy. *Clin Cancer Res* **11,** 2482–2490.

Azad TD, Pan J, Connolly ID, Remington A, Wilson CM, Grant GA (2015). Therapeutic strategies to improve drug delivery across the blood-brain barrier. *Neurosurg Focus* **3,** E9.

Baker MJ, Frazier AE, Gulbis JM, Ryan MT (2007). Mitochondrial protein-import machinery: correlating structure with function. *Trends Cell Biol* **9,** 456–464.

Balaban RS, Nemoto S, Finkel T (2005). Mitochondria, oxidants, and aging. *Cell* **4,** 483–495.

Bandyopadhyay S, Pai SK, Gross SC, Hirota S, Hosobe S, Miura K, Saito K, Commes T, Hayashi S, Watabe M, et al. (2003). The Drg-1 gene suppresses tumor metastasis in prostate cancer. *Cancer Res* **8,** 1731–1736.

Banelli B, Carra E, Barbieri F, Würth R, Parodi F, Pattarozzi A, Carosio R, Forlani A, Allemanni G, Marubbi D, et al. (2015). The histone demethylase KDM5A is a key factor for the resistance to temozolomide in glioblastoma. *Cell Cycle* **21,** 3418–3429.

Batara DCR, Choi M-C, Shin H-U, Kim H, Kim S-H (2021). Friend or Foe: Paradoxical Roles of Autophagy in Gliomagenesis. *Cells* **6,**

Báthori G, Parolini I, Szabó I, Tombola F, Messina A, Oliva M, Sargiacomo M, Pinto V de, Zoratti M (2000). Extramitochondrial porin: facts and hypotheses. *J Bioenerg Biomembr* **1,** 79–89.

Bellot G, Garcia-Medina R, Gounon P, Chiche J, Roux D, Pouysségur J, Mazure NM (2009). Hypoxia-induced autophagy is mediated through hypoxia-inducible factor induction of BNIP3 and BNIP3L via their BH3 domains. *Mol Cell Biol* **10,** 2570–2581.

Benz R (1994). Permeation of hydrophilic solutes through mitochondrial outer membranes: review on mitochondrial porins. *Biochim Biophys Acta* **2,** 167–196.

Berg TO, Fengsrud M, Strømhaug PE, Berg T, Seglen PO (1998). Isolation and characterization of rat liver amphisomes. Evidence for fusion of autophagosomes with both early and late endosomes. *J Biol Chem* **34,** 21883–21892.

Bernardini JP, Lazarou M, Dewson G (2017). Parkin and mitophagy in cancer. *Oncogene* **10,** 1315–1327.

Birgisdottir ÅB, Lamark T, Johansen T (2013). The LIR motif - crucial for selective autophagy. *J Cell Sci* **Pt 15** 3237–3247.

Björkhem I, Meaney S (2004). Brain cholesterol: long secret life behind a barrier. *Arterioscler Thromb Vasc Biol* **5,** 806–815.

Boya P, Kroemer G (2008). Lysosomal membrane permeabilization in cell death. *Oncogene* **50,** 6434–6451.

Bradshaw A, Wickremsekera A, Tan ST, Peng L, Davis PF, Itinteang T (2016). Cancer Stem Cell Hierarchy in Glioblastoma Multiforme. *Front Surg* 21.

Brand MD (2016). Mitochondrial generation of superoxide and hydrogen peroxide as the source of mitochondrial redox signaling. *Free Radic Biol Med* 14–31.

Brojatsch J, Lima H, Palliser D, Jacobson LS, Muehlbauer SM, Furtado R, Goldman DL, Lisanti MP, Chandran K (2015). Distinct cathepsins control necrotic cell death mediated by pyroptosis inducers and lysosome-destabilizing agents. *Cell Cycle* **7,** 964–972.

Bustin SA (2000). Absolute quantification of mRNA using real-time reverse transcription polymerase chain reaction assays. *Journal of molecular endocrinology* **2,**

Cairns RA, Mak TW (2013). Oncogenic isocitrate dehydrogenase mutations: mechanisms, models, and clinical opportunities. *Cancer Discov* **7,** 730–741.

Campos B, Wan F, Farhadi M, Ernst A, Zeppernick F, Tagscherer KE, Ahmadi R, Lohr J, Dictus C, Gdynia G, et al. (2010). Differentiation therapy exerts antitumor effects on stem-like glioma cells. *Clin Cancer Res* **10,** 2715–2728.

Carafoli E (2003). Historical review: mitochondria and calcium: ups and downs of an unusual relationship. *Trends Biochem Sci* **4,** 175–181.

Chaanine AH, Kohlbrenner E, Gamb SI, Guenzel AJ, Klaus K, Fayyaz AU, Nair KS, Hajjar RJ, Redfield MM (2016). FOXO3a regulates BNIP3 and modulates mitochondrial calcium, dynamics, and function in cardiac stress. *Am J Physiol Heart Circ Physiol* **6,** H1540-H1559.

Chakraborty A, Uechi T, Kenmochi N (2011). Guarding the 'translation apparatus': defective ribosome biogenesis and the p53 signaling pathway. *Wiley Interdiscip Rev RNA* **4,** 507–522.

Chakrama FZ, Seguin-Py S, Le Grand JN, Fraichard A, Delage-Mourroux R, Despouy G, Perez V, Jouvenot M, Boyer-Guittaut M (2010). GABARAPL1 (GEC1) associates with autophagic vesicles. *Autophagy* **4,** 495–505.

Chauhan S, Kumar S, Jain A, Ponpuak M, Mudd MH, Kimura T, Choi SW, Peters R, Mandell M, Bruun J-A, et al. (2016). TRIMs and Galectins Globally Cooperate and TRIM16 and Galectin-3 Co-direct Autophagy in Endomembrane Damage Homeostasis. *Dev Cell* **1,** 13–27.

Chen Z-W, Olsen RW (2007). GABAA receptor associated proteins: a key factor regulating GABAA receptor function. *J Neurochem* **2,** 279–294.

Chinnaiyan AM (1999). The apoptosome: heart and soul of the cell death machine. *Neoplasia* **1,** 5–15.

Cianfanelli V, Fuoco C, Lorente M, Salazar M, Quondamatteo F, Gherardini PF, Zio D de, Nazio F, Antonioli M, D'Orazio M, et al. (2015). AMBRA1 links autophagy to cell proliferation and tumorigenesis by promoting c-Myc dephosphorylation and degradation. *Nat Cell Biol* **1,** 20–30.

Clarke MF, Dick JE, Dirks PB, Eaves CJ, Jamieson CHM, Jones DL, Visvader J, Weissman IL, Wahl GM (2006). Cancer stem cells--perspectives on current status and future directions: AACR Workshop on cancer stem cells. *Cancer Res* **19,** 9339–9344.

Clarke PG (1990). Developmental cell death: morphological diversity and multiple mechanisms. *Anat Embryol (Berl)* **3,** 195–213.

Coleman ML, Sahai EA, Yeo M, Bosch M, Dewar A, Olson MF (2001). Membrane blebbing during apoptosis results from caspase-mediated activation of ROCK I. *Nat Cell Biol* **4,** 339–345.

Conradt B (2009). Genetic control of programmed cell death during animal development. *Annu Rev Genet* 493–523.

Cuddapah VA, Robel S, Watkins S, Sontheimer H (2014). A neurocentric perspective on glioma invasion. *Nat Rev Neurosci* **7,** 455–465.

Da Wang, Wang C, Wang L, Chen Y (2019). A comprehensive review in improving delivery of small-molecule chemotherapeutic agents overcoming the blood-brain/brain tumor barriers for glioblastoma treatment. *Drug Deliv* **1,** 551–565.

Dalton SO, Mellemkjaer L, Thomassen L, Mortensen PB, Johansen C (2005). Risk for cancer in a cohort of patients hospitalized for schizophrenia in Denmark, 1969-1993. *Schizophr Res* **2-3** 315–324.

Dalziel K (1980). Isocitrate dehydrogenase and related oxidative decarboxylases. *FEBS Lett* K45-55.

Dang L, White DW, Gross S, Bennett BD, Bittinger MA, Driggers EM, Fantin VR, Jang HG, Jin S, Keenan MC, et al. (2009). Cancer-associated IDH1 mutations produce 2-hydroxyglutarate. *Nature* **7274,** 739–744.

DeBerardinis RJ, Mancuso A, Daikhin E, Nissim I, Yudkoff M, Wehrli S, Thompson CB (2007). Beyond aerobic glycolysis: transformed cells can engage in glutamine metabolism that exceeds the requirement for protein and nucleotide synthesis. *Proc Natl Acad Sci U S A* **49,** 19345–19350.

Degenhardt K, Mathew R, Beaudoin B, Bray K, Anderson D, Chen G, Mukherjee C, Shi Y, Gélinas C, Fan Y, et al. (2006). Autophagy promotes tumor cell survival and restricts necrosis, inflammation, and tumorigenesis. *Cancer Cell* **1,** 51–64.

Degterev A, Huang Z, Boyce M, Li Y, Jagtap P, Mizushima N, Cuny GD, Mitchison TJ, Moskowitz MA, Yuan J (2005). Chemical inhibitor of nonapoptotic cell death with therapeutic potential for ischemic brain injury. *Nat Chem Biol* **2,** 112–119.

Deutsch EW, Csordas A, Sun Z, Jarnuczak A, Perez-Riverol Y, Ternent T, Campbell DS, Bernal-Llinares M, Okuda S, Kawano S, et al. (2017). The ProteomeXchange consortium in 2017: supporting the cultural change in proteomics public data deposition. *Nucleic Acids Res* **D1** D1100-D1106.

Dhingra R, Gang H, Wang Y, Biala AK, Aviv Y, Margulets V, Tee A, Kirshenbaum LA (2013). Bidirectional regulation of nuclear factor-κB and mammalian target of rapamycin signaling functionally links Bnip3 gene repression and cell survival of ventricular myocytes. *Circ Heart Fail* **2,** 335–343.

Dirkse A, Golebiewska A, Buder T, Nazarov PV, Muller A, Poovathingal S, Brons NHC, Leite S, Sauvageot N, Sarkisjan D, et al. (2019). Stem cell-associated heterogeneity in Glioblastoma results from intrinsic tumor plasticity shaped by the microenvironment. *Nat Commun* **1,** 1787.

Dixon SJ, Lemberg KM, Lamprecht MR, Skouta R, Zaitsev EM, Gleason CE, Patel DN, Bauer AJ, Cantley AM, Yang WS, et al. (2012). Ferroptosis: An Iron-Dependent Form of Non-Apoptotic Cell Death. *Cell* **5,** 1060–1072.

Donati G, Brighenti E, Vici M, Mazzini G, Treré D, Montanaro L, Derenzini M (2011). Selective inhibition of rRNA transcription downregulates E2F-1: a new p53-independent mechanism linking cell growth to cell proliferation. *J Cell Sci* **Pt 17** 3017–3028.

Doz F, van Tilburg CM, Geoerger B, Højgaard M, Øra I, Boni V, Capra M, Chisholm J, Chung HC, DuBois SG, et al. (2022). Efficacy and safety of larotrectinib in TRK fusion-positive primary central nervous system tumors. *Neuro Oncol* **6,** 997–1007.

Droga-Mazovec G, Bojic L, Petelin A, Ivanova S, Romih R, Repnik U, Salvesen GS, Stoka V, Turk V, Turk B (2008). Cysteine cathepsins trigger caspase-dependent cell death through cleavage of bid and antiapoptotic Bcl-2 homologues. *J Biol Chem* **27,** 19140–19150.

D'Souza GG, Wagle MA, Saxena V, Shah A (2011). Approaches for targeting mitochondria in cancer therapy. *Biochimica et Biophysica Acta (BBA) - Bioenergetics* **6,** 689–696.

Dufner A, Thomas G (1999). Ribosomal S6 kinase signaling and the control of translation. *Exp Cell Res* **1,** 100–109.

Durán RV, Oppliger W, Robitaille AM, Heiserich L, Skendaj R, Gottlieb E, Hall MN (2012). Glutaminolysis activates Rag-mTORC1 signaling. *Mol Cell* **3,** 349–358.

Eapen VV, Swarup S, Hoyer MJ, Paulo JA, Harper JW (2021). Quantitative proteomics reveals the selectivity of ubiquitin-binding autophagy receptors in the turnover of damaged lysosomes by lysophagy. *Elife*

Ekstrom TL, Pathoulas NM, Huehls AM, Kanakkanthara A, Karnitz LM (2021). VLX600 Disrupts Homologous Recombination and Synergizes with PARP Inhibitors and Cisplatin by Inhibiting Histone Lysine Demethylases. *Mol Cancer Ther* **9,** 1561–1571.

Elmaci I, Altinoz MA (2018). Targeting the cellular schizophrenia. Likely employment of the antipsychotic agent pimozide in treatment of refractory cancers and glioblastoma. *Crit Rev Oncol Hematol* 96–109.

Elmore S (2007). Apoptosis: a review of programmed cell death. *Toxicol Pathol* **4,** 495–516.

Fagan AM, Holtzman DM, Munson G, Mathur T, Schneider D, Chang LK, Getz GS, Reardon CA, Lukens J, Shah JA, et al. (1999). Unique lipoproteins secreted by primary astrocytes from wild type, apoE (-/-), and human apoE transgenic mice. *J Biol Chem* **42,** 30001–30007.

Fang BA, Kovačević Ž, Park KC, Kalinowski DS, Jansson PJ, Lane DJR, Sahni S, Des Richardson R (2014). Molecular functions of the iron-regulated metastasis suppressor, NDRG1, and its potential as a molecular target for cancer therapy. *Biochim Biophys Acta* **1,** 1–19.

Fazal L, Laudette M, Paula-Gomes S, Pons S, Conte C, Tortosa F, Sicard P, Sainte-Marie Y, Bisserier M, Lairez O, et al. (2017). Multifunctional Mitochondrial Epac1 Controls Myocardial Cell Death. *Circ Res* **4,** 645–657.

Fialova JL, Raudenska M, Jakubek M, Kejik Z, Martasek P, Babula P, Matkowski A, Filipensky P, Masarik M (2021). Novel Mitochondria-targeted Drugs for Cancer Therapy. *MRMC* **7,** 816–832.

Filomeni G, Zio D de, Cecconi F (2015). Oxidative stress and autophagy: the clash between damage and metabolic needs. *Cell Death Differ* **3,** 377–388.

Fimia GM, Stoykova A, Romagnoli A, Giunta L, Di Bartolomeo S, Nardacci R, Corazzari M, Fuoco C, Ucar A, Schwartz P, et al. (2007). Ambra1 regulates autophagy and development of the nervous system. *Nature* **7148,** 1121–1125.

Finkel T (2011). Signal transduction by reactive oxygen species. *J Cell Biol* **1,** 7–15.

Freeman BA, Crapo JD (1982). Biology of disease: free radicals and tissue injury. *Lab Invest* **5,** 412–426.

Friedman JR, Nunnari J (2014). Mitochondrial form and function. *Nature* **7483,** 335–343.

Fryknäs M, Zhang X, Bremberg U, Senkowski W, Olofsson MH, Brandt P, Persson I, D'Arcy P, Gullbo J, Nygren P, et al. (2016). Iron chelators target both proliferating and quiescent cancer cells. *Sci Rep* 38343.

Fulda S, Kögel D (2015). Cell death by autophagy: emerging molecular mechanisms and implications for cancer therapy. *Oncogene* **40,** 5105–5113.

Furuya N, Yu J, Byfield M, Pattingre S, Levine B (2005). The evolutionarily conserved domain of Beclin 1 is required for Vps34 binding, autophagy and tumor suppressor function. *Autophagy* **1,** 46–52.

Galluzzi L, Bravo-San Pedro JM, Kepp O, Kroemer G (2016). Regulated cell death and adaptive stress responses. *Cell Mol Life Sci* **11-12** 2405–2410.

Galluzzi L, Bravo-San Pedro JM, Vitale I, Aaronson SA, Abrams JM, Adam D, Alnemri ES, Altucci L, Andrews D, Annicchiarico-Petruzzelli M, et al. (2015). Essential versus accessory aspects of cell death: recommendations of the NCCD 2015. *Cell Death Differ* **1,** 58–73.

Galluzzi L, Vitale I, Aaronson SA, Abrams JM, Adam D, Agostinis P, Alnemri ES, Altucci L, Amelio I, Andrews DW, et al. (2018). Molecular mechanisms of cell death: recommendations of the Nomenclature Committee on Cell Death 2018. *Cell Death Differ* **3,** 486–541.

Gammoh N, Fraser J, Puente C, Syred HM, Kang H, Ozawa T, Du Lam, Acosta JC, Finch AJ, Holland E, et al. (2016). Suppression of autophagy impedes glioblastoma development and induces senescence. *Autophagy* **9,** 1431–1439.

Garofano L, Migliozzi S, Oh YT, D'Angelo F, Najac RD, Ko A, Frangaj B, Caruso FP, Yu K, Yuan J, et al. (2021). Pathway-based classification of glioblastoma uncovers a mitochondrial subtype with therapeutic vulnerabilities. *Nat Cancer* **2,** 141–156.

Geisbrecht BV, Gould SJ (1999). The human PICD gene encodes a cytoplasmic and peroxisomal NADP(+)-dependent isocitrate dehydrogenase. *J Biol Chem* **43,** 30527–30533.

Gelperina S, Maksimenko O, Khalansky A, Vanchugova L, Shipulo E, Abbasova K, Berdiev R, Wohlfart S, Chepurnova N, Kreuter J (2010). Drug delivery to the brain using surfactant-coated poly(lactide-co-glycolide) nanoparticles: influence of the formulation parameters. *Eur J Pharm Biopharm* **2,** 157–163.

Gerstmeier J, Possmayer A-L, Bozkurt S, Hoffmann ME, Dikic I, Herold-Mende C, Burger MC, Münch C, Kögel D, Linder B (2021). Calcitriol Promotes Differentiation of Glioma Stem-Like Cells and Increases Their Susceptibility to Temozolomide. *Cancers (Basel)* **14,**

Giladi M, Schneiderman RS, Voloshin T, Porat Y, Munster M, Blat R, Sherbo S, Bomzon Z, Urman N, Itzhaki A, et al. (2015). Mitotic Spindle Disruption by Alternating Electric Fields Leads to Improper Chromosome Segregation and Mitotic Catastrophe in Cancer Cells. *Sci Rep* 18046.

Gobin M, Nazarov PV, Warta R, Timmer M, Reifenberger G, Felsberg J, Vallar L, Chalmers AJ, Herold-Mende CC, Goldbrunner R, et al. (2019). A DNA Repair and Cell-Cycle Gene Expression Signature in Primary and Recurrent Glioblastoma: Prognostic Value and Clinical Implications. *Cancer Res* **6,** 1226–1238.

Goldschneider D, Mehlen P (2010). Dependence receptors: a new paradigm in cell signaling and cancer therapy. *Oncogene* **13,** 1865–1882.

Gómez-Sintes R, Ledesma MD, Boya P (2016). Lysosomal cell death mechanisms in aging. *Ageing Res Rev* 150–168.

Goulding H, Pinder S, Cannon P, Pearson D, Nicholson R, Snead D, Bell J, Elston CW, Robertson JF, Blamey RW (1995). A new immunohistochemical antibody for the assessment of estrogen receptor status on routine formalin-fixed tissue samples. *Hum Pathol* **3,** 291–294.

Gozuacik D, Kimchi A (2004). Autophagy as a cell death and tumor suppressor mechanism. *Oncogene* **16,** 2891–2906.

Graham FL, Smiley J, Russell WC, Nairn R (1977). Characteristics of a human cell line transformed by DNA from human adenovirus type 5. *The Journal of general virology* **1,**

Grasso CS, Tang Y, Truffaux N, Berlow NE, Liu L, Debily M-A, Quist MJ, Davis LE, Huang EC, Woo PJ, et al. (2015). Functionally defined therapeutic targets in diffuse intrinsic pontine glioma. *Nat Med* **6,** 555–559.

Gravendeel LAM, Kloosterhof NK, Bralten LBC, van Marion R, Dubbink HJ, Dinjens W, Bleeker FE, Hoogenraad CC, Michiels E, Kros JM, et al. (2010). Segregation of non-p.R132H mutations in IDH1 in distinct molecular subtypes of glioma. *Hum Mutat* **3,** E1186-99.

Gregory MA, Nemkov T, Park HJ, Zaberezhnyy V, Gehrke S, Adane B, Jordan CT, Hansen KC, D'Alessandro A, DeGregori J (2019). Targeting Glutamine Metabolism and Redox State for Leukemia Therapy. *Clin Cancer Res* **13,** 4079–4090.

Groth-Pedersen L, Jäättelä M (2013). Combating apoptosis and multidrug resistant cancers by targeting lysosomes. *Cancer Lett* **2,** 265–274.

Grummt I (2003). Life on a planet of its own: regulation of RNA polymerase I transcription in the nucleolus. *Genes Dev* **14,** 1691–1702.

Gubas A, Dikic I (2022). A guide to the regulation of selective autophagy receptors. *FEBS J* **1,** 75–89.

Günther HS, Schmidt NO, Phillips HS, Kemming D, Kharbanda S, Soriano R, Modrusan Z, Meissner H, Westphal M, Lamszus K (2008). Glioblastoma-derived stem cell-enriched cultures form distinct subgroups according to molecular and phenotypic criteria. *Oncogene* **20,**

Guo X, Gu L, Li Y, Zheng Z, Chen W, Wang Y, Wang Y, Xing H, Shi Y, Liu D, et al. (2023). Histological and molecular glioblastoma, IDH-wildtype: a real-world landscape using the 2021 WHO classification of central nervous system tumors. *Front Oncol* 1200815.

Guo Z-L, Des Richardson R, Kalinowski DS, Kovacevic Z, Tan-Un KC, Chan GC-F (2016). The novel thiosemicarbazone, di-2-pyridylketone 4-cyclohexyl-4-methyl-3-thiosemicarbazone (DpC), inhibits neuroblastoma growth in vitro and in vivo via multiple mechanisms. *J Hematol Oncol* **1,** 98.

Gupta PB, Pastushenko I, Skibinski A, Blanpain C, Kuperwasser C (2019). Phenotypic Plasticity: Driver of Cancer Initiation, Progression, and Therapy Resistance. *Cell Stem Cell* **1,** 65–78.

Gutierrez MG, Munafó DB, Berón W, Colombo MI (2004). Rab7 is required for the normal progression of the autophagic pathway in mammalian cells. *J Cell Sci* **Pt 13** 2687–2697.

Gyparaki M-T, Papavassiliou AG (2014). Lysosome: the cell's 'suicidal bag' as a promising cancer target. *Trends Mol Med* **5,** 239–241.

Hailey DW, Rambold AS, Satpute-Krishnan P, Mitra K, Sougrat R, Kim PK, Lippincott-Schwartz J (2010). Mitochondria supply membranes for autophagosome biogenesis during starvation. *Cell* **4,** 656–667.

Halatsch M-E, Kast RE, Karpel-Massler G, Mayer B, Zolk O, Schmitz B, Scheuerle A, Maier L, Bullinger L, Mayer-Steinacker R, et al. (2021). A phase Ib/IIa trial of 9 repurposed drugs combined with temozolomide for the treatment of recurrent glioblastoma: CUSP9v3. *Neurooncol Adv* **1,** vdab075.

Hamacher-Brady A, Brady NR (2016). Mitophagy programs: mechanisms and physiological implications of mitochondrial targeting by autophagy. *Cell Mol Life Sci* **4,** 775–795.

Hamasaki M, Furuta N, Matsuda A, Nezu A, Yamamoto A, Fujita N, Oomori H, Noda T, Haraguchi T, Hiraoka Y, et al. (2013). Autophagosomes form at ER-mitochondria contact sites. *Nature* **7441,** 389–393.

Hanada T, Noda NN, Satomi Y, Ichimura Y, Fujioka Y, Takao T, Inagaki F, Ohsumi Y (2007). The Atg12-Atg5 conjugate has a novel E3-like activity for protein lipidation in autophagy. *J Biol Chem* **52,** 37298–37302.

Hansford RG (1994). Physiological role of mitochondrial Ca2+ transport. *J Bioenerg Biomembr* **5,** 495–508.

Hao Y, Wang L, Zhao Y, Meng D, Li D, Li H, Zhang B, Shi J, Zhang H, Zhang Z, et al. (2015). Targeted Imaging and Chemo-Phototherapy of Brain Cancer by a Multifunctional Drug Delivery System. *Macromol Biosci* **11,** 1571–1585.

Hara T, Takamura A, Kishi C, Iemura S-I, Natsume T, Guan J-L, Mizushima N (2008). FIP200, a ULK-interacting protein, is required for autophagosome formation in mammalian cells. *J Cell Biol* **3,** 497–510.

Hara Y, Yanatori I, Tanaka A, Kishi F, Lemasters JJ, Nishina S, Sasaki K, Hino K (2020). Iron loss triggers mitophagy through induction of mitochondrial ferritin. *EMBO Rep* **11,** e50202.

Harima H, Kaino S, Takami T, Shinoda S, Matsumoto T, Fujisawa K, Yamamoto N, Yamasaki T, Sakaida I (2016). Deferasirox, a novel oral iron chelator, shows antiproliferative activity against pancreatic cancer in vitro and in vivo. *BMC Cancer* **1,** 702.

Hashizume R, Andor N, Ihara Y, Lerner R, Gan H, Chen X, Fang D, Huang X, Tom MW, Ngo V, et al. (2014). Pharmacologic inhibition of histone demethylation as a therapy for pediatric brainstem glioma. *Nat Med* **12,** 1394–1396.

Hay N, Sonenberg N (2004). Upstream and downstream of mTOR. *Genes Dev* **16,** 1926–1945.

Hayashi-Nishino M, Fujita N, Noda T, Yamaguchi A, Yoshimori T, Yamamoto A (2009). A subdomain of the endoplasmic reticulum forms a cradle for autophagosome formation. *Nat Cell Biol* **12,** 1433–1437.

He C, Klionsky DJ (2009). Regulation mechanisms and signaling pathways of autophagy. *Annu Rev Genet* 67–93.

He H, Dang Y, Dai F, Guo Z, Wu J, She X, Pei Y, Chen Y, Ling W, Wu C, et al. (2003). Post-translational modifications of three members of the human MAP1LC3 family and detection of a novel type of modification for MAP1LC3B. *J Biol Chem* **31,** 29278–29287.

He Z, Liu H, Agostini M, Yousefi S, Perren A, Tschan MP, Mak TW, Melino G, Simon HU (2013). p73 regulates autophagy and hepatocellular lipid metabolism through a transcriptional activation of the ATG5 gene. *Cell Death Differ* **10,** 1415–1424.

Heckmann BL, Green DR (2019). LC3-associated phagocytosis at a glance. *J Cell Sci* **5,**

Heo J-M, Ordureau A, Paulo JA, Rinehart J, Harper JW (2015). The PINK1-PARKIN Mitochondrial Ubiquitylation Pathway Drives a Program of OPTN/NDP52 Recruitment and TBK1 Activation to Promote Mitophagy. *Mol Cell* **1,** 7–20.

Hetschko H, Voss V, Horn S, Seifert V, Prehn JHM, Kögel D (2008). Pharmacological inhibition of Bcl-2 family members reactivates TRAIL-induced apoptosis in malignant glioma. *J Neurooncol* **3,** 265–272.

Hirpara J, Eu JQ, Tan JKM, Wong AL, Clement M-V, Kong LR, Ohi N, Tsunoda T, Qu J, Goh BC, et al. (2019). Metabolic reprogramming of oncogene-addicted cancer cells to OXPHOS as a mechanism of drug resistance. *Redox Biol* 101076.

Hoang-Minh LB, Siebzehnrubl FA, Yang C, Suzuki-Hatano S, Dajac K, Loche T, Andrews N, Schmoll Massari M, Patel J, Amin K, et al. (2018). Infiltrative and drug-resistant slow-cycling cells support metabolic heterogeneity in glioblastoma. *EMBO J* **23,**

Holler N, Zaru R, Micheau O, Thome M, Attinger A, Valitutti S, Bodmer JL, Schneider P, Seed B, Tschopp J (2000). Fas triggers an alternative, caspase-8-independent cell death pathway using the kinase RIP as effector molecule. *Nat Immunol* **6,** 489–495.

Horton JD, Shimomura I, Brown MS, Hammer RE, Goldstein JL, Shimano H (1998). Activation of cholesterol synthesis in preference to fatty acid synthesis in liver and adipose tissue of transgenic mice overproducing sterol regulatory element-binding protein-2. *J Clin Invest* **11,** 2331–2339.

Hosokawa N, Hara T, Kaizuka T, Kishi C, Takamura A, Miura Y, Iemura S-I, Natsume T, Takehana K, Yamada N, et al. (2009). Nutrient-dependent mTORC1 association with the ULK1-Atg13-FIP200 complex required for autophagy. *Mol Biol Cell* **7,** 1981–1991.

Howells LM, Berry DP, Elliott PJ, Jacobson EW, Hoffmann E, Hegarty B, Brown K, Steward WP, Gescher AJ (2011). Phase I randomized, double-blind pilot study of micronized resveratrol (SRT501) in patients with hepatic metastases--safety, pharmacokinetics, and pharmacodynamics. *Cancer Prev Res (Phila)* **9,** 1419–1425.

Hu Y-L, DeLay M, Jahangiri A, Molinaro AM, Rose SD, Carbonell WS, Aghi MK (2012). Hypoxia-induced autophagy promotes tumor cell survival and adaptation to antiangiogenic treatment in glioblastoma. *Cancer Res* **7,** 1773–1783.

Hua L, Yan D, Wan C, Hu B (2022). Nucleolus and Nucleolar Stress: From Cell Fate Decision to Disease Development. *Cells* **19,**

Huang T, Xu T, Wang Y, Zhou Y, Yu D, Wang Z, He L, Chen Z, Zhang Y, Davidson D, et al. (2021). Cannabidiol inhibits human glioma by induction of lethal mitophagy through activating TRPV4. *Autophagy* **11,** 3592–3606.

Hubert V, Peschel A, Langer B, Gröger M, Rees A, Kain R (2016). LAMP-2 is required for incorporating syntaxin-17 into autophagosomes and for their fusion with lysosomes. *Biol Open* **10,** 1516–1529.

Iadevaia V, Caldarola S, Biondini L, Gismondi A, Karlsson S, Dianzani I, Loreni F (2010). PIM1 kinase is destabilized by ribosomal stress causing inhibition of cell cycle progression. *Oncogene* **40,** 5490–5499.

Ichikawa T, OTANI Y, Kurozumi K, Date I (2016). Phenotypic Transition as a Survival Strategy of Glioma. *Neurol Med Chir (Tokyo)* **7,** 387–395.

Ichimura Y, Kirisako T, Takao T, Satomi Y, Shimonishi Y, Ishihara N, Mizushima N, Tanida I, Kominami E, Ohsumi M, et al. (2000). A ubiquitin-like system mediates protein lipidation. *Nature* **6811,** 488–492.

Infantino V, Santarsiero A, Convertini P, Todisco S, Iacobazzi V (2021). Cancer Cell Metabolism in Hypoxia: Role of HIF-1 as Key Regulator and Therapeutic Target. *Int J Mol Sci* **11,**

Ishii N, Maier D, Merlo A, Tada M, Sawamura Y, Diserens AC, van Meir EG (1999). Frequent co-alterations of TP53, p16/CDKN2A, p14ARF, PTEN tumor suppressor genes in human glioma cell lines. *Brain Pathol* **3,** 469–479.

Iwashita H, Torii S, Nagahora N, Ishiyama M, Shioji K, Sasamoto K, Shimizu S, Okuma K (2017). Live Cell Imaging of Mitochondrial Autophagy with a Novel Fluorescent Small Molecule. *ACS Chem Biol* **10,** 2546–2551.

Izzo V, Bravo-San Pedro JM, Sica V, Kroemer G, Galluzzi L (2016). Mitochondrial Permeability Transition: New Findings and Persisting Uncertainties. *Trends Cell Biol* **9,** 655–667.

Jacquet M, Guittaut M, Fraichard A, Despouy G (2021). The functions of Atg8-family proteins in autophagy and cancer: linked or unrelated? *Autophagy* **3,** 599–611.

Jagtiani E, Yeolekar M, Naik S, Patravale V (2022). In vitro blood brain barrier models: An overview. *J Control Release* 13–30.

Jandaghi P, Najafabadi HS, Bauer AS, Papadakis AI, Fassan M, Hall A, Monast A, Knebel Doeberitz M von, Neoptolemos JP, Costello E, et al. (2016). Expression of DRD2 Is Increased in Human Pancreatic Ductal Adenocarcinoma and Inhibitors Slow Tumor Growth in Mice. *Gastroenterology* **6,** 1218–1231.

Jiang Z, Yu F, Li M (2018). Upregulation of BCL2 19 kD Protein-Interacting Protein 3 (BNIP3) is Predictive of Unfavorable Prognosis in Uveal Melanoma. *Med Sci Monit* 4711–4717.

Jin L, Alesi GN, Kang S (2016). Glutaminolysis as a target for cancer therapy. *Oncogene* **28,** 3619–3625.

Jin L, Li D, Alesi GN, Fan J, Kang H-B, Lu Z, Boggon TJ, Jin P, Yi H, Wright ER, et al. (2015). Glutamate dehydrogenase 1 signals through antioxidant glutathione peroxidase 1 to regulate redox homeostasis and tumor growth. *Cancer Cell* **2,** 257–270.

Kabeya Y, Mizushima N, Yamamoto A, Oshitani-Okamoto S, Ohsumi Y, Yoshimori T (2004). LC3, GABARAP and GATE16 localize to autophagosomal membrane depending on form-II formation. *J Cell Sci* **Pt 13** 2805–2812.

Kaiser WJ, Sridharan H, Huang C, Mandal P, Upton JW, Gough PJ, Sehon CA, Marquis RW, Bertin J, Mocarski ES (2013). Toll-like Receptor 3-mediated Necrosis via TRIF, RIP3, and MLKL*. *J Biol Chem* **43,** 31268–31279.

Kaizuka T, Morishita H, Hama Y, Tsukamoto S, Matsui T, Toyota Y, Kodama A, Ishihara T, Mizushima T, Mizushima N (2016). An Autophagic Flux Probe that Releases an Internal Control. *Mol Cell* **4,** 835–849.

Kanzawa T, Zhang L, Xiao L, Germano IM, Kondo Y, Kondo S (2005). Arsenic trioxide induces autophagic cell death in malignant glioma cells by upregulation of mitochondrial cell death protein BNIP3. *Oncogene* **6,** 980–991.

Karch J, Kwong JQ, Burr AR, Sargent MA, Elrod JW, Peixoto PM, Martinez-Caballero S, Osinska H, Cheng EH-Y, Robbins J, et al. (2013). Bax and Bak function as the outer membrane component of the mitochondrial permeability pore in regulating necrotic cell death in mice. *Elife* e00772.

Karpathiou G, Sivridis E, Koukourakis M, Mikroulis D, Bouros D, Froudarakis M, Bougioukas G, Maltezos E, Giatromanolaki A (2013). Autophagy and Bcl-2/BNIP3 death regulatory pathway in non-small cell lung carcinomas. *APMIS* **7,** 592–604.

Kast RE (2010). Glioblastoma chemotherapy adjunct via potent serotonin receptor-7 inhibition using currently marketed high-affinity antipsychotic medicines. *Br J Pharmacol* **3,** 481–487.

Katagiri N, Kuroda T, Kishimoto H, Hayashi Y, Kumazawa T, Kimura K (2015). The nucleolar protein nucleophosmin is essential for autophagy induced by inhibiting Pol I transcription. *Sci Rep* 8903.

Katayama H, Kogure T, Mizushima N, Yoshimori T, Miyawaki A (2011). A sensitive and quantitative technique for detecting autophagic events based on lysosomal delivery. *Chem Biol* **8,** 1042–1052.

Katayama M, Kawaguchi T, Berger MS, Pieper RO (2007). DNA damaging agent-induced autophagy produces a cytoprotective adenosine triphosphate surge in malignant glioma cells. *Cell Death Differ* **3,** 548–558.

Kenific CM, Stehbens SJ, Goldsmith J, Leidal AM, Faure N, Ye J, Wittmann T, Debnath J (2016). NBR1 enables autophagy-dependent focal adhesion turnover. *J Cell Biol* **5,** 577–590.

Khatami SH, Karami N, Taheri-Anganeh M, Taghvimi S, Tondro G, Khorsand M, Soltani Fard E, Sedighimehr N, Kazemi M, Rahimi Jaberi K, et al. (2023). Exosomes: Promising Delivery Tools for Overcoming Blood-Brain Barrier and Glioblastoma Therapy. *Mol Neurobiol* **8,** 4659–4678.

Kihara A, Noda T, Ishihara N, Ohsumi Y (2001). Two distinct Vps34 phosphatidylinositol 3-kinase complexes function in autophagy and carboxypeptidase Y sorting in Saccharomyces cerevisiae. *J Cell Biol* **3,** 519–530.

Killackey SA, Philpott DJ, Girardin SE (2020). Mitophagy pathways in health and disease. *J Cell Biol* **11,**

Kirisako T, Ichimura Y, Okada H, Kabeya Y, Mizushima N, Yoshimori T, Ohsumi M, Takao T, Noda T, Ohsumi Y (2000). The reversible modification regulates the membrane-binding state of Apg8/Aut7 essential for autophagy and the cytoplasm to vacuole targeting pathway. *J Cell Biol* **2,** 263–276.

Kirkegaard T, Jäättelä M (2009). Lysosomal involvement in cell death and cancer. *Biochim Biophys Acta* **4,** 746–754.

Kirkin V, Rogov VV (2019). A Diversity of Selective Autophagy Receptors Determines the Specificity of the Autophagy Pathway. *Mol Cell* **2,** 268–285.

Kirson ED, Dbalý V, Tovarys F, Vymazal J, Soustiel JF, Itzhaki A, Mordechovich D, Steinberg-Shapira S, Gurvich Z, Schneiderman R, et al. (2007). Alternating electric fields arrest cell proliferation in animal tumor models and human brain tumors. *Proc Natl Acad Sci U S A* **24,** 10152–10157.

Kischkel FC, Hellbardt S, Behrmann I, Germer M, Pawlita M, Krammer PH, Peter ME (1995). Cytotoxicity-dependent APO-1 (Fas/CD95)-associated proteins form a death-inducing signaling complex (DISC) with the receptor. *EMBO J* **22,** 5579–5588.

Klionsky DJ (2007). Autophagy: from phenomenology to molecular understanding in less than a decade. *Nat Rev Mol Cell Biol* **11,** 931–937.

Klionsky DJ, Abdelmohsen K, Abe A, Abedin MJ, Abeliovich H, Acevedo Arozena A, Adachi H, Adams CM, Adams PD, Adeli K, et al. (2016). Guidelines for the use and interpretation of assays for monitoring autophagy (3rd edition). *Autophagy* **1,** 1–222.

Kögel D, Fulda S, Mittelbronn M (2010). Therapeutic exploitation of apoptosis and autophagy for glioblastoma. *Anticancer Agents Med Chem* **6,** 438–449.

Kooistra SM, Helin K (2012). Molecular mechanisms and potential functions of histone demethylases. *Nat Rev Mol Cell Biol* **5,** 297–311.

Kornhuber J, Muehlbacher M, Trapp S, Pechmann S, Friedl A, Reichel M, Mühle C, Terfloth L, Groemer TW, Spitzer GM, et al. (2011). Identification of novel functional inhibitors of acid sphingomyelinase. *PLoS One* **8,** e23852.

Kornhuber J, Tripal P, Reichel M, Terfloth L, Bleich S, Wiltfang J, Gulbins E (2008). Identification of new functional inhibitors of acid sphingomyelinase using a structure-property-activity relation model. *J Med Chem* **2,** 219–237.

Kouzarides T (2007). Chromatin modifications and their function. *Cell* **4,** 693–705.

Kovar J, Stunz LL, Stewart BC, Kriegerbeckova K, Ashman RF, Kemp JD (1997). Direct evidence that iron deprivation induces apoptosis in murine lymphoma 38C13. *Pathobiology* **2,** 61–68.

Krebs HA, Johnson WA (1980). The role of citric acid in intermediate metabolism in animal tissues. *FEBS Lett* K1-10.

Kreso A, Dick JE (2014). Evolution of the cancer stem cell model. *Cell Stem Cell* **3,** 275–291.

Kristiana I, Sharpe LJ, Catts VS, Lutze-Mann LH, Brown AJ (2010). Antipsychotic drugs upregulate lipogenic gene expression by disrupting intracellular trafficking of lipoprotein-derived cholesterol. *Pharmacogenomics J* **5,** 396–407.

Kroemer G, Levine B (2008). Autophagic cell death: the story of a misnomer. *Nat Rev Mol Cell Biol* **12,** 1004–1010.

Kulikov AV, Luchkina EA, Gogvadze V, Zhivotovsky B (2017). Mitophagy: Link to cancer development and therapy. *Biochem Biophys Res Commun* **3,** 432–439.

Kuma A, Mizushima N, Ishihara N, Ohsumi Y (2002). Formation of the approximately 350-kDa Apg12-Apg5.Apg16 multimeric complex, mediated by Apg16 oligomerization, is essential for autophagy in yeast. *J Biol Chem* **21,** 18619–18625.

Kuramoto K, Yamamoto M, Suzuki S, Sanomachi T, Togashi K, Seino S, Kitanaka C, Okada M (2020). Verteporfin inhibits oxidative phosphorylation and induces cell death specifically in glioma stem cells. *FEBS J* **10,** 2023–2036.

Kurdistani SK, Arizti P, Reimer CL, Sugrue MM, Aaronson SA, Lee SW (1998). Inhibition of tumor cell growth by RTP/rit42 and its responsiveness to p53 and DNA damage. *Cancer Res* **19,** 4439–4444.

Kurz T, Terman A, Gustafsson B, Brunk UT (2008). Lysosomes and oxidative stress in aging and apoptosis. *Biochim Biophys Acta* **11,** 1291–1303.

Kuwana T, Mackey MR, Perkins G, Ellisman MH, Latterich M, Schneiter R, Green DR, Newmeyer DD (2002). Bid, Bax, and lipids cooperate to form supramolecular openings in the outer mitochondrial membrane. *Cell* **3,** 331–342.

Kuzu OF, Gowda R, Noory MA, Robertson GP (2017). Modulating cancer cell survival by targeting intracellular cholesterol transport. *Br J Cancer* **4,** 513–524.

Latham JA, Dent SYR (2007). Cross-regulation of histone modifications. *Nat Struct Mol Biol* **11,** 1017–1024.

Laubach K, Zhang J, Chen X (2021). The p53 Family: A Role in Lipid and Iron Metabolism. *Front Cell Dev Biol* 715974.

Lazarou M, Sliter DA, Kane LA, Sarraf SA, Wang C, Burman JL, Sideris DP, Fogel AI, Youle RJ (2015). The ubiquitin kinase PINK1 recruits autophagy receptors to induce mitophagy. *Nature* **7565,** 309–314.

Lee J-K, Nam D-H, Lee J (2016). Repurposing antipsychotics as glioblastoma therapeutics: Potentials and challenges. *Oncol Lett* **2,** 1281–1286.

Leif H, Sled VD, Ohnishi T, Weiss H, Friedrich T (1995). Isolation and Characterization of the Proton-translocating NADH:ubiquinone Oxidoreductase from Escherichia coli. *Eur J Biochem* **2,** 538–548.

Lemarie A, Grimm S (2011). Mitochondrial respiratory chain complexes: apoptosis sensors mutated in cancer? *Oncogene* **38,** 3985–4003.

Lemberg KM, Gori SS, Tsukamoto T, Rais R, Slusher BS (2022). Clinical development of metabolic inhibitors for oncology. *J Clin Invest* **1,**

Levine B (2007). Cell biology: autophagy and cancer. *Nature* **7137,** 745–747.

Li H, Zhu H, Xu CJ, Yuan J (1998). Cleavage of BID by caspase 8 mediates the mitochondrial damage in the Fas pathway of apoptosis. *Cell* **4,** 491–501.

Li J, Yu L, Zhang H, Wu J, Yuan J, Li X, Li M (2009). Down-regulation of pescadillo inhibits proliferation and tumorigenicity of breast cancer cells. *Cancer Sci* **12,** 2255–2260.

Li J, Zhu S, Kozono D, Ng K, Futalan D, Shen Y, Akers JC, Steed T, Kushwaha D, Schlabach M, et al. (2014). Genome-wide shRNA screen revealed integrated mitogenic signaling between dopamine receptor D2 (DRD2) and epidermal growth factor receptor (EGFR) in glioblastoma. *Oncotarget* **4,** 882–893.

Liang XH, Jackson S, Seaman M, Brown K, Kempkes B, Hibshoosh H, Levine B (1999). Induction of autophagy and inhibition of tumorigenesis by beclin 1. *Nature* **6762,** 672–676.

Liao H, Gaur A, Mauvais C, Denicourt C (2021). p53 induces a survival transcriptional response after nucleolar stress. *Mol Biol Cell* **20,** ar3.

Lill R, Mühlenhoff U (2008). Maturation of iron-sulfur proteins in eukaryotes: mechanisms, connected processes, and diseases. *Annu Rev Biochem* 669–700.

Lin G-M, Chen Y-J, Kuo D-J, Jaiteh LES, Wu Y-C, Lo T-S, Li Y-H (2013). Cancer incidence in patients with schizophrenia or bipolar disorder: a nationwide population-based study in Taiwan, 1997-2009. *Schizophr Bull* **2,** 407–416.

Lin H, Patel S, Affleck VS, Wilson I, Turnbull DM, Joshi AR, Maxwell R, Stoll EA (2017). Fatty acid oxidation is required for the respiration and proliferation of malignant glioma cells. *Neuro Oncol* **1,** 43–54.

Linder B, Kögel D (2019). Autophagy in Cancer Cell Death. *Biology (Basel)* **4,**

Linder B, Wehle A, Hehlgans S, Bonn F, Dikic I, Rödel F, Seifert V, Kögel D (2019). Arsenic Trioxide and (-)-Gossypol Synergistically Target Glioma Stem-Like Cells via Inhibition of Hedgehog and Notch Signaling. *Cancers (Basel)* **3,**

Linkermann A, Green DR (2014). Necroptosis. *N Engl J Med* **5,** 455–465.

Liu B, Cheng J, Zhang X, Wang R, Zhang W, Lin H, Xiao X, Cai S, Chen X, Cheng H (2010). Global histone modification patterns as prognostic markers to classify glioma patients. *Cancer Epidemiol Biomarkers Prev* **11,** 2888–2896.

Liu EY, Ryan KM (2012). Autophagy and cancer--issues we need to digest. *J Cell Sci* **Pt 10** 2349–2358.

Liu Y-S, Huang B-R, Lin C-J, Shen C-K, Lai S-W, Chen C-W, Lin H-J, Lin C-H, Hsieh Y-C, Lu D-Y (2021). Paliperidone Inhibits Glioblastoma Growth in Mouse Brain Tumor Model and Reduces PD-L1 Expression. *Cancers (Basel)* **17,**

Liu Z, Jiang X, Gao L, Liu X, Li J, Huang X, Zeng T (2019). Synergistic Suppression of Glioblastoma Cell Growth by Combined Application of Temozolomide and Dopamine D2 Receptor Antagonists. *World Neurosurg* e468-e477.

Livak KJ, Schmittgen TD (2001). Analysis of relative gene expression data using real-time quantitative PCR and the 2(-Delta Delta C(T)) Method. *Methods* **4,** 402–408.

Louis DN, Perry A, Wesseling P, Brat DJ, Cree IA, Figarella-Branger D, Hawkins C, Ng HK, Pfister SM, Reifenberger G, et al. (2021). The 2021 WHO Classification of Tumors of the Central Nervous System: a summary. *Neuro Oncol* **8,** 1231–1251.

Lui GYL, Obeidy P, Ford SJ, Tselepis C, Sharp DM, Jansson PJ, Kalinowski DS, Kovacevic Z, Lovejoy DB, Des Richardson R (2013). The iron chelator, deferasirox, as a novel strategy for cancer treatment: oral activity against human lung tumor xenografts and molecular mechanism of action. *Mol Pharmacol* **1,** 179–190.

Macintosh RL, Timpson P, Thorburn J, Anderson KI, Thorburn A, Ryan KM (2012). Inhibition of autophagy impairs tumor cell invasion in an organotypic model. *Cell Cycle* **10,** 2022–2029.

Maejima I, Takahashi A, Omori H, Kimura T, Takabatake Y, Saitoh T, Yamamoto A, Hamasaki M, Noda T, Isaka Y, et al. (2013). Autophagy sequesters damaged lysosomes to control lysosomal biogenesis and kidney injury. *EMBO J* **17,** 2336–2347.

Maire CL, Fuh MM, Kaulich K, Fita KD, Stevic I, Heiland DH, Welsh JA, Jones JC, Görgens A, Ricklefs T, et al. (2021). Genome-wide methylation profiling of glioblastoma cell-derived extracellular vesicle DNA allows tumor classification. *Neuro Oncol* **7,** 1087–1099.

Mallm J-P, Windisch P, Biran A, Gal Z, Schumacher S, Glass R, Herold-Mende C, Meshorer E, Barbus M, Rippe K (2020). Glioblastoma initiating cells are sensitive to histone demethylase inhibition due to epigenetic deregulation. *Int J Cancer* **5,** 1281–1292.

Manea AJ, Ray SK (2023). Advanced Bioinformatics Analysis and Genetic Technologies for Targeting Autophagy in Glioblastoma Multiforme. *Cells* **6,**

Manni W, Jianxin X, Weiqi H, Siyuan C, Huashan S (2022). JMJD family proteins in cancer and inflammation. *Signal Transduct Target Ther* **1,** 304.

Mansuy V, Boireau W, Fraichard A, Schlick J-L, Jouvenot M, Delage-Mourroux R (2004). GEC1, a protein related to GABARAP, interacts with tubulin and GABA(A) receptor. *Biochem Biophys Res Commun* **2,** 639–648.

Marinković M, Šprung M, Novak I (2021). Dimerization of mitophagy receptor BNIP3L/NIX is essential for recruitment of autophagic machinery. *Autophagy* **5,** 1232–1243.

Martin SJ, Finucane DM, Amarante-Mendes GP, O'Brien GA, Green DR (1996). Phosphatidylserine externalization during CD95-induced apoptosis of cells and cytoplasts requires ICE/CED-3 protease activity. *J Biol Chem* **46,** 28753–28756.

Marzo I, Brenner C, Zamzami N, Jürgensmeier JM, Susin SA, Vieira HL, Prévost MC, Xie Z, Matsuyama S, Reed JC, et al. (1998). Bax and adenine nucleotide translocator cooperate in the mitochondrial control of apoptosis. *Science* **5385,** 2027–2031.

Matsumoto Y, Ichikawa T, Kurozumi K, Date I (2022). Current Insights into Mesenchymal Signatures in Glioblastoma. *Acta Med Okayama* **5,** 489–502.

Mercer CA, Kaliappan A, Dennis PB (2009). A novel, human Atg13 binding protein, Atg101, interacts with ULK1 and is essential for macroautophagy. *Autophagy* **5,** 649–662.

Meyer (2019). Molecular targeting of autophagy in glioblastoma. Dissertation. Johann Wolfgang Goethe-Universität Frankfurt am Main

Meyer N, Henkel L, Linder B, Zielke S, Tascher G, Trautmann S, Geisslinger G, Münch C, Fulda S, Tegeder I, et al. (2021). Autophagy activation, lipotoxicity and lysosomal membrane permeabilization synergize to promote pimozide- and loperamide-induced glioma cell death. *Autophagy* **11,** 3424–3443.

Meyer N, Zielke S, Michaelis JB, Linder B, Warnsmann V, Rakel S, Osiewacz HD, Fulda S, Mittelbronn M, Münch C, et al. (2018). AT 101 induces early mitochondrial dysfunction and HMOX1 (heme oxygenase 1) to trigger mitophagic cell death in glioma cells. *Autophagy* **10,** 1693–1709.

Mindell JA (2012). Lysosomal acidification mechanisms. *Annu Rev Physiol* 69–86.

Mitchell P (1961). Coupling of phosphorylation to electron and hydrogen transfer by a chemi-osmotic type of mechanism. *Nature* 144–148.

Mizushima N, Kuma A, Kobayashi Y, Yamamoto A, Matsubae M, Takao T, Natsume T, Ohsumi Y, Yoshimori T (2003). Mouse Apg16L, a novel WD-repeat protein, targets to the autophagic isolation membrane with the Apg12-Apg5 conjugate. *J Cell Sci* **Pt 9** 1679–1688.

Mody K, Mansfield AS, Vemireddy L, Nygren P, Gulbo J, Borad M (2019). A phase I study of the safety and tolerability of VLX600, an Iron Chelator, in patients with refractory advanced solid tumors. *Invest New Drugs* **4,** 684–692.

Moehle EA, Shen K, Dillin A (2019). Mitochondrial proteostasis in the context of cellular and organismal health and aging. *J Biol Chem* **14,** 5396–5407.

Mohrenz IV, Antonietti P, Pusch S, Capper D, Balss J, Voigt S, Weissert S, Mukrowsky A, Frank J, Senft C, et al. (2013). Isocitrate dehydrogenase 1 mutant R132H sensitizes glioma cells to BCNU-induced oxidative stress and cell death. *Apoptosis* **11,** 1416–1425.

Molina JR, Sun Y, Protopopova M, Gera S, Bandi M, Bristow C, McAfoos T, Morlacchi P, Ackroyd J, Agip A-NA, et al. (2018). An inhibitor of oxidative phosphorylation exploits cancer vulnerability. *Nat Med* **7,** 1036–1046.

Mosmann T (1983). Rapid colorimetric assay for cellular growth and survival: application to proliferation and cytotoxicity assays. *J Immunol Methods* **1-2** 55–63.

Müller S, Sindikubwabo F, Cañeque T, Lafon A, Versini A, Lombard B, Loew D, Wu T-D, Ginestier C, Charafe-Jauffret E, et al. (2020). CD44 regulates epigenetic plasticity by mediating iron endocytosis. *Nat Chem* **10,** 929–938.

Murakawa T, Yamaguchi O, Hashimoto A, Hikoso S, Takeda T, Oka T, Yasui H, Ueda H, Akazawa Y, Nakayama H, et al. (2015). Bcl-2-like protein 13 is a mammalian Atg32 homologue that mediates mitophagy and mitochondrial fragmentation. *Nat Commun* 7527.

Murphy JM, Czabotar PE, Hildebrand JM, Lucet IS, Zhang J-G, Alvarez-Diaz S, Lewis R, Lalaoui N, Metcalf D, Webb AI, et al. (2013). The pseudokinase MLKL mediates necroptosis via a molecular switch mechanism. *Immunity* **3,** 443–453.

Nagata S (2005). DNA degradation in development and programmed cell death. *Annu Rev Immunol* 853–875.

Nassour J, Radford R, Correia A, Fusté JM, Schoell B, Jauch A, Shaw RJ, Karlseder J (2019). Autophagic cell death restricts chromosomal instability during replicative crisis. *Nature* **7741,** 659–663.

Neuzil J, Dong L-F, Rohlena J, Truksa J, Ralph SJ (2013). Classification of mitocans, anti-cancer drugs acting on mitochondria. *Mitochondrion* **3,** 199–208.

Nguyen AV, Martinez M, Stamos MJ, Moyer MP, Planutis K, Hope C, Holcombe RF (2009). Results of a phase I pilot clinical trial examining the effect of plant-derived resveratrol and grape powder on Wnt pathway target gene expression in colonic mucosa and colon cancer. *Cancer Manag Res* 25–37.

Ni H-M, Williams JA, Ding W-X (2015). Mitochondrial dynamics and mitochondrial quality control. *Redox Biol* 6–13.

Nikoletopoulou V, Markaki M, Palikaras K, Tavernarakis N (2013). Crosstalk between apoptosis, necrosis and autophagy. *Biochim Biophys Acta* **12,** 3448–3459.

Ning K, Shao Y, He Y, Wang F, Cui X, Liu F, Li D, Li F (2020). Histone demethylase Jumonji domain-containing 1A inhibits proliferation and progression of gastric cancer by upregulating runt-related transcription factor 3. *Cancer Sci* **10,** 3679–3692.

Niu Y, Lin Z, Wan A, Chen H, Liang H, Sun L, Wang Y, Li X, Xiong X-F, Wei B, et al. (2019). RNA N6-methyladenosine demethylase FTO promotes breast tumor progression through inhibiting BNIP3. *Mol Cancer* **1,** 46.

Noda NN, Ohsumi Y, Inagaki F (2010). Atg8-family interacting motif crucial for selective autophagy. *FEBS Lett* **7,** 1379–1385.

Nolfi-Donegan D, Braganza A, Shiva S (2020). Mitochondrial electron transport chain: Oxidative phosphorylation, oxidant production, and methods of measurement. *Redox Biol* 101674.

Oh C-K, Park S-H, Kim J, Moon Y (2016). Non-mutagenic Suppression of Enterocyte Ferroportin 1 by Chemical Ribosomal Inactivation via p38 Mitogen-activated Protein Kinase (MAPK)-mediated Regulation: EVIDENCE FOR ENVIRONMENTAL HEMOCHROMATOSIS. *J Biol Chem* **38,** 19858–19872.

Ohsumi Y (2001). Molecular dissection of autophagy: two ubiquitin-like systems. *Nat Rev Mol Cell Biol* **3,** 211–216.

Ojha R, Jha V, Singh SK, Bhattacharyya S (2014a). Autophagy inhibition suppresses the tumorigenic potential of cancer stem cell enriched side population in bladder cancer. *Biochim Biophys Acta* **11,** 2073–2086.

Ojha R, Singh SK, Bhattacharyya S, Dhanda RS, Rakha A, Mandal AK, Jha V (2014b). Inhibition of grade dependent autophagy in urothelial carcinoma increases cell death under nutritional limiting condition and potentiates the cytotoxicity of chemotherapeutic agent. *J Urol* **6,** 1889–1898.

Oliver CL, Miranda MB, Shangary S, Land S, Wang S, Johnson DE (2005). (-)-Gossypol acts directly on the mitochondria to overcome Bcl-2- and Bcl-X(L)-mediated apoptosis resistance. *Mol Cancer Ther* **1,** 23–31.

Oltersdorf T, Elmore SW, Shoemaker AR, Armstrong RC, Augeri DJ, Belli BA, Bruncko M, Deckwerth TL, Dinges J, Hajduk PJ, et al. (2005). An inhibitor of Bcl-2 family proteins induces regression of solid tumours. *Nature* **7042,** 677–681.

O'Malley J, Kumar R, Inigo J, Yadava N, Chandra D (2020). Mitochondrial Stress Response and Cancer. *Trends Cancer* **8,** 688–701.

Ormerod MG, Sun XM, Brown D, Snowden RT, Cohen GM (1993). Quantification of apoptosis and necrosis by flow cytometry. *Acta Oncol* **4,** 417–424.

Padovan M, Maccari M, Bosio A, Vizzaccaro S, Cestonaro I, Corrà M, Caccese M, Cerretti G, Fassan M, Zagonel V, et al. (2022). 289MO Next-generation sequencing (NGS) for identifying actionable molecular alterations in newly diagnosed and recurrent IDHwt-glioblastoma (GBM) patients: A large mono institutional experience. *Annals of Oncology* S671.

Pagotto A, Pilotto G, Mazzoldi EL, Nicoletto MO, Frezzini S, Pastò A, Amadori A (2017). Autophagy inhibition reduces chemoresistance and tumorigenic potential of human ovarian cancer stem cells. *Cell Death Dis* **7,** e2943-e2943.

Pandit R, Chen L, Götz J (2020). The blood-brain barrier: Physiology and strategies for drug delivery. *Adv Drug Deliv Rev* 1–14.

Papadopoulos C, Kirchner P, Bug M, Grum D, Koerver L, Schulze N, Poehler R, Dressler A, Fengler S, Arhzaouy K, et al. (2017). VCP/p97 cooperates with YOD1, UBXD1 and PLAA to drive clearance of ruptured lysosomes by autophagy. *EMBO J* **2,** 135–150.

Parsons DW, Jones S, Zhang X, Lin JC-H, Leary RJ, Angenendt P, Mankoo P, Carter H, Siu I-M, Gallia GL, et al. (2008). An integrated genomic analysis of human glioblastoma multiforme. *Science* **5897,** 1807–1812.

Peng K, Su G, Ji J, Yang X, Miao M, Mo P, Li M, Xu J, Li W, Yu C (2018). Histone demethylase JMJD1A promotes colorectal cancer growth and metastasis by enhancing Wnt/β-catenin signaling. *J Biol Chem* **27,** 10606–10619.

Perera RM, Stoykova S, Nicolay BN, Ross KN, Fitamant J, Boukhali M, Lengrand J, Deshpande V, Selig MK, Ferrone CR, et al. (2015). Transcriptional control of autophagy-lysosome function drives pancreatic cancer metabolism. *Nature* **7565,** 361–365.

Perez-Riverol Y, Csordas A, Bai J, Bernal-Llinares M, Hewapathirana S, Kundu DJ, Inuganti A, Griss J, Mayer G, Eisenacher M, et al. (2019). The PRIDE database and related tools and resources in 2019: improving support for quantification data. *Nucleic Acids Res* **D1** D442-D450.

Pestov DG, Strezoska Z, Lau LF (2001). Evidence of p53-dependent cross-talk between ribosome biogenesis and the cell cycle: effects of nucleolar protein Bop1 on G(1)/S transition. *Mol Cell Biol* **13,** 4246–4255.

Pfister AS (2019). Emerging Role of the Nucleolar Stress Response in Autophagy. *Front Cell Neurosci* 156.

Phillips HS, Kharbanda S, Chen R, Forrest WF, Soriano RH, Wu TD, Misra A, Nigro JM, Colman H, Soroceanu L, et al. (2006). Molecular subclasses of high-grade glioma predict prognosis,

delineate a pattern of disease progression, and resemble stages in neurogenesis. *Cancer Cell* **3,** 157–173.

Pinto V de, Messina A, Lane DJR, Lawen A (2010). Voltage-dependent anion-selective channel (VDAC) in the plasma membrane. *FEBS Lett* **9,** 1793–1799.

Plaut GW, Cook M, Aogaichi T (1983). The subcellular location of isozymes of NADP-isocitrate dehydrogenase in tissues from pig, ox and rat. *Biochim Biophys Acta* **2,** 300–308.

Podergajs N, Brekka N, Radlwimmer B, Herold-Mende C, Talasila KM, Tiemann K, Rajcevic U, Lah TT, Bjerkvig R, Miletic H (2013). Expansive growth of two glioblastoma stem-like cell lines is mediated by bFGF and not by EGF. *Radiol Oncol* **4,** 330–337.

Poulsen HE, Specht E, Broedbaek K, Henriksen T, Ellervik C, Mandrup-Poulsen T, Tonnesen M, Nielsen PE, Andersen HU, Weimann A (2012). RNA modifications by oxidation: a novel disease mechanism? *Free Radic Biol Med* **8,** 1353–1361.

Puissant A, Robert G, Fenouille N, Luciano F, Cassuto J-P, Raynaud S, Auberger P (2010). Resveratrol promotes autophagic cell death in chronic myelogenous leukemia cells via JNK-mediated p62/SQSTM1 expression and AMPK activation. *Cancer Res* **3,** 1042–1052.

Qiang L, Zhao B, Ming M, Wang N, He T-C, Hwang S, Thorburn A, He Y-Y (2014). Regulation of cell proliferation and migration by p62 through stabilization of Twist1. *Proc Natl Acad Sci U S A* **25,** 9241–9246.

Radulovic M, Schink KO, Wenzel EM, Nähse V, Bongiovanni A, Lafont F, Stenmark H (2018). ESCRT-mediated lysosome repair precedes lysophagy and promotes cell survival. *EMBO J* **21,**

Ran FA, Hsu PD, Wright J, Agarwala V, Scott DA, Zhang F (2013). Genome engineering using the CRISPR-Cas9 system. *Nat Protoc* **11,** 2281–2308.

Ranjan A, Kaushik I, Srivastava SK (2020). Pimozide Suppresses the Growth of Brain Tumors by Targeting STAT3-Mediated Autophagy. *Cells* **9,**

Ravi S, Alencar AM, Arakelyan J, Xu W, Stauber R, Wang C-CI, Papyan R, Ghazaryan N, Pereira RMAn Update to Hallmarks of Cancer. *Cureus* **5,**

Ravikumar B, Moreau K, Jahreiss L, Puri C, Rubinsztein DC (2010). Plasma membrane contributes to the formation of pre-autophagosomal structures. *Nat Cell Biol* **8,** 747–757.

Real PJ, Benito A, Cuevas J, Berciano MT, Juan A de, Coffer P, Gomez-Roman J, Lafarga M, Lopez-Vega JM, Fernandez-Luna JL (2005). Blockade of epidermal growth factor receptors chemosensitizes breast cancer cells through up-regulation of Bnip3L. *Cancer Res* **18,** 8151–8157.

Reisbeck L, Linder B, Tascher G, Bozkurt S, Weber KJ, Herold-Mende C, van Wijk S, Marschalek R, Schaefer L, Münch C, et al. (2023). The iron chelator and OXPHOS inhibitor VLX600 induces mitophagy and an autophagy-dependent type of cell death in glioblastoma cells. *Am J Physiol Cell Physiol* **6,** C1451-C1469.

Reynolds N, Salmon-Divon M, Dvinge H, Hynes-Allen A, Balasooriya G, Leaford D, Behrens A, Bertone P, Hendrich B (2012). NuRD-mediated deacetylation of H3K27 facilitates recruitment of Polycomb Repressive Complex 2 to direct gene repression. *EMBO J* **3,** 593–605.

Richardson DR, Kalinowski DS, Lau S, Jansson PJ, Lovejoy DB (2009). Cancer cell iron metabolism and the development of potent iron chelators as anti-tumour agents. *Biochim Biophys Acta* **7,** 702–717.

Robinson JM, Karnovsky MJ (1980). Evaluation of the polyene antibiotic filipin as a cytochemical probe for membrane cholesterol. *J Histochem Cytochem* **2,** 161–168.

Rodger CE, McWilliams TG, Ganley IG (2018). Mammalian mitophagy - from in vitro molecules to in vivo models. *FEBS J* **7,** 1185–1202.

Rodrigues T, Ferraz LS (2020). Therapeutic potential of targeting mitochondrial dynamics in cancer. *Biochem Pharmacol* 114282.

Rohlena J, Dong L-F, Ralph SJ, Neuzil J (2011). Anticancer drugs targeting the mitochondrial electron transport chain. *Antioxid Redox Signal* **12,** 2951–2974.

Romani M, Daga A, Forlani A, Pistillo MP, Banelli B (2019). Targeting of Histone Demethylases KDM5A and KDM6B Inhibits the Proliferation of Temozolomide-Resistant Glioblastoma Cells. *Cancers (Basel)* **6,**

Rouland L, Duplan E, Ramos Dos Santos L, Bernardin A, Katula KS, Manfioletti G, Idbaih A, Checler F, Da Alves Costa C (2021). Therapeutic potential of parkin as a tumor suppressor via transcriptional control of cyclins in glioblastoma cell and animal models. *Theranostics* **20,** 10047–10063.

Russo A, Esposito D, Catillo M, Pietropaolo C, Crescenzi E, Russo G (2013). Human rpL3 induces G_1/S arrest or apoptosis by modulating p21 (waf1/cip1) levels in a p53-independent manner. *Cell Cycle* **1,** 76–87.

Sagiv Y, Legesse-Miller A, Porat A, Elazar Z (2000). GATE-16, a membrane transport modulator, interacts with NSF and the Golgi v-SNARE GOS-28. *EMBO J* **7,** 1494–1504.

Salnikow K, Blagosklonny MV, Ryan H, Johnson R, Costa M (2000). Carcinogenic nickel induces genes involved with hypoxic stress. *Cancer Res* **1,** 38–41.

Sampson JH, Gunn MD, Fecci PE, Ashley DM (2020). Brain immunology and immunotherapy in brain tumours. *Nat Rev Cancer* **1,** 12–25.

Sampson JH, Heimberger AB, Archer GE, Aldape KD, Friedman AH, Friedman HS, Gilbert MR, Herndon JE, McLendon RE, Mitchell DA, et al. (2010). Immunologic escape after prolonged progression-free survival with epidermal growth factor receptor variant III peptide vaccination in patients with newly diagnosed glioblastoma. *J Clin Oncol* **31,** 4722–4729.

Sanati M, Binabaj MM, Ahmadi SS, Aminyavari S, Javid H, Mollazadeh H, Bibak B, Mohtashami E, Jamialahmadi T, Afshari AR, et al. (2022). Recent advances in glioblastoma multiforme therapy: A focus on autophagy regulation. *Biomed Pharmacother* 113740.

Sandoval-Acuña C, Torrealba N, Tomkova V, Jadhav SB, Blazkova K, Merta L, Lettlova S, Adamcová MK, Rosel D, Brábek J, et al. (2021). Targeting Mitochondrial Iron Metabolism Suppresses Tumor Growth and Metastasis by Inducing Mitochondrial Dysfunction and Mitophagy. *Cancer Res* **9,** 2289–2303.

Sanjana NE, Shalem O, Zhang F (2014). Improved vectors and genome-wide libraries for CRISPR screening. *Nat Methods* **8,** 783–784.

Santa F de, Totaro MG, Prosperini E, Notarbartolo S, Testa G, Natoli G (2007). The histone H3 lysine-27 demethylase Jmjd3 links inflammation to inhibition of polycomb-mediated gene silencing. *Cell* **6,** 1083–1094.

Sareddy GR, Viswanadhapalli S, Surapaneni P, Suzuki T, Brenner A, Vadlamudi RK (2017). Novel KDM1A inhibitors induce differentiation and apoptosis of glioma stem cells via unfolded protein response pathway. *Oncogene* **17,** 2423–2434.

Sawada M, Nakashima S, Banno Y, Yamakawa H, Hayashi K, Takenaka K, Nishimura Y, Sakai N, Nozawa Y (2000). Ordering of ceramide formation, caspase activation, and Bax/Bcl-2 expression during etoposide-induced apoptosis in C6 glioma cells. *Cell Death Differ* **9,** 761–772.

Schuster J, Lai RK, Recht LD, Reardon DA, Paleologos NA, Groves MD, Mrugala MM, Jensen R, Baehring JM, Sloan A, et al. (2015). A phase II, multicenter trial of rindopepimut (CDX-110) in newly diagnosed glioblastoma: the ACT III study. *Neuro Oncol* **6,** 854–861.

Schweichel JU, Merker HJ (1973). The morphology of various types of cell death in prenatal tissues. *Teratology* **3,** 253–266.

Serrano-Puebla A, Boya P (2016). Lysosomal membrane permeabilization in cell death: new evidence and implications for health and disease. *Ann N Y Acad Sci* **1,** 30–44.

Shalem O, Sanjana NE, Hartenian E, Shi X, Scott DA, Mikkelson T, Heckl D, Ebert BL, Root DE, Doench JG, et al. (2014). Genome-scale CRISPR-Cas9 knockout screening in human cells. *Science* **6166,** 84–87.

Shao S, Li S, Qin Y, Wang X, Yang Y, Bai H, Zhou L, Zhao C, Wang C (2014). Spautin-1, a novel autophagy inhibitor, enhances imatinib-induced apoptosis in chronic myeloid leukemia. *Int J Oncol* **5,** 1661–1668.

Sharif T, Ahn D-G, Liu R-Z, Pringle E, Martell E, Dai C, Nunokawa A, Kwak M, Clements D, Murphy JP, et al. (2016). The NAD(+) salvage pathway modulates cancer cell viability via p73. *Cell Death Differ* **4,** 669–680.

Shchors K, Massaras A, Hanahan D (2015). Dual Targeting of the Autophagic Regulatory Circuitry in Gliomas with Repurposed Drugs Elicits Cell-Lethal Autophagy and Therapeutic Benefit. *Cancer Cell* **4,** 456–471.

Shen H-M, Codogno P (2011). Autophagic cell death: Loch Ness monster or endangered species? *Autophagy* **5,** 457–465.

Shi DD, Anand S, Abdullah KG, McBrayer SK (2022). DNA damage in IDH-mutant gliomas: mechanisms and clinical implications. *J Neurooncol*

Shimizu S, Narita M, Tsujimoto Y (1999). Bcl-2 family proteins regulate the release of apoptogenic cytochrome c by the mitochondrial channel VDAC. *Nature* **6735,** 483–487.

Sim H-W, Lorrey S, Khasraw M (2023). Advances in Treatment of Isocitrate Dehydrogenase (IDH)-Wildtype Glioblastomas. *Curr Neurol Neurosci Rep*

Singh MM, Johnson B, Venkatarayan A, Flores ER, Zhang J, Su X, Barton M, Lang F, Chandra J (2015). Preclinical activity of combined HDAC and KDM1A inhibition in glioblastoma. *Neuro Oncol* **11,** 1463–1473.

Singh P, Lim B (2022). Targeting Apoptosis in Cancer. *Curr Oncol Rep* **3,** 273–284.

Singh SK, Clarke ID, Terasaki M, Bonn VE, Hawkins C, Squire J, Dirks PB (2003). Identification of a cancer stem cell in human brain tumors. *Cancer Res* **18,** 5821–5828.

Skowyra ML, Schlesinger PH, Naismith TV, Hanson PI (2018). Triggered recruitment of ESCRT machinery promotes endolysosomal repair. *Science* **6384,**

Smith PK, Krohn RI, Hermanson GT, Mallia AK, Gartner FH, Provenzano MD, Fujimoto EK, Goeke NM, Olson BJ, Klenk DC (1985). Measurement of protein using bicinchoninic acid. *Anal Biochem* **1,** 76–85.

Song Q, Meng B, Xu H, Mao Z (2020). The emerging roles of vacuolar-type ATPase-dependent Lysosomal acidification in neurodegenerative diseases. *Transl Neurodegener* **1,** 17.

Sotelo J, Briceño E, López-González MA (2006). Adding chloroquine to conventional treatment for glioblastoma multiforme: a randomized, double-blind, placebo-controlled trial. *Ann Intern Med* **5,** 337–343.

Stein MN, Bertino JR, Kaufman HL, Mayer T, Moss R, Silk A, Chan N, Malhotra J, Rodriguez L, Aisner J, et al. (2017). First-in-Human Clinical Trial of Oral ONC201 in Patients with Refractory Solid Tumors. *Clin Cancer Res* **15,** 4163–4169.

Steinbach JP, Weller M (2004). Apoptosis in Gliomas: Molecular Mechanisms and Therapeutic Implications. *J Neurooncol* **2,** 245–254.

Stirling DR, Swain-Bowden MJ, Lucas AM, Carpenter AE, Cimini BA, Goodman A (2021). CellProfiler 4: improvements in speed, utility and usability. *BMC Bioinformatics* **1,** 433.

Stupp R, Mason WP, van den Bent MJ, Weller M, Fisher B, Taphoorn MJB, Belanger K, Brandes AA, Marosi C, Bogdahn U, et al. (2005). Radiotherapy plus concomitant and adjuvant temozolomide for glioblastoma. *N Engl J Med* **10,** 987–996.

Stupp R, Taillibert S, Kanner A, Read W, Steinberg D, Lhermitte B, Toms S, Idbaih A, Ahluwalia MS, Fink K, et al. (2017). Effect of Tumor-Treating Fields Plus Maintenance Temozolomide vs Maintenance Temozolomide Alone on Survival in Patients With Glioblastoma: A Randomized Clinical Trial. *JAMA* **23,** 2306–2316.

Stupp R, Wong ET, Kanner AA, Steinberg D, Engelhard H, Heidecke V, Kirson ED, Taillibert S, Liebermann F, Dbalý V, et al. (2012). NovoTTF-100A versus physician's choice chemotherapy in recurrent glioblastoma: a randomised phase III trial of a novel treatment modality. *Eur J Cancer* **14,** 2192–2202.

Sui A, Han B, Ren W, He W, Gao C, Han X, Liu S, Zhang Y, Qi X, Guo X (2022). The Epigenetic Regulation of OLIG2 by Histone Demethylase KDM6B in Glioma Cells. *J Mol Neurosci* **5,** 939–946.

Sulistijo ES, MacKenzie KR (2006). Sequence dependence of BNIP3 transmembrane domain dimerization implicates side-chain hydrogen bonding and a tandem GxxxG motif in specific helix-helix interactions. *J Mol Biol* **5,** 974–990.

Sutton EC, McDevitt CE, Prochnau JY, Yglesias MV, Mroz AM, Yang MC, Cunningham RM, Hendon CH, DeRose VJ (2019). Nucleolar Stress Induction by Oxaliplatin and Derivatives. *J Am Chem Soc* **46,** 18411–18415.

Suvà ML, Tirosh I (2020). The Glioma Stem Cell Model in the Era of Single-Cell Genomics. *Cancer Cell* **5,** 630–636.

Suzuki K, Kubota Y, Sekito T, Ohsumi Y (2007). Hierarchy of Atg proteins in pre-autophagosomal structure organization. *Genes Cells* **2,** 209–218.

Szklarczyk D, Gable AL, Lyon D, Junge A, Wyder S, Huerta-Cepas J, Simonovic M, Doncheva NT, Morris JH, Bork P, et al. (2019). STRING v11: protein-protein association networks with

increased coverage, supporting functional discovery in genome-wide experimental datasets. *Nucleic Acids Res* **D1** D607-D613.

Tait SWG, Green DR (2010). Mitochondria and cell death: outer membrane permeabilization and beyond. *Nat Rev Mol Cell Biol* **9,** 621–632.

Takahashi Y, Coppola D, Matsushita N, Cualing HD, Sun M, Sato Y, Liang C, Jung JU, Cheng JQ, Mulé JJ, et al. (2007). Bif-1 interacts with Beclin 1 through UVRAG and regulates autophagy and tumorigenesis. *Nat Cell Biol* **10,**

Takahashi Y, Meyerkord CL, Hori T, Runkle K, Fox TE, Kester M, Loughran TP, Wang H-G (2011). Bif-1 regulates Atg9 trafficking by mediating the fission of Golgi membranes during autophagy. *Autophagy* **1,** 61–73.

Takeshige K, Baba M, Tsuboi S, Noda T, Ohsumi Y (1992). Autophagy in yeast demonstrated with proteinase-deficient mutants and conditions for its induction. *J Cell Biol* **2,** 301–311.

Tinhofer I, Bernhard D, Senfter M, Anether G, Loeffler M, Kroemer G, Kofler R, Csordas A, Greil R (2001). Resveratrol, a tumor-suppressive compound from grapes, induces apoptosis via a novel mitochondrial pathway controlled by Bcl-2. *FASEB J* **9,** 1613–1615.

Todo T, Ito H, Ino Y, Ohtsu H, Ota Y, Shibahara J, Tanaka M (2022). Intratumoral oncolytic herpes virus G47Δ for residual or recurrent glioblastoma: a phase 2 trial. *Nat Med* **8,** 1630–1639.

Torti SV, Manz DH, Paul BT, Blanchette-Farra N, Torti FM (2018). Iron and Cancer. *Annu Rev Nutr* 97–125.

Trachootham D, Alexandre J, Huang P (2009). Targeting cancer cells by ROS-mediated mechanisms: a radical therapeutic approach? *Nat Rev Drug Discov* **7,** 579–591.

Tsukada Y, Fang J, Erdjument-Bromage H, Warren ME, Borchers CH, Tempst P, Zhang Y (2006). Histone demethylation by a family of JmjC domain-containing proteins. *Nature* **7078,** 811–816.

Turton N, Cufflin N, Dewsbury M, Fitzpatrick O, Islam R, Watler LL, McPartland C, Whitelaw S, Connor C, Morris C, et al. (2022). The Biochemical Assessment of Mitochondrial Respiratory Chain Disorders. *Int J Mol Sci* **13,**

Tyanova S, Temu T, Sinitcyn P, Carlson A, Hein MY, Geiger T, Mann M, Cox J (2016). The Perseus computational platform for comprehensive analysis of (prote)omics data. *Nat Methods* **9,** 731–740.

Upton JW, Kaiser WJ, Mocarski ES (2012). DAI/ZBP1/DLM-1 complexes with RIP3 to mediate virus-induced programmed necrosis that is targeted by murine cytomegalovirus vIRA. *Cell Host Microbe* **3,** 290–297.

Vaheri A, Ruoslahti E, Westermark B, Ponten J (1976). A common cell-type specific surface antigen in cultured human glial cells and fibroblasts: loss in malignant cells. *J Exp Med* **1,** 64–72.

Vander Heiden MG, Li XX, Gottleib E, Hill RB, Thompson CB, Colombini M (2001). Bcl-xL promotes the open configuration of the voltage-dependent anion channel and metabolite passage through the outer mitochondrial membrane. *J Biol Chem* **22,** 19414–19419.

Vara-Perez M, Felipe-Abrio B, Agostinis P (2019). Mitophagy in Cancer: A Tale of Adaptation. *Cells* **5,**

Vargas JNS, Hamasaki M, Kawabata T, Youle RJ, Yoshimori T (2023). The mechanisms and roles of selective autophagy in mammals. *Nat Rev Mol Cell Biol* **3,** 167–185.

Veeriah S, Taylor BS, Meng S, Fang F, Yilmaz E, Vivanco I, Janakiraman M, Schultz N, Hanrahan AJ, Pao W, et al. (2010). Somatic mutations of the Parkinson's disease-associated gene PARK2 in glioblastoma and other human malignancies. *Nat Genet* **1,** 77–82.

Venneti S, Dunphy MP, Zhang H, Pitter KL, Zanzonico P, Campos C, Carlin SD, La Rocca G, Lyashchenko S, Ploessl K, et al. (2015). Glutamine-based PET imaging facilitates enhanced metabolic evaluation of gliomas in vivo. *Sci Transl Med* **274,** 274ra17.

Vercellino I, Sazanov LA (2022). The assembly, regulation and function of the mitochondrial respiratory chain. *Nat Rev Mol Cell Biol* **2,** 141–161.

Verhaak RGW, Hoadley KA, Purdom E, Wang V, Qi Y, Wilkerson MD, Miller CR, Ding L, Golub T, Mesirov JP, et al. (2010). Integrated genomic analysis identifies clinically relevant subtypes of glioblastoma characterized by abnormalities in PDGFRA, IDH1, EGFR, and NF1. *Cancer Cell* **1,** 98–110.

Vermes I, Haanen C, Steffens-Nakken H, Reutelingsperger C (1995). A novel assay for apoptosis. Flow cytometric detection of phosphatidylserine expression on early apoptotic cells using fluorescein labelled Annexin V. *J Immunol Methods* **1,** 39–51.

Villa GR, Hulce JJ, Zanca C, Bi J, Ikegami S, Cahill GL, Gu Y, Lum KM, Masui K, Yang H, et al. (2016). An LXR-Cholesterol Axis Creates a Metabolic Co-Dependency for Brain Cancers. *Cancer Cell* **5,** 683–693.

Villar VH, Merhi F, Djavaheri-Mergny M, Durán RV (2015). Glutaminolysis and autophagy in cancer. *Autophagy* **8,** 1198–1208.

Vinogradova M, Gehling VS, Gustafson A, Arora S, Tindell CA, Wilson C, Williamson KE, Guler GD, Gangurde P, Manieri W, et al. (2016). An inhibitor of KDM5 demethylases reduces survival of drug-tolerant cancer cells. *Nat Chem Biol* **7,** 531–538.

Wajant H (2002). The Fas signaling pathway: more than a paradigm. *Science* **5573,** 1635–1636.

Wang B, Fan X, Ma C, Lei H, Long Q, Chai Y (2016a). Downregulation of KDM4A Suppresses the Survival of Glioma Cells by Promoting Autophagy. *J Mol Neurosci* **2,** 137–144.

Wang C-W, Klionsky DJ (2003). The Molecular Mechanism of Autophagy. *Mol Med* **3-4** 65–76.

Wang ES, Frankfurt O, Orford KW, Bennett M, Flinn IW, Maris M, Konopleva M (2015). Phase 1 Study of CB-839, a First-in-Class, Orally Administered Small Molecule Inhibitor of Glutaminase in Patients with Relapsed/Refractory Leukemia. *Blood* **23,** 2566.

Wang H, Bedford FK, Brandon NJ, Moss SJ, Olsen RW (1999). GABA(A)-receptor-associated protein links GABA(A) receptors and the cytoskeleton. *Nature* **6714,** 69–72.

Wang L, Chang J, Varghese D, Dellinger M, Kumar S, Best AM, Ruiz J, Bruick R, Peña-Llopis S, Xu J, et al. (2013). A small molecule modulates Jumonji histone demethylase activity and selectively inhibits cancer growth. *Nat Commun* 2035.

Wang L, Yuan L, Zeng X, Peng J, Ni Y, Er JC, Xu W, Agrawalla BK, Su D, Kim B, et al. (2016b). A Multisite-Binding Switchable Fluorescent Probe for Monitoring Mitochondrial ATP Level Fluctuation in Live Cells. *Angew Chem Int Ed Engl* **5,** 1773–1776.

Wang N, Huang R, Yang K, He Y, Gao Y, Dong D (2022). Interfering with mitochondrial dynamics sensitizes glioblastoma multiforme to temozolomide chemotherapy. *J Cell Mol Med* **3,** 893–912.

Wang N, Li J, Xin Q, Xu N (2021). USP30-AS1 contributes to mitochondrial quality control in glioblastoma cells. *Biochem Biophys Res Commun* 31–37.

Wang Y, Liu N, Lu B (2019). Mechanisms and roles of mitophagy in neurodegenerative diseases. *CNS Neurosci Ther* **7,** 859–875.

Warburg O (1956). On the origin of cancer cells. *Science* **3191,** 309–314.

Warburg O, Wind F, Negelein E (1927). THE METABOLISM OF TUMORS IN THE BODY. *J Gen Physiol* **6,** 519–530.

Wei Y, Chiang W-C, Sumpter R, Mishra P, Levine B (2017). Prohibitin 2 Is an Inner Mitochondrial Membrane Mitophagy Receptor. *Cell* **1-2** 224-238.e10.

Weller M, Butowski N, Tran DD, Recht LD, Lim M, Hirte H, Ashby L, Mechtler L, Goldlust SA, Iwamoto F, et al. (2017). Rindopepimut with temozolomide for patients with newly diagnosed, EGFRvIII-expressing glioblastoma (ACT IV): a randomised, double-blind, international phase 3 trial. *Lancet Oncol* **10,** 1373–1385.

Wen PY, Stein A, van den Bent M, Greve J de, Wick A, Vos FYFL de, Bubnoff N von, van Linde ME, Lai A, Prager GW, et al. (2022). Dabrafenib plus trametinib in patients with BRAFV600E-mutant low-grade and high-grade glioma (ROAR): a multicentre, open-label, single-arm, phase 2, basket trial. *Lancet Oncol* **1,** 53–64.

Werneburg NW, Guicciardi ME, Bronk SF, Kaufmann SH, Gores GJ (2007). Tumor necrosis factor-related apoptosis-inducing ligand activates a lysosomal pathway of apoptosis that is regulated by Bcl-2 proteins. *J Biol Chem* **39,** 28960–28970.

White E (2012). Deconvoluting the context-dependent role for autophagy in cancer. *Nat Rev Cancer* **6,** 401–410.

Wiklund ED, Catts VS, Catts SV, Ng TF, Whitaker NJ, Brown AJ, Lutze-Mann LH (2010). Cytotoxic effects of antipsychotic drugs implicate cholesterol homeostasis as a novel chemotherapeutic target. *Int J Cancer* **1,** 28–40.

Wilhelm LP, Zapata-Muñoz J, Villarejo-Zori B, Pellegrin S, Freire CM, Toye AM, Boya P, Ganley IG (2022). BNIP3L/NIX regulates both mitophagy and pexophagy. *EMBO J* **24,** e111115.

Wilson TA, Karajannis MA, Harter DH (2014). Glioblastoma multiforme: State of the art and future therapeutics. *Surg Neurol Int* 64.

Wong YC, Holzbaur ELF (2014). Optineurin is an autophagy receptor for damaged mitochondria in parkin-mediated mitophagy that is disrupted by an ALS-linked mutation. *Proc Natl Acad Sci U S A* **42,** E4439-48.

Wu W, Tian W, Hu Z, Chen G, Huang L, Li W, Zhang X, Xue P, Zhou C, Liu L, et al. (2014). ULK1 translocates to mitochondria and phosphorylates FUNDC1 to regulate mitophagy. *EMBO Rep* **5,** 566–575.

Xie X, Lin W, Zheng W, Chen T, Yang H, Sun L, Huang F, Wang Z, Lin H, Chen L, et al. (2019). Downregulation of G2/mitotic-specific cyclinB1 triggers autophagy via AMPK-ULK1-dependent signal pathway in nasopharyngeal carcinoma cells. *Cell Death Dis* **2,** 94.

Xu J, Dang Y, Ren YR, Liu JO (2010). Cholesterol trafficking is required for mTOR activation in endothelial cells. *Proc Natl Acad Sci U S A* **10,** 4764–4769.

Xu J, Huang H, Peng R, Ding X, Jiang B, Yuan X, Xi J (2018). MicroRNA-30a increases the chemosensitivity of U251 glioblastoma cells to temozolomide by directly targeting beclinï¿½1 and inhibiting autophagy. *Exp Ther Med* 613.

Yalamarty SSK, Filipczak N, Li X, Subhan MA, Parveen F, Ataide JA, Rajmalani BA, Torchilin VP (2023). Mechanisms of Resistance and Current Treatment Options for Glioblastoma Multiforme (GBM). *Cancers (Basel)* **7,**

Yan C, Gong L, Chen L, Xu M, Abou-Hamdan H, Tang M, Désaubry L, Song Z (2020). PHB2 (prohibitin 2) promotes PINK1-PRKN/Parkin-dependent mitophagy by the PARL-PGAM5-PINK1 axis. *Autophagy* **3,** 419–434.

Yan Y, Xu Z, Dai S, Qian L, Sun L, Gong Z (2016). Targeting autophagy to sensitive glioma to temozolomide treatment. *J Exp Clin Cancer Res* 23.

Yang C, Sudderth J, Dang T, Bachoo RM, McDonald JG, DeBerardinis RJ (2009). Glioblastoma cells require glutamate dehydrogenase to survive impairments of glucose metabolism or Akt signaling. *Cancer Res* **20,** 7986–7993.

Yang G-J, Wang W, Mok SWF, Wu C, Law BYK, Miao X-M, Wu K-J, Zhong H-J, Wong C-Y, Wong VKW, et al. (2018). Selective Inhibition of Lysine-Specific Demethylase 5A (KDM5A) Using a Rhodium(III) Complex for Triple-Negative Breast Cancer Therapy. *Angew Chem Int Ed Engl* **40,** 13091–13095.

Yang G-J, Zhu M-H, Lu X-J, Liu Y-J, Lu J-F, Leung C-H, Ma D-L, Chen J (2021). The emerging role of KDM5A in human cancer. *J Hematol Oncol* **1,** 30.

Yang H, Liu Z, Yuan C, Zhao Y, Wang L, Hu J, Xie D, Wang L, Chen D (2015). Elevated JMJD1A is a novel predictor for prognosis and a potential therapeutic target for gastric cancer. *Int J Clin Exp Pathol* **9,** 11092–11099.

Yang J, Liu X, Bhalla K, Kim CN, Ibrado AM, Cai J, Peng TI, Jones DP, Wang X (1997). Prevention of apoptosis by Bcl-2: release of cytochrome c from mitochondria blocked. *Science* **5303,** 1129–1132.

Yang W-E, Ho C-C, Yang S-F, Lin S-H, Yeh K-T, Lin C-W, Chen M-K (2016). Cathepsin B Expression and the Correlation with Clinical Aspects of Oral Squamous Cell Carcinoma. *PLoS One* **3,** e0152165.

Young D, Guha C, Sidoli S (2023). The role of histone H3 lysine demethylases in glioblastoma. *Cancer Metastasis Rev* **2,** 445–454.

Yuan X, Zhou Y, Casanova E, Chai M, Kiss E, Gröne H-J, Schütz G, Grummt I (2005). Genetic inactivation of the transcription factor TIF-IA leads to nucleolar disruption, cell cycle arrest, and p53-mediated apoptosis. *Mol Cell* **1,** 77–87.

Yun HR, Jo YH, Kim J, Shin Y, Kim SS, Choi TG (2020). Roles of Autophagy in Oxidative Stress. *Int J Mol Sci* **9,**

Yung BY, Yang YH, Bor AM (1991). Nucleolar protein B23 translocation after deferoxamine treatment in a human leukemia cell line. *Int J Cancer* **5,** 779–784.

Zaman S, Wang R, Gandhi V (2014). Targeting the apoptosis pathway in hematologic malignancies. *Leuk Lymphoma* **9,** 1980–1992.

Zamzami N, El Hamel C, Maisse C, Brenner C, Muñoz-Pinedo C, Belzacq AS, Costantini P, Vieira H, Loeffler M, Molle G, et al. (2000). Bid acts on the permeability transition pore complex to induce apoptosis. *Oncogene* **54,** 6342–6350.

Zemrak WR, Kenna GA (2008). Association of antipsychotic and antidepressant drugs with Q-T interval prolongation. *Am J Health Syst Pharm* **11,** 1029–1038.

Zhang F, Xu C-L, Liu C-M (2015). Drug delivery strategies to enhance the permeability of the blood-brain barrier for treatment of glioma. *Drug Des Devel Ther* 2089–2100.

Zhang P, Xia Q, Liu L, Li S, Dong L (2020). Current Opinion on Molecular Characterization for GBM Classification in Guiding Clinical Diagnosis, Prognosis, and Therapy. *Front Mol Biosci* 562798.

Zhang S, Endo S, Koga H, Ichikawa T, Feng X, Onda K, Washiyama K, Kumanishi T (1996). A comparative study of glioma cell lines for p16, p15, p53 and p21 gene alterations. *Jpn J Cancer Res* **9,** 900–907.

Zhang T, Cooper S, Brockdorff N (2015). The interplay of histone modifications - writers that read. *EMBO Rep* **11,** 1467–1481.

Zhang X, Fryknäs M, Hernlund E, Fayad W, Milito A de, Olofsson MH, Gogvadze V, Dang L, Påhlman S, Schughart LAK, et al. (2014). Induction of mitochondrial dysfunction as a strategy for targeting tumour cells in metabolically compromised microenvironments. *Nat Commun* 3295.

Zhao R, Planalp RP, Ma R, Greene BT, Jones BT, Brechbiel MW, Torti FM, Torti SV (2004). Role of zinc and iron chelation in apoptosis mediated by tachpyridine, an anti-cancer iron chelator. *Biochem Pharmacol* **9,** 1677–1688.

Zhen Y, Stenmark H (2023). Autophagosome Biogenesis. *Cells* **4,**

Zhu H, Fearnhead HO, Cohen GM (1995). An ICE-like protease is a common mediator of apoptosis induced by diverse stimuli in human monocytic THP.1 cells. *FEBS Lett* **2,** 303–308.

Zhu H, Wang D, Liu Y, Su Z, Zhang L, Chen F, Zhou Y, Wu Y, Yu M, Zhang Z, et al. (2013). Role of the Hypoxia-inducible factor-1 alpha induced autophagy in the conversion of non-stem pancreatic cancer cells into CD133+ pancreatic cancer stem-like cells. *Cancer Cell Int* **1,** 119.

Zielke S, Meyer N, Mari M, Abou-El-Ardat K, Reggiori F, van Wijk SJL, Kögel D, Fulda S (2018). Loperamide, pimozide, and STF-62247 trigger autophagy-dependent cell death in glioblastoma cells. *Cell Death Dis* **10,** 994.

Zini R, Morin C, Bertelli A, Bertelli AA, Tillement JP (1999). Effects of resveratrol on the rat brain respiratory chain. *Drugs Exp Clin Res* **2-3** 87–97.

Zufferey R, Nagy D, Mandel RJ, Naldini L, Trono D (1997). Multiply attenuated lentiviral vector achieves efficient gene delivery in vivo. *Nat Biotechnol* **9,** 871–875.

10. Supplemental information

Table 33. Top 50 up- and downregulated proteins in U-251 cells measured by mass spectrometry. U-251 wt (A, B), sgEGFP (C, D) and *ATG5* KO (E, F) cells were exposed to 5 µM VLX600 for 24 h. Tables display the top 50 downregulated (A, C, E) or upregulated (B, D, F) proteins.

A) Top 50 downregulated proteins upon VLX600 treatment in U-251 wt cells.

Gene Name	log2 VLX600/DMSO	-log10 adj. p-value
CDKN3	-2,864968384	6,76932555
FADS2	-2,650948411	9,43982251
ZFAND5	-2,522793717	7,56183344
TRIM44	-2,386718732	7,09042288
KIF20A	-2,306081518	10,4451436
CCNF	-2,282167465	7,18340819
CKS2	-2,2142967	10,0533729
PLK1	-2,158114131	9,05276398
ASPM	-2,02998031	7,96732815
CCNB1	-2,027494006	11,6755164
CDC6	-2,010798893	10,1045535
CEBPB	-2,009694104	10,1045535
PI15	-1,946141481	3,960369
ENC1	-1,92535164	10,5033787
GEM	-1,881372194	7,1602939
NRP2	-1,861516195	5,21853752
H3-2	-1,86070858	6,69072245
NUSAP1	-1,815091265	10,1815826
IL7R	-1,799738835	3,83693357
CENPE	-1,751049792	11,1449934
SOX21	-1,736042729	9,23970382
UBE2C	-1,721889515	9,2890133
MBD4	-1,705210169	9,16665302
UBE2T	-1,684639395	9,30543685
TFAP4	-1,669664374	6,46519855
ADI1	-1,634450724	9,66845394
ORC6	-1,630504448	9,35587593
CDC20	-1,614116918	7,41306297
GPSM2	-1,612262082	7,79546705
SPDL1	-1,601971614	9,72926019
CHEK1	-1,524538821	9,03457259
SMIM26	-1,501152718	4,54006893
SQSTM1	-1,491036005	10,1045535
FADS3	-1,473852436	6,64016877
PRR11	-1,429034376	7,56183344
SLC38A2	-1,427335674	6,12167394
TEX30	-1,42584108	5,58812931
STK17B	-1,423324129	6,21419902
SESTD1	-1,422815887	5,19923361
AURKA	-1,398626437	10,5407478

Gene Name	log2 VLX600/DMSO	-log10 adj. p-value
CCNB2	-1,389989704	8,45261833
FDX1	-1,389157463	7,41306297
TCF12	-1,383136328	6,86171988
MIS18A	-1,382147327	8,56798948
STAT2	-1,37766424	8,30571213
IFRD1	-1,374965386	7,92502521
TRO	-1,373825212	2,54967054
ZNF706	-1,365075387	5,89739953
SDC2	-1,341496276	9,49309178
ZFAND6	-1,332878823	7,77760042

B) Top 50 upregulated proteins upon VLX600 treatment in U-251 wt cells.

Gene Name	log2 VLX600/DMSO	-log10 adj. p-value
BNIP3	3,4845419	7,8882745
IGFBP3	3,42527935	9,35587593
MAFF	3,17030271	6,96508116
PFKFB4	3,14153764	9,50116819
AK4	3,0696021	10,1045535
RCOR2	2,96723013	6,81080938
PLOD2	2,88007292	7,99076213
CRABP2	2,84483445	7,50450476
CA9	2,68615717	6,83177487
COL11A1	2,67105931	10,5549423
P4HA2	2,63270366	6,70367015
COL4A2	2,5713027	8,63503463
SLC2A3	2,53489555	5,41045583
RAB20	2,5324969	7,74078764
COL4A1	2,52007165	7,2995262
DUSP9	2,50614946	4,62925401
S100P	2,46782289	7,45811023
SLC16A3	2,41751246	5,92363974
NDRG1	2,36666386	6,76932555
ZNF395	2,28724208	8,82715028
ATF3	2,25927961	4,76739063
P4HA1	2,12092335	8,38235263
EGLN1	2,02259268	10,1045535
HK2	2,01553005	9,66726984
KDM3A	1,96867453	11,7477063
GLRX	1,91221415	5,08577347
ERO1A	1,90855413	10,1045535
CDH5	1,80819613	6,77681442
ENO2	1,80512932	10,5549423
L1CAM	1,79971498	2,3939337
ERRFI1	1,78743707	8,36292877
SLC6A8	1,78523947	4,81263942
PPP2R5B	1,74869499	5,34157983

Gene Name	log2 VLX600/DMSO	-log10 adj. p-value
COL6A1	1,74563636	8,53675692
GFPT2	1,73843511	8,53675692
LOXL2	1,69715154	9,32442083
THEMIS	1,6896988	3,11194935
GYS1	1,6873992	6,53411319
FAM162A	1,65768403	9,32442083
PFKFB3	1,63638853	8,43790844
FOSL1	1,52395815	4,9945765
KDM4B	1,485035	10,1045535
FAM117B	1,4823311	6,72894248
COL6A2	1,48098002	2,86820751
JAG1	1,47505952	7,30658255
TTYH3	1,42681482	6,75765483
IGFBP2	1,41838006	4,43312626
JUN	1,39269093	9,66845394
GBE1	1,38947677	9,3058371
CHSY1	1,33797459	7,64861392

C) TOP 50 downregulated proteins after VLX600 treatment in U-251 sgEGFP cells.

Gene Name	log2 VLX600/DMSO	-log10 adj. p-value
PLK1	-2,97851725	10,6708281
CCNF	-2,84218853	8,3685342
FADS2	-2,62308643	9,46264454
KIF20A	-2,54227735	10,9822582
CKAP2L	-2,52811801	2,05255605
CDKN3	-2,42502385	5,96633057
ZFAND5	-2,40003298	7,38134772
CDC6	-2,25301409	10,7596377
CEBPG	-2,22097289	3,42048945
CEBPB	-2,2002053	10,5825054
CCNB1	-1,97837071	11,6801561
ASPM	-1,95262994	7,83761375
TRIM44	-1,94245065	6,08785023
GEM	-1,92286637	7,2930183
H3-2	-1,89676342	6,80409154
MDM2	-1,89473213	2,54293341
CKS2	-1,88741627	9,34656495
ENC1	-1,78964453	10,321256
CBX6	-1,78526266	4,6699172
CENPE	-1,77559585	11,2419518
NRP2	-1,72331259	4,91252414
SOX21	-1,70520886	9,19761227
UBE2C	-1,70323827	9,29740552
NUSAP1	-1,67818513	10,0338637

Gene Name	log2 VLX600/DMSO	-log10 adj. p-value
PI15	-1,67416529	3,44747901
SPDL1	-1,56224717	9,75154419
ORC6	-1,55450507	9,19453918
MBD4	-1,55083379	8,72032094
UBE2T	-1,55000637	8,91584582
ATAD2	-1,53220421	9,02490043
TCF12	-1,52997399	7,4105872
ZNF706	-1,52709726	6,50847404
PRR11	-1,5035064	7,8936849
NSMCE1	-1,48951317	1,69467302
ADI1	-1,48699847	9,29740552
CDC20	-1,47978868	7,00317359
BLM	-1,46875871	1,35964985
CHEK1	-1,45191805	8,82896657
NDUFV2	-1,44958681	4,22794413
ZNF568	-1,44715109	6,69334667
GYG1	-1,43999301	3,10866858
AURKA	-1,42523839	10,7596377
ZFAND6	-1,42304396	8,18518699
IFRD1	-1,42253308	8,18518699
TSPYL1	-1,40493403	6,42309259
PHF20	-1,40242528	1,51937677
SDC2	-1,39879893	9,79062603
POLE	-1,38368549	10,3779782
OSGIN1	-1,36668911	7,69094473
MIS18A	-1,36165002	8,53764438

D) Top 50 upregulated proteins after VLX600 treatment in U-251 sgEGFP cells.

Gene Name	log2 VLX600/DMSO	-log10 adj. p-value
IGFBP3	4,01357188	10,1548279
MAFF	3,74595554	7,81303045
BNIP3	3,74219883	8,30570836
PFKFB4	3,63700109	10,2693368
PLOD2	3,13722737	8,45527575
CRABP2	3,07496165	7,94477847
AK4	3,03219602	10,1548279
SLC16A3	2,94213218	6,85828487
RCOR2	2,93986617	6,79133975
DUSP9	2,79574357	5,1824514
P4HA2	2,74093666	6,90873146
COL4A2	2,68095021	8,89952985
COL11A1	2,6684783	10,7596377
CA9	2,6357345	6,76802471
NDRG1	2,59538905	7,21594419

Gene Name	log2 VLX600/DMSO	-log10 adj. p-value
COL4A1	2,56310709	7,42220383
ZNF395	2,53334582	9,42901637
ATF3	2,45978296	5,23287591
RAB20	2,37503373	7,46441074
GLRX	2,22802219	5,85106445
S100P	2,20283107	6,94192874
GFPT2	2,19702462	9,75928918
EGLN1	2,1665059	10,5454818
SLC6A8	2,14728998	5,71098952
HK2	2,14600473	10,0550094
L1CAM	2,12979164	2,97690313
ERO1A	2,07604222	10,5558385
FAM162A	2,0688576	10,4430694
KDM3A	2,0396014	11,9957448
COL6A2	2,02447718	4,10801659
P4HA1	2,02129952	8,21029249
ENO2	2,00823973	11,1999289
ERRFI1	1,96030695	8,89952985
LOXL2	1,95003872	10,0870981
CDH5	1,94662984	7,17459945
GYS1	1,85523709	7,00198247
PPP2R5B	1,83903304	5,64954883
PFKFB3	1,83736026	9,09205935
COL6A1	1,80051326	8,73816522
SLC2A3	1,77822617	3,8454892
IGFBP2	1,70293396	5,29352598
GBE1	1,69236127	10,3104929
UPP	1,68339959	5,51388289
KDM4B	1,6546809	10,7596377
FAM117B	1,63530192	7,24897131
THEMIS	1,61042041	2,99167064
JUN	1,59258068	10,3819969
MCFD2	1,59255881	4,58434268
JAG1	1,56877666	7,67469204
FOSL1	1,54487874	5,11359313

E) Top 50 downregulated proteins after VLX600 treatment in U-251 *ATG5* KO cells.

Gene Name	log2 VLX600/DMSO	-log10 adj. p-value
CCNF	-2,66406522	7,94480404
PLK1	-2,58770575	9,953957
CDKN3	-2,35867292	5,77004641
KIF20A	-2,30860197	10,5873895
FADS2	-2,25156569	8,65030315
ZFAND5	-2,24536307	6,97798795

Gene Name	log2 VLX600/DMSO	-log10 adj. p-value
ASPM	-2,01769817	7,92604946
CKS2	-2,00994708	9,61660507
PI15	-1,96550562	3,99636198
CCNB1	-1,9653052	11,4642505
CENPE	-1,86624581	11,4642505
CEBPB	-1,85844364	9,74250583
SOX21	-1,80319625	9,42148132
ENC1	-1,78322486	10,2753272
TRIM44	-1,76787752	5,55351662
IL7R	-1,7086419	3,61569876
UBE2C	-1,69692647	9,1900799
NUSAP1	-1,69426784	9,95425055
GEM	-1,64976502	6,4994944
NRP2	-1,64331223	4,61760897
H3-2	-1,6228786	6,02911353
CDC6	-1,58457712	9,06174729
MLLT11	-1,58034151	4,07554041
KIF18A	-1,54384934	7,23592421
GPSM2	-1,53767745	7,51375549
IFRD1	-1,52026778	8,44803223
CBX6	-1,50463213	3,84694498
STAT2	-1,46833	8,64958421
UBE2T	-1,4365618	8,44252296
STK17B	-1,43150564	6,24494056
AURKA	-1,41413931	10,7737683
MBD4	-1,41166349	8,13997803
BUB1	-1,32640936	7,62796667
ADI1	-1,32537427	8,62858741
CHEK1	-1,32247093	8,25584072
SPDL1	-1,32164544	8,83586275
SDC2	-1,3212868	9,45851467
ORC6	-1,30900836	8,18625848
ZNF568	-1,3060187	6,13399654
TCF12	-1,3026537	6,57107637
CDC20	-1,28005617	6,24179157
IFNGR1	-1,27913544	2,46559572
SGCE	-1,27764227	6,84770445
SESTD1	-1,27209476	4,65570347
MIS18A	-1,26865583	8,08715303
C12orf45	-1,26434907	6,82060405
OSGIN1	-1,26219258	7,18993583
FDX1	-1,25703503	6,89051571
ABHD4	-1,25556976	7,06711189
IVNS1ABP	-1,25477098	2,90321832

F) Top 50 upregulated proteins after VLX600 treatment in U-251 *ATG5* KO cells.

Gene Name	log2 VLX600/DMSO	-log10 adj. p-value
BNIP3	4,06295519	8,65122253
IGFBP3	3,5997672	9,61660507
MAFF	3,46632465	7,34328633
SLC16A3	3,41111026	7,45521942
PFKFB4	3,39228951	9,88175585
PLOD2	3,36960282	8,74305637
P4HA2	3,28734268	7,64700834
CRABP2	3,14983665	7,97195019
RCOR2	3,12028363	7,00063365
COL4A1	3,06799996	8,18625848
COL11A1	3,06638779	11,2320445
AK4	3,02841607	10,0391308
COL4A2	2,90297566	9,21457893
CA9	2,75452405	6,92491911
NDRG1	2,5198567	7,00063365
P4HA1	2,43293649	9,06174729
S100P	2,41448556	7,32323901
HK2	2,40369238	10,5233507
ZNF395	2,35653114	9,03617987
GFPT2	2,33731623	9,95425055
EGLN1	2,26856955	10,7737683
KDM3A	2,24370831	12,6652623
GLRX	2,21992265	5,77748745
FAM162A	2,20884713	10,7737683
RAB20	2,18232157	6,94067029
ERRFI1	2,1800418	9,38706474
ERO1A	2,17352034	10,7737683
PPP2R5B	2,12258643	6,3353834
CDH5	2,11675644	7,51057497
COL6A2	2,03299941	4,06173733
DUSP9	2,01519339	3,70406355
COL6A1	2,00497896	9,24516295
L1CAM	1,94052718	2,62041147
ENO2	1,888783	10,8407259
SLC6A8	1,88187747	5,03375177
LOXL2	1,84090669	9,74250583
GYS1	1,83014603	6,88847631
PFKFB3	1,75330304	8,80933076
ITGA5	1,73254496	6,27347012
KDM4B	1,67841527	10,7737683
JAG1	1,63280585	7,80335991
MCFD2	1,63059047	4,61872369
ATF3	1,59661725	3,27060019

Gene Name	log2 VLX600/DMSO	-log10 adj. p-value
TTYH3	1,57599009	7,18993583
UPP	1,56263101	5,08643565
GBE1	1,56150497	9,85649904
MGAT5	1,55636275	7,87547254
FAM117B	1,53111343	6,85992529
IGFBP2	1,50901424	4,68839888
PLXNB3	1,50038054	4,31132527

Table 34. RNA polymerase subunits significantly (adj. p-value ≥ 1.3) downregulated in U-251 cells measured by mass spectrometry. U-251 wt (A), sgEGFP (B) and *ATG5* KO (C) cells were exposed to 5 µM VLX600 for 24 h.

A) Significantly downregulated proteins after VLX600 treatment in U-251 wt cells.

Gene Name	log2 VLX600/DMSO	-log10 adj. p-value
POLR3C	-1.11897198	7.22579937
POLR2J	-0.72372567	5.93338939
POLR3F	-0.68634808	4.81985744
POLR3B	-0.62152967	4.84173455
POLR3G	-0.60694038	2.83058344
POLR2L	-0.59684176	4.45243176
POLR2K	-0.57979759	2.7940572
POLR2B	-0.51120466	7.43416167
POLR3A	-0.47602418	5.68869272
POLR2C	-0.47023681	5.09770314
POLR2D	-0.41980274	1.46153944
POLR2G	-0.3422774	4.02396501
POLR1F	-0.30918121	3.00466211
POLR2A	-0.29446698	4.6772194
POLR1A	-0.25406687	2.91726114
POLR2E	-0.2273499	1.47605761
POLR1B	-0.18557553	1.55788009
POLR1E	-0.16192489	1.34819126

B) Significantly downregulated proteins after VLX600 treatment in U-251 sgEGFP cells.

Gene Name	log2 VLX600/DMSO	-log10 adj. p-value
POLR3C	-1.08518538	7.09815092
POLR3D	-1.01052105	2.85561999
POLR2J	-0.72007644	5.97341232
POLR3F	-0.56410344	3.98740161
POLR3A	-0.51387702	6.1258596
POLR2B	-0.4823322	7.18339575

Gene Name	log2 VLX600/DMSO	-log10 adj. p-value
POLR2L	-0.45391642	3.35387778
POLR2A	-0.3742134	5.89636694
POLR3B	-0.34238006	2.52426284
POLR2G	-0.31894454	3.7827818
POLR2C	-0.31520555	3.39801485
POLR1F	-0.30774862	3.04555895
POLR1A	-0.25594071	3.00057416

C) Significantly downregulated proteins after VLX600 treatment in U-251 *ATG5* KO cells.

Gene Name	log2 VLX600/DMSO	-log10 adj. p-value
POLR3C	-0.85852405	5.8769397
POLR2J	-0.70525074	5.80993276
POLR3D	-0.67608397	1.64495116
POLR2D	-0.54007297	2.06344146
POLR3F	-0.51750358	3.57029606
POLR3B	-0.46797275	3.58313414
POLR3A	-0.44496517	5.34691351
POLR2B	-0.43120992	6.58640042
POLR2L	-0.4259859	3.05352265
POLR2K	-0.34474157	1.39727654
POLR2C	-0.32339008	3.43424968
POLR1F	-0.3051444	2.95547154
POLR2G	-0.29423169	3.39382612
POLR2A	-0.26296485	4.14784108
POLR1A	-0.24199194	2.74750991
POLR2E	-0.20909415	1.31480477

Table 35. Histone demethylases significantly (adj. p-value ≥ 1.3) down- or upregulated in U-251 cells measured by mass spectrometry. U-251 wt (A), sgEGFP (B) and *ATG5* KO (C) cells were exposed to 5 µM VLX600 for 24 h.

A) Significantly down- or upregulated proteins after VLX600 treatment in U-251 wt cells.

Gene Name	log2 VLX600/DMSO	-log10 adj. p-value
KDM1B	-0.47117826	3.35618481
JMJD1C	-0.35426212	2.24810208
KDM5A	-0.30805238	3.2356989
KDM1A	-0.17539471	3.23029365
KDM4A	0.26605048	1.85286038
KDM2A	0.38865842	5.00197396
KDM5B	0.41231274	1.73085414
KDM2B	0.52817147	3.68259373
JMJD6	0.54986371	4.6208321
KDM5C	0.65279979	5.14120438
KDM4B	1.485035	10.1045535
KDM3A	1.96867453	11.7477063

B) Significantly down- or upregulated proteins after VLX600 treatment in U-251 sgEGFP cells.

Gene Name	log2 VLX600/DMSO	-log10 adj. p-value
JMJD1C	-0.36987704	2.44064813
KDM5A	-0.36094758	3.92121902
KDM1B	-0.30960235	2.03420492
KDM1A	-0.15658161	2.87544112
KDM4A	0.34129121	2.63718898
KDM2A	0.38868379	5.05124819
KDM5B	0.39115952	1.65835662
KDM2B	0.5385332	3.82029423
KDM5C	0.67277652	5.34758146
JMJD6	0.69516098	5.81487455
KDM4B	1.6546809	10.7596377
KDM3A	2.0396014	11.9957448

C) Significantly down- or upregulated proteins after VLX600 treatment in U-251 *ATG5* KO cells.

Gene Name	log2 VLX600/DMSO	-log10 adj. p-value
KDM1B	-0.48993144	3.50645071
JMJD1C	-0.28234082	1.65717405
KDM5A	-0.23307443	2.28456141

Gene Name	log2 VLX600/DMSO	-log10 adj. p-value
KDM1A	-0.10308653	1.62256558
KDM4A	0.24813102	1.686488
KDM2A	0.40180869	5.14835884
KDM5B	0.4305332	1.84130197
JMJD6	0.58569284	4.90359718
KDM2B	0.58832901	4.13083926
KDM5C	0.71007885	5.55356811
KDM4B	1.67841527	10.7737683
KDM3A	2.24370831	12.6652623

11. Appendix

11.1. Abbreviations

Table 36. Abbreviations.

ADCD	autophagy-dependent cell death
ADP	adenosine diphosphate
AMBRA1	autophagy and beclin 1 regulator 1
ATG	autophagy-related gene
ATP	adenosine triphosphate
BAK1	BCL2 antagonist/killer 1
BAX	BCL2 associated X, apoptosis regulator
BBB	blood-brain barrier
BCA	bicinchoninic acid
BCL2	BCL2 apoptosis regulator
BECN1	beclin 1
BID	BH3 interacting domain death agonist
BNIP3	BCL2 interacting protein 3
BNIP3L/NIX	BCL2 interacting protein 3 like
CDKN2A	cyclin dependent kinase inhibitor 2A
cDNA	complementary DNA
con	control
COX4I1	cytochrome c oxidase subunit 4I1
CSC	cancer stem cell
CT	threshold cycle
CTSB	cathepsin B
CTSD	cathepsin D
CYBB/NOX2	cytochrome b-245 beta chain
DFP	deferiprone
DNA	deoxyribonucleic acid
DPBS	Dulbecco's Phosphate-Buffered Saline
DRD2	dopamine receptor D2
EGFP	enhanced green fluorescent protein
EGFR	epidermal growth factor receptor

em	emission
ER	endoplasmic reticulum
ETC	electron transport chain
ex	excitation
FC	fold change
FCS	fetal calf serum
Fe-S	iron-sulfur
FIASMA	functional inhibitor of acid sphingomyelinase
FUNDC1	FUN14-domain containing 1
GABARAP	GABA type A receptor-associated protein
GAPDH	glyceraldehyde 3-phosphate dehydrogenase
GBM	glioblastoma
GFP	green fluorescent protein
GO	gene ontology
GSC	glioma stem-like cell
h	hour(s)
HCl	hydrochloric acid
HIF1A	hypoxia-inducible factor 1 α
HK2	hexokinase 2
HSPD1/HSP60	heat shock protein family D (Hsp60) member 1
HTR7/5-HT7	5-hydroxytryptamine receptor 7
IDH	isocitrate dehydrogenase
IMM	inner mitochondrial membrane
IMS	intermembrane space
JmjC	Jumonji C
JMJD	Jumonji C domain-containing
KD	knockdown
KDM1A/B	lysine demethylase 1A/B
KDM3A	lysine demethylase 3A
KDM4	lysine demethylase 4
KDM5A-D	lysine demethylase 5A-D
KDM6	lysine demethylase 6
KO	knockout

LAMP1/2	lysosomal associated membrane protein 1/2
LAP	LC3-associated phagocytosis
LDCD	lysosome-dependent cell death
LGALS3/Gal3	galectin 3
LIR	MAP1LC3-interacting region
LMP	lysosomal membrane permeabilization
MAP1LC3/LC3	microtubule associated protein 1 light chain 3
MCD	mitophagic cell death
min	minute(s)
MOMP	mitochondrial outer membrane permeabilization
mRFP	monomeric red fluorescent protein
mRNA	messenger RNA
mtDNA	mitochondrial DNA
mTOR	mammalian target of rapamycin
mTORC1	mammalian target of rapamycin complex 1
mtROS	mitochondrial ROS
MTT	3-(4,5-dimethylthiazol-2-yl)-2,5-diphenyltetrazolium bromide
NADH/NAD^+	nicotinamide adenine dinucleotide
NDRG1	N-myc downstream regulated 1
NPM1	nucleophosmin 1
ns	not significant
OLIG2	oligodendrocyte transcription factor 2
OMM	outer mitochondrial membrane
OTC	organotypic brain tissue slice culture
OXPHOS	oxidative phosphorylation
P/S	penicillin/streptomycin
PDGFRA	platelet derived growth factor receptor alpha
PE	phosphatidylethanolamine
PFA	paraformaldehyde
PHD	prolyl hydroxylase
PI	propidium iodide
PIK3C3/VPS34	phosphatidylinositol 3-kinase catalytic subunit type 3
PIK3CA	phosphatidylinositol-4,5-bisphosphate 3-kinase catalytic subunit alpha

PINK1	PTEN-induced kinase 1
PRKAA2/AMPK	protein kinase AMP-activated catalytic subunit alpha 2
PRKN/Parkin	parkin RBR E3 ubiquitin protein ligase
PS	phosphatidylserine
PTEN	phosphatase and tensin homolog
qRT-PCR	quantitative real time polymerase chain reaction
RB1CC1	RB1 inducible coiled-coil 1
RCD	regulated cell death
RNA	ribonucleic acid
ROS	reactive oxygen species
RPS6	ribosomal protein S6
rRNA	ribosomal RNA
RUBCN	rubicon autophagy regulator
SDS-Page	sodium dodecyl sulfate polyacrylamide gel electrophoresis
sec	second(s)
SEM	standard error of the mean
sgRNA	single guide RNA
shRNA	small hairpin RNA
siRNA	small interfering RNA
SLC2A1/GLUT1	solute carrier family 2 member 1
SLC45A1	solute carrier family 45 member 1
SMPD1	sphingomyelin phosphodiesterase 1
SQSTM1/p62	sequestosome 1
SREBP2	sterol regulatory element binding protein 2
TCA	tricarboxylic acid
TMRM	tetramethylrhodamine
TMZ	temozolomide
TOMM20	translocase of outer mitochondrial membrane 20
TP53/p53	tumor protein p53
TP73	tumor protein 73
TTF	tumor treating fields
ULK1/2	unc-51 like autophagy activating kinase 1/2
UPRmt	mitochondrial unfolded protein response

VCP/p97	valosin containing protein
VDAC	voltage dependent anion channel
wt	wildtype

11.2. Figures

11.3. Tables

12. Collaborative work

Whenever a figure, table or text is identical to a previous publication, it is stated explicitly in the figure legend. The following figures or parts of them have been previously published:

> Figure 1 – Figure 6, Figure 9, Figure 11 – Figure 19, Figure 21 – Figure 22, Figure 25 – Figure 31, Figure 34, Figure 36, Figure 38 – Figure 42, Figure 45 – Figure 49, Figure 53 – Figure 55, Figure 57 – Figure 59, Figure 64 – Figure 68.

The following tables or parts of them have been previously published:

> Table 1 – Table 3, Table 33 – Table 35.

Except where stated otherwise by reference or acknowledgment, the work presented was generated by myself under the supervision of my advisors during my doctoral studies. All contributions from colleagues are explicitly referenced in the thesis. The material listed below was obtained in the context of collaborative research:

<u>Figure 15, Figure 16, Figure 17 and Figure 26:</u>

LN-229 *ATG7* KO cells and MZ-54 wt, *ATG5* and *ATG7* KO cells with stable expression of the pMRX-LC3 reporter plasmid were generated by Dr. Svenja Zielke (working group of Prof. Dr. Simone Fulda, Experimental Cancer Research in Pediatrics, Goethe University Hospital, Frankfurt/Main, Germany) (Zielke et al. 2018; Meyer*, Henkel* et al. 2021).

MZ-54 *ATG5* and *ATG7* KO cells were generated by Dr. Nina Meyer (working group of Prof. Dr. Donat Kögel, Experimental Neurosurgery, Goethe University, Frankfurt/Main, Germany) (Zielke et al. 2018; Meyer*, Henkel* et al. 2021).

<u>Figure 23 and Figure 24:</u>

NCH644^{GFP+} wt and NCH421K^{GFP+} spheres were generated by Caterina Roth and Julia Gerstmeier (working group of Prof. Dr. Donat Kögel, Experimental Neurosurgery, Goethe University, Frankfurt/Main, Germany) (Gerstmeier et al. 2021).

Figure 42:

U-251 sgEGFP and *ATG5* KO cells stably expressing the pCHAC-mt-mKeima plasmid as well as the associated measurement of mitophagy induction using flow cytometry was performed by Süleyman Bozkurt (working group of Dr. Christian Münch, Institute of Biochemistry II, Goethe University Hospital Frankfurt/Main, Germany) (Reisbeck et al. 2023).

Figure 53:

GS-5 GFP-Luc cells were generated by Dr. Bushra Rais and Stephan Müller (working group of Prof. Dr. Evelyn Ullrich, Pediatric Stem Cell Transplantation and Immunology, Goethe University Hospital Frankfurt/Main, Germany) (Linder et al. 2019).

Figure 59, Figure 62 and Figure 63:

Liquid chromatography and mass spectrometry (LC-MS/MS) of U-251 wt, sgEGFP and *ATG5* KO cells treated with VLX600 was performed by Dr. Georg Tascher (working group of Dr. Christian Münch, Institute of Biochemistry II, Goethe University Hospital Frankfurt/Main, Germany) (Reisbeck et al. 2023).

Figure 64:

Immunohistochemistry of U-251 cells treated with VLX600 was performed by Dr. Katharina J. Weber (Neurological Institute (Edinger Institute), Goethe University Hospital, Frankfurt/Main, Germany) (Reisbeck et al. 2023).